ULTRASOUND CONTRAST AGENTS

DYNAMICS OF COATED BUBBLES

Marlies Overvelde

ULTRASOUND CONTRAST AGENTS

DYNAMICS OF COATED MICROBUBBLES

Marlies Overvelde

Samenstelling promotiecommissie:

Prof. dr. G. van der Steenhoven (voorzitter, secretaris)	Universiteit Twente, TNW
Prof. dr. rer. nat. D. Lohse (promotor)	Universiteit Twente, TNW
Prof. dr. ir. N. de Jong (promotor)	Universiteit Twente, TNW
Dr. A.M. Versluis (assistent promotor)	Universiteit Twente, TNW
Prof. dr. ir. A.J. Huis in ’t Veld	Universiteit Twente, CTW
Prof. dr. J.L. Herek	Universiteit Twente, TNW
Prof. dr. C.C. Church	University of Mississippi
Dr. P. Marmottant	Université Joseph Fourier

The research described in this thesis is part of the research program of TAMIRUT a Specific Targeted Research (STReP) project supported by the 6th Framework Programme of the European Commission in the Nanosciences, Nanotechnologies, Materials and new Production Technologies area under contract number NMP4-CT-2005-016382. This thesis was carried out at the Physics of Fluids group of the Faculty of Science and Technology of the University of Twente.
Nederlandse titel:
Ultrageluid contrast vloeistoffen - dynamica van gecoate bellen

Publisher:
Marlies Overvelde, Physics of Fluids, University of Twente,
P.O. Box 217, 7500 AE Enschede, The Netherlands
http://pof.tnw.utwente.nl
m.l.j.overvelde@alumnus.utwente.nl

Cover design: Marlies Overvelde
Print: Digital 4 B.V., Goor

© Marlies Overvelde, Enschede, The Netherlands 2010.
No part of this work may be reproduced by print, photocopy or any other means without the permission in writing from the publisher.
ISBN 978-90-365-3006-4

ULTRASOUND CONTRAST AGENTS

DYNAMICS OF COATED BUBBLES

PROEFSCHRIFT

ter verkrijging van
de graad van doctor aan de Universiteit Twente,
op gezag van de rector magnificus,
prof. dr. H. Brinksma,
volgens besluit van het College voor Promoties
in het openbaar te verdedigen
op vrijdag 9 april 2010 om 16.45 uur

door

Maria Levina Joanna Overvelde

geboren op 9 juli 1980

te Hardenberg

Dit proefschrift is goedgekeurd door de promotoren:
Prof. dr. rer. nat. Detlef Lohse
Prof. dr. ir. N. de Jong
en de assistent promotor:
Dr. A.M. Versluis

Contents

1 Introduction

Echolocation provides animals such as bats and dolphins with an advanced bioacoustic system to catch their prey, to navigate, and to avoid obstacles [1]. The principle of echolocation is based on the localization of objects by acoustic detection of the echoes of these objects. The very same technique is used in SONAR (acronym for sound navigation and ranging) to locate target vessels in naval defense operations or to find schools of fish in commercial trawler fishing. Even human's use echolocation for navigation [2]. Some blind people click with their tongue and interpret the sound waves reflected. The distance to the object is captured from the echo travel time. The lateral position is determined from a clever internal signal processing of the ear first to receive the echo. However, humans produce sound of low frequency and the located objects are therefore relatively large. Marine mammals use higher frequencies in ultrasound, moreover they have the ability to use adjustable pulse rate, pulse sequencing and automatic gain control to increase the precision of the location and to identify smaller objects.

Robert Hooke predicted already in the 17^{th} century that in the future we could image the human body with sound [1]. It was however not until the 1940's before the first ultrasound scan was made of the brain. Nowadays, ultrasound imaging is the most widely used medical imaging technique. Ultrasound imaging is relatively inexpensive as compared to computer tomography (CT) and magnetic resonance imaging (MRI). The machines are small and flexible and can be used at bed-side. Finally, the biggest advantage is that ultrasound imaging provides real-time images.

Imaging with ultrasound is based on the reflection of the transmitted sound wave at interfaces, where the wave encounters an acoustic impedance mismatch, i.e. the reflection takes place at the interface of two materials with different density and speed of sound. The frequency of ultrasound used for medical imaging is in the Megahertz range (1-50 MHz). The short wavelength associated with the highest frequency would increase the resolution. On the other hand, attenuation increases with increasing frequency, which decreases the penetration depth. The choice of

Figure 1.1: Ultrasound echo of a fetus.

the ultrasound imaging frequency is therefore always a compromise between resolution and the desired imaging depth.

The most common medical imaging application is the “echo” of a fetus, see Fig. 1.1. Tissue contains many inhomogeneities which scatter the ultrasound and which then appear as white speckles in the ultrasound image. The amniotic fluid around the fetus contains only very few scatterers and consequently the image is completely black. We observe the same features in echocardiography, i.e. medical ultrasound imaging of the heart. Blood is a poor ultrasound scatterer, resulting in a low contrast echo. To enhance the visibility of the blood pool, ultrasound contrast agents (UCA) are injected in the blood stream, see Fig. 1.2. Highly efficient scattering of the contrast agent enables the quantification of the perfusion of the myocardium and other organs.

It was only by accident that ultrasound contrast agents were discovered some decades ago during an intravenous injection of a saline solution [3]. The microbubbles contained in the solution scattered ultrasound highly efficiently. To date, the second and third generation ultrasound contrast agents are composed of a suspension of microbubbles with a of radius 1 to 5 μm, see Fig 1.3A and B. The bubbles are of a size in the order of those of red blood cells, allowing them to reach even the smallest capillaries. The microbubbles are coated with a phospholipid, albumin or polymer shell, see Fig. 1.3C. The coating decreases the surface tension σ and therefore the capillary pressure $2\sigma/R$, where R is the radius of the bubble. In addition the coating counteracts diffusion through the interface, thus preventing the bubble from quickly dissolving in the blood.

The resonance frequency of microbubbles with a radius of 1-5 μm is in the megahertz range, which nicely (and for obvious reasons) coincides with the optimum imaging frequencies used in medical ultrasound imaging. The mechanism

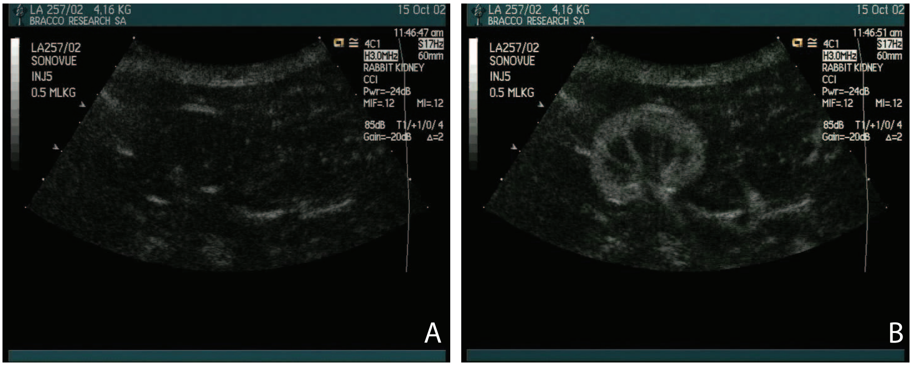

Figure 1.2: Ultrasound echo of a rabbit kidney. A) Before the Ultrasound Contrast Agent is injected, and B) after the ultrasound contrast agent is injected. Images by courtesy of Bracco Research S.A.

by which microbubbles enhance the contrast in ultrasound medical imaging is two-fold. First, microbubbles reflect ultrasound more efficiently than tissue due to the larger difference in acoustic impedance with their surroundings. Second, in response to the oscillating pressure field microbubbles undergo radial oscillations due to their compressibility, which in turn generates a secondary sound wave. The oscillations are highly nonlinear, i.e. the frequency response contains harmonic frequency of the fundamental insonation frequency.

The most basic method in pulse-echo imaging is fundamental imaging, where no filtering of the echo is applied and the reflected intensity at the fundamental frequency is detected. New imaging techniques have been developed in the last 2 decades which are based on the non-linear response of the microbubbles. The most straightforward nonlinear technique is harmonic imaging where the 3rd and higher harmonic response is processed for imaging [4]. Other approaches combine the response of multiple transmitted ultrasound pulses. Pulse inversion imaging [5] was proposed where two pulses are transmitted with opposite phase. Addition of the echo's causes the linear response to be canceled out. The nonlinear contribution of the bubbles results in the harmonic signal. Power modulation imaging [6] is a second popular pulse-echo scheme based on the nonlinear bubble responses. Again two pulses are sent, this time with different acoustic pressures. Subtraction of the echo signals, while correcting for the difference in applied acoustic pressure, leads to a cancelation of the linear signal, while the nonlinear signal remains. There are two major drawbacks of these pulse-echo schemes. First the amplitude of the remaining echo is very much lower. Second, nonlinear propagation of the ultrasound wave produces higher harmonics, especially for deep-tissue imaging, which makes the pulse-echo schemes less efficient. An interesting technique is subhar-

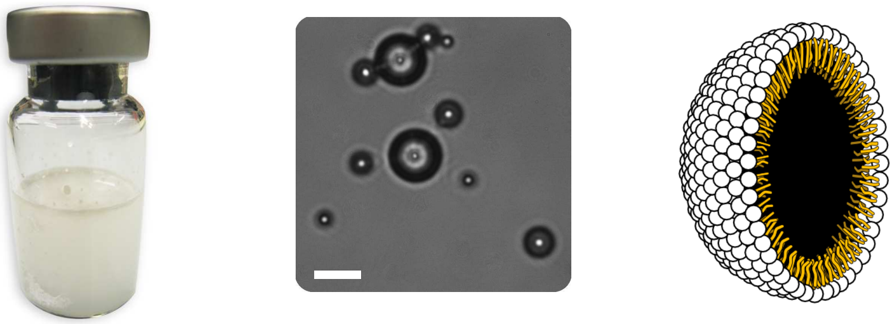

Figure 1.3: A) Vial containing ultrasound contrast agents. B) Ultrasound contrast agent microbubbles captured in optical microscopy. The scale bar represents 5 μm. C) Schematic drawing of a microbubble coated with a phospholipid monolayer (Courtesy of T. Rozendal).

monic imaging with microbubbles, as no subharmonic components are produced through propagation of the ultrasound [7].

A promising new application of ultrasound contrast agents is in non-invasive molecular imaging for the diagnosis of disease at the molecular level with ultrasound [8, 9]. The ultrasound contrast agents are covered with targeting ligands that bind specifically to selective biomarkers on the membrane of endothelial cells, which constitute the blood vessel wall. In general, the approach of imaging adherent microbubbles is to wait 5 - 10 minutes for all the freely circulating microbubbles to be washed-out of the blood pool by the lungs and liver. After this wash-out time the adherent microbubbles can be imaged with ultrasound. The wash-out approach can be avoided when we would be able to acoustically distinguish the echo of adherent bubbles and of freely circulating bubbles. This would be highly beneficial for molecular imaging applications.

The pulse-echo techniques for contrast-enhanced ultrasound imaging are designed to exploit the nonlinear response of ultrasound contrast agents. Due to the high concentration of bubbles in the blood pool, the echo of the ultrasound pulse is the bulk response of an ensemble of bubbles. The response of the bubble dispersion is a complex summation of the polydisperse size distribution and the bubble-bubble interactions. The first step in our understanding of the response of a collection of targeted bubbles, as would be required for molecular imaging application, is to separate the individual contributions leading to the collective response. This would require, first, the full understanding of the dynamics of single ultrasound contrast agent microbubbles. Nonlinearities have been observed for phospholipid-coated microbubbles which are not present for uncoated bubbles. De

Jong *et al.* [10] observed that bubbles compress significantly more than that they expand, which was named “compression-only” behavior. Furthermore it was observed that small bubbles only oscillate above a certain threshold pressure [11]. The origin of this so-called “thresholding” behavior is still unknown. Second, we need to study the complex interaction between bubbles and the interaction of single bubbles with a wall. Finally, we need to identify those conditions that lead to an improved differentiation between the response of adherent and freely circulating microbubbles. as the coating on the dynamics is still not fully understood. Further research will be focused on the interaction between bubbles or the interaction of a bubble near a wall can be investigated in detail. Understanding of the circumstances of which the response of adherent and freely circulating microbubbles differs the most, can result in pulse-echo techniques specifically designed for molecular imaging applications to diagnose up to the cellular level.

We now discuss the outline of this thesis, see also Fig. 1.4. Following the discussion in the previous paragraph, the thesis can be divided into three parts. In the first part the focus is on the influence of the phospholipid coating on the bubble dynamics. We start with an introduction of the known behavior of coated microbubbles in chapter 2. In chapter 3 we reveal the origin of the so-called “thresholding” behavior. Furthermore, we show why apparently identical bubbles show completely different behavior by implementing the shell-buckling model by Marmottant *et al.* [12]. In chapter 4 we explore in detail the so-called “compression-only” behavior by means of a weakly nonlinear analysis of the shell-buckling model. Furthermore, we demonstrate buckling of the phospholipid-coating optically in the Megahertz range. Subharmonic behavior of coated bubbles is investigated in chapter 5 as this behavior is particularly interesting for pulse-echo imaging. In the second part of the thesis the influence of a boundary on the dynamics of the coated bubbles is investigated. The Brandaris 128 ultra-high speed camera is combined with an optical tweezers setup allowing for 3D manipulation of the bubble position and for temporally resolving the bubble dynamics, see chapter 6. The full parameter space of ultrasound frequency, acoustic pressure and distance to the interfering wall is investigated in detail in chapter 7. The results are compared to a bubble dynamics model accounting for an interaction with a thin viscoelastic wall. As the bubble also translates near the boundary due to an interaction with its “image” bubble, leading to a secondary radiation force, we investigate the translatory oscillations on an isolated two-bubble system in chapter 8. The third part of the thesis explores the dynamics of bubbles adherent to a wall. The experimental methods developed and explored in the preceding chapters are applied to a study of the changed response for a functionalized bubble adherent to a target wall. In chapter 10 we discuss the obtained results of the thesis and we anticipate on a variety of future applications of ultrasound contrast agents in medical diagnosis.

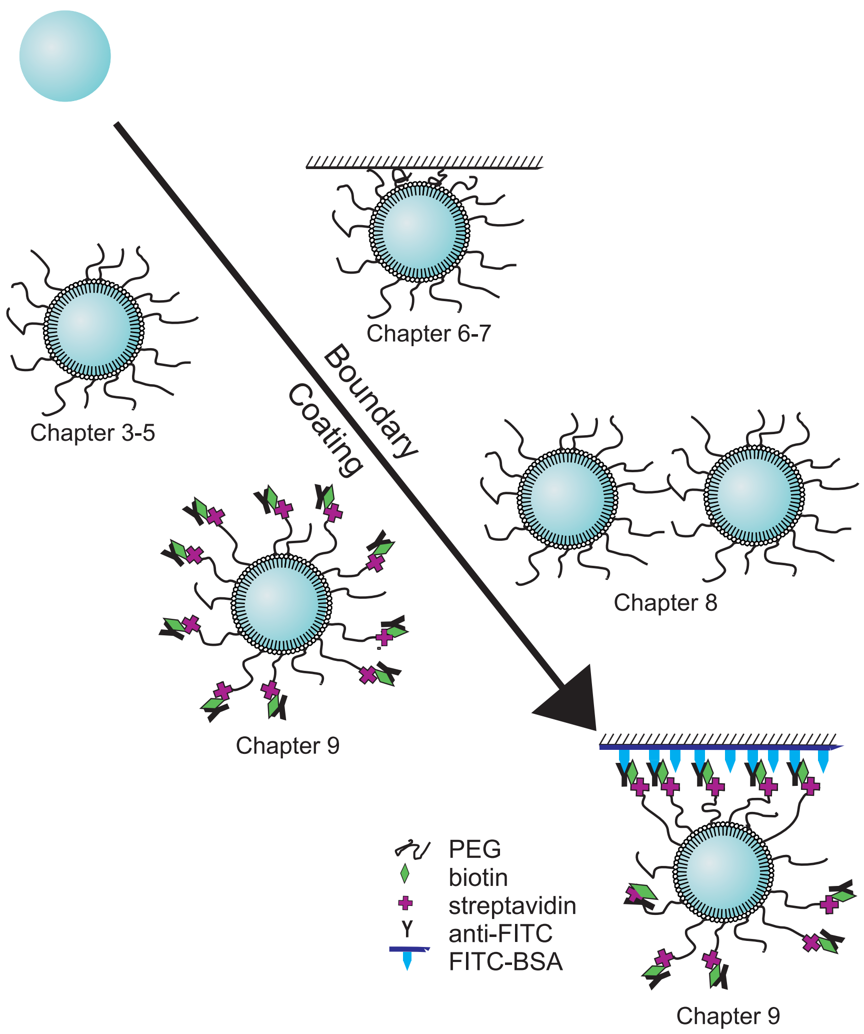

Figure 1.4: Guide through the thesis. Part I: the influence of the phospholipid-coating is discussed in Ch. 3 to 5. Part II: the bubble-wall interactions are investigated in Ch. 6 and 7. Ch. 8 reveals the bubble-bubble interaction. Part III: the influence of targeting ligands on the dynamics as well as the dynamics of adherent bubbles is discussed in Ch.9.

2 Dynamics of coated bubbles: an introduction[1]

In this chapter an introduction is given on the known behavior of phospholipid-coated microbubbles. The contrast agent microbubble behavior is described starting from the details of free bubble dynamics leading to a set of equations describing the dynamics of coated microbubbles. The response of an uncoated, a coated, and an uncoated bubble near a rigid boundary are compared in the case of small amplitude oscillations where the equations of motion can be linearized. We report the nonlinear phenomena of phospholipid-coated microbubbles that were observed experimentally such as "compression-only" behavior, "thresholding" behavior, and subharmonic response. Furthermore, we describe the ultra-high speed camera Brandaris 128, which was especially built to investigate coated microbubbles and which was also used here to experimentally investigate the radial dynamics of single microbubbles.

[1]Based on: M. Overvelde, H. J. Vos, N. de Jong and M. Versluis, *Ultrasound contrast agent microbubble dynamics*, Ultrasound Contrast Agents: Targeting and Processing Methods for Theranostics, ISBN 978-88-470-1494-7, Springer-Verlag Italia (2010)

2.1 Introduction

The dynamics of ultrasound contrast agents has been investigated extensively in the last two decades. In this chapter we give an introduction into the known dynamics of coated bubbles both in theory and experiments. We start with the well-known Rayleigh-Plesset equation and discuss existing theoretical models for coated microbubbles. The resonance frequency and damping are obtained in case of small amplitude oscillations by linearizing the equations and by comparing the results for the coated bubbles with those of the uncoated bubbles. The influence of a rigid boundary is discussed in the simplest case using the method of images to elaborate on the expected changes in the bubble dynamics in the proximity of a boundary. In the experimental section we describe the ultra-high speed camera Brandaris 128 which will be used to temporally resolve the radial dynamics of the microbubbles in the following chapters. After the theoretical section we give an overview of the experimentally observed behavior of phospholipid-coated bubbles. Finally, we summarize the questions still open on the dynamics of phospholipid-coated bubbles which we investigate in further detail in this thesis.

2.2 Theory

2.2.1 Dynamics of an uncoated gas bubble

The dynamics of an uncoated bubble in free space was first described by Lord Rayleigh [13] and was later refined by Plesset [14], Noltingk & Neppiras [15, 16] and Poritsky [17] to account for surface tension and viscosity of the liquid. A popular version of the equation of motion describing the bubble dynamics (often referred to as *the* Rayleigh-Plesset equation) is given by:

$$\rho\left(\ddot{R}R+\frac{3}{2}\dot{R}^2\right)=\left(P_0+\frac{2\sigma_w}{R_0}\right)\left(\frac{R_0}{R}\right)^{3\kappa}\left(1-\frac{3\kappa\dot{R}}{c}\right) - P_0 - P(t) - 4\mu\frac{\dot{R}}{R} - \frac{2\sigma_w}{R} \tag{2.1}$$

where ρ is the liquid density, μ the dynamic viscosity of the liquid, c the speed of sound in the liquid, σ_w the surface tension of the gas-liquid system and κ the polytropic exponent of the gas inside the bubble. P_0 is the ambient pressure and $P(t)$ the applied acoustic pressure. R_0 is the initial bubble radius, R represents the time-dependent radius of the bubble, while $\dot{R}$ and $\ddot{R}$ represent the velocity and the acceleration of the bubble wall, respectively. The bubble is assumed to be surrounded by an infinite medium and it remains spherical during oscillations. The bubble radius is small compared to the acoustic wavelength. The gas content of the bubble is constant. Damping of the bubble dynamics is governed by viscous damping of the surrounding liquid and by acoustic radiation damping, through sound radiated away from the bubble [18–25]. For the sake of simplicity the thermal damping is not included here. More information on the thermal damping can be found in [26–28]. Finally, the density of the liquid is large compared to the gas density.

Linearized equations

We often use the linearized equations to describe the bubble dynamics at low driving pressures. For small amplitudes of oscillation an oscillating bubble behaves as a harmonic oscillator. The time-dependent radius R can be written as $R = R_0(1 + x(t))$ and through a linearization of the Rayleigh-Plesset [29, 30] equation around the initial radius R_0 the relative radial excursion is obtained:

$$\ddot{x} + \omega_0 \delta \dot{x} + \omega_0^2 x = F(t) \tag{2.2}$$

with x the relative radial excursion, $\omega_0 = 2\pi f_0$ where f_0 is the eigenfrequency of the system and δ the dimensionless damping coefficient . $F(t) = F_0 sin(\omega t)$ is the acoustic forcing term. The eigenfrequency of the system follows from (2.1) and (2.2).

$$f_0 = \frac{1}{2\pi}\sqrt{\frac{1}{\rho R_0^2}\left(3\kappa P_0 + (3\kappa - 1)\frac{2\sigma_w}{R_0}\right)} \tag{2.3}$$

The total damping coefficient (δ) is given by the sum of the individual damping coefficients. The contribution from the sound radiated by the bubble (δ_{rad}) is:

$$\delta_{rad} = \frac{\frac{3\kappa}{\rho c R_0}\left(P_0 + \frac{2\sigma_w}{R_0}\right)}{\omega_0} \approx \frac{\omega_0 R_0}{c} \tag{2.4}$$

and the viscous contribution (δ_{vis}) is:

$$\delta_{vis} = \frac{4\nu}{\omega_0 R_0^2} \tag{2.5}$$

The resonance frequency of the system is then obtained from:

$$f_{res} = f_0\sqrt{1 - \frac{\delta^2}{2}} \tag{2.6}$$

For a free gas bubble the damping coefficient is negligible. The surface tension is negligible in the mm size range and the resonance frequency is given by the Minnaert frequency [31] :

$$f_{res} \approx f_0 = \frac{1}{2\pi}\sqrt{\frac{3\kappa P_0}{\rho R_0^2}} \tag{2.7}$$

For an air bubble in water we then recover the common rule of thumb for the bubble resonance $f_0 R_0 \approx 3$ mmkHz. It should be noted that for bubbles with a radius $< 10\ \mu$m the surface tension cannot be neglected.

Assuming a steady-state response ($t \to \infty$) and substitution into Eq. 2.2 gives the absolute relative amplitude of oscillation:

$$|x_0| = \frac{F_0}{\sqrt{\left(\omega_0^2 - \omega^2\right)^2 + \left(\delta\omega\omega_0\right)^2}} \tag{2.8}$$

For small damping, as in the case of a free gas bubble, the amplitude of oscillations of a bubble driven at a frequency well below its resonance frequency is inversely proportional to the effective “mass” and the eigenfrequency squared of the system (*stiffness-controlled*). Well above the resonance frequency the amplitude of oscillation is inversely proportional to the effective “mass” of the system (*inertia-driven*). Close to resonance the amplitude of oscillation is inversely proportional to the damping coefficient, the eigenfrequency squared and the effective “mass” of the system [32].

2.2.2 Coated bubbles

Ultrasound contrast agents are encapsulated with a phospholipid, protein, palmitic acid or polymer coating. The coating shields the water from the gas, reducing the surface tension and inhibits the gas diffusion to prevent the bubbles from dissolution. Several Rayleigh-Plesset type models have been derived for coated bubbles. Church [1995] derived a theoretical model for a coated bubble assuming that the gas core is separated from the liquid by a layer of an incompressible, solid elastic material. The shell has a finite thickness and the shell elasticity and the shell viscosity depend on the rigidity of the shell and the thickness of the shell. Commercial 1^{st} generation Albunex (Mallinckrodt) microbubbles have an albumin shell and remain stable for an extended period of time at atmospheric pressure. Therefore, in Church’ model it was assumed that the elastic shell counteracts the capillary pressure ($P_{g0} = P_0$) which stabilizes the bubble against dissolution.

The second generation contrast agents have a more flexible phospholipid shell. The commercially available contrast agents Sonovue® (Bracco), Definity (Lan-

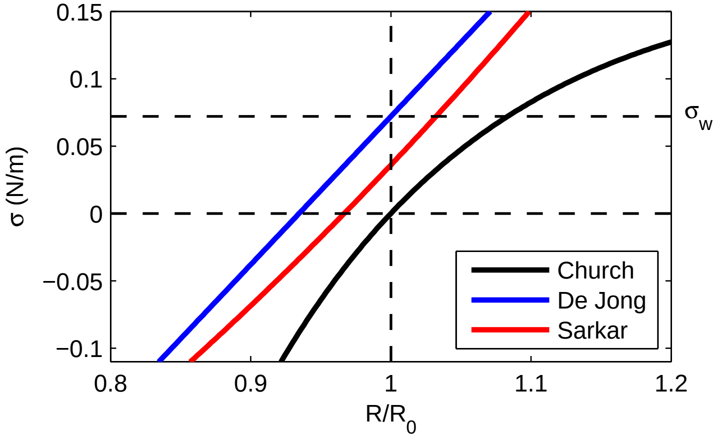

Figure 2.1: The effective surface tension as a function of the bubble radius ($R_0 = 2\ \mu$m) for the different models accounting for a purely elastic shell.

theus Medical Imaging) and Sonazoid (GE) consist of a monolayer of phospholipids with a thickness of a few nanometers. Various models account for a coating by assuming a viscoelastic thin shell, see for example [34], [35] and more recently [36]. The Rayleigh-Plesset type models account for the shell by an elastic term P_{elas} and a viscous term P_{vis}.

$$\rho\left(\ddot{R}R+\frac{3}{2}\dot{R}^2\right) = P_{g0}\left(\frac{R_0}{R}\right)^{3\kappa}\left(1-\frac{3\kappa\dot{R}}{c}\right)-P_0-P(t)-4\mu\frac{\dot{R}}{R}-P_{\mathrm{elas}}-P_{\mathrm{vis}} \tag{2.9}$$

The elasticity of the coating causes the surface tension to vary with the radius of the bubble:

$$P_{\mathrm{elas}} = \frac{2\sigma(R)}{R}, \tag{2.10}$$

The viscous term can be expressed as:

$$P_{\mathrm{vis}} = 4S_{\mathrm{vis}}\frac{\dot{R}}{R^2} \tag{2.11}$$

with the shell viscosity S_{vis}. Hoff *et al.* [35] modified Church' model to account for the thin shell by reducing the equation of Church to a form similar to that of Eq. 2.9. The effective surface tension and the shell viscosity in the various models are given in table 2.1. The effective surface tension changes as a function of the bubble radius, see Fig. 2.1 for a plot for the various shell models. The parameters

Table 2.1: Values for the initial gas pressure in the bubble (P_{g0}), the effective surface tension $\sigma(R)$ and the shell viscosity S_{vis} for three elastic shell models. For comparison the values for an uncoated bubble (Rayleigh-Plesset) are also given.

Model	P_{g0} $[\text{N/m}^2]$	$\sigma(R)$ [N/m]	S_{vis} [kg/s]
Rayleigh-Plesset	$P_0 + \frac{2\sigma_w}{R_0}$	σ_w	-
Church [1995], Hoff *et al.* [2000]	P_0	$6G_s d_{sh0} \frac{R_0^2}{R^2}\left(1 - \frac{R_0}{R}\right)$	$3\mu_s d_{sh0} \frac{R_0^2}{R^2}$
De Jong *et al.* [1994]	$P_0 + \frac{2\sigma_w}{R_0}$	$\sigma_w + S_p\left(\frac{R}{R_0} - 1\right)$	$\frac{S_f}{16\pi}$
Sarkar *et al.* [2005]	P_0	$\sigma(R_0) + E_S\left(\frac{R^2}{R_E^2} - 1\right)$	κ_s

are chosen to be comparable in the models ($S_p = 2E_s = 12G_s d_{sh0} = 1.1$ N/m) for the shell elasticity and ($S_f = 16\pi\kappa_s = 48\pi\mu_s d_{sh0} = 2.7 \cdot 10^{-7}$ kg/s) for the shell viscosity, as reported by [37]. In this regime, the slope of the effective surface tension as a function of the bubble radius is similar for the models by De Jong *et al.* [34] (blue) and Sarkar *et al.* [36] (red). The main difference between the models is found for the effective surface tension at the initial bubble radius $(\sigma(R_0))$. It equals σ_w for the model by De Jong *et al.* [34] and it varies for the model by Sarkar *et al.* [36]. In this example we choose $\sigma(R_0) = 0.036$ N/m for the model of Sarkar *et al.*. The model of Church [33], modified by Hoff *et al.* [35] for a thin shell, has a lower initial effective surface tension, $\sigma(R_0) = 0$ N/m, and has a different slope (black). Note that the effective surface tension in these models is not bound to an upper or lower limit and the effective surface tension can become negative and larger than σ_w.

Marmottant *et al.* [12] introduced a model which seems to be more applicable for high amplitude oscillations. The model accounts for an elastic shell and also for buckling and rupture of the shell. Compression of the bubble leads to an increased phospholipid concentration. Therefore, in the elastic regime the effective surface tension decrease is a linear function of the area under compression. Further compression leads to such high phospholipid concentrations that the shell tends to buckle leading to a tensionless state where the surface tension is effectively zero. On the other hand expansion of the bubble decreases the phospholipid concentration and leads to rupture. It is assumed that the surface tension will effectively

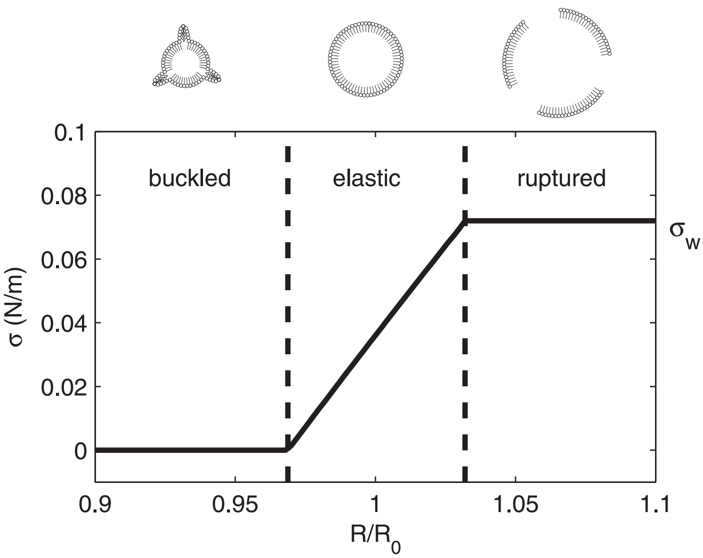

Figure 2.2: The effective surface tension as a function of the bubble radius ($R_0 = 2\ \mu$m) for the model of Marmottant *et al.* [12] including an elastic regime and buckling and rupture of the shell.

relax to σ_w. The effective surface tension using Eq. 2.9 for the three regimes is given by:

$$\sigma(R) = \begin{cases} 0 & \text{if } R \leq R_b \\ \chi\left(\dfrac{R^2}{R_b^2} - 1\right) & \text{if } R_b \leq R \leq R_r \\ \sigma_w & \text{if ruptured and } R \geq R_r \end{cases} \tag{2.12}$$

with χ the shell elasticity and R_b and R_r the buckling and rupture radius, respectively. The effective surface tension as a function of the radius is shown in Fig. 2.2 for the Marmottant model. The initial surface tension is chosen to be $\sigma(R_0) = 0.036$ N/m similar to the example of the Sarkar model. The choice of $\sigma(R_0)$ in combination with the typical value for the shell elasticity $\chi = S_p/2 = 0.55$ N/m results in $R_b = 0.97\ R_0$ and $R_r = 1.03\ R_0$. In this example the bubble is assumed to rupture when the surface tension reaches σ_w. The shell viscosity in Eq. 2.9 is given by $S_{\text{vis}} = \kappa_s$. As will be shown in the following paragraph, the elasticity of the shell increases the eigenfrequency of the bubble while the shell viscosity increases the total damping of the system.

Linearized equations

The bubble resonance frequency and its corresponding damping coefficient for the coated bubble is derived in a similar way as in Sec. 2.2.1. For the model of De Jong *et al.* [34] the eigenfrequency and the total damping $(\delta_{tot} = \delta_{rad} + \delta_{vis} + \delta_{shell})$ are given by:

$$f_0 = \frac{1}{2\pi}\sqrt{\frac{1}{\rho R_0^2}\left(3\kappa P_0 + (3\kappa - 1)\frac{2\sigma_w}{R_0} + \frac{2S_p}{R_0}\right)} \tag{2.13}$$

$$\delta_{tot} = \frac{\frac{3\kappa}{\rho c R_0}\left(P_0 + \frac{2\sigma_w}{R_0}\right)}{\omega_0} + \frac{4\nu}{\omega_0 R_0^2} + \frac{S_f}{4\pi\rho R_0^3\omega_0} \tag{2.14}$$

The eigenfrequency of a coated bubble has two contributions: one part that is identical to the eigenfrequency of an uncoated bubble and an elastic shell contribution. The shell viscosity S_f increases the damping for a coated bubble. Fig. 2.3A shows the eigenfrequency and resonance frequency for an uncoated and coated bubble. The resonance frequency and the eigenfrequency of the uncoated bubble agree to within graphical resolution. The eigenfrequency of a coated bubble in comparison to an uncoated microbubble is higher due to the shell elasticity. The

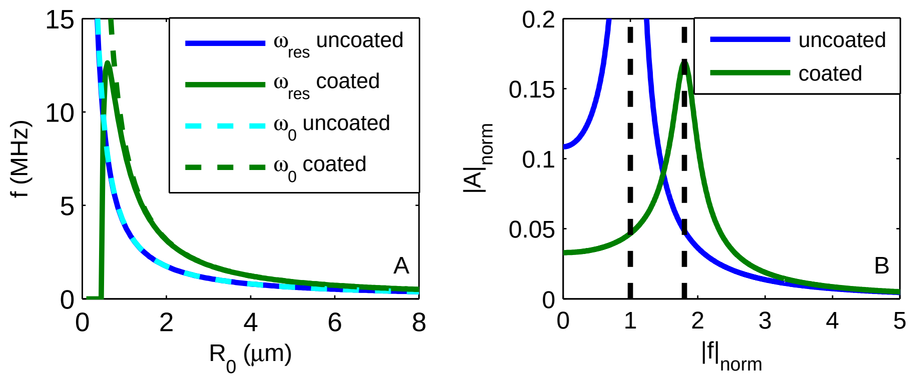

Figure 2.3: A) The resonance frequency as a function of the initial bubble radius (R_0) for an uncoated (blue solid line) and coated microbubble (green solid line). For comparison the eigenfrequency is plotted (dashed lines). The resonance frequency and the eigenfrequency of the uncoated bubble agree to within graphical resolution. B) The amplitude of oscillation for an uncoated (blue) and coated (green) bubble with $R_0 = 2\ \mu$m, normalized with the maximum amplitude of oscillation of the uncoated microbubble. The driving frequency is normalized to the resonance frequency of the uncoated microbubble.

damping has a negligible influence on the resonance frequency for an uncoated bubble and for coated bubbles with $R_0 > 1\ \mu$m. Fig. 2.3B shows the resonance curve of an uncoated and coated microbubble with a resting radius of 2 μm. The amplitude of oscillation and the resonance frequency are normalized to the maximum amplitude of oscillation and the resonance frequency of the uncoated bubble, respectively. Both the damping and eigenfrequency increase for a coated microbubble, while the effective "mass" stays the same. The amplitude of oscillations at resonance is therefore lower when the bubble has a shell, see Fig. 2.3B. Below resonance, neglecting the influence of the damping, the system is stiffness driven. The shell increases the stiffness of the system and the amplitude of oscillation below resonance is therefore lower for a coated microbubble. Far above resonance the amplitude of oscillations is inversely proportional to the effective "mass" of the system. Consequently well above resonance the amplitude of oscillations does not depend on the shell properties.

2.2.3 Bubble dynamics near a rigid wall

In this section we discuss the influence of a rigid wall on the bubble dynamics. We start with the simplest approach, the so-called *method of images*, to simulate the influence of a wall. In literature several extensions to the bubble dynamics equations have been made to account for the presence of a rigid wall. All the models described here are based on the method of images depicted in Fig. 2.4. If the wall is rigid, the specific acoustic impedance $Z = \rho\, c$ is infinite, and no energy crosses the wall. To describe the acoustic (or equivalently the fluid-mechanical field) the wall is replaced by an identical image bubble oscillating in-phase with the real bubble and positioned at the mirrored image point. The dynamics of the real bubble is influenced by the pressure emitted by the image bubble. The dynamics of a coated bubble near a rigid wall is therefore described by a Rayleigh-Plesset type equation including the radiated pressure of the image bubble:

$$\begin{aligned}\rho\left(\ddot{R}R+\frac{3}{2}\dot{R}^2\right) &= P_{g0}\left(\frac{R_0}{R}\right)^{3\kappa}\left(1-\frac{3\kappa\dot{R}}{c}\right)-P_0\\ &\quad -P(t)-4\mu\frac{\dot{R}}{R}-\frac{2\sigma(R)}{R}-4S_{\text{vis}}\frac{\dot{R}}{R^2}-\rho\frac{\partial}{\partial t}\left(\frac{\dot{R}R^2}{2d}\right)\end{aligned} \tag{2.15}$$

where d represents the distance between the bubble and the wall. For a bubble positioned directly at the wall, such as bubbles floating up against the capillary wall, the distance d is simply given by the bubble radius R. In this particular case

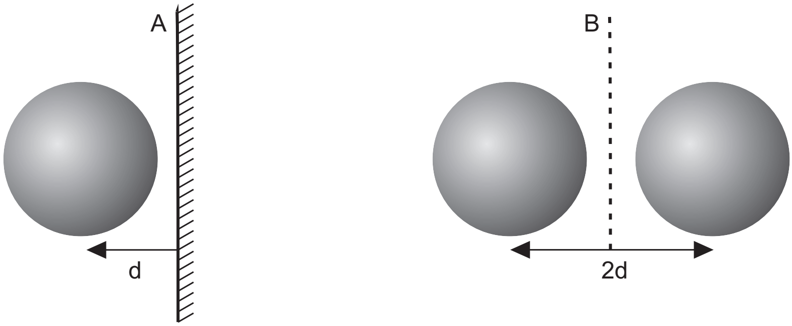

Figure 2.4: In (A) the actual situation, where the bubble is located at a distance *d* from the rigid wall, (B) shows the method of images in which the wall is replaced by an image bubble.

the bubble dynamics equation becomes:

$$\rho\left(\frac{3}{2}\ddot{R}R+2\dot{R}^2\right)=P_{g0}\left(\frac{R_0}{R}\right)^{3\kappa}\left(1-\frac{3\kappa\dot{R}}{c}\right)-P_0 \\ -P(t)-4\mu\frac{\dot{R}}{R}-\frac{2\sigma(R)}{R}-4S_{\text{vis}}\frac{\dot{R}}{R^2} \tag{2.16}$$

The difference between the uncoated bubble in in the unbounded fluid and floating against the wall are the pre-factors in the left hand side of Eq. 2.16. Note that all assumptions made previously for the Rayleigh-Plesset equation for an uncoated microbubble remain valid. Therefore the bubble must remain spherical, which may not be strictly true in the experimental situation. For example we know that bubbles deform close to the wall [38].

Linearized equations

For an (un)coated bubble at a wall the eigenfrequency and damping can be derived in a similar way as in Sec. 2.2.1. The rigid wall increases the effective "mass" of the bubble by a factor $3/2$ resulting in a decrease of the eigenfrequency and the damping. The eigenfrequency and damping can be derived in a similar way as in Sec.2.2.1. The eigenfrequency and damping for an uncoated bubble at a rigid wall reduce to:

$$f_0^{wall}=\sqrt{\frac{2}{3}}f_0^{free}\approx 0.8f_0^{free} \\ \delta^{wall}=\sqrt{\frac{2}{3}}\delta^{free}\approx 0.8\delta^{free} \tag{2.17}$$

Fig. 2.5 shows the resonance curve of a coated bubble in free space (blue) and at the wall (red). The amplitude of oscillation and the applied frequency are normalized to that of the bubble in free space. The amplitude of oscillations at resonance is $\sqrt{3/2}$ larger for a bubble at a wall than for bubble in the unbounded fluid. Well below the resonance frequency the amplitude of oscillations is unchanged as the stiffness of the system dominates the amplitude of oscillations. Well above the resonance frequency the amplitude of oscillation is $3/2$ times smaller for a bubble at a rigid wall than in the unbounded fluid because of the increased effective "mass" of the system.

2.3 Experiments

2.3.1 Optical and acoustical characterization

The theoretical models are validated through experiments on single bubbles. Acoustical and optical experiments reveal the response of UCA microbubbles and both have there own particular advantages and disadvantages. In acoustical experiments the scattered pressure, or pressure-time *P(t)* curve, is recorded. Acoustic characterization has the advantage of a high sampling rate using long pulse sequences. The scattered pressure of a single bubble however is limited (order 1 Pa) and close

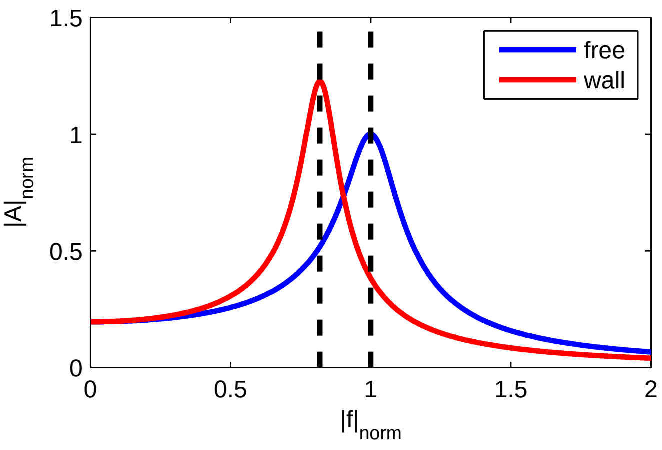

Figure 2.5: Resonance curves for an uncoated bubble with a initial radius of 2 μm in free space (blue) and at a rigid wall (red). The frequency and the amplitude are normalized with the resonance frequency and amplitude of oscillation at resonance in the free case.

to the noise level of our detection system. The size of the transducer focus is in the order of the acoustic wavelength and in order to prevent the detection of multiple bubble echoes the bubble must be isolated in the *in-vitro* setup. In optical experiments a high-speed camera is used to record the radial response, or radius-time *R(t)* curve, of single bubbles. Such a camera must temporally resolve the dynamics of the microbubbles which is driven at MHz frequencies. Therefore framerates of tens of millions of frames per second are required. The Brandaris 128 camera, see Fig. 2.6, was especially designed for this purpose [39]. The camera uses a fast rotating mirror (max 20,000 rps) to sweep the image across 128 highly sensitive CCDs (charge-coupled device). At maximum speed an interframe time of 40 nanoseconds is obtained, which corresponds to a framerate of 25 Mfps. Fig. 2.7 shows a sequence of 25 frames recorded with the Brandaris 128 camera at a framerate of 13.5 Mfps. The driving pulse has a frequency of 2.7 MHz and an acoustic pressure amplitude of 30 kPa. The accompanying *R(t)* curve of the microbubble derived from the Brandaris recording is shown in Fig. 2.8. The maximum amplitude of oscillation is 200 nm corresponding to a relative amplitude of 10%.

The first characterization of SonoVue® was performed acoustically on a microbubble suspension by Gorce *et al.* [37]. Recently, optical *R(t)* curves of single UCA microbubbles (SonoVue®) were recorded and fitted, to an elastic shell model (Hoff's model), by Chetty *et al.* [40]. In the model the values of the shell thickness and shell viscosity were fixed and it was found that the shell elasticity increases with increasing bubble radius. The experiments were performed with a single applied frequency of 0.5 MHz and a pressure amplitude between 40 and 80 kPa. To test the validity of the shell parameters for the very same bubble the bubble should be exposed to a set of frequencies and pressures. Van der Meer *et al.* [41] insonified single UCA microbubbles (BR-14) consecutively with 11 ultrasound pulses, increasing the frequency for each pulse, near resonance. With this method named microbubble spectroscopy, the resonance curve was then obtained by plotting the amplitude of oscillation as a function of the applied frequency. A fit of the linearized shell model of Marmottant *et al.* [12] then resulted in the shell elasticity and shell viscosity. In contrast to Chetty *et al.* [40], Van der Meer *et al.* [41] found that the shell elasticity was nearly constant while the shell viscosity decreases with decreasing dilatation rate $\left(\dot{R}/R\right)$. One should note that all above experiments were performed at or in close proximity to a (capillary) wall.

De Jong *et al.* [10] reported on an observation of coated microbubbles at low applied acoustic pressures, where the bubbles compress, but hardly expand. An example of this highly nonlinear effect, referred to as "compression-only" behavior, is shown in Fig. 2.9. De Jong *et al.* showed that "compression-only" behavior occurs for 40% of the bubbles even at pressures as low as 50 kPa. Remarkably all bubbles with an initial radius less than 2 μm show "compression-only" behavior

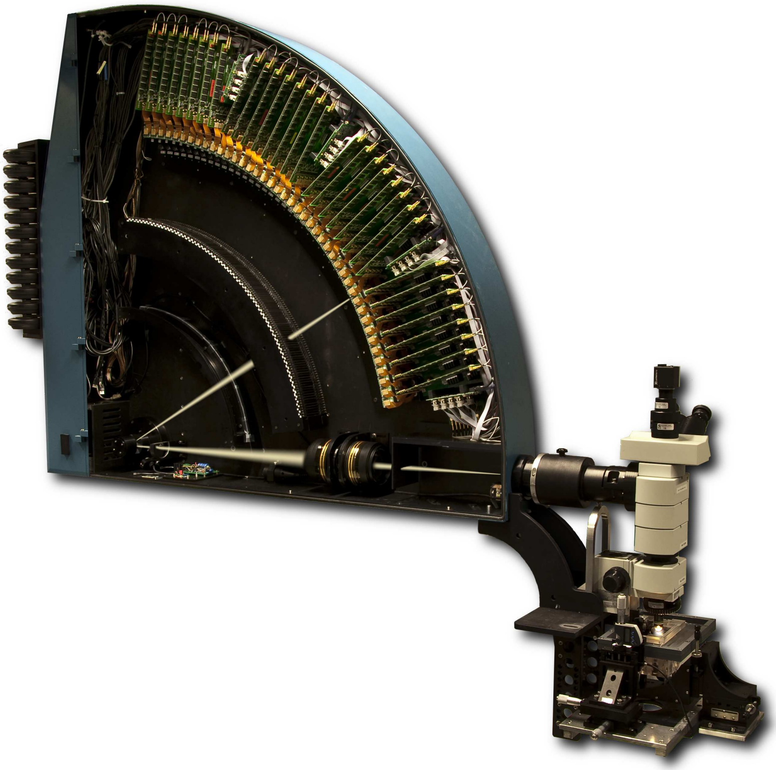

Figure 2.6: Schematic drawing of the Brandaris 128 camera. The rotating mirror sweeps the light beam projecting the microscope image on the CCD's. The mirror sweeps the image over the CCD's with a minimum interframe time of 40 ns or equivalent a maximum framerate of 25 Mfps. (courtesy: E.C. Gelderblom)

at a frequency of 1 MHz. "Compression-only" behavior has never been observed for uncoated bubbles and cannot be described by a model accounting purely for an elastic shell. Actually, the purely elastic shell models even predict a decrease of the nonlinear behavior of the coated microbubbles as compared to the dynamics of an uncoated microbubble. The model of Marmottant *et al.* [12] accounting for an elastic shell and for buckling and rupture of the shell has been very successful in predicting "compression-only" behavior. As stated by Marmottant *et al.* the compression modulus in the elastic state is much higher than in the buckled or ruptured state. For a bubble where the resting radius very close to buckling it is much harder to expand than to compress resulting in "compression-only" behavior of the bubble [12].

Emmer *et al.* [11] showed an oscillation threshold for coated microbubbles with

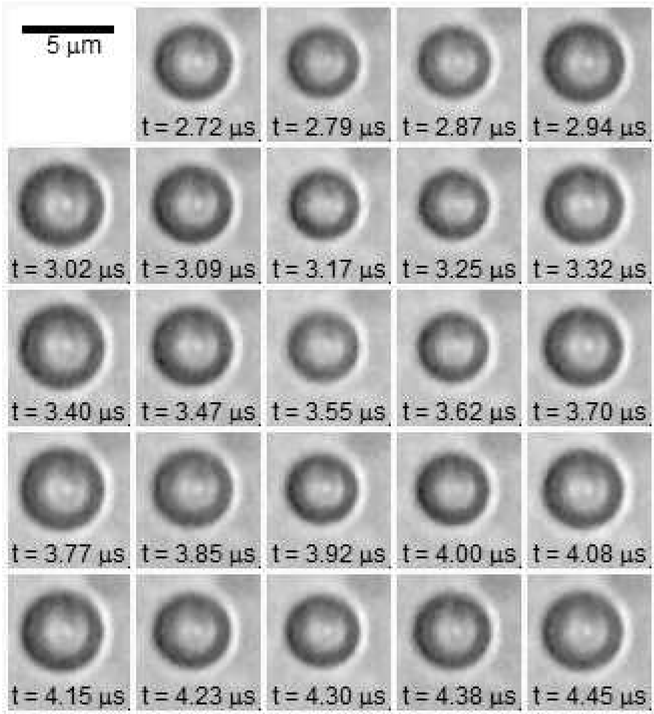

Figure 2.7: Sequence of 50 frames of a 2.2 μm radius bubble recorded with the Brandaris 128 camera at a framerate of 13.5 Mfps.

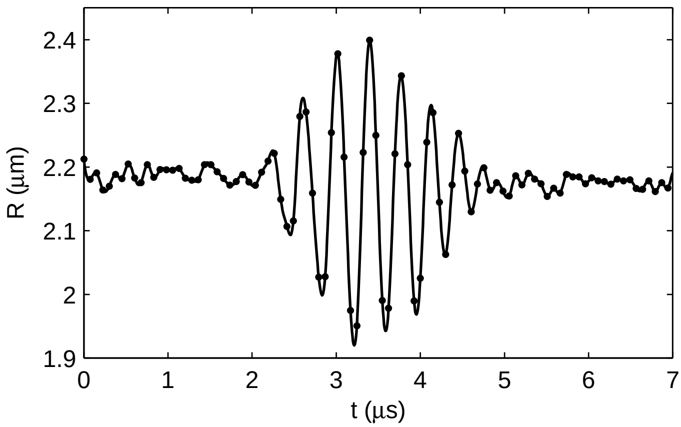

Figure 2.8: The *R(t)* curve of the same bubble as in Fig. 2.7. The bubble is insonified with an ultrasound pulse with a frequency of 2.7 MHz and an acoustic pressure of 30 kPa.

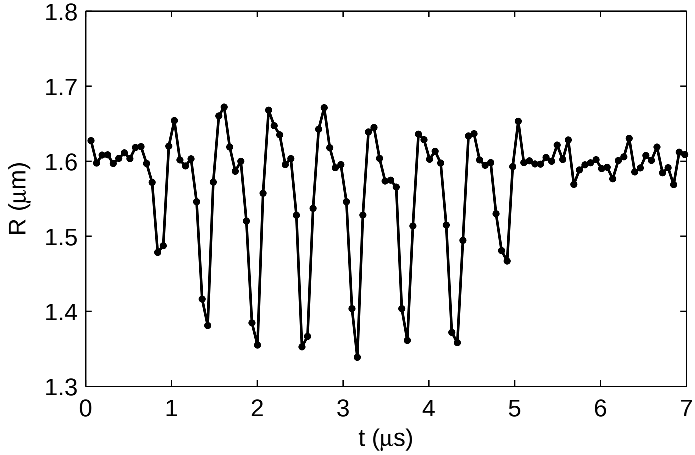

Figure 2.9: Example of a bubble showing "compression-only" behavior, i.e. the oscillating bubble hardly expands and strongly compresses. The bubble with a radius $R_0 = 1.6\ \mu$m is insonified with an acoustic pressure $P_a = 55$ kPa and a frequency $f = 1.7$ MHz.

a radius smaller than 2.5 μm at a driving frequency of 1.7 MHz. Below a certain pressure optically no oscillations where observed, while above this threshold the amplitude of oscillation increases linearly with the applied acoustic pressure. An example this so-called "thresholding" behavior is shown in Fig. 2.10. At pressures below 28 kPa the bubble hardly oscillates, while a sudden increase of the amplitude of oscillation is observed for higher acoustic pressures. The cause of this nonlinear "thresholding" behavior is not understood. A third nonlinear effect that is often observed for coated bubbles are strong subharmonic frequency components. Subharmonic behavior is well-known for uncoated bubbles and is only observed above a certain pressure threshold which increases with increasing damping, see e.g. Prosperetti [42]. As the oscillations of coated bubbles are considerably stronger damped it has been assumed that subharmonic behavior for coated bubbles must occur at higher acoustic pressures. However, it has been shown experimentally that subharmonic behavior of coated bubbles occurs at lower acoustic pressures even lower than those for uncoated bubbles [7, 43–49]. The Fourier transform of the radius-time curve of an oscillating coated bubble insonified at a frequency of 2 MHz shows a strong subharmonic component at a frequency of 1 MHz, see Fig. 2.11. No explanation has been found for the increased subharmonic behavior found for coated microbubbles.

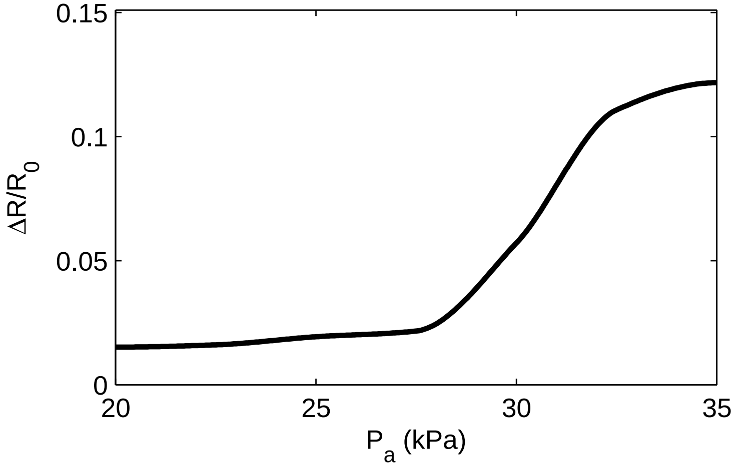

Figure 2.10: Example of "thresholding" behavior. The relative amplitude of oscillation increases strongly nonlinear as a function of the applied acoustic pressure. The bubble has a radius $R_0 = 1.9\ \mu$m and is insonified at a frequency of 2.7 MHz.

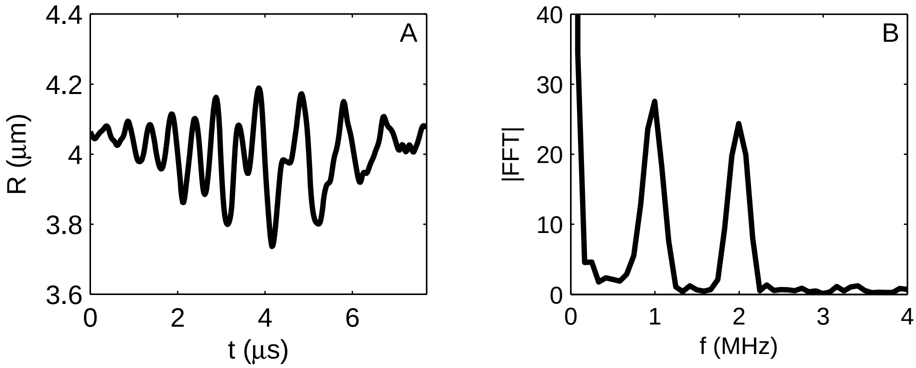

Figure 2.11: A) Radius-time curve of a bubble with a radius $R_0 = 4\ \mu$m is insonified with an acoustic pressure $P_a = 80$ kPa and a frequency $f = 2$ MHz. B) The frequency domain of the *R(t)*-curve shows besides the fundamental component at $f = 2$ MHz the presence of a strong subharmonic component at $f = 1$ MHz.

2.4 Open questions

The goal of this thesis is to acoustically distinguish between adherent and freely circulating microbubbles. The first step is to optimize current pulse-echo techniques and to develop new techniques based on the nonlinear dynamics of the coated microbubbles. It has indeed been observed that phospholipid-coated microbubbles show strong nonlinear behavior, such as "compression-only" behavior, "thresholding" behavior, and subharmonic frequencies at low acoustic pressures. These nonlinear dynamics are ideal for medical imaging with ultrasound as they allow to distinguish between the tissue echo and the bubble echo. However, in the experiments the bubbles are injected in an in vitro setup (e.g. capillary or flow cell) and float up due to buoyancy until they reach the top wall. Due to the limited focal depth of the microscope objective the rising bubbles are difficult to capture in free space. The radial bubble dynamics is therefore traditionally captured with the bubbles positioned against the top wall of the capillary. In these experiments the optical axis was perpendicular to the flow cell wall, i.e. it was always observed in top-view. Vos *et al.* [38] showed, with a setup allowing both, a side-view (optical axis parallel to the wall) and a top-view that the oscillations of UCA microbubbles may appear spherical in top-view and can be quite asymmetric in side-view. Therefore, the influence of the coating and the capillary boundary cannot be separated. Besides the cause of the strong nonlinearly observed behavior we would like to answer some questions in more detail. What causes "thresholding" behavior? Are the effects we observe bubble-size dependent or are they mainly influenced by resonance? Is there a model that predicts all these nonlinear phenomena? Can we optimize the current pulse-echo techniques to exploit this nonlinear behavior? Can we possibly develop new more efficient pulse-echo techniques?

When the influence of the phospholipid coating on the bubble dynamics is known we can investigate the proximity of a boundary and for targeting applications the adherence to a boundary on the bubble dynamics. From the simulations described above we expect a change in the resonance frequency and the amplitude at resonance. In the simulations the wall was considered as an infinitely thick rigid wall. No energy passes the wall and the ultrasound will be fully reflected at the wall. In our experiments however the wall is acoustically transparent to allow ultrasound to enter the flow cell and to prevent unwanted reflections. For such a compliant wall the (complex) amplitude of the image bubble needs to be adapted to the wall properties. There are still several questions related to the influence of the boundary. Do we observe a change in the dynamics close to a boundary? Is there a difference in the dynamics between floating bubbles near a boundary and that of adherent bubbles? Can we predict the bubble dynamics near a wall? Is the change in dynamics sufficient to distinguish acoustically between adherent and freely circulating microbubbles?

3 Nonlinear shell behavior of phospholipid-coated microbubbles[1]

*The key feature of ultrasound contrast agents microbubbles in distinguishing blood pool echo from tissue echo is their nonlinear behavior. Here, we investigate experimentally the influence of the stabilizing phospholipid-coating on the dynamics of ultrasound contrast agent microbubbles. We record the radial dynamics of individual microbubbles with an ultra-high speed camera as a function of the driving pressure and frequency. The shell was found to enhance the nonlinear bubble response at acoustic pressures as low as 10 kPa. For increasing acoustic pressures a decrease of the frequency of maximum response was observed for one set of bubbles, leading to a pronounced skewness of the resonance curve, which we show to be the origin of the "thresholding" behavior [Emmer et al., UMB **33**(6), 2007]. For another set of bubbles the frequency of maximum response was found to lie just above the resonance frequency of an uncoated microbubble, and to be independent of the applied acoustic pressure. The shell-buckling bubble model by Marmottant et al. [JASA **118**(6), 2005], which accounts for buckling and rupture of the shell, captures both cases for a unique set of the viscoelastic shell parameters. The difference in the observed nonlinear dynamics between the two sets of bubbles can be explained by a difference in the initial surface tension $\sigma(R_0)$ which is directly related to the phospholipid concentration at the bubble interface.*

[1]Submitted as: M. Overvelde, V. Garbin, J. Sijl , B. Dollet, N. de Jong, D. Lohse, and M. Versluis, Nonlinear shell behavior of phospholipid-coated microbubbles, Ultrasound Med. Biol.

3.1 Introduction

Ultrasound is the most commonly used medical imaging technique. As compared to computer tomography (CT) and magnetic resonance imaging (MRI) ultrasound offers the advantage that the hardware is relatively inexpensive and that it provides real-time images. Imaging with ultrasound is based on the reflection of the transmitted sound wave at tissue interfaces, where the wave encounters an acoustic impedance mismatch, and scattering due to inhomogeneities in the tissue. Unlike tissue, blood is a poor ultrasound scatterer, resulting in a low contrast echo. To enhance the visibility of the blood pool, ultrasound contrast agents (UCA) have been developed, enabling the visualization of the perfusion of organs. A promising new application of UCA is in molecular imaging [8] with ultrasound and in local drug delivery [9].

The typical UCA is composed of a suspension of microbubbles (radius 1-5 μm) which are coated with a phospholipid, albumin or polymer shell. The coating decreases the surface tension σ and therefore the capillary pressure $2\sigma/R$ and in addition counteracts diffusion through the interface, thus preventing the bubble from quickly dissolving in the blood. The mechanism by which microbubbles enhance the contrast in ultrasound medical imaging is two-fold. First, microbubbles reflect ultrasound more efficiently than tissue due to the larger difference in acoustic impedance with their surroundings. Second, in response to the oscillating pressure field microbubbles undergo radial oscillations due to their compressibility, which in turn generates a secondary sound wave. The oscillations are highly nonlinear, and likewise the sound emitted by the oscillating bubbles. Several pulse-echo techniques have been developed to increase the contrast-to-tissue ratio (CTR), making use of the nonlinear components in the acoustic response of microbubbles, which are not found in the tissue, e.g. pulse-inversion [5] and power modulation [6]. The nonlinear response specific to coated microbubbles offers the potential for new strategies for the optimization of the CTR.

The bubble dynamics in an ultrasound field can be described by a Rayleigh-Plesset type equation [29, 50]. The influence of the coating has been investigated in the last two decades, resulting in various extensions of the Rayleigh-Plesset equation. De Jong *et al.* [34] describe the coating as a thin homogeneous viscoelastic solid with a shell elastic parameter S_p and a shell friction parameter S_f. A more theoretical approach was provided by Church [33] who considered a viscoelastic surface layer of finite thickness. The models by De Jong *et al.* and Church were both developed for the albumin-coated contrast agent Albunex. [35] reduced the model developed by Church to the limit of a thin shell. Sarkar *et al.* [36] proposed a model for a thin shell of a viscoelastic solid where the effective surface tension depends on the area of the bubble and the elasticity of the shell. In the model by

Stride [51] the coating is a molecular monolayer, which is treated as a viscoelastic homogeneous material, and the shell parameters depend on the surface molecular concentration. Doinikov *et al.* [52] addressed the lipid shell as a viscoelastic fluid of finite thickness described by the linear Maxwell constitutive equation.

The models accounting for a viscoelastic solid predict that the elasticity of the shell increases the resonance frequency. Van der Meer *et al.* [41] scanned the insonation frequency at constant acoustic pressure to obtain resonance curves. The acoustic pressure was maintained below 40 kPa to ensure linear bubble dynamics. Van der Meer *et al.* [41] indeed found an increase of the resonance frequency with respect to uncoated microbubbles.

Emmer *et al.* [11] investigated the nonlinear dynamics of phospholipid-coated microbubbles $R_0 = 1 - 5\ \mu$m by increasing the applied acoustic pressure at a constant frequency of 1.7 MHz. They found that a threshold pressure exists, for microbubbles smaller than $R_0 = 2\ \mu$m, for the onset of bubble oscillations, and that the threshold pressure decreases with increasing bubble size. Bubbles with a radius larger than 2 μm show a linear increase in the amplitude of oscillation with the applied acoustic pressure.

De Jong *et al.* [10] observed another nonlinear phenomenon which was termed "compression-only" behavior, where the coated bubbles compress significantly more than they expand. In the study of De Jong *et al.* "compression-only" behavior was observed in 40 out of 100 experiments on phospholipid-coated bubbles, for acoustic pressures as low as 50 kPa. "Compression-only" behavior was most pronounced for small bubbles. Models accounting for a *linear* viscoelastic shell do not predict the "thresholding" or "compression-only" behavior.

Marmottant *et al.* [12] developed a model that incorporates the viscoelastic shell and in addition accounts for buckling and rupture of the shell that predicts the "compression-only" behavior in great detail. The model is based on the behavior of a phospholipid monolayer for quasi-static compression [53–55]. Depending on the number of phospholipid molecules per unit area the gas-water interface is shielded to a different extent, resulting in a different effective surface tension. In a small range of expansion and compression the phospholipid-shell behaves elastically as in the previous models and the effective surface tension is linear with the surface area of the bubble. In the elastic regime, compression of the bubble decreases the surface area and assuming a constant number of phospholipids thus increases the packing density and decreases the effective surface tension. For further compression the bubble reaches a critical packing density where the dense phospholipid monolayer starts to buckle. Below the buckling radius the effective surface tension vanishes. On the other hand, expansion of the bubble results in a lower packing density. Above a critical radius for the expansion, the concentration of the phospholipids at the interface is so low that the monolayer ruptures. If the gas is in direct contact with the liquid the effective surface tension reaches the surface tension of water.

Van der Meer *et al.* measured the resonance curves at low acoustic pressure. For uncoated bubbles it is well known that the resonance curve becomes asymmetrical and that the frequency of maximum response decreases with increasing acoustic pressure [56, 57]. Emmer *et al.* scanned the acoustic pressure, keeping the frequency constant and showed that small bubbles have the highest threshold pressure. The question remains whether this effect is bubble-size or frequency dependent. Therefore some questions remained unanswered since the experiments performed up to now did not cover the full parameter space. A better insight in the nonlinear phenomena of coated bubbles can be gained by changing both the applied acoustic pressure and the insonation frequency on the same bubble.

In this chapter, we measure the resonance curve of a bubble as a function of the acoustic pressure to study the influence of the acoustic pressure on the resonance curve. Similarly, we study the influence of the frequency on the “thresholding” behavior. The experimental results are compared to the existing models and the influence of the phospholipid-coating on the nonlinear dynamics of UCA microbubbles is discussed in detail. The chapter is organized as follows. In Sec. 3.2 the predictions of three types of models are discussed. The setup and reproducibility of the experiments is addressed in Sec. 3.3. The full dynamics of single phospholipid microbubbles are described and compared with simulations to obtain the shell parameters in Sec. 3.4. In Sec. 3.5 the influence of the shell parameters are discussed on the bubble dynamics and the conclusions are given in Sec. 3.6.

3.2 Models

The most general equation describing the radial dynamics of a coated bubble is given by an extended Rayleigh-Plesset equation [12]:

$$\begin{aligned}\rho\left(\ddot{R}R+\frac{3}{2}\dot{R}^2\right) &= \left(P_0+\frac{2\sigma(R_0)}{R_0}\right)\left(\frac{R_0}{R}\right)^{3\kappa}\left(1-\frac{3\kappa\dot{R}}{c}\right)\\ &\quad -P_0-P(t)-4\mu\frac{\dot{R}}{R}-\frac{2\sigma(R)}{R}-4\kappa_s\frac{\dot{R}}{R^2}\end{aligned} \tag{3.1}$$

where ρ is the liquid density, μ the dynamic viscosity of the liquid, c the speed of sound in the liquid, and κ the polytropic exponent of the gas inside the bubble. P_0 is the ambient pressure and $P(t)$ is the driving pressure pulse with a pressure amplitude P_a. R_0 is the initial bubble radius, $R(t)$ the time-dependent radius of the bubble and the overdots denote the time derivatives. κ_s accounts for the surface dilatational viscosity of the shell and $\sigma(R)$ is the effective surface tension which in some models is a function of the radius.

In this section we discuss the results of three different models: a model for an uncoated bubble, a model for a bubble with a *linear* viscoelastic shell and a model including buckling and rupture of the shell. In the case of an uncoated bubble there is no shell and the surface viscosity $\kappa_s = 0$. The gas is in direct contact with the water, resulting in the surface tension of the gas-liquid system $\sigma(R) = \sigma_w$.

The shell-buckling model by Marmottant *et al.* [12] accounts for three regimes of the shell behavior: elastic, buckled, and ruptured and the model is applicable to high amplitude oscillations. Fig. 3.1 shows the effective surface tension in the three regimes which is given by:

$$\sigma(R) = \begin{cases} 0 & \text{if } R \leq R_b \\ \chi\left(\dfrac{R^2}{{R_b}^2} - 1\right) & \text{if } R_b < R < R_r \\ \sigma_w & \text{if } R \geq R_r \end{cases} \tag{3.2}$$

with χ the elasticity of the shell and σ_w the surface tension of the gas-water interface. The shell buckles for radii below the buckling radius R_b and is in the ruptured state for radii larger than $R_\mathrm{r} = R_b\sqrt{\frac{\sigma_w}{\chi} + 1}$. The effective surface tension in the elastic regime depends on the concentration of phospholipids and therefore on the area of the bubble. The initial state is defined by the initial surface tension $\sigma(R_0)$ which is directly related to the buckling radius $R_b = R_0/\sqrt{\frac{\sigma(R_0)}{\chi} + 1}$, see

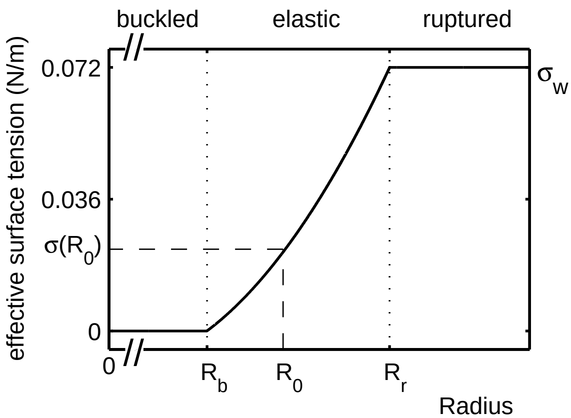

Figure 3.1: Effective surface tension in the shell-buckling model as a function of the bubble radius. The effective surface tension in the model has three regimes. The bubble buckles for $R \leq R_b$, is ruptured for $R \geq R_r$, and behaves elastically in for $R_b < R < R_r$.

Fig. 3.1. We prefer to define $\sigma(R_0)$ instead of R_b as was done by Marmottant *et al.* [12] because $\sigma(R_0)$ immediately reveals the initial state of the shell with respect to the buckled and ruptured regime. The results will also be compared to a coated bubble model accounting for a *linear* viscoelastic shell which is valid in the limit of small amplitude oscillations. We use the linearized effective surface tension of the shell-buckling model in the elastic regime:

$$\sigma(R) = \sigma(R_0) + 2\chi\left(\frac{R}{R_0} - 1\right) \tag{3.3}$$

In the case $\sigma(R_0) = \sigma_w$ we obtain the well-known equation for the effective surface tension of De Jong *et al.* [34].

For small amplitude oscillations we can obtain the eigenfrequency of the bubble. For a coated bubble the eigenfrequency of the bubble with a *linear* viscoelastic shell equals the eigenfrequency of the model by Marmottant *et al.* in the elastic regime. The eigenfrequency of a bubble with a *linear* viscoelastic shell f_0^c is given by [41]:

$$f_0^{\text{coated}} = \frac{1}{2\pi}\sqrt{\frac{1}{\rho R_0^2}\left(3\kappa P_0 + (3\kappa-1)\frac{2\sigma(R_0)}{R_0} + \frac{4\chi}{R_0}\right)} \tag{3.4}$$

In the case of an uncoated bubble the eigenfrequency is [29, 30]:

$$f_0^{\text{uncoated}} = \frac{1}{2\pi}\sqrt{\frac{1}{\rho R_0^2}\left(3\kappa P_0 + (3\kappa-1)\frac{2\sigma_w}{R_0}\right)} \tag{3.5}$$

To investigate the dynamics as a function of the applied frequency and acoustic pressure, simulations are performed for a bubble with a radius $R_0 = 3.2$ μm with the three different models described above. Fig. 3.2 shows the resonance curves obtained from numerical simulations as a function of the acoustic pressure for an uncoated microbubble (A), a microbubble with a *linear* viscoelastic shell (B), and a microbubble with a viscoelastic shell including buckling and rupture of the shell (C). To investigate the linearity of the resonance curves, the relative fundamental amplitude of oscillation A_1 is divided by the acoustic pressure P_a. In the case of a linear resonance curve the shape and amplitude are identical at each pressure. For all three models the value A_1/P_a is normalized to the response of an uncoated bubble at $P_a = 1$ kPa. The uncoated bubble has a resonance frequency near 1 MHz, see Fig. 3.2A. The maximum amplitude $(A_1/P_a)_{\text{norm}}$ slightly decreases with increasing pressure which reflects the onset of its nonlinear behavior. In Fig. 3.2B the response of a bubble with the *linear* viscoelastic shell is shown. Its resonance frequency is almost 3 times the resonance frequency of the uncoated bubble, owing

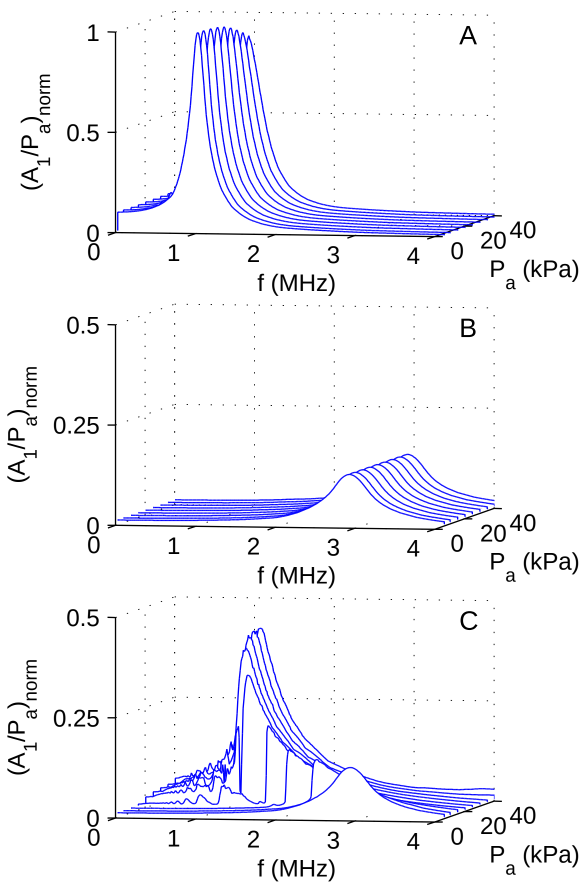

Figure 3.2: Simulations of the resonance curve as a function of the acoustic pressure. The relative amplitude of oscillation A_1 is divided by the acoustic pressure amplitude P_a and normalized with the response of the uncoated bubble at $P_a = 1$ kPa. A) Uncoated. B) *Linear* viscoelastic shell. C) Elastic shell including buckling and rupture of the shell. The initial radius of the bubble is $R_0 = 3.2\ \mu$m, and in case of a coating $\chi = 2.5$ N/m, $\sigma(R_0) = 0.02$ N/m, and $\kappa_s = 6 \cdot 10^{-9}$ kg/s.

to the elasticity while its maximum amplitude response is 8 times lower than that of the uncoated bubble as a result of the combined effect of the increased damping and elasticity of the shell. The oscillation amplitude is independent of the applied acoustic pressure and indicates a linear response. Fig. 3.2C shows the simulations performed with the shell-buckling model, showing dependence on the applied acoustic pressure. For the initial surface tension of the bubble $\sigma(R_0) = 0.02$ N/m and for low acoustic pressure $P_a = 1$ kPa, the bubble is oscillating in the elastic regime. Therefore the resonance curve is identical to the response of the bubble with the *linear* viscoelastic shell. An increase of the acoustic pressure induces strong nonlinear behavior and skewing of the resonance curves is observed. For linear oscillations the response is maximal at the resonance frequency while in the case of nonlinear behavior this need to be the case. In general, there is a frequency of maximum response which decreases with increasing acoustic pressure. At $P_a = 40$ kPa the frequency of maximum response decreased and approaches the eigenfrequency of the uncoated bubble. The relative amplitude of oscillation at the frequency of maximum response increases with increasing acoustic pressure which reveals another nonlinear response. The resonance behavior obtained with the three models is significantly different. An experimental study of the resonance curves as a function of the acoustic pressure applied to UCA microbubbles may therefore reveal the influence of the phospholipid-coating on the bubble dynamics.

3.3 Experimental setup

Fig. 3.3 shows a schematic drawing of the experimental setup. The ultrasound contrast agent BR-14 (Bracco S.A., Geneva, Switzerland) was injected in an OptiCell cell culture chamber (NUNC^{TM}, Thermo Fisher Scientific) filled with a saline solution. The OptiCell chamber was mounted in a water bath and connected to a 3D micropositioning stage. A water tank mounted on a planar-stage was designed to hold an illumination fiber and the ultrasound transducer (PA168, Precision Acoustics). The driving pulse for the transducer was generated by an arbitrary waveform generator (8026, Tabor Electronics) and amplified by a RF-amplifier (350L, ENI). The sample was imaged with an upright microscope equipped with a water-immersed 100× objective (Olympus). The dynamics of the microbubble was captured with the ultra high-speed Brandaris 128 camera [39] at a framerate of 15 million frames per second (Mfps). An optical tweezers setup allowed for the positioning of a single microbubble in 3D [58]. The infrared laser beam of the optical tweezers was coupled into the microscope using a dichroic mirror. The optical trap was formed through the imaging objective. The setup combining the Brandaris 128 camera with optical tweezers will be described in detail in chapter 6 and 7.

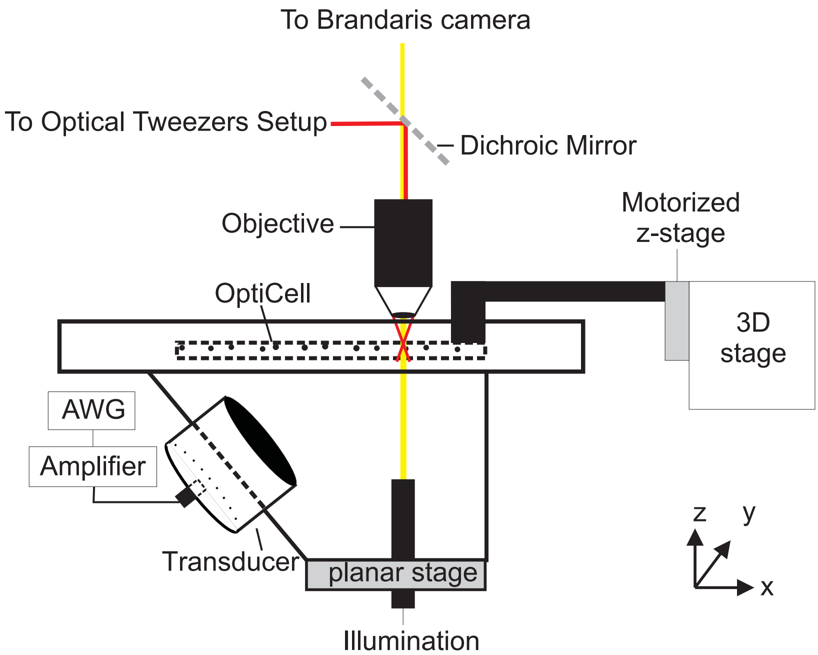

Figure 3.3: (color online) Schematic drawing of the experimental setup. The solution containing contrast agent microbubbles is injected in an OptiCell chamber. The chamber is located in a water tank which holds the transducer and illumination fiber. The driving ultrasound pulse is produced by an arbitrary waveform generator (AWG), amplified, and sent to the transducer. The bubbles are imaged and manipulated with optical tweezers through the same 100$\times$ objective.

The bubbles were insonified with an ultrasound burst of 10 cycles whose first and last 3 cycles were tapered with a Gaussian envelope. To scan the frequency with a constant acoustic pressure the transducer was calibrated prior to the experiments with a needle hydrophone (HPM02/1, Precision Acoustics). To align the acoustical focus of the transducer and the optical focus of the objective the OptiCell was removed, the tip of the hydrophone was positioned in the focus of the objective, and the transducer was aligned with the planar-stage. The 3D-stage connected to the OptiCell chamber allowed for the movement of the sample independently of the transducer to keep the acoustical and optical focus aligned. A motorized stage (M110-2.DGm, PI) was used to accurately control the distance between the bubble in the trap and the OptiCell wall. In all experiments the minimum distance between the bubble and the wall was 100 μm.

The experimental protocol is based on the microbubble spectroscopy method by Van der Meer *et al.* [41]. Each resonance curve is a result of 2 runs of the Brandaris 128 camera recording 6 movies of 128 frames with 12 increasing frequencies at

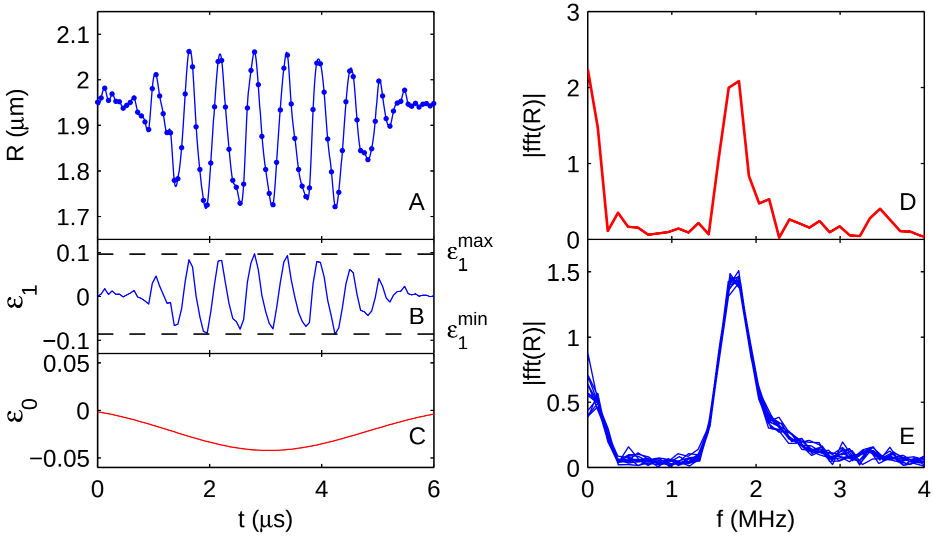

Figure 3.4: A) Experimental *R(t)*-curve of a bubble $R_0 = 2\ \mu$m, insonified with an acoustic pressure $P_a = 37.5$ kPa and a frequency $f = 1.7$ MHz. B) The relative fundamental response ε_1, C) the low frequency response ε_0. D) The frequency response of the *R(t)*-curve. E) The frequency response of a single 2.4 μm radius bubble insonified with $P_a = 30$ kPa and $f = 1.7$ MHz is reproducible over 12 separated experiments.

constant acoustic pressure. The experiment was repeated several times for increasing acoustic pressure on the very same bubble, until the full parameter space of acoustic pressure and frequency ranges was covered (typically 8 pressures). Each one of the 96 (8×12) movies therefore captured the radial dynamics at a single acoustic pressure and frequency. The radius vs. time curve (*R(t)*-curve) of the bubble was determined by tracking the contour of the bubble in each frame with a code programmed in Matlab®.

To ensure that the observed nonlinear phenomena were not caused by changes in the bubble properties due to repeated insonation, we performed a set of control experiments. In the first control experiment we sent 12 pulses at constant acoustic pressure and frequency and confirmed the reproducibility of the 12 *R(t)*-curves. The same protocol was then repeated for a higher acoustic pressure and we found that the relative standard deviation at the fundamental frequency was below 7% unless a bubble visibly reduced in size during the experiments. Fig. 3.4E shows the reproducibility of the bubble frequency response of a 2.4 μm radius bubble insonified 12 times with an acoustic pressure $P_a = 30$ kPa and frequency $f = 1.7$ MHz. The second test consisted in repeating a resonance frequency experiment on a single bubble at a fixed acoustic pressure, to verify that the bubble behavior would not change due to repetitive insonation. We observed that the frequency of maximum response was constant for a given acoustic pressure. Finally, to ensure that by repetitive frequency scans at increasing acoustic pressures the bubble properties were not altered, we repeated one run with low acoustic pressure after a few runs with increasing acoustic pressure and compared the response with the one obtained in a previous run at the same pressure. These experiments confirmed that the observed nonlinear phenomena are a result of the phospholipid-coated bubble dynamics and not a side effect due to aging of the bubble.

Fig. 3.4A shows a typical oscillation of a $R_0 = 2\ \mu$m bubble insonified at a frequency $f = 1.7$ MHz and at an acoustic pressure $P_a = 37.5$ kPa. The compression phase of the oscillations is larger than the expansion phase. The compression phase of the oscillations is larger than the expansion phase. This “compression-only” behavior [10] causes a low frequency component, see chapter 4. The authors showed through a weakly nonlinear analysis that the “compression-only” behavior can be excluded by filtering out the low frequency component. The relative excursion at the fundamental frequency ε_1 (blue) and the low frequency response ε_0 (red) are shown in Fig. 3.5B and C. We use as a measure for the maximum relative radial amplitude at the fundamental frequency A_1:

$$A_1 = \frac{\varepsilon_1^{\max} - \varepsilon_1^{\min}}{2} \tag{3.6}$$

where $\varepsilon_1^{\max}$ is the maximum relative expansion and $\varepsilon_1^{\min}$ the minimum relative expansion, see Fig. 3.4B.

In the following we nondimensionalize the frequency with the resonance frequency of the uncoated bubble:

$$\Omega = \frac{f}{f_0^{\text{uncoated}}} \tag{3.7}$$

and with the frequency of maximum response:

$$\Omega_{\text{MR}} = \frac{f_{\text{MR}}}{f_0^{\text{uncoated}}} \tag{3.8}$$

The resonance curves will be obtained from A_1 as a function of Ω.

3.4 Results

Fig. 3.5 shows the resonance curve for three values of the acoustic pressure $P_a = 7.5, 12.5,$ and 25 kPa. The bubble has a radius of $R_0 = 3.2\ \mu$m and is positioned 150 μm from the wall while the applied frequency is between 0.75 and 3 MHz. The experimental data (circles) are compared to the three different models, the uncoated bubble (blue), the coated bubble with a *linear* viscoelastic shell (black) and the coated bubble including buckling and rupture of the shell (red). For comparison the amplitude of oscillation A_1 is normalized to the maximum simulated response of an uncoated bubble (A_1^{norm}). For an acoustic pressure $P_a = 7.5$ kPa (top) the experimental data show a maximum response $\Omega_{\rm MR} = 2.5$. The frequency of maximum response decreases to $\Omega_{\rm MR} = 1.7$ at $P_a = 12.5$ kPa (middle) and to

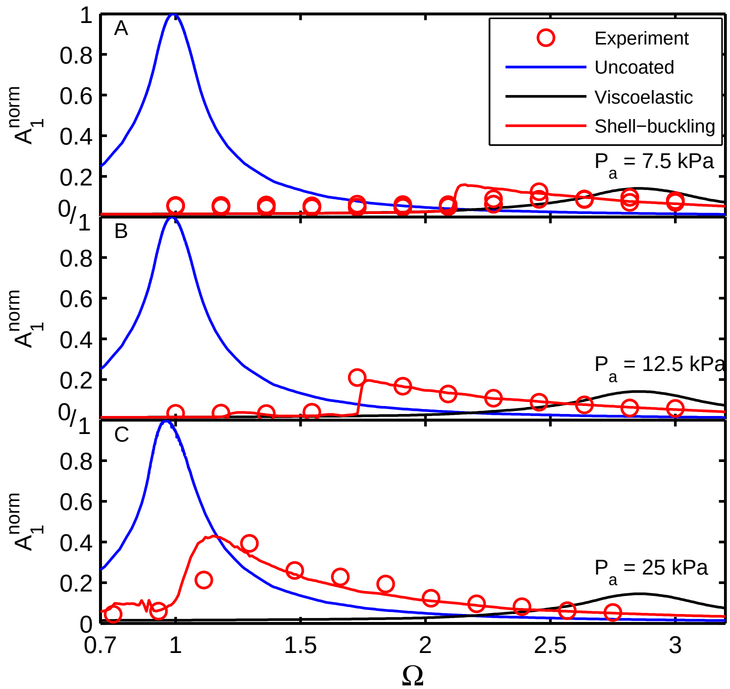

Figure 3.5: Skewing of the resonance curve of a coated microbubble at low acoustic pressures ($P_a = 7.5$, 12.5, and 25 kPa). The model for the uncoated bubble (blue) and a *linear* elastic shell model (black) cannot predict skewing of the resonance curve at low acoustic pressures. The shell model [12] including buckling and rupture (red) captures the skewness of the experimental resonance curve (circles). The bubble radius is 3.2 μm and the shell parameters are the same for both coated bubble models: $\chi = 2.5$ N/m, $\kappa_s = 6 \cdot 10^{-9}$ kg/s and $\sigma(R_0) = 0.02$ N/m.

$\Omega_{MR} = 1.4$ at $P_a = 25$ kPa (bottom). Besides a decrease in the frequency of maximum response the resonance curves at $P_a = 12.5$ and 25 kPa are strongly skewed. At low acoustic pressure ($P_a = 7.5$ kPa) the observed maximum amplitude of oscillation is small compared to the simulated amplitude of an uncoated microbubble $A_1^{norm} = 0.1$. The maximum amplitude of oscillation relative to an uncoated bubble increases with increasing acoustic pressure, and at $P_a = 25$ kPa the amplitude of oscillation is $A_1^{norm} = 0.4$. The experiment at $P_a = 7.5$ kPa was repeated to ensure that the change in behavior for increasing acoustic pressure is not an artifact due to a change in the properties of the bubble. The comparison with the models showed that the shell-buckling model accounting for an elastic regime, buckling and rupture of the shell (red) captures the decrease in the frequency of maximum response, the asymmetry of the resonance curves, and the relative amplitude of oscillation with a single set of shell parameters.

We present the experimentally obtained relative amplitude of oscillation A_1 for the full acoustic pressure and frequency scan in an iso-contour plot in Fig. 3.6A. A total of 120 *R(t)*-curves have been measured near the frequency of maximum response Ω_{MR} in the acoustic pressure range $P_a = 7.5 - 25$ kPa at an interval of 2.5 kPa. Fig. 3.6B shows the simulations with the shell-buckling model with the same shell parameters as in Fig. 3.5. The comparison of the frequency of maximum response Ω_{MR} obtained from the experiments (circles) and the simulations for the three different models is shown in Fig. 3.6C. Ω_{MR} decreases by 50% for an increase of the acoustic pressure from $P_a = 7.5$ to $P_a = 25$ kPa. The frequency of maximum response Ω_{MR} simulated with the shell-buckling model (red) is in excellent agreement with the experimental results. For comparison the frequency of maximum response obtained with the model for an uncoated bubble and the *linear* viscoelastic model are shown. In the shell-buckling model at low acoustic pressures $P_a < 2$ kPa the oscillations are in the elastic regime and the frequency of maximum response equals the resonance frequency of a coated bubble that follows from the *linear* viscoelastic model. Above acoustic pressures $P_a > 2$ kPa the shell starts to buckle and the frequency of maximum response decreases rapidly, approaching the resonance frequency of an uncoated bubble at $P_a > 20$ kPa.

A vertical scan line of Fig. 3.6A and B results in the typical resonance curves shown in Fig. 3.5. A horizontal scan line on the other hand results in the pressure-dependent response for different applied frequencies. De facto this is the same experiment as performed by Emmer *et al.* [11] with the exception that Emmer *et al.* varied bubble radius R_0, not frequency. Such a horizontal scan-line is depicted in Fig. 3.7 where the relative amplitude of oscillation A_1 is shown for three applied frequencies $\Omega = 2.1$ (A), $\Omega = 1.5$ (B), and $\Omega = 1$ (C). For each frequency, the experimentally observed amplitude of oscillations (circles) increases nonlinearly with increasing acoustic pressure. In particular, the so-called “thresholding”

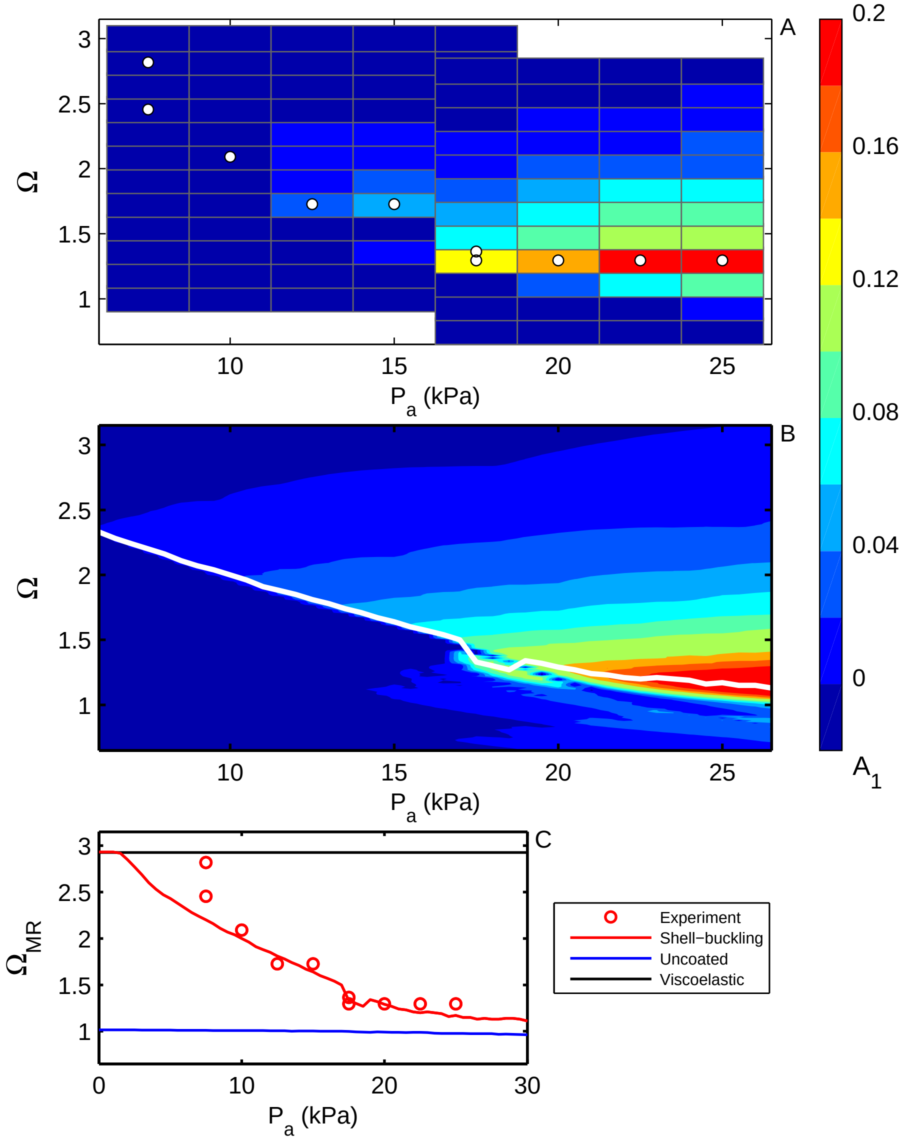

Figure 3.6: The relative amplitude of oscillations A_1 as a function of the acoustic pressure P_a and frequency Ω. A) Experimentally measured A_1 as a function of P_a and Ω for a bubble $R_0 = 3.2\ \mu$m. The frequency of maximum response Ω_{MR} (white dots) B) Simulations with the model including buckling and rupture of the shell. The white line shows the frequency of maximum response Ω_{MR}. The bubble has a radius of 3.2 μm and the values for the shell parameters are $\chi = 2.5$ N/m, $\kappa_s = 6 \cdot 10^{-9}$ kg/s and $\sigma(R_0) = 0.02$ N/m. C) The frequency of maximum response Ω_{MR} as a function of P_a.

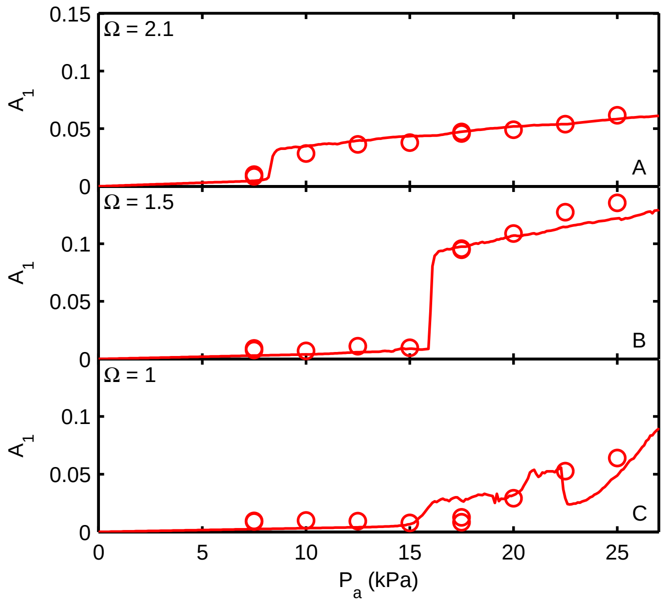

Figure 3.7: Relative amplitude of oscillation A_1 as a function of the acoustic pressure P_a. A_1 increases nonlinearly and displays the "thresholding" behavior. The prediction of the shell-buckling model is plotted (lines) for each value of the frequency and captures the experimental data (circles).

behavior is apparent. The threshold pressure for the onset of oscillations depends on the frequency and is most pronounced for $\Omega = 1.5$, where the bubble shows no oscillations if driven below $P_a = 15$ kPa and abruptly starts to oscillate ($A_1 \sim 0.1$) at $P_a = 17.5$ kPa. The shell-buckling model (solid lines) reproduces the data accurately and predicts the "thresholding" behavior.

The decrease of the resonance frequency with increasing pressure as shown in Fig. 3.6C does not uniquely describe the bubble response. We observe a different behavior for different bubbles, even for bubbles of the same size. Fig. 3.8 shows the frequency of maximum response Ω_{MR} of two equally sized bubbles $R_0 = 2.4$ μm. To compare the response of different bubbles we plot Ω_{MR} as a function of A_1 instead of P_a. One bubble has a frequency of maximum response $\Omega_{\mathrm{MR}} = 2.2$ at $A_1 = 0.03$ and shows a decrease in the frequency of maximum response of 40% with increasing A_1, reaching a value of $\Omega_{\mathrm{MR}} = 1.4$ at $A_1 = 0.12$ (triangles). The second bubble shows a different trend, $\Omega_{\mathrm{MR}} = 1.4$ and independent of A_1 (squares). The experimental results are compared to the results of the shell-buckling model.

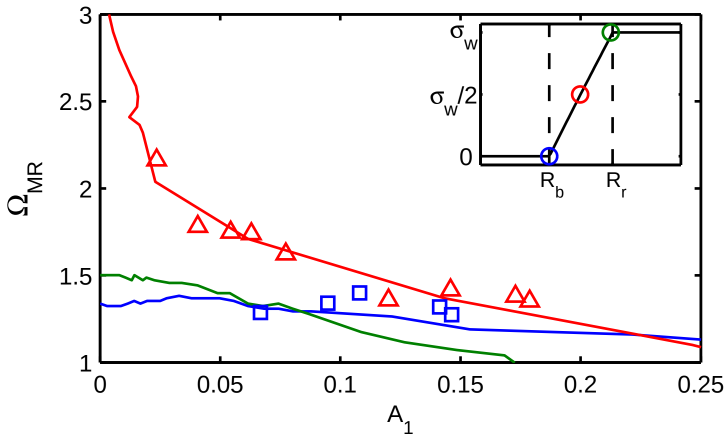

Figure 3.8: Normalized frequency of maximum response Ω_{MR} as a function of the relative amplitude of oscillation A_1 for two equally sized microbubbles $R_0 = 2.4$ μm. One of the bubbles shows a decrease in the frequency of maximum response Ω_{MR} (triangles), while the other bubble has a constant frequency of maximum response (squares). Simulations are shown with the shell-buckling model for three initial cases: the bubble is initially in the buckled state (blue), the ruptured state (green), and the elastic regime (red), see inset. The shell elasticity and shell viscosity are respectively, $\chi = 2.5$ N/m, $\kappa_s = 6 \cdot 10^{-9}$ kg/s.

Simulations performed for different values of the shell parameters χ and κ_s show that these parameters do not change the observed trend in Ω_{MR} with A_1. Therefore simulations were performed to calculate the frequency of maximum response for a bubble $R_0 = 2.4$ μm for the same shell elasticity $\chi = 2.5$ N/m and shell viscosity $\kappa_s = 6 \cdot 10^{-9}$ kg/s and only the initial surface tension $\sigma(R_0)$, which depends on the phospholipid concentration on the bubble surface, is varied to investigate its influence, see Fig. 3.8. The simulations with $\sigma(R_0) = \sigma_w/2$ (red) capture the decrease in the Ω_{MR} (triangles), while simulations with $\sigma(R_0) = 0$ N/m capture the constant Ω_{MR} (squares).

Over 4000 *R(t)*-curves were obtained experimentally on 45 bubbles ranging in size between $R_0 = 1.2 - 3.4$ μm. The resulting 168 frequencies of maximum response Ω_{MR} are shown as a function of A_1 (dots) for all bubbles in Fig. 3.9. For small amplitude of oscillations ($A_1 < 0.05$) the experimental data (dots) are scattered between $\Omega_{MR} = 1.2$ and $\Omega_{MR} = 3$. For increasing amplitude of oscillations the frequency of maximum response converges to a value of $\Omega_{MR} = 1.2$. For comparison the regimes of Ω_{MR} are shown for the smallest bubble $R_0 = 1.2$ μm (red) and largest bubble $R_0 = 3.4$ μm (blue) are shown. The overlapping regime of both bubbles is highlighted in green. The minimum Ω_{MR} is obtained with $\sigma(R_0) = 0$ N/m and the maximum Ω_{MR} with $\sigma(R_0) = \sigma_w/2$. Similar to the ex-

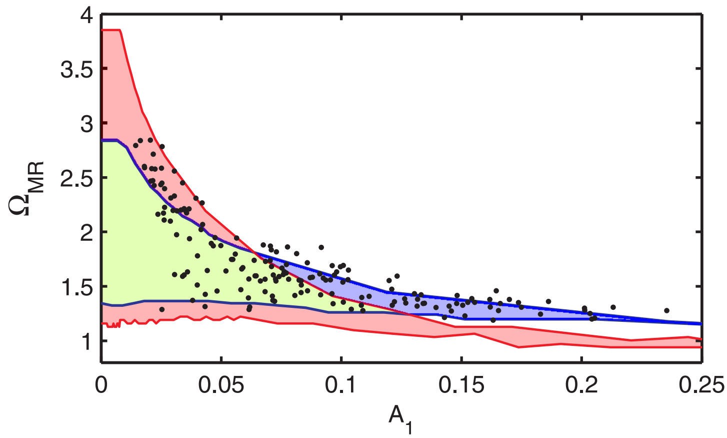

Figure 3.9: Experimental obtained Ω_{MR} as a function of the relative amplitude of oscillation A_1 (dots) for all bubbles $R_0 = 1.2 - 3.4\ \mu$m. The simulated regimes of the frequency of maximum response Ω_{MR} for a small bubble $R_0 = 1.2\ \mu$m (red) and a large bubble $R_0 = 3.4\ \mu$m (blue) are plotted. The overlapping regime of both bubbles is colored green. The lines show Ω_{MR} for $\sigma(R_0) = 0$ N/m (bottom) and $\sigma(R_0) = \sigma_w/2$ (top). The shell elasticity and shell viscosity are kept constant, $\chi = 2.5$ N/m, $\kappa_s = 6 \cdot 10^{-9}$ kg/s.

perimental results Ω_{MR} is strongly scattered at low A_1, while at $A_1 > 0.15$ the frequency of maximum response is practically indistinguishable from the resonance frequency of an uncoated bubble.

3.5 Discussion

3.5.1 Initial surface tension

In the previous section we found a large variability in the frequency of maximum response Ω_{MR} as a function of the relative amplitude of oscillation A_1 even for equally sized bubbles. Simulations showed that the variability in the trend in Ω_{MR} can be explained by a difference in the initial surfactant concentration, expressed in the effective surface tension at rest $\sigma(R_0)$. To investigate the influence of $\sigma(R_0)$ on the "compression-only" behavior, skewing of the resonance curves, and the "thresholding" behavior, we perform simulations with the shell-buckling model. The simulations were performed for a bubble with a radius $R_0 = 2\ \mu$m, with a shell elasticity $\chi = 2.5$ N/m, and a shell viscosity $\kappa_s = 6 \cdot 10^{-9}$ kg/s.

"Compression-only" behavior was first observed in experiments by De Jong *et al.* [10]. Marmottant *et al.* [12] showed that the initial state of the bubble, i.e. the initial surface tension $\sigma(R_0)$, is essential to determine whether "compression-only" behavior appears. They showed that the most pronounced "compression-

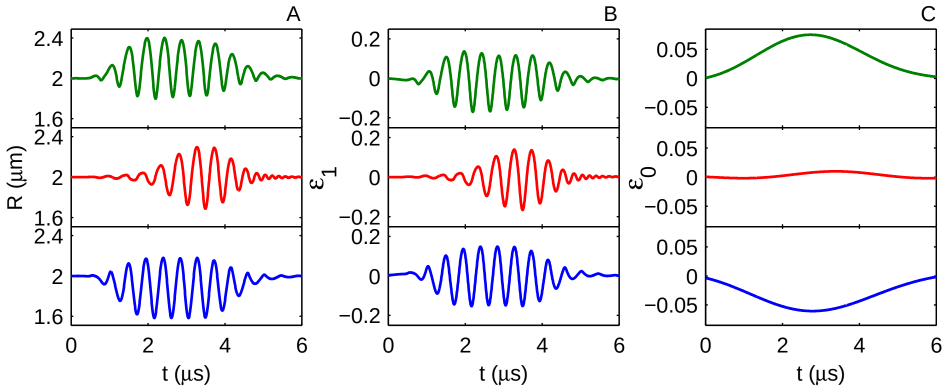

Figure 3.10: Influence of the initial surface tension on the radial dynamics, $\sigma(R_0) = 0$ N/m (bottom), $\sigma(R_0) = \sigma_w/2$ (middle), and $\sigma(R_0) = \sigma_w$ (top). The acoustic pressure and frequency are 40 kPa and $\Omega = 1.3$, respectively. A) *R(t)*-curve, B) fundamental response $\varepsilon_{\text{fund}}$, and C) low frequency response ε_0.

only" behavior is observed for a bubble with a radius R_0 close to its buckling radius R_b which is equivalent to $\sigma(R_0) = 0$ N/m. The authors pointed out that the compression modulus $-V\dfrac{dP}{dV}$ of the coated bubble is much higher in the elastic state than in the buckled or ruptured state. In our simulations, the shell elasticity $\chi = 2.5$ N/m and indeed the compression modulus of the bubble is 10 times higher in the elastic regime. Fig. 3.10 shows the simulated bubble dynamics for a "ruptured" bubble $\sigma(R_0) = \sigma_w$ (top), an "elastic" bubble $\sigma(R_0) = \sigma_w/2$ (middle), and a "buckled" bubble $\sigma(R_0) = 0$ N/m (bottom), see also inset Fig. 3.8. The *R(t)*-curves (A) are divided in the fundamental response $\varepsilon_{\text{fund}}$ (B) and the low frequency response ε_0 (C), the latter being a measure for the "compression-only" behavior of the bubble 4. The "buckled" bubble shows more compression than expansion as expected. The expansion of the "ruptured" bubble is more pronounced as compared to its compression, hence we term this behavior "expansion-only" behavior in analogy of the "compression-only" behavior for the "buckled" bubble. The explanation is similar to that of "compression-only" behavior. The compression modulus in the ruptured regime is much lower than in the elastic regime and for a "ruptured" bubble it is easier to expand than to compress. In the case of an "elastic" bubble the bubble starts to oscillate in the midpoint of the elastic regime and the oscillations are symmetrical.

In our experiments, we predominantly observe "compression-only" behavior. Only occasionally ($\leq 3\%$) the expansion was observed to be larger than the compression. From the above simulations we conclude that most bubbles have an ini-

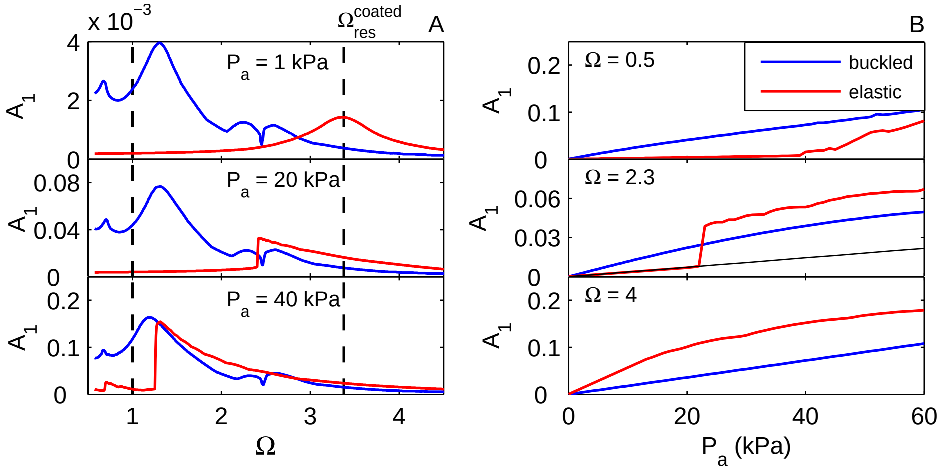

Figure 3.11: Simulations for two values of the initial surface tension: $\sigma(R_0) = 0$ N/m (blue) and $\sigma(R_0) = \sigma_w/2$ (red). A) Simulated resonance curves for three values of the acoustic pressure $P_a = 1$ kPa (top), $P_a = 20$ kPa (middle), and $P_a = 40$ kPa (bottom). B) Simulated relative amplitude of oscillations A_1 as a function of the acoustic pressure P_a for three different applied frequencies: $\Omega = 0.5$ (top), $\Omega = 2.3$ (middle), and $\Omega = 4$ (bottom).

tial surface tension $\sigma(R_0) = 0$ N/m and therefore R_0 close to the buckling radius. This can be explained as the capillary pressure forces the bubbles to a new equilibrium, and tensionless state, as previously pointed out by Marmottant *et al.* [12].

Fig. 3.5, 3.6, and 3.7 reveal that a bubble with a skewed resonance curve shows a decrease of the frequency of maximum response with increasing acoustic pressure. In addition it displays "thresholding" behavior [11]. The initial surface tension of this particular bubble was found to be $\sigma(R_0) = 0.02$ N/m. Here we will focus on the influence of $\sigma(R_0)$ on the shape of the resonance curves and the "thresholding" behavior for the two cases most relevant to our experiments, a "buckled" bubble and an "elastic" bubble. Fig. 3.11A shows the resonance curves for three values of the acoustic pressure $P_a = 1,\ 20,$ and 40 kPa (top-bottom). The shape of the resonance curve of the "buckling" bubble (blue) is hardly changed for all three pressures. The frequency of maximum response is almost independent of the acoustic pressure and lies just above the resonance frequency of an uncoated bubble, $\Omega_{\mathrm{MR}} = 1.3$. For $P_a = 1$ kPa (top) the "elastic" bubble (red) oscillates only in the elastic regime and behaves like a bubble modeled with a *linear* viscoelastic shell as can be inferred from its frequency of maximum response $\Omega_{\mathrm{MR}} = \Omega_{\mathrm{res}} = 3.3$. On the other hand, the frequency of maximum response Ω_{MR} of the "elastic" bubble decreases with increasing pressure $P_a = 20$ kPa (middle). Since the radius of the "elastic" bubble now exceeds the elastic regime between R_b and R_r, the bubble is now also oscillating in the buckled and ruptured regime. The frequency of maximum response of the "elastic" bubble decreases even more for $P_a = 40$ kPa (bottom), approaching the resonance frequency of an uncoated bubble. The resonance curves of the "elastic" bubble are strongly skewed at $P_a = 20$ kPa and 40 kPa and practically no oscillations are observed for frequencies below its maximum response frequency.

Fig. 3.11B shows the influence of $\sigma(R_0)$ on the "thresholding" behavior. The amplitude of oscillations for the "buckled" bubble (blue) increases almost linearly with the acoustic pressure at all three frequencies (top-bottom). On the contrary, the "elastic" bubble (red) shows strong nonlinear behavior. For a driving frequency below the resonance frequency of the coated bubble ($\Omega_{\text{res}} = 3.3$), the amplitude of oscillations increases slowly with increasing acoustic pressure, until the slope suddenly changes and we observe "thresholding" behavior at $P_a = 40$ kPa (top) or $P_a = 22$ kPa (middle). The "elastic" bubble is initially oscillating in the elastic regime and A_1 increases very slowly with P_a. At a certain amplitude of oscillation the bubble starts to buckle and A_1 rapidly increases with P_a, leading to an apparent "thresholding" behavior. For comparison the linear increase in the response A_1 of a bubble with a *linear* viscoelastic shell is shown (black, middle).

3.5.2 Ambient pressure

The variability in the experimentally observed dynamics, such as skewing of the resonance curve, "thresholding" behavior, and "compression-only" behavior, can be explained by a change in the initial surface tension $\sigma(R_0)$, which depends on the concentration of phospholipids at the bubble interface. Provided that the total amount of phospholipids at the interface is constant, a change in the radius of the bubble would change $\sigma(R_0)$. The extent of the elastic regime can be calculated from Eq. 3.3 with $R = R_r$, $R_0 = R_b$, $\chi = 2.5$ N/m, and $\sigma(R_r) - \sigma(R_b) = \sigma_w$. The total size of the elastic regime is $0.01R_0$ and a bubble with $R_0 = R_b$ is only 1% smaller than a bubble starting to oscillate in the ruptured regime. As the volume scales with R^3 we can deduce from the ideal gas law that a change in the ambient pressure of 3% is sufficient to obtain a decrease of 1% in R_0. Therefore, we anticipate that a slight change of the ambient pressure will cause a change in the initial surface tension leading to a change in the observed bubble dynamics phenomena. The change in "compression-only" and subharmonic behavior caused by a change in the ambient pressure has been shown very recently by Frinking *et al.* [59].

3.5.3 Shell elasticity

Values of the shell elasticity of phospholipid-coated microbubbles were previously obtained by fitting the data to models accounting for a *linear* viscoelastic shell. By recalculating these values to the elasticity as defined in this paper the parameters correspond to a $\chi = 0.5 - 1$ N/m [37, 40, 41]. In these papers the amplitude of oscillation A_1 was in the order of 0.1 and the oscillations were expected to be in the elastic regime of the bubble. In the present chapter, we show that at oscillation amplitudes of $A_1 > 0.01$ the bubble is not oscillating purely in the elastic regime. The obtained shell elasticities fitted to a *linear* viscoelastic model can therefore be seen as effective shell elasticities. By definition the effective shell elasticities are lower than the shell elasticity obtained for the model including buckling and rupture of the shell and they decrease with increasing applied acoustic pressure.

3.5.4 Shell viscosity

In this chapter we showed that the relative amplitude of oscillation A_1 is well predicted with a constant shell viscosity $\kappa_s = 6 \cdot 10^{-9}$ kg/s. With the *linear* viscoelastic model of De Jong *et al.* [34] Gorce *et al.* [37] found a shell friction parameter of $S_f = 0.45 \cdot 10^{-6}$ kg/s, which is corresponds to a shell viscosity $\kappa_s = 9 \cdot 10^{-9}$ kg/s. Chetty *et al.* [40] used the model described by Hoff *et al.* [40]. The authors used a shell viscosity $\mu_s = 1$ Pas and a shell thickness $d_s = 2.5$ nm taking $R = R_0$ the shell viscosity is recalculated $\kappa_s = 8 \cdot 10^{-9}$ kg/s . On the other hand, Van der Meer *et al.* [41] obtained the damping from the width of the obtained resonance curves and found a shell viscosity in the same order. In addition the authors found that the shell viscosity decreases with increasing dilation rate. In some cases the resonance curves obtained by Van der Meer *et al.* were observed to be asymmetrical and the simple analogy with a harmonic oscillator is not valid anymore.

On the other hand, the *R(t)*-curves show detailed information of the bubble response at a single applied frequency and pressure. Fig. 3.12B shows the experimental *R(t)*-curve (blue) and the simulation (red) of a 3.2 μm radius bubble insonified with $P_a = 25$ kPa and $f = 1.5$ MHz (Fig. 3.12A). The maximum amplitude of oscillation is indeed well predicted by the simulations with $\kappa_s = 6 \cdot 10^{-9}$ kg/s. However, the simulations show oscillations after insonation, while in the experiments the bubble stops oscillating immediately after insonation. Using a higher κ_s for the simulations the bubble stops oscillating immediately after the ultrasound is turned of, but these simulations predict a too low amplitude of oscillation A_1. Possible explanations can be the thinning behavior as found by Van der Meer *et al.*. However, we have obtained strongly skewed resonance curves which cannot be described by the response of a simple harmonic oscillator. Another possibility is that the shell viscosity depends on the initial state of the bubble, i.e. is the bubble oscillating in the elastic, in the buckled, or in the ruptured state. But in the end, the damping of the shell is of less importance on the dynamics of the bubble than the nonlinear behavior as a result of buckling and rupture of the shell.

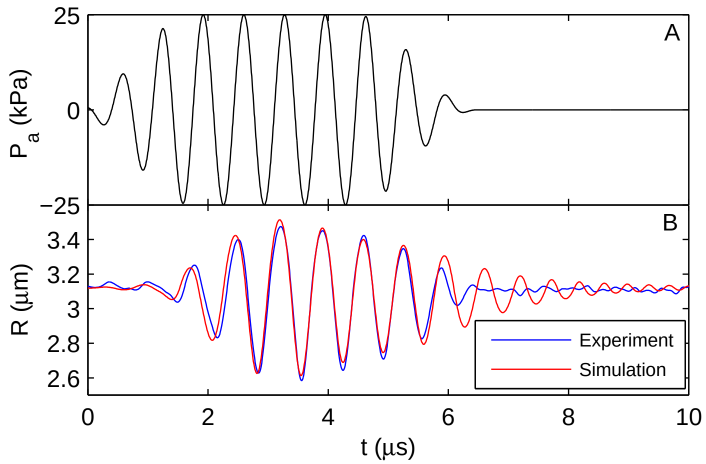

Figure 3.12: A) Applied acoustic pressure, $P_a = 25$ kPa and $f = 1.5$ MHz. B) Comparison of an experimental *R(t)*-curve (blue) with a simulated *R(t)*-curve (red).

3.6 Conclusions and outlook

We have studied experimentally the resonance curves of individual ultrasound contrast agent microbubbles as a function of the acoustic pressure. The experiments were performed by positioning the microbubbles with the aid of optical tweezers so that they can be regarded as if in an unbounded fluid. In this way we were able to exclude wall effects, and isolate the influence of the phospholipid monolayer only. Coated microbubbles show strong nonlinear dynamics at low acoustic pressures, such as “compression-only” behavior and skewing of the resonance curve, which could not be predicted by models accounting for a *linear* viscoelastic shell. The model by Marmottant *et al.* [12] accounting for an elastic regime and including buckling and rupture of the shell accurately predicts the observed nonlinear behavior of the phospholipid-coated microbubbles. We found that the dynamics of the BR-14 microbubbles can be explained with a single shell elasticity $\chi = 2.5$ N/m independent of the bubble radius. The maximum amplitude response of the bubbles is well predicted with a shell viscosity $\kappa_s = 6 \cdot 10^{-9}$ kg/s.

In general, in the experiments the bubbles show more compression than expansion limiting the initial surface tension $\sigma(R_0)$ in the regime $0 \leq \sigma(R_0) \leq \sigma_w/2$. Roughly, the observed phenomena can be divided into two regimes depending on the initial surface tension. A bubble initially in the buckled state $\sigma(R_0) = 0$ N/m or $R_0 = R_b$ shows strong compression-only behavior. The frequency of maximum response is near $\Omega = 1.3$ and almost independent of the acoustic pressure. A bubble initially in the elastic regime $0 \leq \sigma(R_0) \leq \sigma_w/2$ shows a rapid decrease of the frequency of maximum response with increasing acoustic pressure and a pronounced skewing of the resonance curves which we show is the origin of the so-called "thresholding" behavior.

The fundamental understanding of the nonlinear dynamics of phospholipid-coated bubbles at low acoustic pressures is important to optimize the frequencies and pressures used in the ultrasound imaging techniques. The model including buckling and rupture of the shell allows for the development of new imaging techniques using the observed phenomena of phospholipid-coated bubbles. For instance, "elastic" bubbles show "thresholding" behavior and are interesting for power modulation [6] due to the nonlinear increase in the amplitude of oscillation with applied pressure. On the other hand, engineering of bubbles for specific techniques is a promising application. Stride *et al.* [60] added nanoparticles to the shell restricting the bubbles to compress and behave nonlinearly. Further research on the influence of a phospholipid-coating on "compression-only" behavior and subharmonic behavior of UCA microbubbles is conducted and described in detail in chapter 4 and 5. Another exciting prospect is the development of ultra high-speed fluorescence imaging to visualize the time-resolved distribution of phospholipids at the interface during buckling and rupture of the shell.

4 “Compression-only” behavior of phospholipid-coated microbubbles[1,2]

Oscillating phospholipid-coated ultrasound contrast agent microbubbles display a so-called “compression-only” behavior, where it is observed that the bubbles compress efficiently while their expansion is suppressed. Here a theoretical understanding of the source of this nonlinear behavior is provided through a weakly nonlinear analysis of the shell buckling model proposed by Marmottant et al.. It is shown that the radial dynamics of the bubble can be considered as a superposition of a linear response at the fundamental driving frequency and a second order nonlinear low-frequency response that describes the negative offset of the mean bubble radius. The analytical solution deduced from the weakly nonlinear analysis shows that the “compression-only” behavior results from a rapid change of the shell elasticity with bubble radius. In addition, the radial dynamics of single phospholipid-coated microbubbles was recorded as a function of both the amplitude and the frequency of the driving pressure pulse. The comparison between the experimental data and the theory shows that the magnitude of “compression-only” behavior is mainly determined by the initial phospholipids concentration on the bubble surface, which slightly varies from bubble to bubble.

[1]Submitted as: Jeroen Sijl, Marlies Overvelde, Benjamin Dollet, Valeria Garbin, Nico de Jong, Detlef Lohse and Michel Versluis, “Compression-only” behavior: A second order nonlinear response of ultrasound contrast agent microbubbles, J. Acoust. Soc. Am.

[2]The experimental work in this chapter is part of the present thesis. The analytical and numerical work was performed by Jeroen Sijl.

4.1 Introduction

The contrast in medical ultrasound imaging is enhanced through the use of micron-sized bubbles which owing to their compressibility increase the scattering cross section of the blood pool. The typical bubble radius of ultrasound contrast agent (UCA) microbubbles is 2 to 3 μm. The gas core consists of air or an inert gas and the bubbles are coated with a thin protein, lipid or polymer layer. The microbubbles are resonant scatterers at medical ultrasound frequencies of 1 to 5 MHz. Moreover, unlike tissue, the contrast agents scatter at harmonic frequencies of the driving ultrasound frequency f, mainly at the second harmonic frequency $2f$, which opens up improved imaging modalities in ultrasound, termed harmonic imaging [61]. Power modulation imaging [62] and pulse inversion imaging [5], including many of its derivatives are now standard pulse-echo techniques found on ultrasound scanner equipment. These imaging modalities all exploit the nonlinear behavior of the ultrasound contrast agents. A thorough and fundamental understanding of the interaction of the ultrasound with the bubbles, the induced bubble dynamics and its resulting nonlinear acoustic response is therefore of prime importance for the development of improved contrast-enhanced ultrasound imaging.

The nonlinear dynamics of bubbles is described by the Rayleigh-Plesset (RP) equation. For coated bubbles the RP equation is extended with a set of shell parameters to model the rheological behavior of the viscoelastic coating. De Jong *et al.* [63] introduced a shell stiffness parameter and a shell friction parameter for Albunex, a human serum albumin-coated microcapsule. Church [33] refined the physical modeling for Albunex, while Hoff *et al.* [35] introduced a thin shell limit to model the phospholipid monolayer of Sonazoid, a second generation contrast agent. The volumetric oscillations predicted by the Rayleigh-Plesset equation were then used to predict attenuation and acoustic backscatter of the agent. Experiments on a representative sample of the UCA, containing many microbubbles, confirm the general trends and the influence of the bubble coating as predicted by the models. The resonance frequency is observed to shift to higher frequencies due to the shell stiffness and the extra damping introduced by the shell decreases the overall acoustic response [37, 41, 63].

At a detailed level and particularly on a single bubble level the agreement between theory and experiment is less convincing. Recent optical characterization studies using high-speed imaging revealed some interesting features of single bubble dynamics that could not be described by the traditional coated bubble models. One of them is “compression-only” behavior reported by De Jong *et al.* [10], where the bubble oscillations are non-symmetric with respect to the resting radius; the bubbles compress more than they expand.

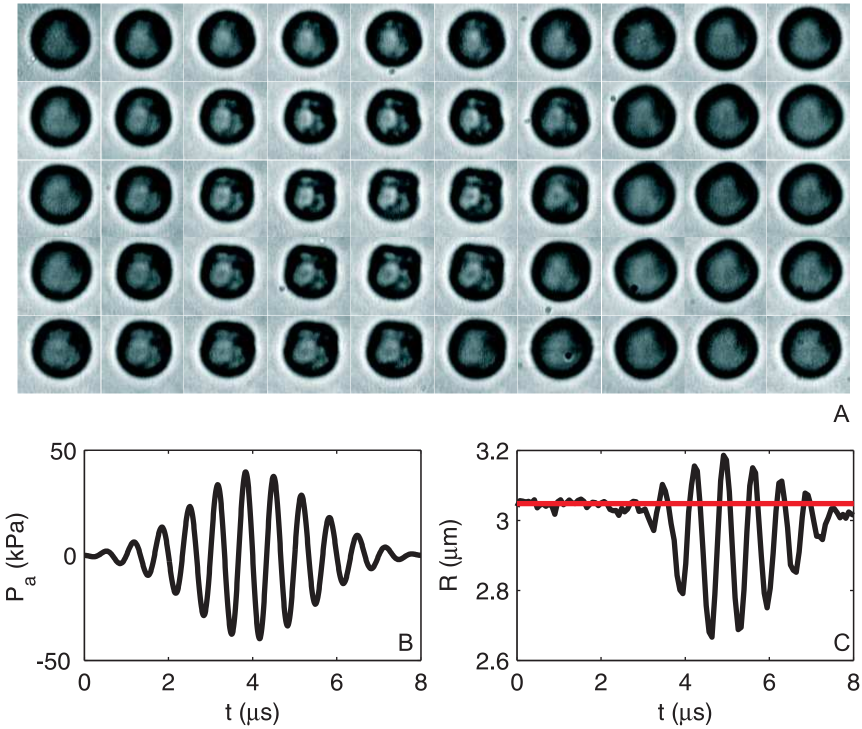

Figure 4.1: An example of "compression-only" behavior of a phospholipid-coated microbubble, recorded with the Brandaris ultrahigh-speed camera. A) optical images, showing buckling of the phospholipid shell B) the driving pressure pulse C) corresponding radius time curve.

A typical example of "compression-only" behavior is shown in Fig. 4.1. A selection of a high-speed recording displays the dynamics of a 3 μm radius phospholipid-coated BR-14 (Bracco Research S.A., Geneva, Switzerland) contrast agent bubble exited with a driving pulse with an amplitude of 40 kPa and a frequency of 1.5 MHz. Each row in Fig. 4.1A corresponds to one acoustic cycle. The frames to the left and to the right show the bubble during expansion, while the center frames show the bubble during compression at maximum pressure. The radius time curve of the bubble displays "compression-only" behavior, the bubble compresses twice as much relative to its expansion, see Fig. 4.1C. Another feature that can be identified in the recording is that the coating of the bubble appears to buckle during compression. Buckling also known as the 3-D collapse of a phospholipid monolayer occurs when a phospholipid monolayer is compressed beyond its saturated phospholipid concentration. At this point which is marked by zero surface tension the monolayer starts to fold. The buckling is shown to be reversible and repeatable. It should be noted that in typical recordings the buckling is not always as pronounced as shown in Fig. 4.1A. The “compression-only” behavior occurs quite frequently, 50% in a typical sample, see De Jong *et al.* [10].

Buckling is well-known for macroscopic phospholipid monolayers which has inspired Marmottant *et al.* [12] to develop a coated bubble dynamics model based on the quasi-static behavior of a phospholipid monolayer [64–68]. The model relates the lipids concentration at the gas-liquid interface to an effective surface tension. The total number of phospholipids on the interface is fixed and consequently the effective surface tension changes with bubble radius when the bubble pulsates. Marmottant *et al.* [12] show that this description of the phospholipid shell of a microbubble is able to capture correctly the “compression-only” behavior shown by these bubbles.

Experimental data presented in the paper by Marmottant *et al.* show very good agreement with the model calculations for each individual bubble where the shell parameters are free to vary for each case. So far we have not come to a generalized description of “compression-only” behavior with a unique and dedicated set of shell parameters; the overall trends are difficult to model. This has become evident in the work of De Jong *et al.* [10] where no clear dependency was found on either the initial bubble radius, the driving pulse frequency or pressure amplitude. The goal of this paper is therefore to come to a more universal description of the “compression-only” behavior. Following previous successful work on uncoated bubbles we linearize the generalized model of the Rayleigh-Plesset equation for coated bubbles up to second order to come to an analytical solution. The analytical solution is shown to give direct and detailed insight on how the shell parameters govern the “compression-only” behavior. We have also studied experimentally the radial dynamics and related “compression-only” behavior of single BR-14 microbubbles using the Brandaris 128 ultra-high speed camera [39]. Both the frequency and the amplitude of the driving pulse were varied to enable a full characterization of this phenomenon.

In the following section, Sec. 4.2, details of the model and the linearization will be discussed. In Sec. 4.3 we will discuss and show the implications of the results from the analytical solution on the full model of Marmottant *et al.* and the effect of the shell parameters. In Sec. 4.4 the experimental setup is described and in Sec. 4.5 the experimental results are discussed and related to the full numerical model. In Sec. 4.6 we end with a discussion. The conclusions are presented in Sec. 4.7.

4.2 Weakly nonlinear analysis

To describe the radial dynamics of a phospholipid-coated microbubble, different models have been proposed [12, 33, 35, 36, 63]. In general, the phospholipid shell is assumed to increase the damping of the system and is taken into account through a shell viscosity κ_s. In earlier models the increase of the maximum response frequency of coated microbubbles was accounted for by incorporating a shell stiffness that is described by the compression modulus or shell elasticity χ [35, 41, 63].

For a phospholipid-coated microbubble the shell elasticity can be expressed as the gradient that describes the change of the effective surface tension as a function of the bubble surface area A according to $\chi = A(d\sigma/dA)$ [12]. For a bubble oscillating with a small amplitude the effective surface tension may be expressed as a linear function of the bubble radius R through $\sigma(R) \simeq 2\chi(R/R_0 - 1)$. For larger amplitudes of oscillation the relation between the effective surface tension $\sigma(R)$ and bubble radius R deviates from this linear relation. Some authors assume a linear relationship between σ and R, with constant χ also for larger amplitudes of oscillation, while others explore more complex behavior of the viscoelastic shell. For now we assume that the relation $\sigma(R)$ is unknown. The generalized form of the bubble dynamics equation for a phospholipid-coated microbubble then reads:

$$\begin{aligned} \rho\left(R\ddot{R}+\frac{3}{2}\dot{R}^2\right) &= \left(P_0+\frac{2\sigma(R_0)}{R_0}\right)\left(\frac{R_0}{R}\right)^{3\kappa}\left(1-\frac{3\kappa\dot{R}}{c}\right) \\ &\quad -\frac{2\sigma(R)}{R}-4\mu\frac{\dot{R}}{R}-4\kappa_s\frac{\dot{R}}{R^2}-P_0-P_{\mathrm{A}}(t) \end{aligned} \tag{4.1}$$

In this equation R, $\dot{R}$ and $\ddot{R}$ are the radius, velocity and acceleration of the bubble wall, respectively. The initial bubble radius is given by R_0 and the ambient pressure by P_0. The properties of the surrounding water are described by the viscosity $\mu = 10^{-3}$ Pa s, the density $\rho = 10^3$ kg/m^3 and the speed of sound $c = 1500$ m/s. The driving pressure pulse is described by $P_{\mathrm{a}}(t)$. The relation between the internal gas pressure P_g, the gas temperature and bubble volume is described by the polytropic ideal gas law, $P_g \propto R^{-3\kappa}$ where κ is the polytropic exponent. For isothermal oscillations $\kappa = 1$ and for adiabatic oscillations κ is equal to the ratio of the specific heats of the gas inside the bubble, C_p/C_v. The thermal diffusion length scale inside the gas during one oscillation cycle can be shown to be smaller than the bubble radius [12, 41]. Therefore we approximate the oscillations as adiabatic. For the experimental agent BR-14 the gas core consists of perfluorocarbon-gas with $\kappa = C_p/C_v = 1.07$ [12, 41]. Following Eller [27] we can show that thermal damping is small but not zero in this problem. We account for thermal damping through a slight increase of the liquid viscosity $\mu = 2 \cdot 10^{-3}$ Pa s.

To understand why a phospholipid-coated microbubble shows “compression-only” behavior it is insightful to approximate Eq. 4.1 with a second order linearization. The linearized equations can be solved analytically as shown before for similar equations [33, 69]. As a most general assumption we approximate $\sigma(R)$ around $\sigma(R_0)$ for small amplitude oscillations around R_0 through a second-order

Taylor expansion:

$$\sigma(R) \;=\; \sigma(R_0)+2\chi_{eff}\left(\frac{R}{R_0}-1\right)+\frac{1}{2}\zeta_{eff}\left(\frac{R}{R_0}-1\right)^2 \tag{4.2}$$

where we have defined,

$$\chi_{eff} = \frac{1}{2}R_0\frac{\partial\sigma(R)}{\partial R}\bigg|_{R_0} \tag{4.3}$$

$$\zeta_{eff} = R_0^2\frac{\partial^2\sigma(R)}{\partial R^2}\bigg|_{R_0} \tag{4.4}$$

To come to an analytical solution of Eq. 4.1 we substitute Eq. 4.2 into Eq. 4.1 and we use a perturbation technique where we substitute,

$$R(t) = R_0(1+x) \tag{4.5}$$

into Eq. 4.1. Here, x represent the bubble’s relative radial excursion, where $x << 1$. After substitution we keep only the first and second order terms. This results in the following equation.

$$\ddot{x}+\omega_0\delta\dot{x}+\omega_0^2x = P_A(t)+4b_2\dot{x}x+\alpha x^2-\frac{3}{2}\dot{x}^2-\ddot{x}x \tag{4.6}$$

where ω_0 is the linear eigenfrequency of the system. We can show that the results of the weakly nonlinear analysis presented in the following are independent of the choice of the initial surface tension $\sigma(R_0)$. To simplify the calculations we therefore choose $\sigma(R_0)$ to be zero. The eigenfrequency is then given by:

$$\omega_0^2 = \frac{3P_0\kappa}{R_0^2\rho}+\frac{4\chi_{eff}}{R_0^3\rho} \tag{4.7}$$

From Eq. 4.7 it is clear that the shell elasticity increases the eigenfrequency of the coated bubble compared to that of an uncoated bubble. The linear dimensionless damping coefficient of the system consists of three parts,

$$\delta = \frac{3P_0\kappa}{\omega_0 cR_0\rho}+\frac{4\mu}{\omega_0 R_0^2\rho}+\frac{4\kappa_s}{\omega_0 R_0^3\rho} \tag{4.8}$$

where the first term represents acoustic radiation damping, the second represents viscous damping and the third represents shell viscous damping. The shell viscous damping is the largest and accounts for nearly 80% of the total damping of the system. The second order terms (resonance and damping) are given by:

$$\alpha = \frac{9P_0\kappa(\kappa+1)}{2R_0^2\rho}-\frac{(\zeta_{eff}-8\chi_{eff})}{R_0^3\rho} \tag{4.9}$$

$$b_2 = \frac{P_0 3\kappa(3\kappa+1)}{R_0\rho 4c} + \frac{2\mu}{R_0^2\rho} + \frac{3\kappa_s}{R_0^3\rho} \tag{4.10}$$

The solution of Eq. 4.6 depends on the driving pressure which we take, $P_A(t) = P_A sin(\omega t)$. Next, following Church [33] we assume Eq. 4.6 has a solution of the form,

$$x(t) \ = \ A_0 + A_1 sin(\omega t + \phi_1) + A_2 cos(2\omega t + \phi_2) \tag{4.11}$$

The amplitude A_1 is of first order and both A_0 and A_2 are of second order. In this solution A_0 describes the time-averaged offset of the radius time curve. A_2 represents the amplitude of the second harmonic response at two times the driving pressure frequency.

Eq. 4.11 is inserted into Eq. 4.6 and if only the first order terms are considered the well-known differential equation of a harmonic oscillator is obtained:

$$\ddot{x} + \omega_0\delta\dot{x} + \omega_0^2(x) = P_A(t) \tag{4.12}$$

The solution of Eq. 4.12 gives the amplitude A_1 which describes the linear resonance curve of the microbubble,

$$A_1 = \left(\frac{P_a}{\rho\omega_0^2 R_0^2}\right)\left(\frac{1}{\sqrt{(1-\Omega^2)^2 + \Omega^2\delta^2}}\right) \tag{4.13}$$

where the phase of the linear solution is described by,

$$\phi_1 = arctan\left[\frac{\delta\Omega}{\Omega^2 - 1}\right] \tag{4.14}$$

where Ω representing the non-dimensional driving frequency,

$$\Omega = \frac{\omega}{\omega_0} \tag{4.15}$$

The second order terms from Eq. 4.6 and Eq. 4.11 give the amplitude and phase of the second harmonic response,

$$A_2 = \frac{A_1^2\alpha}{2\omega_0^2}\sqrt{\left[\left[1 + \frac{5\omega^2}{2\alpha}\right]^2 + \frac{16b_2^2\omega^2}{\alpha^2}\right]\left[\frac{1}{\sqrt{(1-4\Omega^2)^2 + 4\Omega^2\delta^2}}\right]} \tag{4.16}$$

and its phase,

$$\phi_2 = arctan\left[\frac{B_r sin(2\phi_1) - B_i cos(2\phi_1)}{B_r cos(2\phi_1) + B_i sin(2\phi_1)}\right] \tag{4.17}$$

with:

$$B_r = \frac{4b_2\omega}{\alpha}(1-4\Omega^2) - 2\delta\Omega\left[1 + \frac{5}{2}\frac{\omega}{\sqrt{\alpha}}\right] \tag{4.18}$$

$$B_i = (1-4\Omega^2)\left[1+\frac{5}{2}\Omega_2^2\right]+2\delta\Omega\frac{4b_2\omega}{\alpha} \tag{4.19}$$

While the second harmonic response is important for medical imaging purposes, here our main interest goes to the “compression-only” behavior of the bubble which is characterized by the time-averaged offset of the bubble radius A_0. Inserting Eq. 4.11 into Eq. 4.6 gives us:

$$A_0 = \frac{A_1^2}{2\omega_0^2}\left(\alpha-\frac{1}{2}\omega^2\right) \tag{4.20}$$

with α described by Eq. 4.9. For a coated and an uncoated bubble the expressions for A_0 are the same. Differences between the average offset of a coated and an uncoated bubble result from differences in the resonance frequency ω_0 and α. The derivation of Eq. 4.20 is based on a *continuous* driving pressure wave and A_0 is therefore a zero order frequency component. For a driving pressure with a finite length the offset A_0 has a frequency of the order of the reciprocal length of the driving pressure waveform.

Equation 4.20 shows a linear relationship between A_0 and A_1^2. This has two important consequences. First, since A_1 increases linearly with the amplitude of the driving pressure pulse P_a, A_0 increases quadratically with P_a. Furthermore, since A_1 is maximum at the resonance frequency, A_0 will also be maximum at the resonance frequency of the bubble. This is shown in Fig. 4.2, where A_1 and A_0 are plotted as a function of the driving frequency both for an uncoated bubble and for a coated bubble with an initial bubble radius of R_0=3.8 μm. For both bubbles A_1 and A_0 are normalized with respect to their maximum fundamental response $max(A_1)$. For this reason the decrease of the maximum amplitude of oscillation of the coated bubble as a result of shell damping with respect to the uncoated bubble is not visible. The increase of the resonance frequency and broadening of the resonance curve that results from the viscoelastic shell of the bubble can be clearly identified. The most striking difference between the time-averaged offset A_0 of the uncoated and the coated bubble is the sign of A_0. For the uncoated bubble A_0 is positive while for the coated bubble it has a negative amplitude. This remarkable difference results from the difference in α, see Eq. 4.9. For an uncoated bubble the effective surface tension does not vary with bubble radius R. Therefore both χ_{eff} and ζ_{eff} are zero and Eq. 4.9 reduces to the first term only, which is always positive. For a coated bubble on the other hand, the value of α can become negative for a sufficiently large ζ_{eff}, in which case A_0 becomes negative, leading to a decrease of the initial bubble radius during the forcing. This is in agreement with what was found by Marmottant *et al.* [12] who showed that a bubble with an initial bubble radius close to the transition from the elastic to the buckled regime ($R_0 = R_{\text{buckling}}$) shows most “compression-only” behavior. This sudden buckling

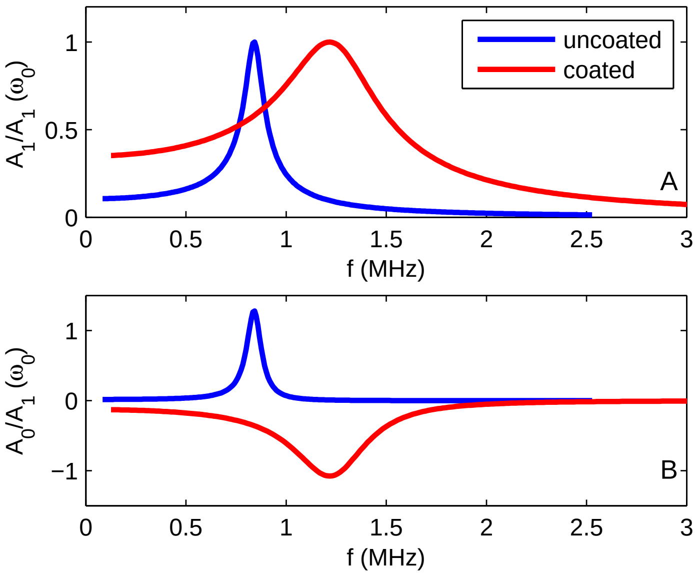

Figure 4.2: The top figure shows the resonance curve (fundamental response (A_1) as a function of driving frequency) of a R_0=3.8 μm radius uncoated gas bubble (blue) and a coated microbubble (red) as determined from the linearized Rayleigh-Plesset equations. Both are normalized to their maximum amplitude. The bottom figure shows the corresponding zero order frequency component (A_0) as a function of frequency, also normalized to the corresponding maximum fundamental response (A_1). Both for the uncoated bubble and the coated microbubble the zero order frequency component is maximal at the resonance frequency. The free gas bubble shows a positive offset whereas the coated microbubble shows a negative offset. The parameters used in the simulation were, P_A = 40 kPa, χ_{eff}=0.55 N/m, $\kappa_s = 3 \cdot 10^{-8}$ kg/s and $\zeta_{eff} = 42.2$ N/m.

transition is characteristic for a collapsing phospholipid monolayer [68] and marks a large positive second derivative of the effective surface tension with respect to radius ζ_{eff}.

A few comments on the elasticity χ_{eff} and its first order correction ζ_{eff} are in order. In the most general form both χ and ζ are a function of the radius R. In the model by De Jong *et al.* [63] the bubble shell is assumed to have a constant elasticity, χ = constant. Consequently the first order correction and derivative of χ, $2R_0(\partial\chi/\partial R) = \zeta$ is zero. Using a constant elasticity to model a more complex elastic behavior, results in an effective elasticity χ_{eff} which is different from an elasticity $\chi(R)$ that varies with radius, R. As the linear eigenfrequency ω_0 originates from a first order linearization, the elasticity in Eq. 4.7 is assumed to be constant, χ_{eff}. This analysis holds similarly for the description of $\zeta(R)$

where we have introduced a constant effective first order correction ζ_{eff} for the linearized equations. In the analytical solutions presented in Fig. 4.2 χ_{eff} was taken to be 0.55 N/m, following Van der Meer *et al.* [41] who deduced the elasticity of phospholipid-coated bubbles from an analysis of linear resonance curves; the use of χ_{eff} is therefore adequate. ζ_{eff} was taken to be 42.2 N/m. For this value of ζ_{eff} we observe in Eq. 4.9 and Eq. 4.20 that the zero order offset of the radius of the bubble at resonance is larger even than the linear/harmonic oscillation amplitude. This indeed results in the very asymmetric radius-time curves similar to the curves found experimentally by Marmottant *et al.* [12] and by De Jong *et al.* [10].

Let us reconsider the radius-time curve of Fig. 4.1C. If we now view the radius-time curve, not as a set of bubble expansions and compressions from a reference resting radius R_0, but instead we recover the radius-time curve from a superposition of R_0, a negative zero-order offset A_0, and a linear oscillation A_1, we obtain the picture plotted in Fig. 4.3. As the frequency of A_0 is an order lower than that of A_1, a segmentation in the frequency domain can be performed after subtraction of the resting radius R_0. This results in the temporal evolution of A_0 and A_1, Fig. 4.3 to the right. Note that strictly speaking A_1 analyzed in this way may contain higher order harmonics of the form given in Eq. 4.16, which we will neglect here. Details of the Fourier segmentation will be given in the experimental section.

Equation 4.20 has shown that the zero-order offset A_0 is negative for sufficiently large ζ_{eff} and that the maximum “compression-only” behavior is recovered for a maximum A_1. It can also be shown that the driving frequency has very little effect on the relation between A_0 and A_1 when “compression-only” behavior is observed. In this case ζ_{eff} is large as to make α sufficiently large and the contribution of ω is negligible. Something that is less obvious from the equation is that the “compression-only” behavior is most pronounced for the smallest bubbles. This finding will be confirmed by full numerical simulations in the following section and is in agreement with the recent observations of “compression-only” behavior of phospholipid-coated Sonovue and BR-14 by De Jong *et al.* [10].

4.3 Numerical Model

From the analytical solutions for A_0 presented in the previous section it was observed that “compression-only” behavior of phospholipid-coated microbubbles is predominately determined by the initial increase of the shell elasticity with bubble oscillation amplitude $\zeta_{eff} = 2R_0\partial\chi_{eff}/\partial R$. Earlier models such as proposed by De Jong *et al.* [63] assume a constant shell elasticity and are therefore unable to explain such behavior. Equation.4.2 is valid for small bubble oscillation amplitudes only. For larger bubble oscillation amplitudes the effective surface tension as pre-

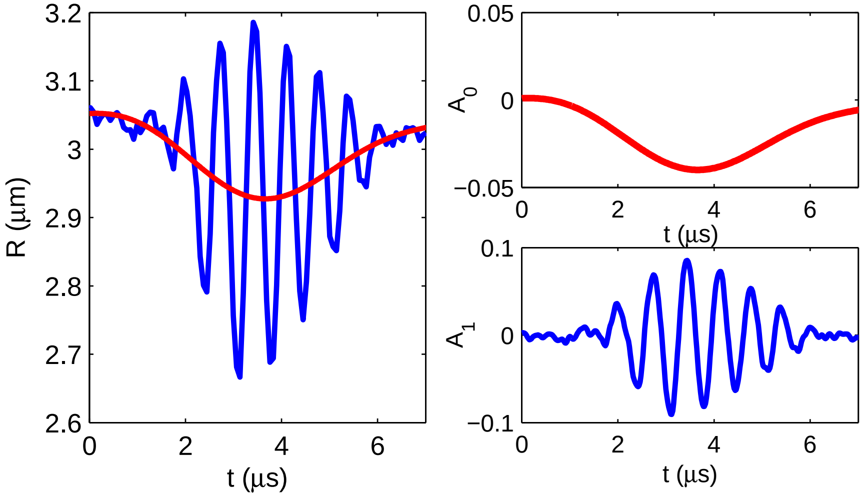

Figure 4.3: The radius time curve presented in Fig. 4.1C can be decomposed into two components. The fundamental response A_1 and a low frequency component A_0 expressing the "compression-only" behavior of the bubble. The frequency of A_0 is of the order of the reciprocal of the length of the driving pressure pulse.

dicted by Eq. 4.2 grows indefinitely with R and could become negative. Therefore in this chapter we will use the model proposed by Marmottant *et al.* [12] where the shell elasticity is assumed to change with bubble oscillation amplitude and the effective surface tension is bound between $\sigma = 0$ N/m and $\sigma = 0.072$ N/m.

As a first approximation Marmottant *et al.* assumed three regimes for $\sigma(R)$, one elastic regime, for small bubble oscillations, where the effective surface tension is described in the spirit of the model of De Jong *et al.* [63] and two regimes where the shell elasticity is assumed to be zero $\chi = 0$ N/m. The shell elasticity χ in the elastic regime is assumed to be fixed and the function $\sigma(R)$ as a whole is assumed to be same for all bubbles independent of the initial bubble radius. Therefore this model introduces only one additional parameter as compared to the model proposed by De Jong *et al.* [63]: the initial surface tension of the bubble $\sigma(R_0)$, which directly relates to the phospholipid concentration on the interface of the bubble.

In the model described by Marmottant *et al.* $\sigma(R)$ is defined as a piecewise affine function, implying that $\zeta(R)$ is zero except at the two transition points $\sigma(R) = 0$ and $\sigma(R) = \sigma_{\text{water}}$, where this quantity is not defined. As already pointed out by Marmottant *et al.* [12], this is a practical idealization of the shell response which is smoother in reality. Furthermore, the weakly nonlinear analysis presented in the previous section has shown that ζ_{eff} and thus $\zeta(R)$ is of prime importance to explain “compression-only” behavior. In order to have $\zeta(R)$ defined for all R we propose to introduce two quadratic crossover functions, $Y_1(R)$ and $Y_2(R)$ in the two transition regions as depicted in Fig. 4.4. In order for both the effective surface tension and the shell elasticity to remain continuous at the two transition points the two quadratic functions at the two different transitions should each satisfy a set of boundary conditions. For the transition from the so called ’buckling’ regime to the ’elastic’ regime the function $Y_1(R)$ should be chosen such that $\sigma(R)$ satisfies,

$$\begin{aligned} \sigma(R_{\text{Buck}}) &= 0\ N/m \\ \partial\sigma(R_{\text{Buck}})/\partial R &= 0\ N/m^2 \\ \partial\sigma(R_{\text{Elas}})/\partial R &= 2\chi_{max}/R_0\ N/m^2 \end{aligned} \tag{4.21}$$

where R_{Buck} marks the transition to the buckling regime and R_{Elas} to the elastic regime. In a separate experiment shown in chapter 3 resonance curves of phospholipid-coated BR-14 microbubbles were measured at extremely low driving pressures. This allowed measurements of the resonance curves of bubble in a purely elastic state as the oscillations were confined to the ’elastic’ regime. In this way the *maximum* shell elasticity in the elastic regime could be determined and was found $\chi_{max} = 2.5\ N/m$. For radii between R_{Buck} and R_{Elas} the shell elasticity is determined by Y_1 as shown in Fig. 4.4. To limit the number of free parameters of the model we have assumed the transition from the ’buckling’ regime to the ’elastic’ regime and from the ’elastic’ regime to the ’ruptured’ regime are the same. The boundary condition that should be satisfied for this last transition are therefore,

$$\begin{aligned} \sigma(R_{\text{Free}}) &= 0.072\ N/m \\ \partial\sigma(R_{\text{Elas2}})/\partial R &= 2\chi_{max}/R_0\ N/m^2 \\ \partial\sigma(R_{\text{Free}})/\partial R &= 0\ N/m^2 \end{aligned} \tag{4.22}$$

The end of the elastic regime is now marked by R_{Elas2} and the start of the ’ruptured’ regime is marked by R_{free}. From the boundary conditions we find the following quadratic functions.

$$Y_1 = \frac{1}{2}\zeta\left(\frac{R}{R_{\text{Buck}}} - 1\right)^2 \qquad if \quad R_{Buck} < R < R_{\text{Elas}} \tag{4.23}$$

$$Y_2 = \sigma_{\text{water}} - \frac{1}{2}\zeta\left(\frac{R}{R_{\text{Buck}}} - \frac{R_{\text{Free}}}{R_{\text{Buck}}}\right)^2 \qquad if \quad R_{\text{Elas2}} < R < R_{\text{Free}} \tag{4.24}$$

With these two new quadratic functions the final function of $\sigma(R-\Delta R)$ becomes,

$$\sigma(R-\Delta R) = \begin{cases} 0 & \text{if } (R-\Delta R) < R_{\text{Buck}} \\ Y_1(R-\Delta R) & \text{if } R_{\text{Buck}} < (R-\Delta R) < R_{\text{Elas}} \\ 2\chi_{max}\left(\frac{(R-\Delta R)}{R_0}-1\right) & \text{if } R_{\text{Elas}} < (R-\Delta R) < R_{\text{Elas2}} \\ Y_2(R-\Delta R) & \text{if } R_{\text{Elas2}} < (R-\Delta R) < R_{\text{Free}} \\ \sigma_{\text{water}} & \text{if } (R-\Delta R) > R_{\text{Free}} \end{cases} \quad (4.25)$$

Here ΔR defines the shift of the $\sigma(R)$ curve with respect to R_0, i.e. ΔR defines $\sigma(R_0)$.

In the original model ζ was undefined in the two transition regions. With the introduction of the two quadratic function the constant ζ can be defined. This implies that another shell parameter must be introduced. However, since in the original model ζ was undefined and in fact was determined by the step size of the numerical code, the original model could also be considered as having already incorporated (in an uncontrolled way) the ζ shell parameter. Note that once ζ, $\sigma(R_0)$ and χ_{max} are defined, the parameters, R_{Buck}, R_{Elas}, R_{Elas2} and R_{Free} are fixed and are therefore not to be considered free shell parameters. Furthermore, as in the original model we assume that $\sigma(R)$ is valid for all bubble radii.

Since χ_{max} is known and the same for all bubbles, the only parameters that affect the "compression-only" behavior of bubbles and that can vary from bubble to

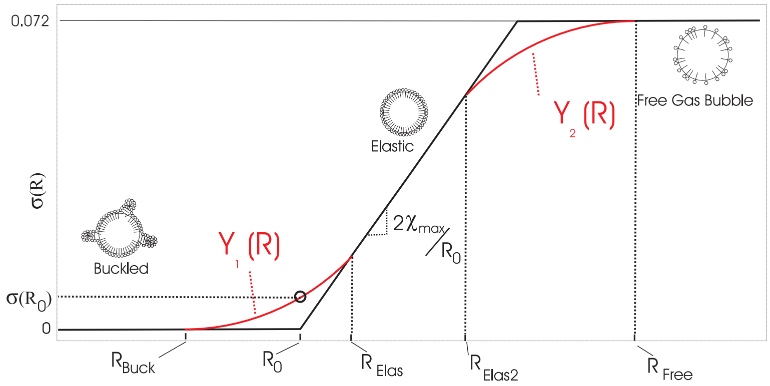

Figure 4.4: In the model of Marmottant *et al.* [12] the second derivative of $\sigma(R)$ with respect to R is undefined in the transitions from the buckling regime to the elastic regime, and from the elastic regime to the free gas bubble regime. To correct this, we propose to expand the original model with two quadratic functions Y_1 and Y_2 that describe the two transition points.

bubble are ζ and $\sigma(R_0)$. To investigate the effect of these two free parameters and the initial bubble radius R_0 on the “compression-only” behavior of phospholipid-coated microbubbles we have conducted a parameter study of the full numerical model described by Eq. 4.1 where $\sigma(R)$ is described by Eq. 4.25. The results are presented in Fig. 4.5. Through a variation of the driving pressure amplitude the zero order offset A_0, i.e. the “compression-only” behavior, was determined as a function of the oscillation amplitude A_1^2. By varying both ζ and $\sigma(R_0)$ independently for a bubble with an initial bubble radius $R_0 = 1.2\ \mu$m the influence of these two parameters on the relation between A_0 and A_1 was determined. Finally, also the effect of the initial bubble radius R_0 on the “compression-only” behavior was investigated by varying R_0. In the weakly nonlinear analysis it was found that A_0/A_1^2 is nearly independent of the driving pressure frequency. We therefore chose the frequency close to resonance, as to promote large amplitude oscillations to cover a reasonable range of A_1. We used a frequency of 4 MHz in the case of the 1.2 μm bubble and 2 MHz and 1 MHz for the 2.3 μm and 3.4 μm bubble, respectively. Similarly the shell viscosity κ_s does not affect the quantity A_0/A_1^2 and a difference in the shell viscosity for different bubbles therefore not alters the results presented in Fig. 4.5. In the simulations presented in Fig. 4.5 a shell viscosity of $\kappa_s = 1 \cdot 10^{-9}$ kg/s was taken for the 1.2 μm bubble and the 2.3 μm and 3.4 μm bubble were assumed to have a shell viscosity of $\kappa_s = 1 \cdot 10^{-8}$ kg/s and $\kappa_s = 2.5 \cdot 10^{-8}$ kg/s respectively, in agreement with the values found by Van der Meer *et al.* [41] for the same type of bubbles. To determine A_1 from the individual radius-time curve, the zero-order frequencies were first filtered out with an ideal high-pass filter with a cut-off frequency of 1 MHz. The resulting radius time curve was normalized to the initial bubble radius R_0. Note again that strictly speaking the A_1 defined here differs slightly from the A_1 of the analytical solutions, since the numerical data may contain higher harmonics. To determine A_0, the initial bubble radius R_0 is first subtracted from the full radius time curve $R(t)$. After the resulting curve is normalized with the initial bubble radius R_O we apply an ideal low-pass filter with a cut-off frequency of 1 MHz to the curve. The amplitude of the resulting low frequency offset shown in Fig. 4.3 is defined as A_0.

As was found from the weakly nonlinear analysis presented in the previous section, we find from the numerical simulations using the full numerical model that the zero-order frequency component A_0 is indeed negative and decreases for increasing oscillation amplitude A_1. Furthermore, from Fig. 4.5B we find that the “compression-only” behavior slightly increases for increasing ζ however the increase is limited even for a two order of magnitude increase of ζ. This confirms that the relation between A_0 and A_1^2 depends on an effective $\zeta_{eff} = (\int \zeta(R)dR)/(\int dR)$. ζ_{eff} is less dependent on the initial $\zeta(R_0)$ but depends both on the size of the regime of ζ and the value of ζ itself. This is confirmed by the decrease of the

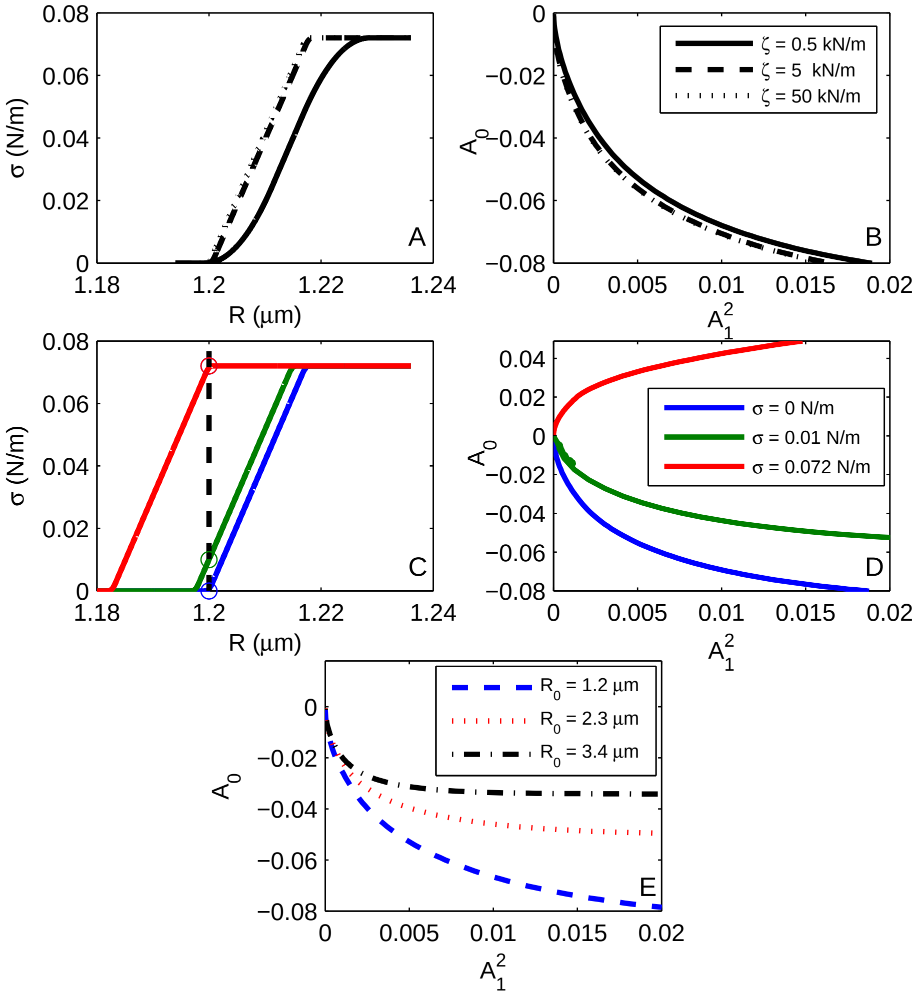

Figure 4.5: A parameter study of the "compression-only" behavior of phospholipid-coated microbubbles. Three parameters were varied, ζ (B), $\sigma(R_0)$ (D) and R_0 (E) which resulted in different relations for $\sigma(R)$ as shown in the two left figures A and C. The "compression-only" behavior was expressed as the relation between A_1^2 and A_0, where A_1^2 was varied by changing the driving pressure amplitude with a fixed driving frequency of 4 MHz. The right top figure B shows the "compression-only" behavior for three different values of ζ with $\sigma(R_0) = 0$ N/m and $R_0 = 1.2$ μm. The middle right figure D) shows how the "compression-only" behavior changes for different $\sigma(R_0)$ with $\zeta = 5$ kN/m and $R_0 = 1.2$ μm fixed. Finally in the bottom figure, E) the "compression-only" behavior for differently sized bubbles is shown ($\zeta = 5$ kN/m, $\sigma(R_0) = 0$ N/m). In all figures it was assumed that the maximum shell elasticity equals $\chi_{max} = 2.5$ N/m.

"compression-only" behavior that we observe for larger A_1^2 but also by the strong dependency of the A_0/A_1^2 on the initial surface tension $\sigma(R_0)$. In Fig. 4.5D we observe that for a bubble with an initial surface tension $\sigma(R_0)$ close to the buckling regime A_0/A_1^2 is smaller, i.e. we observe more "compression-only" behavior. For a bubble with a larger initial surface tension $\sigma(R_0)$ the region with a large positive ζ is reached only for larger oscillation amplitudes. Furthermore the transition from the elastic regime to the ruptured regime is marked by a negative ζ and is reached for much smaller oscillation amplitudes, explaining why the minimum A_0 reached for bubbles with a large $\sigma(R_0)$ is higher. For an initial surface tension $\sigma(R_0)$ sufficiently large $\sigma(R_0) > 0.036$ N/m (=0.072/2) we may even observe "expansion only" instead of "compression-only" behavior, see also experimental evidence in Marmottant *et al.* [12]. Finally, we observe that the full numerical simulations predict that smaller bubbles show more "compression-only" behavior in agreement with recent observations by De Jong *et al.* [10].

4.4 Experimental

From the weakly nonlinear analysis and the numerical calculations with the full shell-buckling model we found that the amount of "compression-only" behavior that a microbubble exhibits depends on the initial bubble radius R_0, the initial surface tension $\sigma(R_0)$ and the amplitude of oscillation A_1. The other parameters of the model, the shell elasticity, shell viscosity, and the driving pressure amplitude and frequency are all included in A_1. The relation between A_0 and A_1 is unaltered by these parameters. To investigate how and if these theoretical findings can be confirmed experimentally we recorded the radial dynamics of 45 individual microbubbles with the Brandaris ultra-high speed camera [39] as a function of both the driving pressure frequency and of the driving pressure pulse. To study purely the effect of "compression-only" on the bubble dynamics, the bubble under study was isolated and located away from neighboring objects (walls, bubbles) by means of optical tweezers.

4.4.1 Experimental setup

BR-14 (Bracco S.A., Geneva, Switzerland) contrast agent microbubbles were injected in an OptiCell® chamber (Nunc^{TM}). The chamber was positioned on top of a custom-built water tank, see Fig. 4.6. The water tank contained a light fiber and an ultrasound transducer (PA168, Precision Acoustics). A needle hydrophone (HPM02/1, Precision Acoustics) replacing the OptiCell was used to align the ultrasound with the focus of the objective. A XYZ-stage controlled the OptiCell position separately from the watertank in order to keep the ultrasound aligned with the objective. For accurate control of the distance between the bubble and the wall a motorized stage (M-110.2DG, PI) was used.

The ultra high-speed Brandaris 128 camera [39] was coupled to a set of optical tweezers. A dichroic mirror (CVI laser) reflected the infrared laser beam (λ = 1064 nm) into the back aperture of the objective (LUMPLFL100xW, Olympus). Individual bubbles were trapped in the low intensity region of a Laguerre-Gaussian beam. The imaging and trapping of the microbubble was performed through the same objective. The dichroic mirror transmitted the visible light used for imaging. Details of the optical tweezers setup coupled to the Brandaris camera can be found in chapter 6.

The ultrasound pulses were generated by an arbitrary waveform generator (8026, Tabor Electronics). The signal was amplified (ENI, Model 350L with 50 Ω input impedance, Rochester, NY) and sent to the ultrasound transducer. The transducer was calibrated prior to the experiments in a separate water tank over a broad range

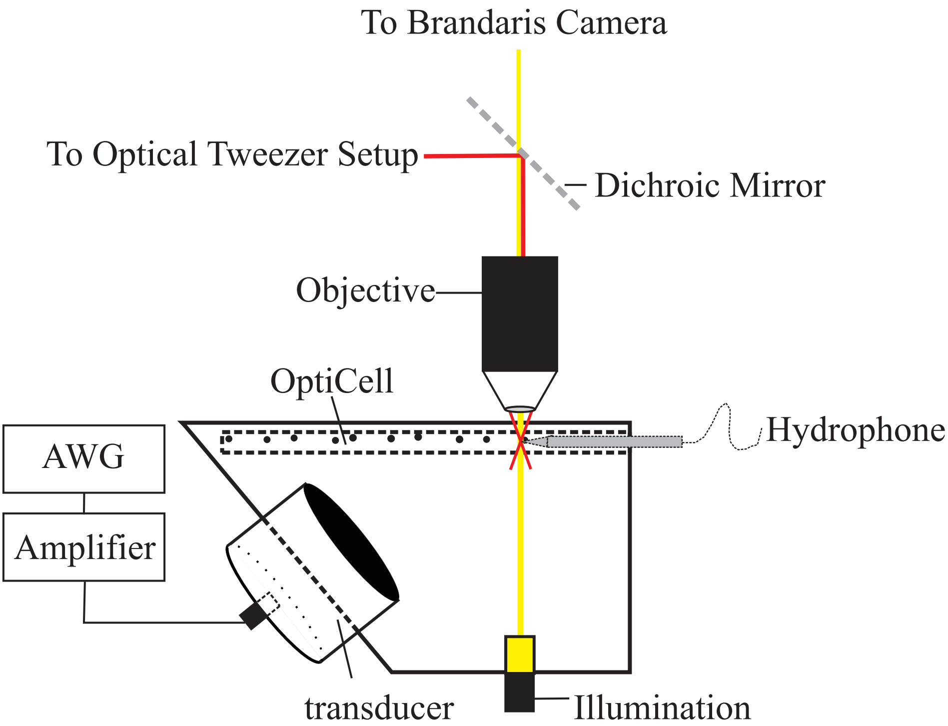

Figure 4.6: A schematic overview of the experimental setup. Single microbubbles were investigated with the combined Brandaris 128 camera and optical tweezers setup. The driving waveform produced by an arbitrary waveform generator was amplified and transmitted by a focused transducer.

of frequencies (0.75-5 MHz) and ultrasound pressures. The driving pressure waveform had a length of 10 cycles and was apodized with a 3 cycle Hanning window. One experiment consisted of 2×6 movies of 128 frames. The bubble dynamics of the very same bubble was recorded while scanning the applied frequency at constant pressure in each of the 12 movies.

4.4.2 Data analysis

The images from the high-speed movies were analyzed off-line with Matlab (The Mathworks, Natick, MA). The radius of the bubble as a function of time $R(t)$ was determined from each image sequence through a semi-automatic minimum cost algorithm [41]. A typical radius-time curve is shown in Fig. 4.7A. The radius R was normalized to the initial bubble radius R_0. The linear oscillation amplitude A_1 was determined from the individual radius-time curve through filtering (B) with a step function shaped high-pass filter with a cut-off frequency of 1 MHz. To determine A_0, the initial bubble radius R_0 was first subtracted from the full radius-time curve $R(t)$, then normalized to R_0. A step function shaped low-pass filter with a cut-off frequency of 1 MHz was applied to the curve. The amplitude of the resulting low frequency offset shown in Fig. 4.7E is defined as A_0.

4.5 Results

In total, 324 resonance curves at different driving pressure amplitudes were obtained for 45 individual microbubbles. In 24% of the experiments A_0 was found to be positive, i.e. 76% of the experiments showed a negative time average offset. Furthermore the amount of compression-only behavior was observed to vary for different bubbles, even for bubbles with the same size.

Figure 4.8 shows the linear resonance curves of two microbubbles, both having an initial bubble radius of 2.3 μm. A_1 and the corresponding A_0 are plotted as a function of the driving frequency. Both bubbles were excited with the same driving pressure amplitudes and driving pressure frequencies. The driving pressure amplitude for both resonance curves shown in Fig. 4.8 was 18.5 kPa. We observe that the bubbles have the same resonance frequency of 2.5 MHz, which following Eq. 4.7 indicates that the bubbles have the same effective elasticity χ_{eff}. We can identify a good agreement between the experimental data and the theoretical linear resonance curve based on $\chi_{eff} = 0.55$ N/m. We also observe for both bubbles that the time average offset A_0 is minimal at the resonance frequency, in agreement with our earlier findings in Eq. 4.20. On the other hand, there is a difference in the amplitude of A_0 between the two bubbles, one of them shows less “compression-only” behavior. To explain the difference between the two bubbles the experimental data

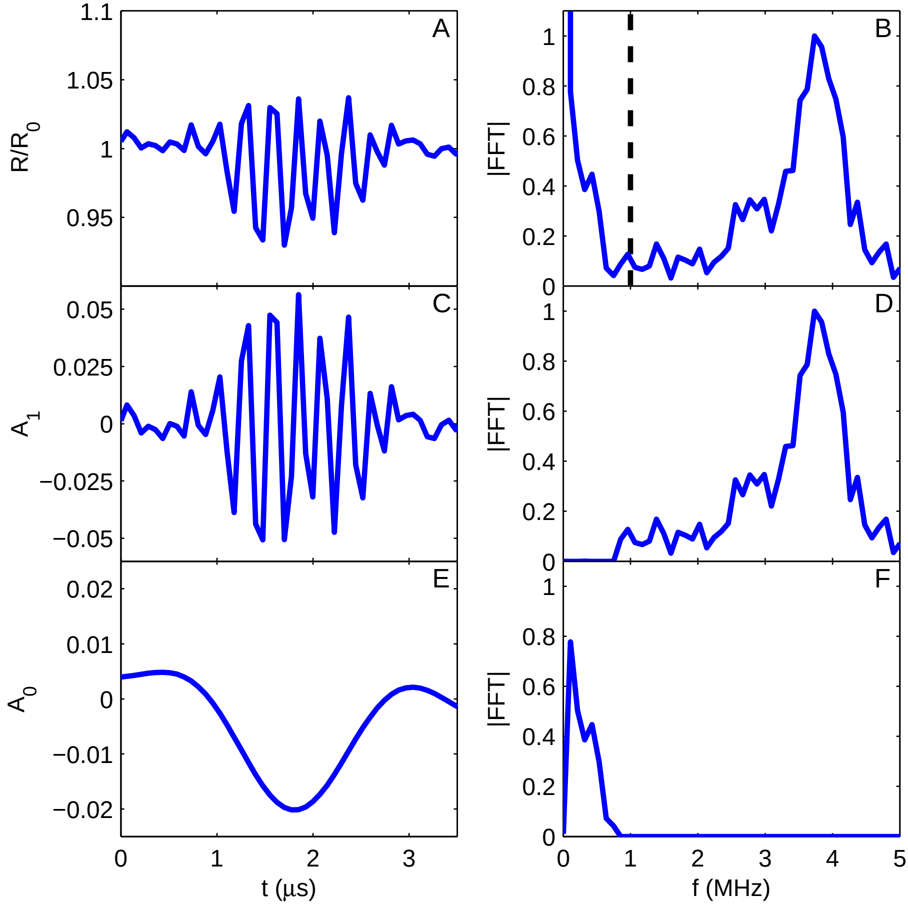

Figure 4.7: A) An example of a radius time curve of a 1.9 μm radius phospholipid-coated bubble recorded with the ultra-high speed Brandaris camera. B) shows the corresponding Fourier transform. The Fourier transform besides a zero-order component from the initial bubble radius R_0 also shows another low frequency component which is associated with the "compression-only" behavior of the microbubble. The radial response can be decomposed into a fundamental/linear response (C,D) and a low frequency component of the order of the length of the driving pressure pulse (E,F). For the phospholipid-coated microbubble the low frequency component has a negative amplitude which is contrary to what we observe for the free gas bubble where it is positive.

is fitted to the two theoretical predictions for A_0 based on Eq. 4.20. From the two fitted curves we find that the difference between the two bubbles results from a difference in the second derivative of the effective surface tension with respect to R, ζ_{eff}. For the bubble that shows most "compression-only" we find $\zeta_{eff} = 91$ N/m and for the other $\zeta_{eff} = 41$ N/m.

If we relate this finding to the model proposed by Marmottant *et al.* where it is assumed that all microbubbles follow the same relation for $\sigma(R)$ a difference in ζ_{eff} can only result from a difference in the initial phospholipid surface concentration of the bubble, i.e. a difference in $\sigma(R_0)$. For a bubble with an initial phospholipid surface concentration close to the saturation concentration of the bubble wall, i.e. $\sigma(R_0) \approx 0$ N/m, the shell elasticity will vary strongly with the bubble radius R. Already for small amplitudes of oscillation the bubble will go from the elastic regime with a shell elasticity of around $\chi(R) = 2.5$ N/m into the buckled regime with $\chi(R) = 0$ N/m. This rapid change of the shell elasticity corresponds to a large $\zeta_{eff} = 2R_0 \partial\chi_{eff}/\partial R$. The bubble with the smaller ζ_{eff} has an initial phospholipid surface concentration that is lower. The bubble therefore remains in the elastic regime for larger amplitudes of oscillation. As a result the shell elasticity

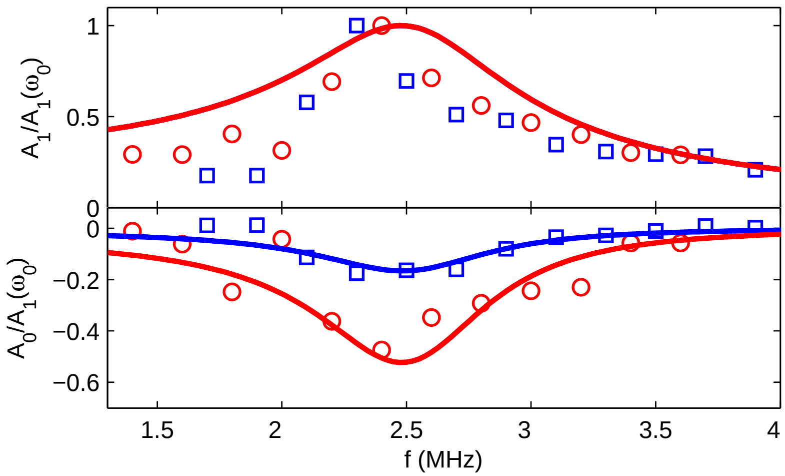

Figure 4.8: Experimentally determined resonance curve for two 2.3 μm radius bubbles with the two corresponding time average offsets A_0. Both A_0 and A_1 are normalized on the maximum value of A_1. Though the resonance frequency and thus the shell elasticity χ is the same for both bubbles the time average offset is different for both, as in Fig. 4.9. The experimental data is in good agreement with the analytically calculated resonance curves which are based on $\chi(R) = 0.55$ N/m determined by Van der Meer *et al.* [41]. The two theoretical predictions for A_0 are based on two different values for ζ_{eff}, $\zeta_{eff} = 91$ N/m (blue squares) and $\zeta_{eff} = 41$ N/m (red circles).

will not vary strong with bubble radius effectively reducing ζeff.

Figure 4.9 shows the negative time average offset A_0 plotted as a function of A_1^2. The experimental data shown in Fig. 4.9 is obtained at different driving pressure amplitudes and frequencies. For each of the two bubbles all the different resonance curves are observed to collapse onto each other showing the same relation between A_0 and A_1^2. This confirms our previous findings that both the driving pressure amplitude and frequency do not change the relation between A_0 and A_1^2. The shape of the relation between A_0 and A_1^2 is the same as was found from the numerical simulations, see Fig. 4.5D. As mentioned before, the flattening of the curve for increasing A_1 results from the transition from the elastic regime to the ruptured regime. For the two different bubbles we observe that both the change of the gradient and the minimum A_0 are different. From the numerical simulations we found that ζ was a parameter of relatively little importance, and therefore the difference between the two curves can only be explained by a difference in $\sigma(R_0)$. To fit the full model to the experimental data therefore requires the vari-

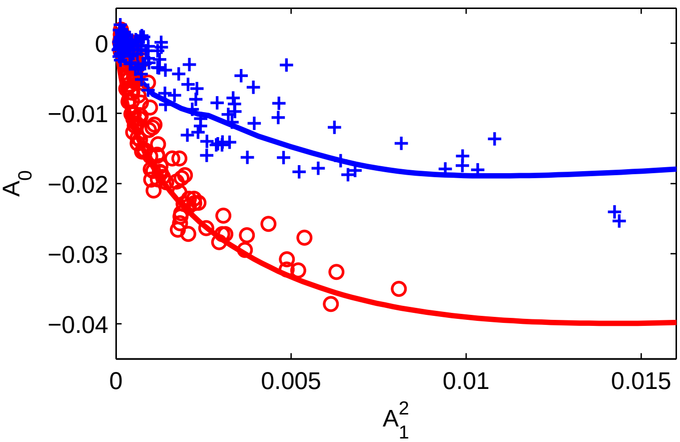

Figure 4.9: Two different microbubbles with the same radius $R_0 = 2.3\ \mu$m show different "compression-only" behavior though the experimental data was obtained for similar driving pressure amplitudes and frequencies. Even though the two curves look qualitative the same, quantitatively they are different. The experimental data of both bubbles is correctly described by a single parameter fit of $\sigma(R_0)$ of the full numerical model. The best fit through the red circles corresponds to a $\sigma(R_0) = 0.008$ N/m and for the blue crosses it is $\sigma(R_0) = 0.02$ N/m. In the full numerical simulations the other shell parameters were taken from the literature to be $\kappa_s = 1 \cdot 10^{-8}$ kg/s, $\chi = 2.5$ N/m, and $\zeta = 5$ kN/m. The driving pressure frequency was fixed on 2 MHz and the driving pressure amplitude was varied.

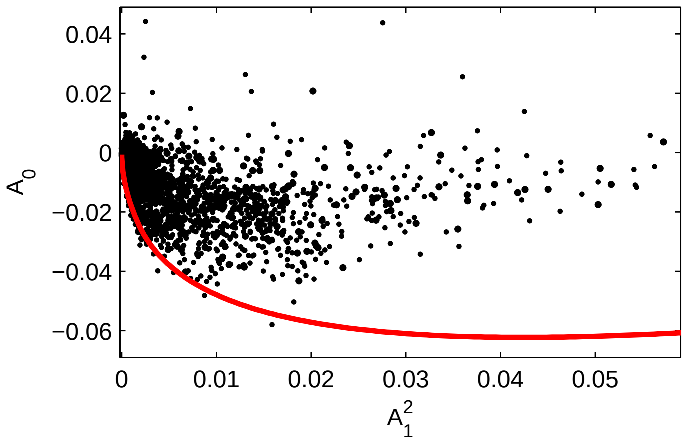

Figure 4.10: According to the numerical model the amount of “compression-only” behavior exhibited by a phospholipid-coated microbubble is restricted. The initial condition of the phospholipid shell, $\sigma(R_0)$ and the initial bubble radius R_0 determine the maximal time average offset A_0 a bubble can show in its $R(t)$ curve. This hypothesis is confirmed by the clear boundary we observe on the left/bottom flank in this scattered plot where A_0 is plotted as a function of A_1^2 for all experimental data. This boundary is correctly described by the red line corresponding to the numerically calculated relation between A_0 and A_1^2 for a bubble with an initial bubble radius $R_0 = 1.2\mu$m (smallest bubble in the experimental data) and $\sigma(R_0) = 0$ N/m.

ation of only one parameter. A least-squares fits of the full model to the two experimental data sets are shown in Fig. 4.9. The data set corresponding to the bubble showing most “compression-only” behavior is best fitted with a value for $\sigma(R_0) = 0.008$ N/m, the other data set is shown to nicely fit with the numerical model for $\sigma(R_0) = 0.02$ N/m. The other shell parameters of the numerical model were taken as before from the literature $\kappa_s = 1 \cdot 10^{-8}$ kg/s, $\chi = 2.5$ N/m and $\zeta = 5$ kN/m.

In Fig. 4.10 all experimental data is shown for all bubbles. Where we plot A_0 as a function of A_1^2. The smallest initial bubble radius in the experimental data is 1.2 μm and the largest bubble has a radius of 3.4 μm. The shape of the scattered experimental data is determined by the limiting number of values $\sigma(R_0)$ can have. The smallest value for $\sigma(R_0$ is 0 N/m for the smallest bubble size and determines the maximum amount of “compression-only” behavior. This is confirmed by the numerical simulation of the full model of Marmottant *et al.* for $\sigma(R_0) = 0$ N/m and $R_0 = 1.2\mu$m, which was shown before in Fig. 4.5 and now shown in Fig. 4.10. The numerical simulation confines the left/bottom side of the experimental data.

4.6 Discussion

From the results presented here it is clear that the shell elasticity of the phospholipid shell varies with bubble oscillation amplitude. To explain the observed "compression-only" behavior the shell elasticity of the coated microbubble will first rapidly increase with bubble radius and then decrease as the bubble shell reaches the ruptured regime. This finding confirms the assumption of Marmottant *et al.* that the behavior of a phospholipid-coated microbubble oscillating in the MHz frequency range is similar to the static behavior of phospholipid monolayers [64–68].

The rapid increase of the shell elasticity with increasing bubble radius is a result of a collapse of the phospholipid monolayer [68]. The collapse of the monolayer is a result of the compression of a saturated layer of phospholipids with the highest possible packing. If the monolayer is compressed beyond this point, 3D structures of phospholipids are formed on the surface of the monolayer. This phenomenon is termed buckling of the monolayer and can be observed in microscopic detail as shown in Fig. 4.1A. If the monolayer is in the buckled state the effective surface tension is zero (or at least very close to zero) and does not vary with bubble radius. Once the bubble surface is expanded beyond its buckled state, the monolayer extends into an elastic state where the effective surface tension increases with bubble radius as a result of a decrease of the phospholipids concentration. The surface elasticity is described by the change of the effective surface tension with the bubble radius. The buckling point of the phospholipid monolayer marks the rapid increase of the shell elasticity.

The effective surface tension cannot increase indefinitely as the phospholipid concentration becomes so small that the bubble ruptures and the phospholipids segregate in lipid islands on the interface and the surface tension recovers to that of the water/air interface ($\sigma = 0.072$ N/m). The decrease of the effective shell elasticity with bubble radius for larger oscillation amplitudes is a result of this upper limit to the effective surface tension. Therefore the shell elasticity effectively decreases to zero for larger bubble radius.

For a bubble with a known resonance frequency the "compression-only" behavior of a phospholipid microbubble quantified by A_0/A_1^2, provides a direct measure of the initial state of the phospholipid shell. Furthermore, assuming the resonance frequency of the bubble is known the relation between A_0 and A_1^2 for different oscillation amplitudes A_1 can be fitted to the full numerical model proposed by Marmottant *et al.* with the variation of a single parameter $\sigma(R_0)$. This fit will therefore provide an accurate measure of the initial surface tension of the bubble. This provides a quantitative way to dynamically measure the phospholipid concentration on the interface of the bubble. This quantitative information deduced from the "compression-only" behavior of a phospholipid-coated microbubble will also help to predict other nonlinear properties of these microbubbles. The enhanced subharmonic behavior shown by phospholipid-coated microbubbles for example is shown to also depend strongly on the initial surface tension of the phospholipid shell of the microbubble $\sigma(R_0)$ see chapter 5.

4.7 Conclusions

In this paper we have investigated the negative time average offset of the bubble radius of acoustically driven oscillating phospholipid-coated microbubbles, often referred to as "compression-only" behavior. We show that the radial dynamics of the bubble can be considered as a superposition of a linear response at the fundamental driving frequency and a second order nonlinear low-frequency response that describes the "compression-only" behavior of the bubble. We have linearized the model proposed by Marmottant *et al.* [12] up to second order to show that the negative time average offset results from an initial shell elasticity that rapidly increases with bubble radius. This is known to happen for statically collapsing phospholipid monolayers [68]. We propose to quantify the "compression-only" behavior of a microbubble according to its second order time average offset amplitude A_0. From the linearized equations it follows that the negative time average offset A_0 is strongly correlated with the fundamental oscillation amplitude A_1^2. We also show both experimentally and from numerical simulations that for larger oscillation amplitudes A_1^2 the negative time average offset A_0 reaches a plateau level. This effect is also described by the model proposed by Marmottant *et al.* when the break up tension as proposed in this model is set to $\sigma_{max} = 0.072$ N/m, i.e. the surface tension of water. The saturation is shown to result from a decrease of the shell elasticity for larger oscillation amplitudes when the maximum effective surface tension/break-up tension is reached for low surface concentrations of phospholipids. Finally, we show through numerical simulations that the relation between A_0 and A_1^2 in the model proposed by Marmottant *et al.* is predominately determined by the initial effective surface tension of the phospholipid shell $\sigma(R_0)$.

5 Subharmonic behavior of phospholipid-coated microbubbles[1,2]

Coated microbubbles, unlike tissue are able to scatter sound subharmonically. Therefore, the subharmonic behavior of coated microbubbles can be used to enhance the contrast in ultrasound contrast imaging. Theoretically, a threshold amplitude of the driving pressure can be calculated above which subharmonic oscillations of microbubbles are initiated. Interestingly, earlier experimental studies on coated microbubbles demonstrated that the threshold for these bubbles is much lower than predicted by the traditional linear viscoelastic shell models. This paper presents an experimental study on the subharmonic behavior of differently sized individual phospholipid-coated microbubbles. The radial subharmonic response of the microbubbles was recorded with the Brandaris ultrahigh-speed camera as a function of both the amplitude and the frequency of the driving pulse. Threshold pressures for subharmonic generation as low as 5 kPa were found near a driving frequency equal to twice the resonance frequency of the bubble. An explanation for this low threshold pressure is provided by the shell buckling model proposed by Marmottant et al. Marmottant et al. [JASA ***118****(6), 2005]. It is shown that the change in the elasticity of the bubble shell as a function of bubble radius as proposed in this model, enhances the subharmonic behavior of the microbubbles.*

[1] Submitted as: Jeroen Sijl, Benjamin Dollet, Marlies Overvelde, Valeria Garbin, Timo Rozendal, Nico de Jong, Detlef Lohse and Michel Versluis, Subharmonic behavior of phospholipid-coated ultrasound contrast agent microbubbles, J. Acoust. Soc. Am.

[2] The numerical simulations leading to the understanding and the influence of the shell parameters on the subharmonic behavior are part of this thesis. The experimental work and the weakly nonlinear analysis were performed by Jeroen Sijl.

5.1 Introduction

Microbubbles scatter ultrasound effectively and nonlinearly, which makes them ideal contrast agents for medical ultrasound imaging. The bubbles are coated with a protein, lipid or polymer layer and they are filled with air or an inert gas. Ultrasound contrast agents are clinically used on a daily basis to visualize blood flow at the microvascular level to image organ perfusion in e.g the liver, kidney and the myocardium [70]. Contrast enhancement is expressed as the ratio between the response of microbubbles in the blood pool and that of the surrounding tissue, termed the contrast-to-tissue ratio (CTR). Improvement of the CTR for current contrast imaging modalities such as power modulation [62] and pulse inversion imaging [5] is accomplished by exploiting the nonlinear response of the microbubbles, predominantly at the second harmonic frequency of the driving frequency [71, 72]. The typical enhancement of the CTR in nonlinear harmonic imaging is 40 dB. For deep tissue imaging, however, the contrast enhancement is limited by the nonlinear propagation of the ultrasound. Linear scattering of the second harmonic component of the driving pulse interferes with the bubble's second harmonic response. Non-linear propagation of the ultrasound is limited on the other hand only to higher harmonics of the driving frequency. For this reason the subharmonic response of the bubbles at half the driving frequency has received increased interest for ultrasound contrast imaging [7]. Moreover the subharmonic response is attenuated less than both the fundamental and higher harmonic bubble responses. Given the transducer bandwidth limitations, subharmonic imaging is particularly interesting for high frequency imaging applications [73, 74].

Subharmonic bubble responses were first described following experimental observations by Esche [75] already in 1952. Additional experimental work has been conducted to investigate the nature of this nonlinear behavior [76, 77] followed by several theoretical descriptions of subharmonic behavior of bubbles in a sound field [42, 56, 57, 78, 79]. Prosperetti [42] showed through a weakly nonlinear analysis of the Rayleigh-Plesset equation that the subharmonic behavior of bubbles can only exist if the driving pressure amplitude exceeds a threshold pressure. It was found that the threshold pressure for subharmonic behavior is minimum when the bubble is driven at twice its resonance frequency. It was also shown that the threshold pressure increases for increased damping [42, 78, 80].

The viscoelastic shell of ultrasound contrast agent microbubbles is known to increase the damping considerably [36, 41, 63]. Therefore, it has always been suggested that the threshold pressure to excite subharmonic behavior for coated microbubbles should be increased. Shankar *et al.* [44] studied the subharmonic behavior of coated bubbles following the analysis of Prosperetti [42] and confirmed, by using a purely *linear* viscoelastic shell model as by De Jong [63], Church [33], or Hoff [35], that indeed the threshold for subharmonic generation is increased as a result of the increased damping. There exists, however, experimental evidence in the literature showing that for both the albumin-coated contrast agents Optison™ and Albunex® and the phospholipid-coated contrast agent SonoVue®, the threshold pressure to excite subharmonic behavior is lower than that of uncoated bubbles [7, 43–49]. Other work reports no significant change in the threshold pressure, neither for albumin-coated bubbles [81] nor for the phospholipid-coated Definity™ contrast agent microbubbles [82].

Here, we show that a lower threshold for the initiation of subharmonic behavior of phospholipid-coated microbubbles can be explained with the model proposed by Marmottant *et al.* [12]. Similarly to Shankar *et al.* [44] we employ a weakly nonlinear analysis along the earlier work on uncoated bubbles by Prosperetti [42], and instead of using a purely *linear* viscoelastic model, we assume the shell elasticity of the phospholipid shell to vary with the bubble radius R. It is shown that the rapid change in the elasticity of the bubble shell as proposed in the model of Marmottant *et al.*, is responsible for the enhancement of the nonlinear subharmonic behavior of phospholipid-coated ultrasound contrast agent microbubbles. Furthermore we have used ultrahigh-speed imaging with the Brandaris camera [39] to characterize the subharmonic behavior of individual microbubbles from the experimental agent BR-14, which contains microbubbles with a phospholipid shell and a perfluorocarbon gas core (Bracco Research S.A., Geneva, Switzerland). We have investigated the full subharmonic resonance and threshold behavior of individual coated microbubbles for small acoustic pressures and driving pulse frequencies near two times the resonance frequency of the microbubbles.

Details of the model and the weakly nonlinear analysis will be presented in Sec. 5.2. The experimental setup is discussed in Sec. 5.3. In Sec. 5.4 the experimental results are presented and compared with the full numerical model of Marmottant *et al.*. Finally we end with a discussion in Sec. 5.5 and our conclusions in Sec. 5.6.

5.2 Theory

5.2.1 Analytical solution

The most general description of the dynamics of phospholipid-coated microbubbles is given by,

$$\rho\left(R\ddot{R}+\frac{3}{2}\dot{R}^2\right)=\left(P_0+\frac{2\sigma(R_0)}{R_0}\right)\left(\frac{R_0}{R}\right)^{3\kappa}\left(1-\frac{3\kappa\dot{R}}{c}\right) -\frac{2\sigma(R)}{R}-4\mu\frac{\dot{R}}{R}-4\kappa_s\frac{\dot{R}}{R^2}-P_0-P(t) \tag{5.1}$$

Here, the radius of the bubble is described by $R(t)$ and its velocity and acceleration are given by $\dot{R}$ and $\ddot{R}$, respectively. The initial bubble radius is given by R_0 and the ambient pressure by P_0. The liquid viscosity is $\mu = 10^{-3}$ Pa·s, its density $\rho = 10^3$ kg/m^3 and the speed of sound in the liquid is $c = 1500$ m/s. The applied acoustic pressure pulse is described by $P(t)$. We approximate the microbubble oscillations as adiabatic. Therefore we assume the polytropic exponent κ to be the ratio of the specific heats of the gas inside the bubble. For the experimental agent BR-14 the gas core consists of perfluorocarbon gas with $\kappa = C_p/C_v = 1.07$ [12, 41]. Thermal damping is accounted for by a slightly increasing the liquid viscosity $\mu = 2 \cdot 10^{-3}$ Pa s. The effect of the phospholipid coating is taken into account through a shell viscosity κ_s kg/s and an effective surface tension which is assumed to depend on the concentration of phospholipid molecules on the surface of the bubble. Consequently, the surface tension depends on the radius of the bubble $\sigma(R)$ (N/m). In earlier models [35, 63] the effective surface tension was assumed to increase linearly with the bubble radius , $\sigma(R) = 2\chi(R/R_0 - 1)$, where χ represents the shell elasticity. Based on the static properties of phospholipid monolayers, Marmottant *et al.* [12] introduced a relation for $\sigma(R)$ where also the shell elasticity is varied with bubble radius $\chi(R)$.

Solving Eq. 5.1 numerically for a certain relation, $\sigma(R)$, provides a specific radius time curve, $R(t)$, with possibly subharmonic oscillations. Depending on the relation $\sigma(R)$ the subharmonic content of the numerically calculated radius time curve changes. To investigate the effect of $\sigma(R)$ on the subharmonic response, Eq. 5.1 can be solved numerically for different functions $\sigma(R)$.

However to come to a more fundamental understanding of the effect of $\sigma(R)$ on the subharmonic behavior of ultrasound contrast agents it is insightful to solve Eq. 5.1 analytically. Hereto we perform a weakly nonlinear analysis of Eq. 5.1 where we follow the approach of Prosperetti [42, 44, 56, 80]. The principal steps of the weakly nonlinear analysis will be repeated here.

As a most general approximation, we assume that, for small oscillations around R_0, $\sigma(R)$ can be described as a second order Taylor expansion:

$$\sigma(R) = \sigma(R_0) + 2\chi_{eff}\left(\frac{R}{R_0} - 1\right) + \frac{1}{2}\zeta_{eff}\left(\frac{R}{R_0} - 1\right)^2 \tag{5.2}$$

where we have defined for any function $\sigma(R)$

$$\chi_{eff} = \frac{1}{2}R_0 \frac{\partial \sigma(R)}{\partial R}\bigg|_{R_0} \tag{5.3}$$

$$\zeta_{eff} = R_0^2 \frac{\partial^2 \sigma(R)}{\partial R^2}\bigg|_{R_0} \tag{5.4}$$

χ_{eff} (N/m) and ζ_{eff} (N/m) are the effective shell elasticity and the derivative of the effective shell elasticity around the equilibrium point R_0. In the model of Marmottant *et al.* $\chi(R)$ and $\zeta(R)$ depend on the bubble radius R. The effective shell elasticity χ_{eff} and ζ_{eff} defined in Eq. 5.3 and Eq. 5.4 are constants. The shell elasticity as determined by Van der Meer *et al.* [41] for BR-14 microbubbles was assumed to be independent of the bubble radius R and is therefore equal to χ_{eff}.

We can show that the results of the weakly nonlinear analysis presented in the following are independent of the choice of the initial surface tension $\sigma(R_0)$. To simplify the calculations presented here we therefore assume $\sigma(R_0)$ to be zero. We insert Eq. 5.2 into Eq. 5.1 and assume the radius R of the bubble is correctly described by

$$R = R_0(1+x), \tag{5.5}$$

where x is small. Following Prosperetti [42] we define a dimensionless timescale, frequency and driving pressure amplitude:

$$\tau = \sqrt{\frac{P_0}{\rho}}\frac{t}{R_0}, \quad \omega = R_0\Omega\sqrt{\frac{\rho}{P_0}}, \quad \xi = \frac{P_\text{a}}{P_0} \tag{5.6}$$

where Ω is the dimensional driving frequency and P_a is the driving pressure amplitude. Because we assume the surface tension at rest $\sigma(R_0)$ to be zero, the pressure inside the bubble is equal to P_0.

Inserting all these relations into Eq. 5.1, performing a series expansion in x, and ignoring third and higher order terms we obtain

$$\frac{\mathrm{d}^2x}{\mathrm{d}\tau^2}+\omega_0^2x = -\frac{3}{2}\left(\frac{\mathrm{d}x}{\mathrm{d}\tau}\right)^2+\alpha_1x^2-\xi x\cos(\omega\tau)-2b\frac{\mathrm{d}x}{\mathrm{d}\tau}+\xi\cos(\omega\tau) \tag{5.7}$$

where we have assumed the driving pressure to be described by $P(t)/(P_\text{a}P_0) = \xi cos(\omega\tau)$. Eq. 5.7 is identical to Eq. (4) from Prosperetti [42] except for the third order terms which we neglect since we are only interested in the solution of this equation for $\omega \approx 2\omega_0$, for which the second-order terms are sufficient [42]. Furthermore we have defined

$$\omega_0^2 = 3\kappa+\frac{4\chi_{eff}}{P_0R_0} \tag{5.8}$$

$$b = \frac{2\mu}{R_0\sqrt{\rho P_0}}+\frac{2\kappa_s}{R_0^2\sqrt{\rho P_0}}+\frac{3\kappa}{2c}\sqrt{\frac{P_0}{\rho}} \tag{5.9}$$

$$\alpha_1 = \frac{9}{2}\kappa(\kappa+1)-\frac{(\zeta_{eff}-8\chi_{eff})}{P_0R_0} \tag{5.10}$$

where b describes the non-dimensional damping of the system. Note that the resonance frequency in dimensional form follows directly from Eq. 5.8 inserted into Eq. 5.6. Around $\omega \approx 2\omega_0$ the solution of Eq. 5.7 reads

$$x = \frac{\xi}{\sqrt{(\omega^2-\omega_o^2)^2+4b^2\omega^2}}\cos(\omega\tau+\delta)+C\cos\left(\frac{1}{2}\omega\tau+\varphi\right) \tag{5.11}$$

where δ is the phase angle of the linear solution which satisfies

$$\tan\delta = \frac{2b\omega}{\omega^2-\omega_0^2} \tag{5.12}$$

The amplitude of the first subharmonic solution either vanishes ($C = 0$), or becomes

$$C = \sqrt{\frac{\omega_o^2-\frac{1}{4}\omega^2+g_1\xi^2+\sqrt{\beta^2\xi^2-\omega^2b^2}}{g_0}} \tag{5.13}$$

where

$$\beta = \left|\frac{1}{2}-\frac{\alpha_1-\frac{3}{4}\omega^2}{\omega_0^2-\omega^2}\right| \tag{5.14}$$

$$g_0 \;=\; \alpha_1\left(\frac{\alpha_1-\frac{3}{8}\omega^2}{\omega_0^2}+\frac{1}{2}\frac{\alpha_1+\frac{3}{8}\omega^2}{\omega_0^2-\omega^2}\right)+\frac{3}{8}\omega^2\left(\frac{1}{4}-\frac{\alpha_1+\frac{3}{8}\omega^2}{\omega_0^2-\omega^2}\right) \tag{5.15}$$

and:

$$\begin{aligned} g_1 \;=\; & \frac{\alpha_1}{\omega_0^2(\omega_0^2-\omega^2)}\left(1-\frac{\alpha_1-\frac{3}{2}\omega^2}{\omega_0^2-\omega^2}\right)-\frac{3}{4}\frac{\omega^2}{(\omega_0^2-\omega^2)^2}-\frac{1}{\omega_0^2-\omega^2} \\ & +\left(\omega_0^2-\frac{9}{4}\omega^2\right)\left(\frac{\alpha_1+\frac{3}{4}\omega^2}{\omega_0^2-\omega^2}-\frac{1}{2}\right)\left(\frac{1}{2}-\frac{\alpha_1-\frac{9}{4}\omega^2}{\omega_0^2-\omega^2}\right), \end{aligned} \tag{5.16}$$

Note that near $\omega = 2\omega_0$ all three quantities, β, g_0 and g_1 are positive.

Theoretically the solution of Eq. 5.13 can only exist if the term $\beta^2\xi^2 - \omega^2 b^2$ is positive. This corresponds to the well-known theoretical threshold for the existence of subharmonics

$$\xi_{\text{th}}(\omega) = \frac{\omega b}{\beta} \tag{5.17}$$

The threshold determines the regime where the subharmonic solution is stable. However, as discussed by Prosperetti and others [78, 80], depending on the initial conditions the subharmonic solution may still not exist. Another threshold is provided by the regime where the linear solution of Eq. 5.11 becomes unstable. In this regime the only stable solution is the subharmonic solution. The instability threshold, ξ_{in} is given by [78, 80]

$$\xi_{\text{in}}(\omega) = \sqrt{\frac{\beta^2 - 2g_1\left(\omega_0^2 - \frac{1}{4}\omega^2\right)}{2g_1^2}} - \sqrt{\frac{\sqrt{\beta^4 - 4g_1\left[\left(\omega_0^2 - \frac{1}{4}\omega^2\right)\beta^2 + g_1\omega^2 b^2\right]}}{2g_1^2}} \tag{5.18}$$

which for $\omega = 2\omega_0$ reduces to $\xi_{\text{in}} = \xi_{\text{th}}$.

From Eq. 5.17 it is clear that the threshold for subharmonics increases with increased damping. However from Eq. 5.10 and Eq. 5.14 it follows that β and consequently ξ_{th} vary with $\zeta_{eff} - 8\chi_{eff}$. $\zeta_{eff} - 8\chi_{eff}$ is determined by the initial condition of the phospholipid shell. In Fig. 5.1 we have plotted ξ_{th} at $\omega = 2\omega_0$ as a function of $\zeta_{eff} - 8\chi_{eff}$ for the linearized uncoated gas bubble model from Prosperetti [42] and for the coated bubble model with $\sigma(R)$ described by Eq. 5.2 for $R_0 = 3.8\ \mu$m. The damping for the coated bubble is determined by Eq. 5.9 where we assume the shell viscosity is equal to $\kappa_s = 3 \cdot 10^{-8}$ kg/s as determined by Van der Meer *et al.* for the same type of bubbles [41]. This brings the total damping for the coated bubble to $b_{\text{coated}} = 0.5$. For the uncoated bubble the damping is determined by the bubble size and κ only, bringing the total damping of the uncoated bubble to $b_{\text{uncoated}} = 0.1$. We observe that depending on the initial condition of the shell $\zeta_{eff} - 8\chi_{eff}$, the threshold for a coated bubble can vary. In the case $\zeta_{eff} - 8\chi_{eff}$ is sufficiently large the threshold for the coated bubble can be lower than the threshold for an uncoated bubble. This provides a possible explanation that even for a fivefold increase of the damping as a result of the shell, the threshold for the existence of subharmonics for coated bubbles can be lower than for uncoated bubbles depending on the initial conditions of the bubble shell.

The ultrasound contrast agent models with a purely elastic shell regime [33, 36, 63] cannot predict a decrease in the threshold pressure as a function of the initial conditions since in these models ζ_{eff} is either zero or of the same order as χ_{eff}, hence $|\zeta_{eff} - 8\chi_{eff}|$ remains about 1 N/m, which is too low to explain subharmonic enhancement for contrast agents. In the model shell buckling model proposed by Marmottant *et al.* [12] we can identify that close to the transition point from the elastic to the buckled regime, $\chi(R)$ changes rapidly from $\chi_{max} \approx 2.5$ N/m to $\chi = 0$ N/m, corresponding to a large $\zeta(R)$. In fact, in the current model of Marmottant $\zeta(R)$ is undefined at the transition points. At the transition points $\zeta(R_0) \sim \zeta_{eff}$ can be much higher than $\chi(R_0) \sim \chi_{eff}$, hence $|\zeta_{eff} - 8\chi_{eff}|$ can be large enough

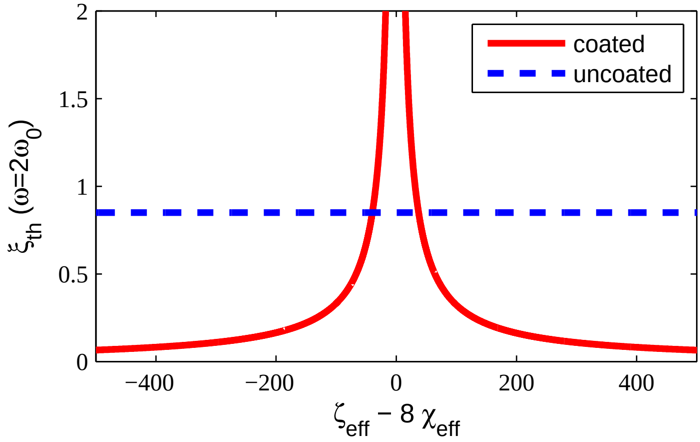

Figure 5.1: The mathematical threshold ξ_{th} at $\omega/\omega_0 = 2$ given by Eq. (5.17) plotted as a function of the term $\zeta_{eff} - 8\chi_{eff}$ for $R_0 = 3.8\ \mu$m with fixed $\chi_{eff} = 0.55$ N/m. We observe that if $|\zeta_{eff} - 8\chi_{eff}|$ is large enough, the threshold for a coated bubble can decrease below the threshold of an uncoated gas bubble despite its additional shell damping. The damping for the uncoated gas bubble is determined by the reradiation damping and the liquid viscosity, for this bubble $b = 0.1$. For the coated bubble model the shell damping introduces and extra damping described by the shell viscosity which is taken $3 \cdot 10^{-8}$ kg/s resulting in a total damping of $b_{\mathrm{coated}} = 0.5$.

to enable subharmonic enhancement for contrast agents. In Fig. 5.2 we have fixed $\chi_{eff} = 0.55$ N/m (corresponding to the average shell elasticity χ_{eff} found by Van der Meer *et al.* [41] for the same type of bubbles) and $\zeta_{eff} = 502.2$ N/m. In Fig. 5.2 we have plotted both ξ_{th} and ξ_{in} as a function of ω/ω_0 for both the uncoated gas bubble and the coated bubble model with $\sigma(R)$ described by Eq. 5.2. As a result of the initial conditions we observe that both thresholds (ξ_{th} and ξ_{in}) for a coated microbubble are as low as 6 kPa, much lower than those for an uncoated gas bubble where the threshold is near 90 kPa.

5.2.2 Full numerical solution

The analytical solutions presented in the previous section provide a fundamental understanding of the source of subharmonic behavior of coated microbubbles. However, for these calculations we have assumed an infinitely long driving pressure pulse and a sufficiently small amplitude of oscillation neglecting higher order terms in Eq. 5.7. In practice, the driving pressure pulse has a finite length and the

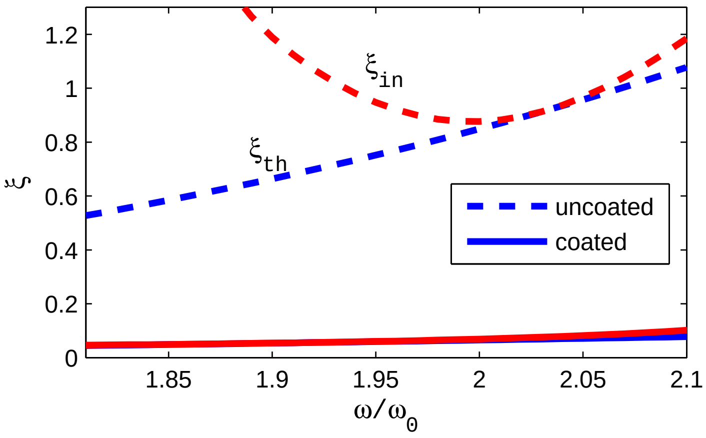

Figure 5.2: The mathematical threshold ξ_{th} (blue) and the instability threshold ξ_{in} (red) as a function of ω/ω_0 for $R_0 = 3.8\ \mu$m. The damping for the coated and the uncoated bubble are the same as in Fig. 5.1, i.e. the damping coefficient for the coated bubble is five times as large as for the uncoated bubble. Even so, the threshold for a coated bubble is only 6 kPa, much lower than for an uncoated bubble which has a threshold of 90 kPa. This decrease of the threshold for the coated bubble results from the rapid change of in the effective surface tension as a function of R described by $\chi_{eff} = 0.55$ N/m and $\zeta_{eff} = 502.2$ N/m $(\zeta_{eff} - 8\chi_{eff} = 500$ N/m)

amplitudes of oscillation of the microbubbles exceed the small amplitude limit. In the following we will therefore solve Eq. 5.1 numerically. Solving the equation numerically requires a model for the relation between the bubble radius and the effective surface tension $\sigma(R)$.

We will assume $\sigma(R)$ to be described as proposed in the model of Marmottant *et al.* [12]. In agreement with what is known for the static behavior of phospholipid monolayers, Marmottant assumes it is the surface concentration of phospholipids on the surface of the bubble that determines the surface tension experienced by the bubble. For low surface concentrations of phospholipids, the surface tension of the water-air interface of the bubble is unaltered and thus equal to $\sigma_{\text{water}} = 0.072$ N/m. This regime corresponding to an expanded bubble (area) is referred to as the ruptured regime. If the surface concentration of phospholipids on the surface of the bubble increases for example by compressing the bubble, the surface tension of the bubble decreases and the bubble enters the elastic regime. In the model of Marmottant it is assumed that in the elastic regime the surface tension of the bubble varies linearly with the radius of the bubble according to $\sigma(R) = 2\chi_{max}(R/R_0 - 1)$

as in the model of De Jong *et al.* [63]. The shell elasticity in the elastic regime is referred to as the maximum shell elasticity χ_{max}. We know from Chapter 3 that the maximum shell elasticity in the elastic regime for these type of microbubbles is $\chi_{max} = 2.5$ N/m. Below a certain radius the surface concentration of phospholipids can not increase more and at this point the bubble enters the buckled regime with a corresponding minimum surface tension of $\sigma(R) = 0$. In the model of Marmottant *et al.* $\zeta(R)$ is undefined near the two transition points from the buckled regime to the elastic regime and from the elastic regime to the ruptured regime. In order to have $\zeta(R)$ defined for all R we assume $\zeta(R)$ in the two transition regimes to be defined by two quadratic functions. This modification to the original model of Marmottant is described in more detail in Sec. 4.3. The section starts with a more detailed description of the model of Marmottant after which the two quadratic functions and their corresponding boundary conditions are introduced. The shell parameters of the model that are undetermined up to now are the initial surface tension $\sigma(R_0)$, the shell viscosity κ_s and finally the value of ζ in the two transition regimes of the effective surface tension. From the theoretical threshold for the existence of subharmonics (Eq. 5.17) we expect that these three shell parameters strongly influence the subharmonic behavior. The shell viscosity increases the damping b of the system and is therefore expected to decrease the subharmonic response. On the other hand, the initial surface tension $\sigma(R_0)$ and the quadratic transition determined by ζ strongly affect ζ_{eff} and thus β in Eq. 5.17.

The effect of $\sigma(R_0)$ on the subharmonic behavior of phospholipid-coated microbubbles is shown in Fig. 5.3. In Fig. 5.3C and D two different responses of a 3.8 μm radius bubble driven at an acoustic pressure of 40 kPa with a frequency of 2.4 MHz are shown. We observe that the bubble with a small initial surface tension, $\sigma(R_0)$ close to the buckled regime shows a large subharmonic response. In contrast, for a bubble with an initial surface tension in the elastic regime where no subharmonic response is observed. Note also that the fundamental response for both bubbles is similar and is almost unaffected by $\sigma(R_0)$.

To investigate the effect of the shell parameters on the subharmonic behavior, a parameter study was conducted. The results are shown in Fig. 5.4. In the parameter study the driving pulse pressure amplitude and frequency were kept constant at 40 kPa and 2.4 MHz, respectively. The driving frequency corresponds to two times the resonance frequency of the bubble. The corresponding pulse shape of the driving pressure pulse is shown in Fig. 5.3A and is the same as was used in the experiments which will be discussed in the next section. The initial bubble radius was 3.8 μm and it was found that the results presented in Fig. 5.4 are similar for all bubbles with an initial bubble radius between 1 μm and 5 μm. Finally, while one of the shell parameters was varied the other four parameters were fixed as in Fig. 5.3, i.e. $\sigma(R_0) = 0.001$ N/m, ζ =2000 N/m, $\kappa_s = 3 \cdot 10^{-8}$ kg/s and $\chi_{max} = 2.5$ N/m.

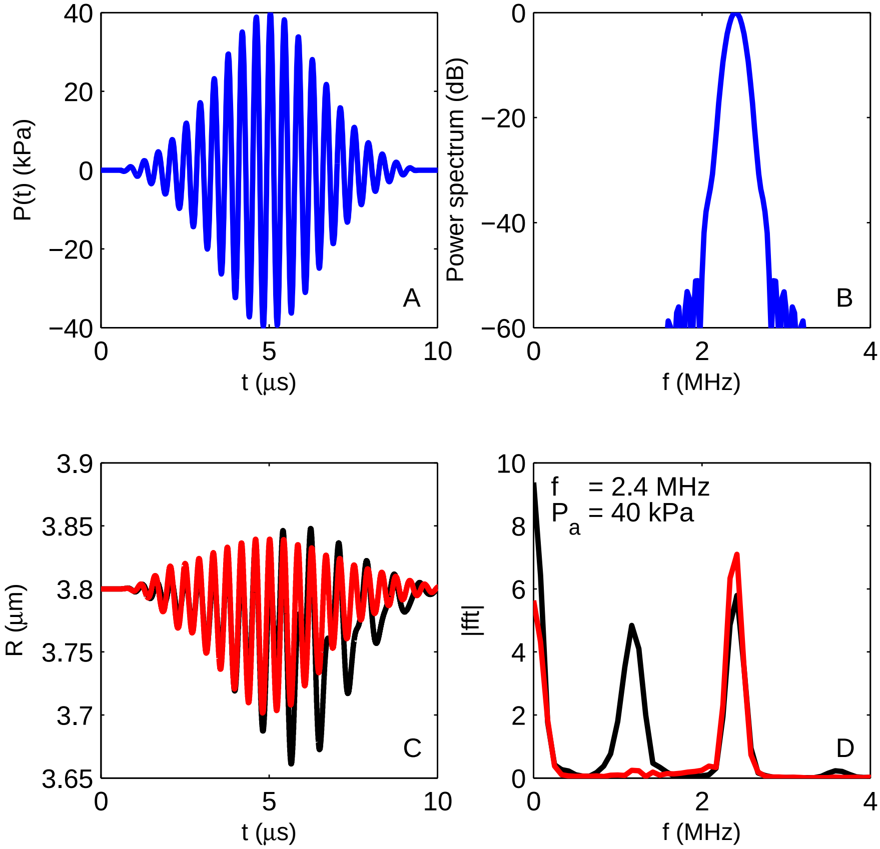

Figure 5.3: Top figures: An example of the driving pressure waveform (A), and (B) its corresponding power spectrum. Bottom figures: The radius time curve (C) and the corresponding Fourier transform (sampling rate 1 GHz, 12001 datapoints, multiplied with a factor 50 MHz/1 GHz to enable comparison with Fourier transform of experimental data) (D) for two bubbles with a different initial surface tension $\sigma(R_0)$ driven with the top driving pressure of 40 kPa with a frequency of 2.4 MHz. The dotted black line represents the numerical simulation for a bubble with $\sigma(R_0) = 0.001$ N/m and the solid red line corresponds to a bubble with $\sigma(R_0) = 0.01$ N/m. The initial bubble radius and the other shell parameters are the same for both bubbles, $\zeta = 2000$ N/m, $\kappa_s = 3 \cdot 10^{-8}$ kg/s and $\chi_{max} = 2.5$ N/m.

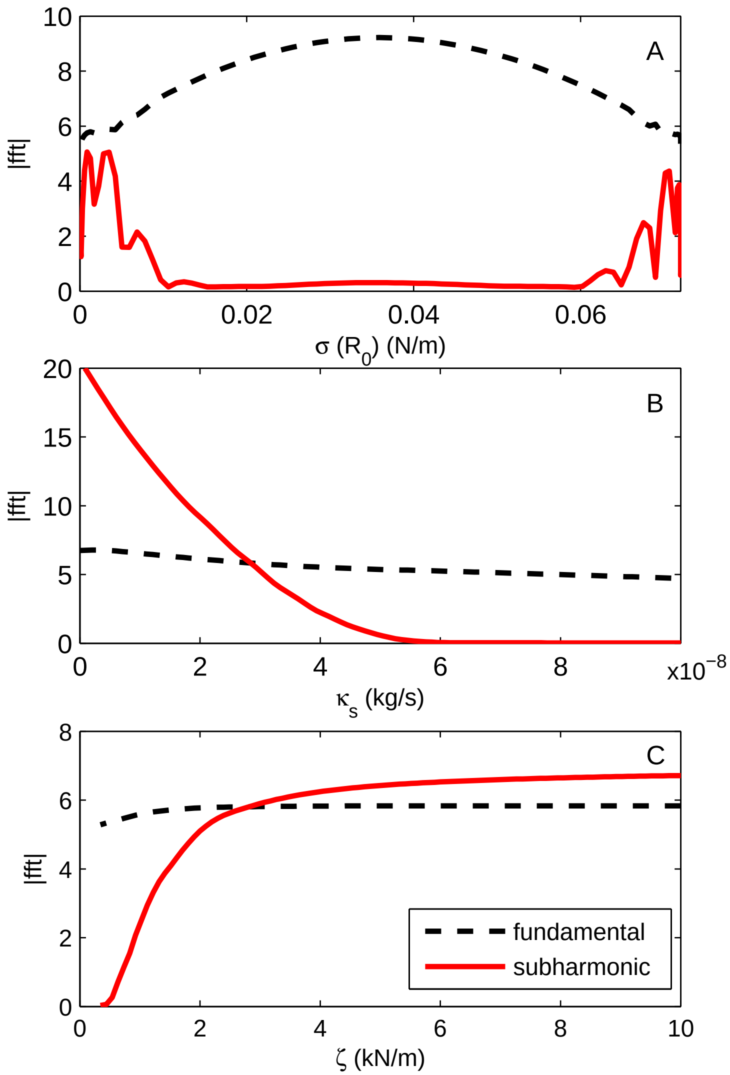

Figure 5.4: The absolute value of the Fourier transforms of a parameter study on the simulated radius-time curve presented in Fig. 5.3. The fundamental response to the driving pressure of 2.4 MHz is clearly visible in all three figures while the subharmonic response is observed to strongly vary for each shell parameter varied independently. A) For $\sigma(R_0)$ varied between 0 and σ_{water} the subharmonic response is only visible for the initial condition of the bubble satisfying $\sigma(R_0) \approx 0$ or $\sigma(R_0) \approx \sigma_{\text{water}}$ B) As expected the subharmonic response is observed to decrease for κ_s increasing from 0 to 10^{-7} kg/s. C) For ζ increasing from 342 to 10000 N/m the subharmonic is observed to increase but for $\zeta > 5000$ N/m the amplitude of the subharmonic response saturates.

The fundamental response in all three cases in Fig. 5.4 is observed to vary little as compared to the subharmonic response which strongly depends on shell parameters. The subharmonic threshold is observed to strongly depend on the damping κ_s. In Fig. 5.4B we observe that for $\kappa_s = 6 \cdot 10^{-8}$ kg/s the threshold for the initiation of subharmonics is 40 kPa corresponding to the driving pressure amplitude. For smaller κ_s the subharmonic response is observed to increase. In agreement with what was found in the weakly nonlinear analysis we find that the subharmonic response depends strongly on the change of the initial shell elasticity. Indeed, the subharmonic behavior is only observed for microbubbles that have an initial surface tension close to $\sigma(R_0) \approx 0$ or $\sigma(R_0) \approx \sigma_{\text{water}}$, close to the transitions from the elastic regime to the two other regimes corresponding to a large second derivative of the effective surface tension. The local minima observed in the subharmonic response in Fig. 5.4A are a result of transient effects resulting from the finite length of the driving pressure pulse. These local minima disappear for an increased length of the driving pressure pulse. As with the linearized model we can conclude that the change in the effective surface tension is of fundamental importance to be able to predict subharmonic behavior for phospholipid-coated microbubbles at low driving pressure amplitudes. Furthermore a difference in the initial surface tension of bubbles caused by the initial phospholipid surface concentration explains why in some experiments subharmonics are observed at low driving pressures while in other experiments no subharmonics are observed for microbubbles similar to the ones used in this study [7, 43–47, 81, 82].

Finally, the subharmonic response is also observed to increase with increasing ζ, see Fig. 5.4C. For an increased ζ also $\zeta_{eff} = 2R_0(\partial(\chi(R_0))/\partial R)$ increases. The transition from the elastic regime to the other two regimes becomes sharper. Following Fig. 5.1 such an increase would result in a decrease of the threshold for the generation of subharmonics. The maximum subharmonic response is observed to saturate for a value of $\zeta > 5000$ N/m.

5.3 Experimental

The previous sections have shown that the subharmonic behavior of phospholipid-coated bubbles is predominantly determined by the driving pulse frequency, pressure amplitude, and the initial phospholipid surface concentration of the microbubble. Experimentally, the initial phospholipid surface concentration of the phospholipid shell of the microbubble is difficult to control as opposed to the frequency and the amplitude of the driving pulse. We therefore have recorded the radial dynamics of 39 different isolated microbubbles with the Brandaris ultrahigh-speed camera [39] as a function of both the driving pressure pulse frequency and amplitude.

5.3.1 Setup

The experimental setup is schematically shown in Fig. 5.5. The setup consists of a cylindrical Plexiglass container that was mounted under an upright microscope (BXFM, Olympus Optical, Japan). Within the container the microbubbles were confined inside an OptiCell cell culture chamber (Thermo Fisher Scientific, Waltham, MA, USA). The acoustic transmit circuit consists of a focused 3-MHz center frequency transducer (PA168, Precision Acoustics Ltd., Dorset, UK) that was mounted under an angle of 45° under the OptiCell. A 0.2 mm needle hydrophone (Precision Acoustic Ltd., Dorset, UK) that moves in and out of the combined optical and acoustical focus was used to calibrate and align the transducer. The transmit transducer was excited with a sequence of pulses generated by an arbitrary waveform generator (Tabor Electronics Ltd, Model 8026, Haifa, Israel) and amplified by a power amplifier (ENI, Model 350L with 50 Ω input impedance, Rochester, NY). To calibrate and align the transmit transducer, a broadband chirp function was used to excite the transducer. The output response of the transducer was measured with the calibrated needle hydrophone in the focus of the transducer. From the response the transmit transfer function of the transducer was determined as is described in [83]

The optical focus of a 100× microscope objective was positioned in the acoustical focus of the transducer. It was illuminated from below with a highintensity xenon flashlight (MVS 7010 XE, Perkin Elmer, Waltham, MA). A continuous-wave light source (ACE I, Schott, NY) in combination with a CCD camera (LCL-902K, Qwonn) was used to monitor the bubble in between experiments. The image plane of the microscope objective was coupled into the Brandaris 128 ultrahigh speed imaging facility. The high-speed camera consists of 128 separate highly sensitive CCD (Charge Coupled Device) sensors that are illuminated consecutively by a rotating mirror. The mirror turbine is driven by a mass-flow controlled flow of Helium, at a revolving rate of up to 20,000 revolutions per second, corresponding to a frame rate of 25 million frames per second. Six consecutive movies of 128 frames each can be stored in a memory buffer with a time interval of 80 ms. We employed the microbubble spectroscopy method detailed in [41] to characterize the bubbles. The microbubbles were excited with a smoothly windowed driving pressure waveform with a frequency ranging from 1 to 4 MHz, all with peak rarefactional amplitudes ranging from 5 to 150 kPa and a fixed length of 8.9 μs. An example of a driving pressure waveform is shown in Fig. 5.3A. In preparation of the experiment 12 driving pressure pulses were uploaded to the arbitrary waveform generator. The frequencies of each of the waveforms were varied and equally spaced near two times the resonance frequency of the microbubble. In this way the radial subharmonic resonance behavior of the bubble was quantified. The optical recordings consisted of two times six movies at a frame rate near 13 Mfps.

The movies were stored on a PC, and all data were post-processed using Matlab (The Mathworks, Natick, MA). The image sequence of the oscillating bubble was analyzed with Matlab through a semi-automatic minimum cost algorithm [41] to give the radius of the bubble as a function of time $R(t)$.

All the results discussed in this paper were conducted with microbubbles located against the top wall of the OptiCell. The experimental setup is compatible with an optical tweezers setup that was coupled through the microscope into the microscope objective. With this combined setup we could also position the microbubbles 100 μm away from the top wall. The details of this setup are described in full detail in previous work [84, 85]. To investigate the effect of the wall on the subharmonic behavior of coated microbubbles we have conducted several scans around the subharmonic resonance of different microbubbles both when the bubble was located against the top wall of the OptiCell and when brought 100 μm away from the wall. Based on these experiments we conclude that the presence of

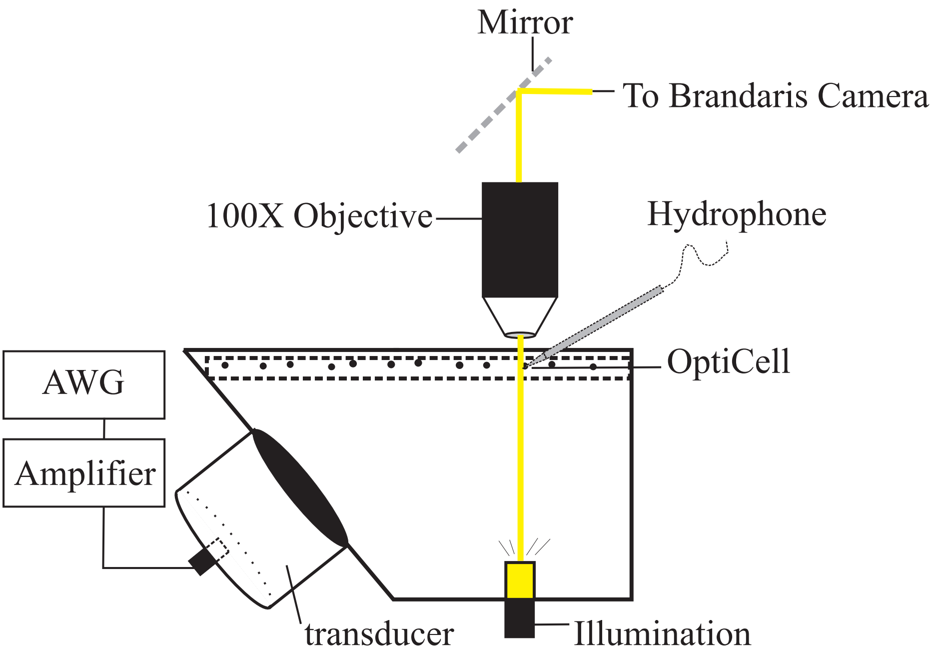

Figure 5.5: A schematic overview of the experimental setup that was used to optically record the radial dynamics of coated microbubbles located inside an optically and acoustically transparent OptiCell chamber. The driving pressure waveform produced by an arbitrary waveform generator (AWG) was amplified and transmitted by a focused transducer. The radial dynamics were recorded through a 100× objective coupled through an inverted microscope into the Brandaris ultrahigh-speed camera.

a wall does not alter the subharmonic behavior of ultrasound contrast agents to be experimentally observable in the current setup. In the following we therefore only consider the results based on the setup without the optical tweezers.

5.4 Results

In total 39 individual microbubbles were included in this study. Subharmonic responses were observed for approximately 50% of the microbubbles. The other 50% of the microbubbles could not be forced into subharmonic oscillations for the driving pressure amplitudes and/or pulse lengths employed in this study which were always smaller than 150 kPa. This finding confirms previous results by Bhagavatheeshwaran *et al.* [81] and by Kimmel *et al.* [82]. In those cases where subharmonic oscillations were observed these were initiated already at driving pressure amplitudes smaller than 40 kPa confirming the results found by another set of authors [7, 43–47].

Fig. 5.6 shows a typical example of an ultrahigh speed recording of a microbubble with an initial bubble radius of 3.8 μm. The bubble was excited with 12 different frequencies near two times its resonance frequency, which was 1.3 MHz following Van der Meer *et al.* [41]. The subharmonic response is clearly visible both in the time and frequency domain. We observe a maximum for the amplitude of the subharmonic response around a driving pressure frequency of 2.4 MHz corresponding to a 1.2 MHz subharmonic oscillation. At this frequency the amplitude of the (radial) subharmonic response is even higher than the amplitude of the fundamental response. Both above and below the resonance frequency the subharmonic response decreases and a subharmonic resonance curve (data not shown) can be obtained similar to the resonance curve produced with microbubble spectroscopy by Van der Meer *et al.* [41]. Furthermore, as expected, the fundamental response of the microbubble does not show a resonance behavior since it is excited far above its resonance frequency, which also explains why the fundamental response is observed to decrease for increasing driving pulse frequency. Finally, note that most of the responses presented in Fig. 5.6 show a zero order frequency component even though the initial bubble radius was subtracted from the radius-time curve before the Fourier transform was performed. The zero order component results from the compression-only behavior of the bubble, i.e. the bubble appears to compress more than it expands [10].

The experimental data is compared to the theoretical predictions. Fig. 5.7 shows a best fit of the model of Marmottant *et al.* [12] for the radius-time curve that shows the maximum subharmonic response in Fig. 5.6 (e). The unknown parameters of the model, ζ, the shell viscosity κ_s and the initial surface tension $\sigma(R_0)$ of the bubble are varied using the iterative fit function *fit* in Matlab. The driving pressures

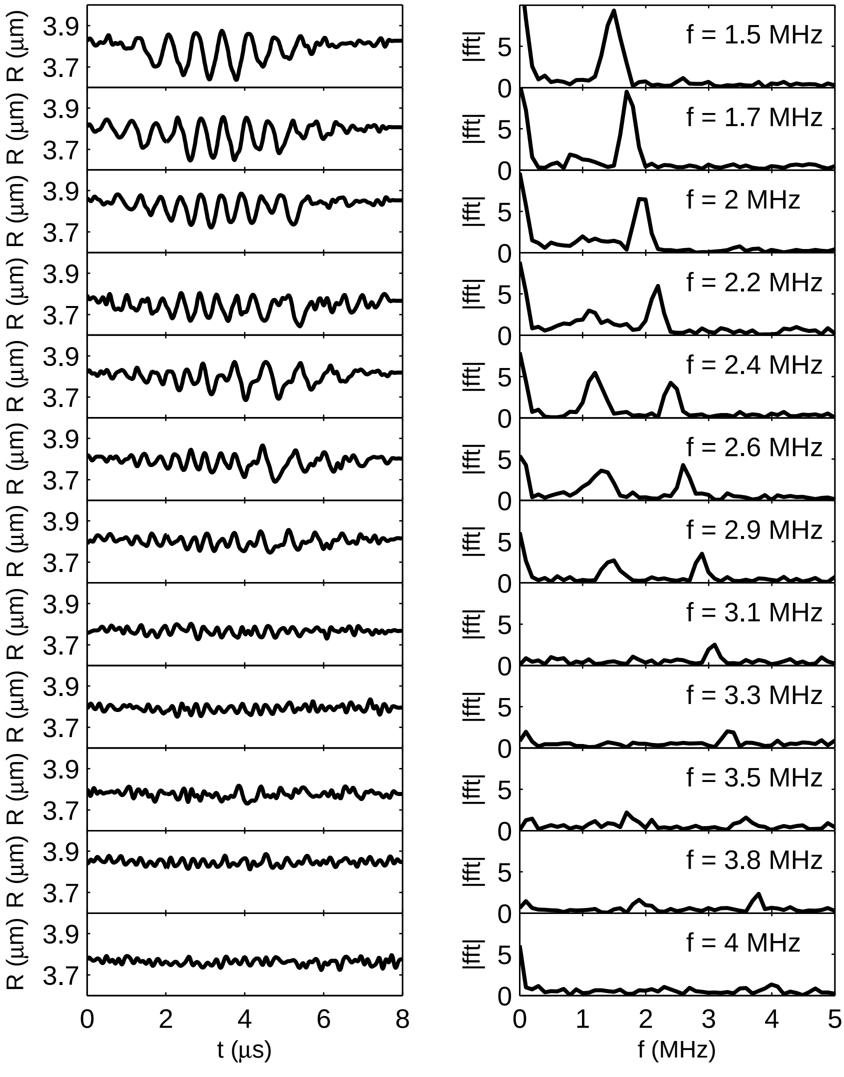

Figure 5.6: The radius-time curves (left column) of a 3.8 μm microbubble excited with twelve different driving pulses all with an amplitude of 40 kPa and different frequencies. In the corresponding absolute value of the Fourier transform (sampling rate 50 MHz, length pulse 501 points) of the radius-time curves (right column) we observe clear subharmonic behavior. We can identify a subharmonic resonance curve that peaks at a driving frequency of 2.4 MHz, about twice the resonance frequency of the bubble.

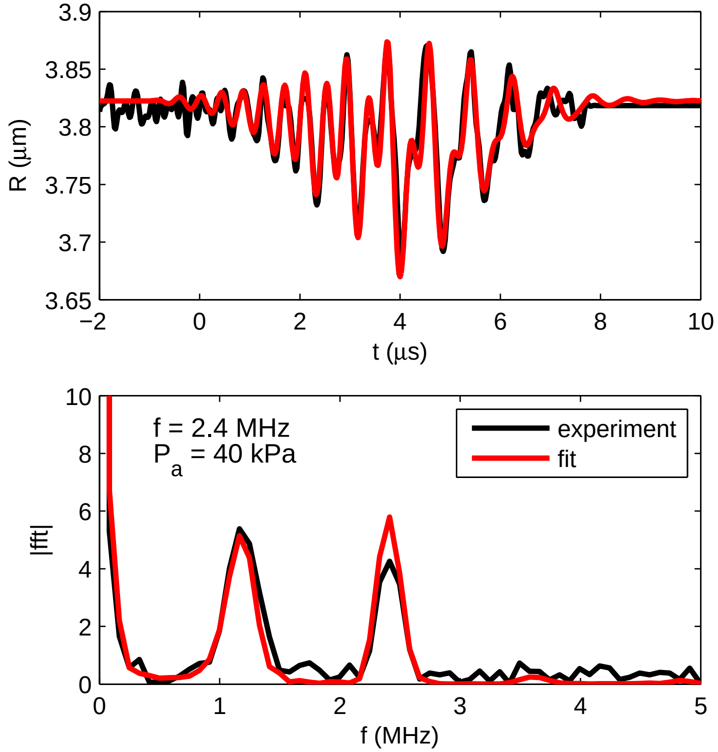

Figure 5.7: The best fit of the fifth radius-time curve from Fig. 5.6E with the model proposed by Marmottant *et al.* with the shell parameters $\chi_{max} = 2.5$ N/m, $\zeta = 2000$ N/m $\kappa_s = 3 \cdot 10^{-8}$ kg/s and $\sigma(R_0) = 0.001$ N/m both in A) the time domain and B) in the frequency domain (sampling rate both curves 50 MHz, 501 points).

for the simulated and measured radius-time curve are identical. The goal of the fit was not to determine the definitive values for the three shell parameters but to see if the model proposed by Marmottant *et al.* is able to predict subharmonic behavior of coated microbubbles at these low driving pressure amplitudes as observed in the experiments.

The agreement between the two radius-time curves is good. The best fit parameters found are in good agreement with the parameter study presented in Sec. 5.2.2 and the values found elsewhere in the literature. The best fit value for the shell viscosity $\kappa_s = 3 \cdot 10^{-8}$ kg/s is in agreement with Van der Meer et al.[41]. To explain the amplitude of the subharmonic oscillations observed in Fig. 5.7 we observe in Fig. 5.4 that the amount of damping depicted by $\kappa_s = 3 \cdot 10^{-8}$ kg/s requires a large value for ζ. This is in agreement with the value for ζ found in the best fit, namely $\zeta = 2000$ N/m. Furthermore, in Sec. 5.2.2 and from the analytical solutions in Sec. 5.2.1, we found $\sigma(R_0)$ should be close to zero which agrees well with the best fit value found in Fig. 5.7, $\sigma(R_0) = 0.001$ N/m.

To investigate the frequency dependence of the subharmonic behavior of phospholipid-coated microbubbles we varied the driving frequency as shown in Fig. 5.6. An overview of the frequency behavior presented in Fig. 5.6 is shown as a single plot in the spectrogram in Fig. 5.8B. The horizontal axis of the figure is divided into twelve columns representing the twelve driving frequencies. The vertical axis represents the response frequencies corresponding to the horizontal axis of the figures in the right column of Fig. 5.6. A frequency of 50 MHz was used to interpolate the radius-time curves. The color coding in Fig. 5.8 represents the absolute value of the Fourier transform of the radius-time curves. The zero order frequency component was filtered out completely. Two other spectrograms for different bubble radii are presented in Fig. 5.8A and Fig. 5.8C.

Figure 5.9 shows the full (sub)harmonic resonance behavior of the very same bubbles presented in Fig. 5.8. The initial surface tension and ζ were assumed to be equal to the values found in the previous fit (see Fig. 5.7) and the shell viscosity was assumed to vary with initial bubble radius as shown by Van der Meer *et al.* [41]. The color coding for the simulated spectra is identical to those in Fig. 5.8 allowing for a quantitative comparison between the experimental an theoretical subharmonic behavior. Both the simulated spectra and the measured spectra show subharmonic resonance behavior at the same frequencies. Furthermore, we identify a good agreement between the absolute amplitude of the subharmonic response between the simulated and the measured spectra.

To determine the threshold pressure for the initiation of subharmonic oscillations for coated bubbles the experiment as presented in Fig. 5.6 was repeated for different driving pressure amplitudes. The maximum response frequency for the experimentally determined subharmonic oscillations was observed to decrease from 1.4 MHz (<5 kPa) to 1 MHz (>80 kPa) for increased driving pressures. This can be attributed to a nonlinear phenomenon, where the frequency of maximum response of the bubble decreases for increased driving pressure, see chapter 3. In Fig. 5.10A the subharmonic oscillation amplitude at the maximum subharmonic response frequency is plotted as a function of the driving pressure amplitude. We observe that the threshold pressure for the initiation of subharmonic oscillations is smaller than 5 kPa, much lower than that of an uncoated gas bubble without a shell and much lower than is expected based on the additional damping introduced by the phospholipid shell of the bubble [7, 43–47]. For the 5 kPa driving pressure the only driving frequency showing a subharmonic response was 2.8 MHz corresponding to a resonance frequency of 1.4 MHz.

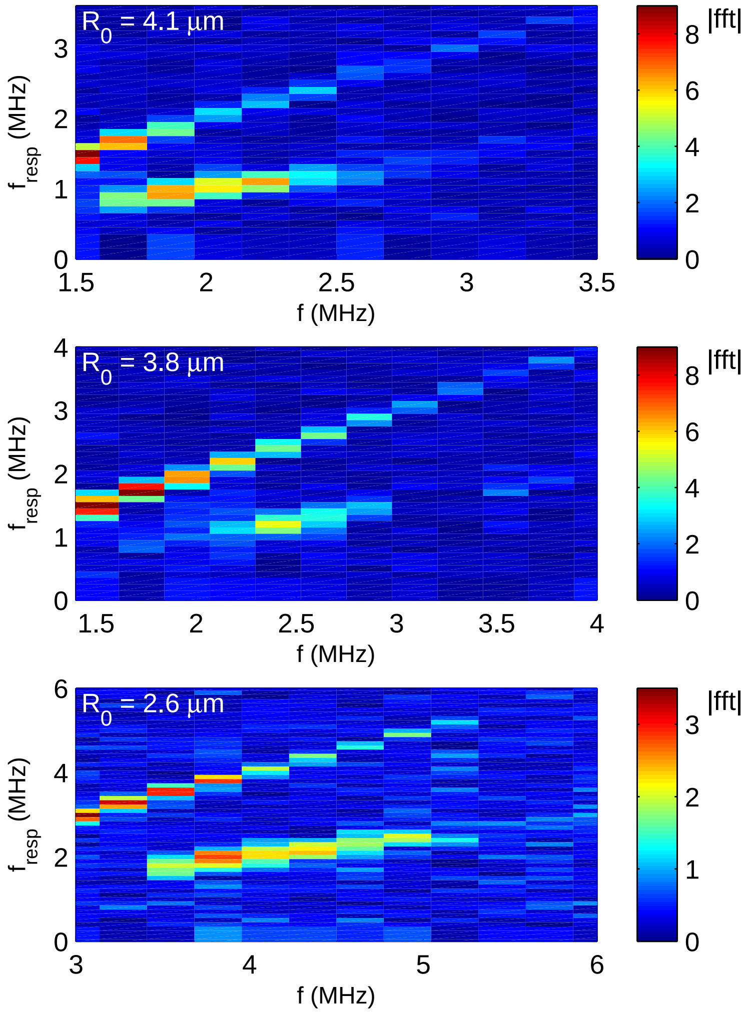

Figure 5.8: The amplitude of the Fourier transform of the radial response of three differently sized bubbles as measured with the Brandaris ultrahigh-speed camera represented by a color. The horizontal axis represents twelve different driving pressure frequencies with a fixed driving pressure amplitude of 40 kPa. The response frequency is represented by the vertical axis.

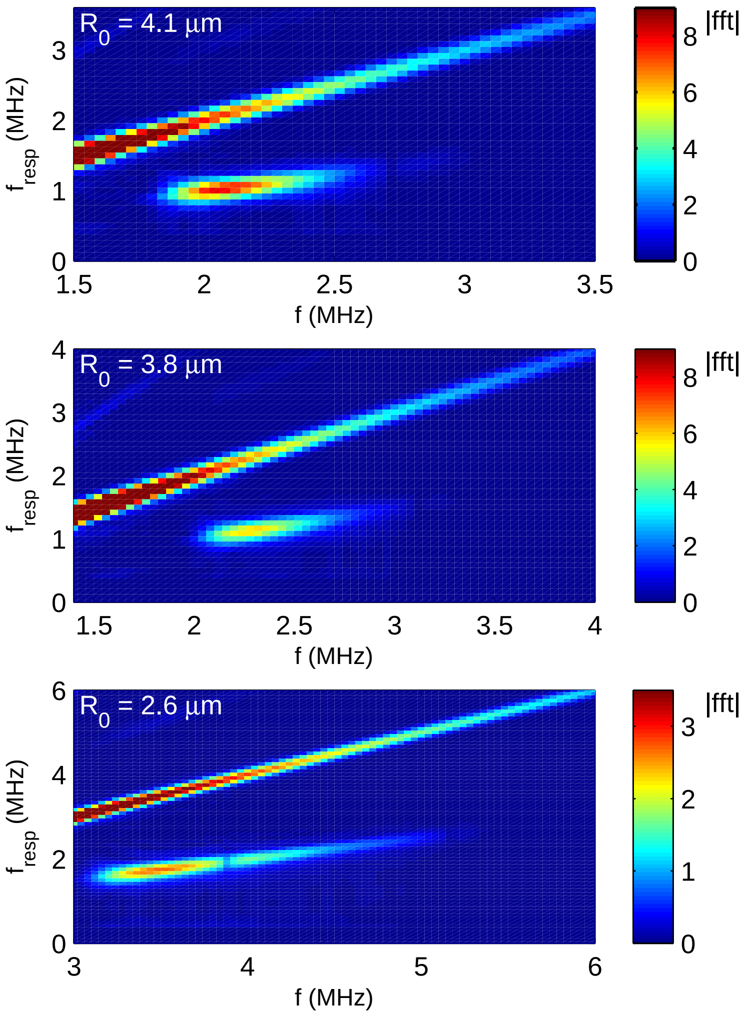

Figure 5.9: Simulated subharmonic resonance behavior of coated microbubbles with the same initial bubble radii as in Fig. 5.8 using the best fit shell parameters found in Fig. 5.7.

Interestingly, we observe that the subharmonic amplitude decreases for increasing driving pressure amplitudes above a pressure of 80 kPa. To investigate these results in more detail we conducted numerical simulations using three different models, an uncoated gas bubble model as described by Lotsberg *et al.* [43], a purely *linear* viscoelastic shell model [63] and the model proposed by Marmottant *et al.* [12]. The shell parameters for the model of Marmottant were taken from the best fit from Fig. 5.7. For the *linear* viscoelastic shell model we used the very same shell viscosity. The shell elasticity was taken from Van der Meer *et al.* [41], $\chi_{eff} = 0.55$ N/m, who determined the shell elasticity for a *linear* viscoelastic shell model. The initial surface tension in the *linear* viscoelastic shell model is assumed to be the same as found in the best fit from Fig. 5.7. In the numerical simulations, the initial bubble radius and driving pressures were those of the experiments. As discussed before, the maximum subharmonic/linear response frequency varies slightly for increased driving amplitudes. Therefore, similar to the experiments, we varied the driving frequency around twice the resonance frequency of the bubble to find the maximum subharmonic response frequency. The maximum subharmonic oscillation amplitude for the three different models at the maximum subharmonic response frequency was plotted against the driving pressure amplitude together with the experimental data in Fig. 5.10A. From this figure it is clear that the uncoated gas bubble model starts to show subharmonic behavior for driving pressure amplitudes between 50 kPa and 80 kPa whereas the experimental data shows subharmonic behavior already at a driving pressure amplitudes of 5 kPa. As a result of the increased damping introduced by the bubble shell, the *linear* viscoelastic shell model shows no subharmonics up to a driving pressure amplitude of 240 kPa. The model by Marmottant on the other hand predicts that the threshold pressure for the initiation of subharmonics almost vanishes, which is in agreement with what is found experimentally. Overall the agreement between the theoretical predictions of the model proposed by Marmottant *et al.* [12] and the experimental data is very good. In both theory and experiment we observe that the oscillation amplitude at the subharmonic frequency can be as high as 4 % of the initial bubble radius already at a driving pressure amplitude of 40 kPa. Also the decrease of the subharmonic oscillation amplitude for higher pressures seems to be correctly predicted by the model. The very same experiments and numerical simulations were conducted for two other microbubbles: one for a bubble with an initial bubble radius of 4.8 μm and one for a 2.4 μm radius bubble; these are presented in Fig. 5.10B and Fig. 5.10C, respectively. The shell viscosity was adapted to the initial bubble radius of the bubble in accordance with the results of Van der Meer *et al.* [41], who found a shell viscosity depending on bubble size, or more precisely on dilatation rate. The shell viscosity was directly taken from *Fig.8 (b)* from Van der Meer *et al.* [41]. For the 4.8 μm radius bubble the shell viscosity

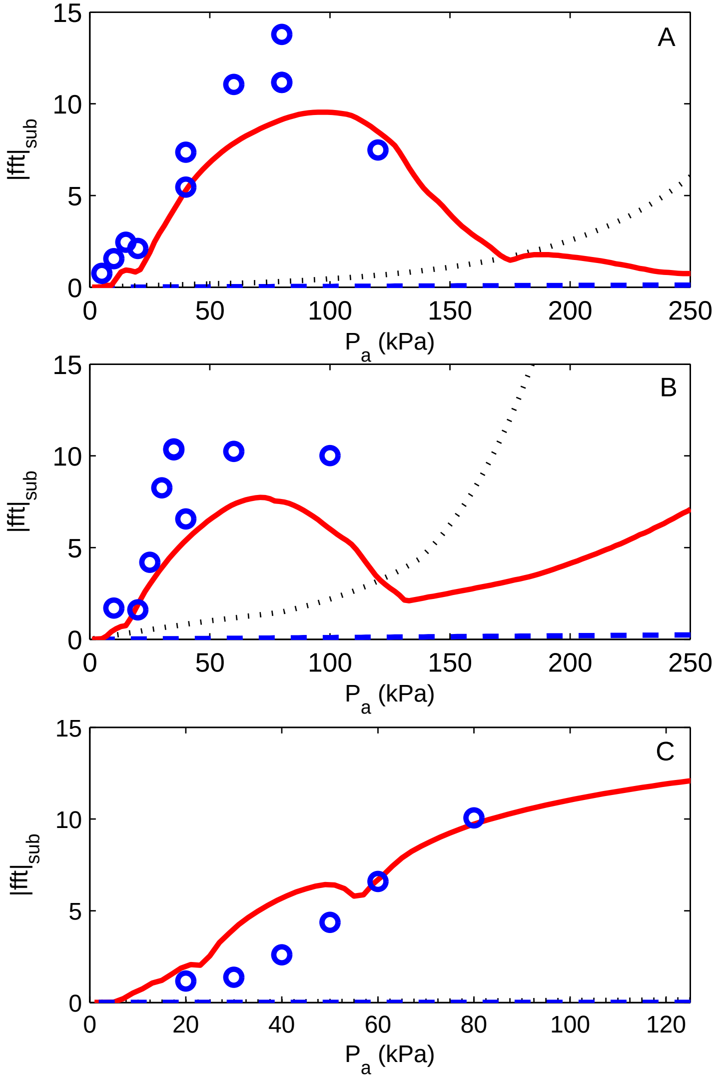

Figure 5.10: The maximum amplitude of the subharmonic oscillations of a A) 3.8 μm bubble, B) 4.8 μm and C) 2.4 μm bubble as a response to different driving pressure amplitudes. The measured responses are compared with the subharmonic responses for the same initial bubble radii predicted by three different models. The model proposed by Marmottant *et al.*[12] (solid red line), and a purely *linear* viscoelastic shell model (dashed blue line) and a free gas bubble model (dotted black line).

was therefore taken to be equal to $4.3 \cdot 10^{-8}$ kg/s and for the 2.4 μm radius bubble it was taken to be equal to $1.2 \cdot 10^{-8}$ kg/s.

In Fig. 5.10C and Fig. 5.10B we again observe that the subharmonic threshold pressure has decreased considerably compared to the threshold pressure predicted for an uncoated gas bubble of the same size. The *linear* viscoelastic shell model is unable to predict subharmonics at such low driving pressure amplitudes.

Comparing Fig. 5.10A, Fig. 5.10B and Fig. 5.10C we observe that the maximum subharmonic oscillation amplitude of the largest and smallest bubble are comparable. Furthermore it is found that the threshold pressure for the initiation of subharmonic oscillations does not vary strongly with bubble radius. We also observe that for all three bubble sizes the model of Marmottant predicts a maximum for the subharmonic oscillation amplitude between a driving pressure of 50 kPa and 100 kPa.

5.5 Discussion

From the comparison between the analytical, numerical and experimental results we conclude that the subharmonic behavior of phospholipid-coated microbubbles at low acoustic driving pressure amplitudes can be explained by a rapid change of the effective surface tension of the bubble shell. We also find that the subharmonic behavior of phospholipid-coated microbubbles is predominantly determined by the initial phospholipid surface concentration on the bubble wall. The description of the effective surface tension of a phospholipid-coated microbubble as a function of bubble radius proposed by Marmottant *et al.* [12] is based on the quasi-static behavior of phospholipid monolayers [64, 65]. Here we show that the main features of the model responsible for the subharmonic behavior of phospholipid-coated microbubbles, such as the large change of the initial shell elasticity, also provide excellent agreement with experimental observations at higher frequencies. The phospholipid molecules covering the surface of BR-14 microbubbles, are distearoylphosphatidylcholine (DSPC), and dipalmytoylphosphatidylglycerol (DPPG). These are well known pulmonary surfactants [86] and their dynamic behavior has been the subject of numerous studies. Hereto, researchers make use of a so-called pulsating bubble surfactometer [87]. In a pulsating bubble surfactometer a bubble of around 500 μm is coated with the surfactant of interest while the radius of the bubble is varied through an externally applied pressure. The pressure in and outside the bubble, which is monitored during the oscillations, provides direct information on the dynamic surface tension of the bubble. From dynamic surface tension measurements conducted by Wen *et al.* [66] and Cheng *et al.* [67] on DPPC (similar to DPPG and DSPC) we observe that the change of the shell elasticity is indeed much larger than the shell elasticity itself for an initial surface tension close to the phospholipid surface saturation concentration (which can be appreciated from the sharp peaks for low effective surface tension and round peaks for large effective surface tension in Fig.2 of [66] and Fig.1 of [67].

The functional form of the effective surface tension figure proposed by Marmottant *et al.* [12] is based on a few approximations: a perfectly elastic regime can be defined, the elasticity is zero in the buckled regime and after rupture of the shell, buckling and rupture are reversible, the surface tension goes to zero in the buckled state. Furthermore, a more realistic description should account for several factors that are known to influence the dynamic behavior of phospholipids monolayer, such as the ionic strength and pH of the solution, temperature, impurities and dissolved surfactants [86].

An explanation why around 50% of the microbubbles studied in this paper and similar studies by other authors [81, 82] showed no subharmonic behavior at low acoustic driving pressures could be that the surface of these bubbles was insufficiently saturated with phospholipids. This would result in an insufficiently large change of the initial shell elasticity to initiate subharmonic behavior.

The findings presented in this paper are valuable for the application of phospholipid-coated microbubbles in medical ultrasound imaging. By controlling the initial conditions of the microbubbles, their subharmonic behavior can be enhanced leading to an improved contrast to tissue ratio in contrast-enhanced ultrasound imaging. One way of changing and controlling the initial conditions of the phospholipid shell is through a change of the ambient pressure. This idea has very recently been shown by Frinking *et al.* [49] and provides new possibilities for non-invasive *in vivo* hydrostatic pressure estimations inside the heart and large vessels.

5.6 Conclusions

Through a weakly nonlinear analysis we provided an explanation for the decrease of the threshold amplitude of the driving pressure above which the subharmonic behavior of phospholipid-coated microbubbles is initiated. We show that a decrease of the subharmonic threshold for coated microbubbles can only be explained if the shell elasticity of the bubble shell, $\chi(R)$, varies rapidly with the amplitude of oscillation. Unlike the purely *linear* viscoelastic models [33, 35, 36, 63] the model of Marmottant *et al.* [12] assumes that the shell of a phospholipid-coated microbubble is elastic only in a small radius domain. Outside this domain the shell elasticity is zero. It is shown that as a result of this rapid change in the shell elasticity, the subharmonic behavior of coated microbubbles is likely to occur already for driving pressure amplitudes as low as 6 kPa.

In a full parameter study of the model we show that the initial surface tension of the bubble shell, i.e. the initial phospholipid surface concentration, determines whether or not subharmonics occur. If the initial surface tension of the bubble is sufficiently close to the buckled regime and the collapse of the phospholipid monolayer from the elastic regime to the buckled regime determined by ζ is sufficiently abrupt subharmonic behavior is enhanced. Furthermore it is confirmed that the subharmonic behavior is enhanced for a smaller shell viscosity.

Experimentally the subharmonic radial dynamics of differently sized microbubbles was studied for different driving pressure frequencies near two times the resonance frequency of the bubble for different driving pressure amplitudes. Subharmonic oscillations were observed for bubbles insonified with driving pressures with amplitudes as low as 5 kPa. This indicates that the threshold pressure above which subharmonic oscillations may occur is even smaller for phospholipid-coated microbubbles than for uncoated gas bubbles, even though as a result of the shell viscosity coated bubbles are more heavily damped.

6 Bubble-wall interactions: Changes in microbubble dynamics[1]

The authors report optical observations of the change in the dynamics of one and the same ultrasound contrast agent microbubble due to the influence of interfaces and neighboring bubbles. The bubble is excited by a 2.25 MHz ultrasound burst and its oscillations are recorded with an ultrahigh-speed camera at 15 million frames per second. The position of an individual bubble relative to a rigid wall or second bubble is precisely controlled using optical tweezers based on Laguerre-Gaussian laser beams [P. Prentice et al., Opt. Express 12, 593 (2004); V. Garbin et al., Jpn. J. Appl. Phys. 44, 5773 (2005)]. This allows for repeated experiments on the very same bubble and for a quantitative comparison of the effect of boundaries on bubble behavior.

[1]Based on: V. Garbin, D. Cojoc, E. Ferrari, E. Di Fabrizio, M. Overvelde, S.M. van der Meer, N. de Jong, D. Lohse, and M. Versluis, *Changes in microbubble dynamics near a boundary revealed by combined optical micromanipulation and high-speed imaging,* Applied Physics Letters **90** (2007)

6.1 Introduction

Micron-sized gas bubbles are effectively used as a contrast agent in ultrasound medical imaging. They contain an inert gas and are encapsulated by a phospholipid, protein or polymeric shell. In the ultrasound field, with typical medical imaging frequencies between 1 and 10 MHz, they undergo linear and nonlinear oscillations leading to an acoustical response that allows the discrimination of the blood pool from the surrounding tissue [88]. The study of the acoustical response of ultrasound contrast agent (UCA) microbubbles has attracted wide interest from both the medical and acoustical communities, not only for providing a better understanding of their complex dynamics, but also for their potential use for drug delivery and therapeutic applications [8]. Bubble oscillations at ultrasound frequencies can be recorded optically [89–91] with the advantage of providing direct visualization of nonlinear oscillations [12], bubble rupture [92] and interactions with vesicles or cells [93, 94]. In our experiments, ultra-high speed optical imaging is performed using a digital rotating mirror camera specifically developed for investigating microbubble dynamics [39]. The camera system is capable of recording 128 frames at a frame rate of up to 25 million frames per second (Mfps), thereby fully resolving the oscillation dynamics at nanoseconds timescale.

For molecular imaging applications in ultrasound, i.e. the non-invasive detection of a specific disease at a molecular level, it will be crucial to develop methods for selectively detecting adherent UCA microbubbles that have bound to specific molecular targets from freely flowing ones, primarily based on a change in their acoustic response. Considerable differences in the amplitude of oscillations [95, 96] and in the spectral response [97] were reported recently. In general, the studies on UCA microbubble dynamics suffer from the lack of control on bubble position, however, and they are therefore based on ensemble averaging and statistical observations of many different bubbles. To the best of our knowledge, time-resolved dynamics of one and the same UCA microbubble under controlled well-defined conditions has not been reported previously.

In this chapter, we report the use of optical tweezers for UCA microbubble manipulation, enabling the study of bubble dynamics with controlled boundary conditions. A quantification of the acoustical and fluid dynamical forces for the very same bubble when it is freely floating and when it is close to a boundary is therefore feasible, provided that the initial bubble properties remain unchanged in consecutive experiments. Three-dimensional optical trapping of single and multiple UCA microbubbles has been demonstrated by various groups, either by focusing an optical vortex beam, e.g. a Laguerre-Gaussian beam [58, 98] or by rapidly scanning the beam in a circular trajectory [99]. The ability to position UCA microbubbles with optical tweezers was also successfully exploited for studying cell sonoporation phenomena induced by violently collapsing microbubbles [100].

6.2 Setup

The setup for combined optical trapping and ultra-high speed imaging is based on an upright microscope (BXFM, Olympus), see Fig. 6.1A. A Gaussian beam from a 1064 nm continuous wave Yb fiber laser (YLM, IPG Photonics) is converted into a Laguerre-Gaussian (LG) mode (Fig. 6.1B) by a phase diffractive optical element (DOE) [58] implemented on a spatial light modulator (SLM) (X8267-11,

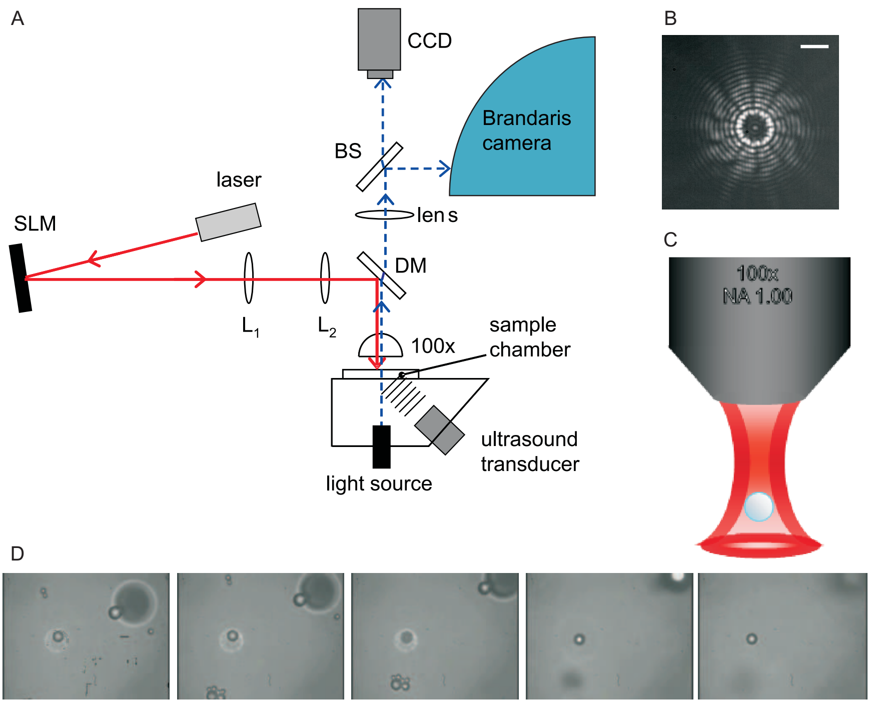

Figure 6.1: A) Setup for combined UCA microbubble trapping, acoustical driving and ultra-high speed optical recordings. The laser beam is converted by the spatial light modulator (SLM) into a Laguerre-Gaussian mode; upon reflection on a dichroic mirror (DM) it enters the objective (100x) and is focused into the sample volume. The ultrasound beam overlaps the optical focal volume. BS: beam splitter, enables two imaging modes: monitor mode on a CCD camera (T = 20%) and imaging mode on the ultra-high speed camera Brandaris (R = 80%). L1 and L2: lenses. B) A focused Laguerre-Gaussian beam; scalebar 5 μm. C) Schematic view of microbubble trapping in a Laguerre-Gaussian beam.D) Image sequence of a trapped microbubble which is positioned in 3D

Hamamatsu). Upon reflection on the dichroic mirror, the beam is focused by a 100x microscope objective (LUMFPL, Olympus; NA = 1.00, water immersion) into an OptiCell cell culture chamber (BioCrystal, Inc.), where bubbles are injected. The beam divergence is adjusted to compensate for the mismatch between the trapping plane and the image plane. The chamber is positioned on top of a water-filled container with an unfocused 2.25 MHz transducer (V306, Panametrics Inc.) mounted at 45°incidence angle with the optical axis. The acoustical beam (5 mm diameter) fully overlaps the optical field of view ($100 \times 100\ \mu\text{m}^2$). Bright-field transmission imaging is performed through the same objective. The ultra-high speed camera is directly connected to the imaging port of the microscope and records the bubble oscillations during ultrasound insonation at 15 Mfps. A charge-coupled device (CCD) camera (LCL-902HS, Watec, 6% efficiency at 1000 nm) monitors the trapping beam shape and position, and the bubble selected to be trapped. The trapped bubble (Fig. 6.1C) can be positioned at a prescribed distance from the wall by positioning the chamber upwards with 0.5 μm accuracy, using a micropositioning stage. An image sequence of the 3D manipulation of the bubble is shown in Fig. 6.1D. In the first image the bubble is trapped at the wall. The following two images the chamber is moved in XY-direction to reposition the trapped bubble. In the last two images the sample is moved upwards as seen from the free bubbles which are floating at the upper sample wall, while the trapped

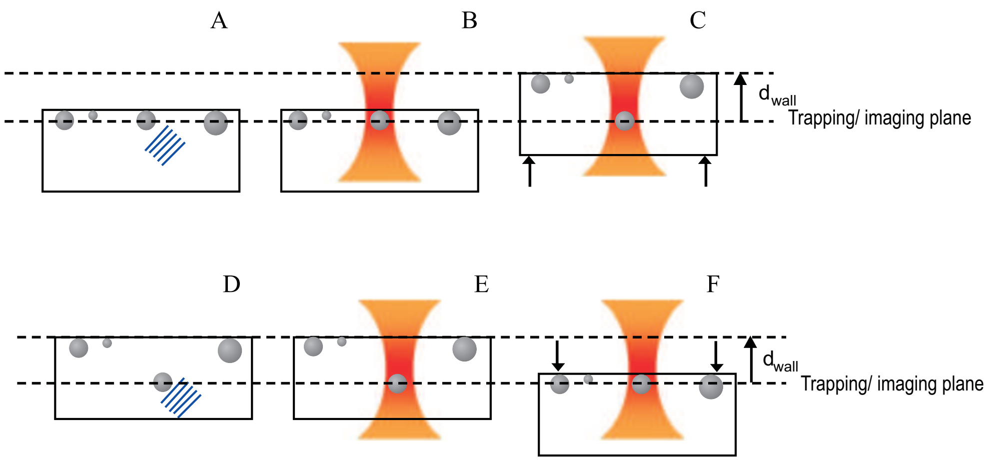

Figure 6.2: Schematic of an experiment. A) The dynamics of a bubble at the wall are recorded. B) The laser trap is turned on which allows manipulation of the bubble position, C) the bubble is positioned in free space by moving the chamber wall up, and D) the trap is turned of and the dynamics of the bubble at a distance d_{wall} are recorded. E) After the recordings the bubble is immediately trapped at the same position, F) the chamber is moved to change the distance from the wall and the experiment can be repeated.

bubble remains in focus at a controlled distance from the wall.

The dynamic implementation of DOEs on a programmable spatial light modulator enables fully flexible trap configurations. The size of a trap can be controlled by changing the Laguerre-Gaussian mode [101] and adapted to the full range of UCA microbubble size. All studies were performed with the experimental contrast agent BR-14 (Bracco S.A., Geneva, Switzerland), an agent containing phospholipid-stabilized microbubbles with a perfluorobutane gas core. The bubbles have a mean radius of 1.5 μm and 95% of the bubbles are smaller than 10 μm.

The schematic of a typical experiment is shown in Fig. 6.2. A bubble is insonified at the wall (Fig. 6.2A) with an ultrasound wave which consists of an eight cycle burst at a frequency of 2.25 MHz, with a peak negative pressure of 150 to 200 kPa (M.I.= 0.12). After the experiment the laser trap is turned on to trap the bubble (Fig. 6.2B). The sample is moved upwards and the trapped bubble remains in the optical focus at a distance d_{wall} from the wall, while the other bubbles float up against the upper wall (Fig. 6.2C). The laser is blocked during the recording to avoid interfering optical forces (Fig. 6.2D). Directly after the experiment the bubble was trapped again at the same position (Fig. 6.2E). While the bubble is in the trap the distance between the bubble and the wall is changed (Fig. 6.2F) and the experiment is repeated. For analysis and comparison with theoretical models, the 2D bubble contours (which are always observed to be symmetrical in our experiments) were processed to track the bubble radius as a function of time, resulting in a so-called radius-time (*R(t)*)-curve of the bubble.

6.3 Results and Discussion

We investigated the influence of the chamber wall on the dynamics of an individual bubble. The radius-time curves of a bubble with a resting radius of $R_0 = 2.45\ \mu$m are shown in Fig. 6.3. First a movie was recorded when the bubble was insonified and positioned at the wall, while a second movie was recorded when the bubble was positioned 50 μm away from the wall. One last movie was recorded after positioning the bubble back at the wall, to double-check if the bubble properties were not changed during the previous insonations. The radius-time curves indicate that the vicinity of the wall suppresses the amplitude of oscillations for one and the same microbubble by more than 50%. This finding can be attributed to three distinct effects. First, the vicinity of a rigid wall is expected to cause a shift in the resonance frequency of the bubble [102]. The effect of a rigid wall is commonly described by the so-called 'method of images' (see, e.g, Refs. [32] and [103]), where an acoustic image bubble is located in the mirrored position; a system of two bubbles having the same size and oscillating in phase indeed generates the same potential flow at the wall position. As our experiments were carried out at a

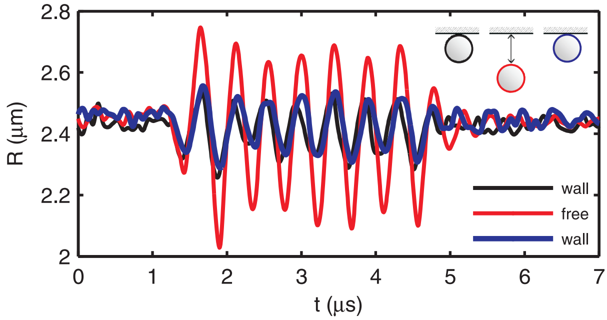

Figure 6.3: Three *R*-*t* curves of a single bubble with an initial radius $R_0 = 2.45\ \mu$m, insonified with a 8-cycle ultrasound burst at 2.25 MHz with an applied pressure of 200 kPa. The frame rate is 15 Mfps. The solid line represents the amplitude of oscillations at the wall; the dash-dotted line is recorded with the bubble at a distance of 50 μm from the wall. The dashed line is the radius-time curve of the same bubble repeated at the wall is identical to the first one showing that repeated insonations have not altered the initial bubble properties.

fixed insonation frequency of 2.25 MHz, a shift in the resonance frequency results in different amplitudes of oscillations being observed at the wall and away from the wall. Second, a full description of the bubble-wall system has to account also for a dissipation introduced by the viscous boundary layer at the wall, which is not taken into account when applying the image bubble method. This phenomenon contributes to the damping of the oscillations, in addition to the other damping mechanisms for coated bubbles (bulk and shell viscosity, thermal diffusion, re-radiation of sound). Finally, asymmetric oscillations may arise in the vicinity of the wall. The eccentricity of bubbles in the vicinity of a capillary wall and driven at comparable pressures has been indeed reported to be close to 0.7 [95], although these observations were made on adherent bubbles. In our experiments, the possible adhesion to the wall was excluded by verifying with the optical tweezers whether bubbles were indeed non-adherent, yet in contact with the wall. In order to visualize asymmetric oscillations the behavior in a plane orthogonal to the wall should be observed, however this was not possible in our present setup without major modifications.

The optical tweezers setup presented here, nonetheless, allows decoupling of the mechanisms listed above. The resonance frequency shift induced by the image bubble can be observed by studying a real two-bubbles system. Then the viscous boundary layer induced by the wall is not present. Furthermore in this case the system is imaged in the plane containing both the bubbles. Should asymmetric oscillations arise, they would then be detected from this point of observation. Two-trap DOEs are produced by dividing the full SLM active area into two sections,

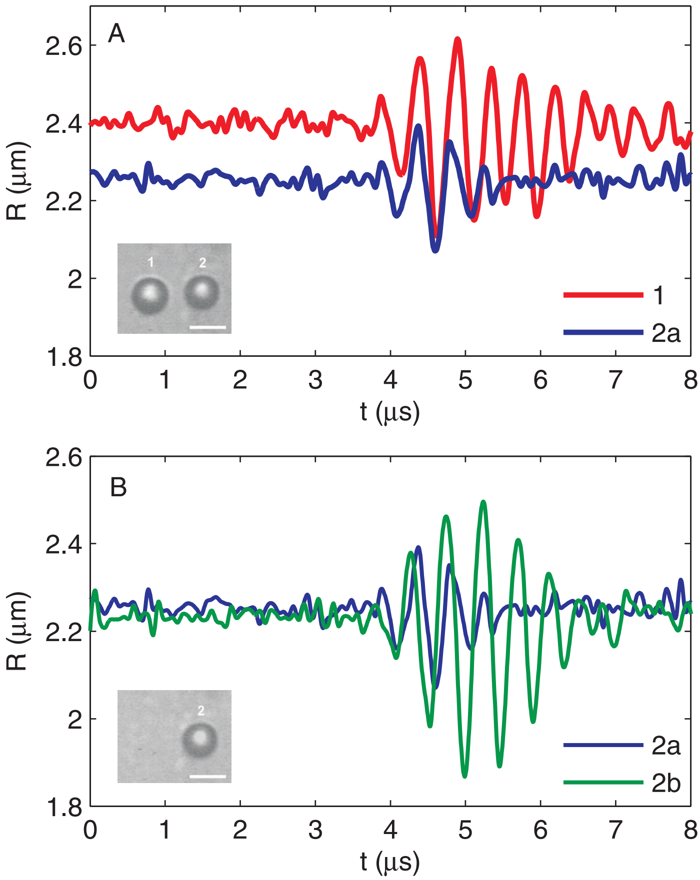

Figure 6.4: Radius-time curves taken at 15 Mfps for two interacting bubbles. A) *R*-*t* curves of the two bubbles trapped at 8 μm distance from each other and positioned 50 μm away from the wall. The dashed curve 1 corresponds to bubble 1, the solid line 2a corresponds to bubble 2. B) The dashed line 2B represents the *R*-*t* curve of bubble 2 oscillating after bubble 1 has been released. The *R*-*t* curve 2a is also plotted for comparison. White scalebar in pictures: 5 μm.

each containing a DOE for a single-trap. The distance between the two traps can be controlled in real-time with sub μm precision by changing the distance between the two DOEs, with a minimum distance corresponding to the two bubbles being in contact, and a maximum distance corresponding to several bubble diameters separation between the bubbles. The same approach can be used to efficiently generate larger arrays of traps (up to 10-20 in our setup) each one individually tuned for a prescribed bubble size.

Two bubbles having similar size were trapped with a separation distance in the same order as their diameter. The bubble pair was then positioned 50 μm away from the wall to reduce wall effects as previously discussed, and to extract information purely on the bubble-bubble interaction. We investigated the radial dynamics of the bubble pair, then released one bubble by switching off the corresponding trap, and studied the behavior of the remaining bubble.

Fig. 6.4 shows the result of this experiment: the initial radius of the bubbles is 2.25 μm and 2.40 μm, respectively, the bubble centers being 8 μm apart. The dynamics of the bubble pair in ultrasound ($f = 2.25$ MHz, $P_a = 150$ kPa) was first recorded at 15 Mfps, see the radius-time curves of Fig. 6.4A. In Fig. 6.4B the radius-time curve for the residual bubble is shown, together with the radius-time curve previously recorded for the very same bubble in the presence of the second one. When comparing the two curves it is apparent that bubble oscillations are highly suppressed by the presence of the neighboring bubble. In repeated experiments the two bubbles always retained their spherical symmetry. In this case we can thus ascribe the change in the bubble response to the shift in resonance frequency. A change in the distance between the bubbles was also observed (data not presented here), due to an attractive secondary Bjerknes force (see e.g. [32] for an overview of the topic). A detailed study and quantification is presented in chapter 8.

6.4 Conclusion

In this chapter we presented a setup that enables for a quantitative characterization of the boundary-dependent UCA microbubble dynamics at the single-bubble level. We compared the behavior of the very same UCA microbubble under different boundary conditions, by a well-controlled positioning of individual bubbles using Laguerre-Gaussian optical tweezers and by recording their ultrasound-driven oscillations with an ultra-high speed camera. We therefore introduced a powerful tool for investigating how the bubble dynamics changes with varying distance to neighboring objects. A deeper understanding of these phenomena may lead to novel imaging modalities together with the use of functionalized microbubbles specifically designed for targeted diagnostic ultrasound imaging.

7 Bubble-wall interactions near a thin compliant wall[1]

The influence of a thin boundary on the dynamics of single ultrasound contrast agent microbubbles is investigated. Experiments were performed with the ultra-high speed camera Brandaris 128 coupled to an optical tweezers setup allowing for micromanipulation of the microbubbles in 3D space and temporally resolving their dynamics. The proximity of the boundary is investigated by recording the radial dynamics of one and the very same bubble at controlled distances from the wall. Influences of the coating on the bubble dynamics are minimized by insonifying the bubbles above their frequency of maximum response. The observed radial response of the bubbles decreases with decreasing distance from the wall. Resonance curves of the microbubbles were obtained by scanning the insonation frequency at various distances from the wall. The frequency of maximum response is found to decrease in the vicinity of the wall with respect to the bubble oscillating far from the wall in case shell effects are minimized. The experimental results are compared to simulations performed with a numerical model, which accounts for the interaction of a coated bubble with a compliant boundary. The experiments and simulations are in good agreement when the bubble is driven above resonance where the shell contributions are small. Below resonance, where the bubble response is dominated by the nonlinear shell behavior, the coupled system allows for an extremely sensitive assessment of the boundary conditions of the bubble-wall interaction.

[1]M. Overvelde, T. Hay, B. Dollet, V. Garbin, Y. Ilinkskii, N. de Jong, D. Lohse, and M. Versluis

7.1 Introduction

Ultrasound contrast agents [104] (UCA) are widely used in medical imaging with ultrasound, e.g. to enhance endocardial border delineation and to quantify organ perfusion. A contrast agent solution contains microbubbles with a radius of 1 to 5 μm. The bubbles are coated with a phospholipid monolayer or with a polymeric shell to reduce the capillary pressure and to prevent them from dissolving in the blood. The compressibility of the microbubbles causes them to pulsate in response to the driving pressure field which leads to a strong scattering echo. The bubble oscillations are strongly non-linear, which improves its contrast with respect to tissue, the non-linear behavior being even more enhanced by the non-linear material properties of the bubble coating. Pulse-echo techniques in medical ultrasound imaging exploit the non-linear response of UCA microbubbles; examples include pulse inversion imaging [5] and power modulation imaging [6].

An emerging application of UCA microbubbles is in molecular imaging with ultrasound, where the coated bubbles are functionalized with a targeting ligand, which adheres to specific markers on endothelial cells. Targeting allows for diagnosis at the cellular level and for local drug delivery applications [8, 9]. The close proximity of the vessel wall changes the dynamics of the microbubbles. Assuming potential flow, the interaction with the wall can be modeled through the "method of images" by placing a virtual bubble with identical source strength (the image bubble) in the mirrored position of the wall plane. The models predict a decrease of the resonance frequency and translatory oscillations near the wall [29, 32, 105–109]. Other phenomena that possibly occur are shape oscillations [38] or asymmetrical collapse of the bubbles leading to jet formation [110, 111]. The changed dynamics of the bubbles has direct consequences for the applied imaging protocols. On the other hand, molecular imaging applications with ultrasound would greatly benefit from an imaging modality that can acoustically distinguish freely circulating microbubbles from targeted ones.

The interaction of free gas bubbles of millimeter size with a rigid wall is well-understood, both theoretically [29, 105, 106] and experimentally [110, 112, 113]. However, our understanding of the interaction of microscopic bubbles with a wall are rather limited because of experimental complexity. Microbubbles are difficult to produce, they dissolve rapidly and single bubbles are difficult to image, both acoustically and optically. For optical detection we need high magnification which results in a very limited optical depth of field. Therefore the microbubbles are usually confined in space through a cellulose membrane wall or an elastic capillary fiber. Then to prevent bubble shrinkage these bubbles must be stabilized through a surface active coating, which altogether results in a highly complex bubble-wall interaction as a result of many combined effects. Only a complete decoupling of all contributing effects would allow us to fully understand the bubble-wall interactions for coated microbubbles. This would require, first, a full understanding of the non-linear coated bubble behavior, which we derived in Chapter 3. Second, control over the bubble position with respect to the wall, and finally a model that would incorporate, in complex representation, the acoustic properties of the compliant wall.

In chapter 6 the influence of a boundary on the dynamics of a single UCA microbubble was investigated. Full control over the distance to the wall was assured using an optical tweezers setup, which was combined to the ultra-high speed camera Brandaris 128 [39] to optically record the radial dynamics of the microbubble. The dynamics of a single bubble positioned at a distance of 50 μm was compared to the dynamics of the very same bubble at the wall. The authors found that the amplitude of oscillations at the wall was over 50% lower than the response away from the wall. From the reported experiments it was not clear how far the influence of the wall on the bubble dynamics extends. Furthermore, the experiments failed to identify the frequency dependence of the bubble-wall interaction, which is expected from previous work on mm-sized bubbles.

While the “method of images” facilitates the theoretical description of the interaction of bubbles with an acoustically rigid wall, in experiment the bubbles are contained in a capillary tube or a polystyrene cell, which are acoustically transparent. Recent numerical work is performed on the interaction of uncoated bubbles with elastic boundaries using the boundary element method (BEM) [114] and finite element method (FEM) [115]. Hay *et al.* [116] account for a bubble between two compliant walls with a model similar to the “method of images”, where the complex source strength of the image bubble depends on the acoustic wall properties and the thickness of the wall. The model is applicable to phospholipid-coated microbubbles.

Here, we investigate the interaction of a single UCA microbubble with a thin compliant wall. We explore the bubble dynamics above, at and below the resonance frequency. The distance from the wall is controlled by means of an optical tweezers setup. The insonation frequency is scanned to determine the resonance curve of the bubble at varying distances from the wall. The results of the experiment are compared to the model by Hay *et al.* [116], which explicitly accounts for a compliant wall.

7.2 Theoretical background

The model by Hay *et al.* [116] accounts for the change of the radial dynamics of a gas bubble as a result of its close proximity to a viscoelastic plate. The bubble dynamics is described by:

$$\rho\left(\ddot{R}R+\frac{3}{2}\dot{R}^2\right)=P_{\text{gas}}-P_{\text{ref}}, \tag{7.1}$$

where R is the time-dependent bubble radius, overdots indicate differentiation with respect to time, P_{ref} is the pressure due to reflections from the plate and P_{gas} is the pressure at the bubble wall in the liquid. As explained in Ref. [116], a theoretical description for encapsulated bubbles may be obtained by substituting an appropriate expression for the gas pressure P_{gas}. For lipid encapsulated microbubbles the appropriate expression for this pressure is given by:

$$\begin{aligned}P_{\text{gas}}=&\left(P_0+\frac{2\sigma\left(R_0\right)}{R_0}\right)\left(\frac{R_0}{R}\right)^{3\kappa}\left(1-\frac{3\kappa\dot{R}}{c}\right)\\&-P_0-P(t)-4\mu\frac{\dot{R}}{R}-\frac{2\sigma\left(R\right)}{R}-4\kappa_s\frac{\dot{R}}{R^2}\end{aligned} \tag{7.2}$$

where R_0 is the equilibrium bubble radius. The fluid properties are the density ρ, the kinematic viscosity μ, the speed of sound c. At the fast oscillations normally imposed on the microbubbles it is assumed that the process behaves adiabatically and the polytropic exponent is $\kappa=1.07$ for C_4F_{10} gas. The additional pressure terms in the equation are the ambient pressure P_0 and the external driving pressure $P(t)$. The dilatational viscosity of the phospholipid coating is given by κ_s. The surface tension at the gas-liquid interface here is radius-dependent through a dependence on the concentration of phospholipids on the bubble surface. A model to account for the physical behavior of the viscoelastic shell, which includes elasticity, viscosity, but also shell buckling and rupture, was introduced by Marmottant *et al.* [109] and is discussed in more detail in chapter 3. The above nonlinear shell behavior is described in the model in terms of an effective surface tension in the following way:

$$\sigma\left(R\right)=\begin{cases}0 & \text{if } R\leq R_b\\ \chi\left(\frac{R^2}{{R_b}^2}-1\right) & \text{if } R_b\leq R\leq R_r\\ \sigma_w & \text{if } R\geq R_r\end{cases} \tag{7.3}$$

with the buckling radius R_b, the rupture radius R_r, the shell elasticity χ, and the surface tension of the gas-water interface $\sigma_w=0.072$ N/m.

Reflections from a planar wall may be included by introducing the pressure term

$$P_{\mathrm{ref}} = P_{\mathrm{unb}}(t) * h(t) = -\rho \left[\frac{\partial \phi}{\partial t} + \frac{1}{2}(\nabla \phi)^2 \right] \Bigg|_{r=R} * h(t)$$
$$= \rho \left(R\ddot{R} + \frac{3}{2}\dot{R}^2 \right) * h(t) \tag{7.4}$$

where P_{unb} is the pressure at the bubble wall in the unbounded fluid due to pulsation, $\phi = -\dot{R}R^2/r$ is the velocity potential due to bubble pulsation, $h(t)$ is the impulse response of the environment, and $*$ denotes convolution. For a viscoelastic wall the impulse response $h(t)$ is the inverse Fourier transform of the frequency domain quantity

$$H_{\mathrm{wall}}(\omega) = R_0 \int_0^\infty K_{\mathrm{LL}} \frac{\kappa}{\kappa_l} \mathrm{d}\kappa \tag{7.5}$$

which represents the frequency response of the wall, derived using angular spectrum decomposition. In Eq. (7.5) K_{LL} denotes the reflection coefficient relating the incident L_{inc} and reflected components L_{ref} of the angular spectrum, which is represented by longitudinal waves corresponding to wave number κ, with κ_l the eigenvalue of the longitudinal mode in the fluid. A complete derivation of Eq. (7.5) is provided in Ref. [116].

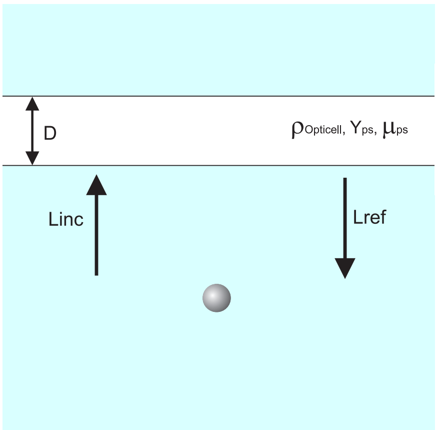

Figure 7.1: Schematic drawing of the bubble near the OptiCell wall.

Calculation of $H(\omega)$ requires that the elastic parameters and density of the wall to be known. The OptiCell membrane is a $D = 75$ μm polystyrene layer with a Young's modulus $Y_{\mathrm{ps}} = 3.3$ GPa and a shear modulus $\mu_{\mathrm{ps}} = 1.23$ GPa, see Fig. 7.1. The density of the material is obtained experimentally $\rho_{\mathrm{OptiCell}} = 1020$ kg/m^3. Throughout the paper the OptiCell wall is referred to as a viscoelastic wall and in all simulations we use the material properties as described above. The model includes effects of both bulk longitudinal and transverse waves in the fluid and wall as well as surface waves. The viscous boundary layer has a thickness of approximately $\delta = \sqrt{(}2\nu/\omega)$ which is of the order of the bubble radius [116] and is therefore negligible for distances larger than a few bubble radii. The dominant material parameter influencing the bubble dynamics is therefore the stiffness of the wall material.

For comparison with the viscoelastic wall we also present results for a lossless rigid wall. In this case the reflection coefficient becomes [116]

$$H_{\text{rigid}}(\omega) = \frac{R_0}{2d}\exp(2i\omega d/c), \tag{7.6}$$

or equivalently, $h_{\text{rigid}}(t) = \delta(t-2d/c)R_0/2d$, where d is the distance between the bubble center and the wall. For the rigid wall, attenuation of the reflected pressure is due solely to spherical spreading over the round trip distance between the bubble and wall ($2d$), and the phase is shifted by the round-trip flight time.

7.2.1 Simulations

Simulations were performed on an uncoated bubble to exclude shell effects and focus instead on effects purely due to the confining environments, i.e. a rigid wall and a viscoelastic OptiCell wall. The material properties of the OptiCell wall used in the simulations are described in the previous section. The gas pressure in the uncoated bubble is given by:

$$\begin{aligned} P_{\text{gas}} = &\left(P_0 + \frac{2\sigma_w}{R_0}\right)\left(\frac{R_0}{R}\right)^{3\kappa}\left(1 - \frac{3\kappa\dot{R}}{c}\right) \\ &- P_0 - P(t) - 4\mu\frac{\dot{R}}{R} - \frac{2\sigma_w}{R} \end{aligned} \tag{7.7}$$

The radius of the bubble is 1.5 μm and has a resonance frequency of 2.2 MHz in the unbounded fluid. Fig. 7.2 shows the amplitude of oscillation as a function of the distance for the rigid wall (A) and the OptiCell wall (B). The simulations were performed for three different applied frequencies below and above the resonance frequency of the bubble in the unbounded fluid, and at a frequency intermediate to the resonance frequency of the bubble in the unbounded fluid and that at the wall. For both the rigid wall and the OptiCell wall, above resonance the amplitude decreases with decreasing distance from the wall, while below resonance the amplitude increases with decreasing distance. Just below the resonance frequency in the free bubble case and above the resonance frequency of the bubble at the

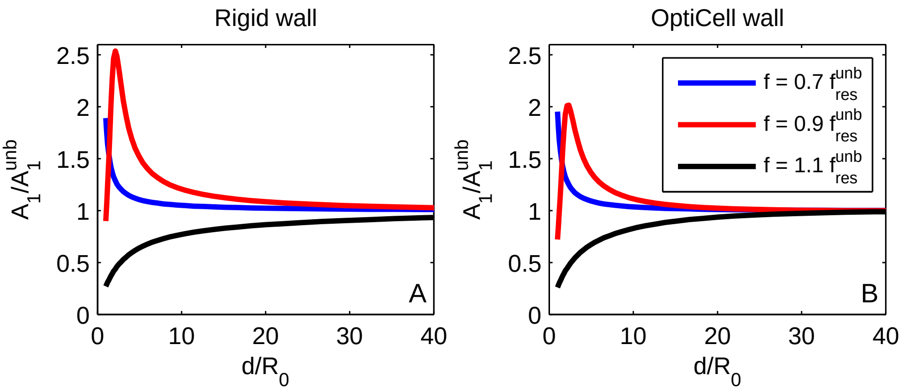

Figure 7.2: Simulated response for an uncoated bubble with a radius of 1.5 μm and an applied pressure $P_a = 10$ kPa. The applied frequencies are below (blue) and above (black) the resonance frequency of the uncoated bubble in the unbounded fluid. The dash-dotted line shows the influence of the wall in the case the applied frequency is in between the resonance frequency of the free bubble and the bubble at the wall (red). A) bubble near a rigid wall; B) bubble near a viscoelastic OptiCell wall. The material properties of the OptiCell membrane are a 75 μm thick polystyrene layer with a Young's modulus $Y_{ps} = 3.3$ GPa, a shear modulus $\mu_{ps} = 1.23$ GPa, and a density $\rho_{\text{OptiCell}} = 1020$ kg/m^3, see Sec. 7.2.

wall the amplitude of oscillation first increases and then decreases with decreasing distance from the wall. The maximum amplitude in case of the rigid wall is a maximum of 2.5 times the amplitude of oscillation of the bubble in the unbounded fluid $A_1^{max} = 2.5 A_1^{unb}$, while for the viscoelastic wall a maximum amplitude of $A_1^{max} = 2 A_1^{unb}$ is obtained. The influence of the rigid wall is still noticed at a distance $d = 40 R_0$, while no influence is observed at $d > 25 R_0$ in case of the viscoelastic wall. However, at all distances from the wall it is difficult to distinguish the response of the bubble at the rigid wall from that at the viscoelastic OptiCell wall.

For a bubble at a wall (red) the amplitude of oscillations is calculated as function of the frequency and plotted in Fig. 7.3. The influence of a rigid wall (A) and a viscoelastic OptiCell wall (B) on the bubble dynamics are compared with the response in the unbounded fluid (blue). The amplitude of oscillation and the frequency are normalized to the maximum amplitude of oscillation and the resonance frequency of the bubble in the unbounded fluid, respectively. In both cases the resonance frequency decreases with decreasing distance to the wall by about 20%. The rigid wall increases the maximum oscillation amplitude slightly and its contribution is found to be less than the increase expected from the "method of

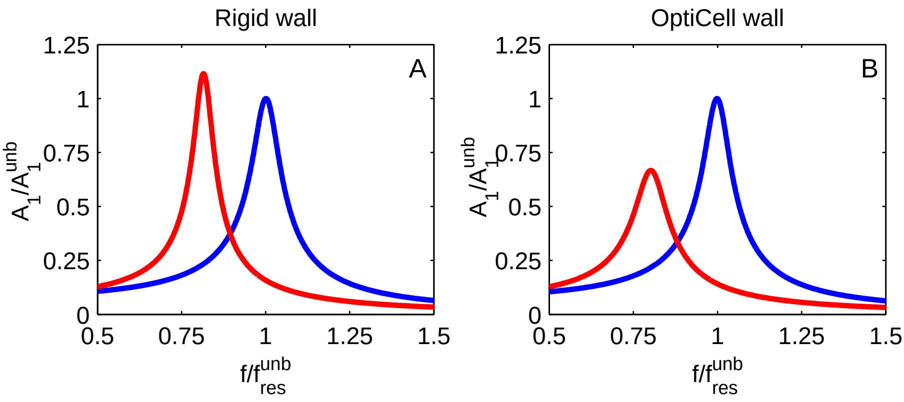

Figure 7.3: Simulated resonance curve for an uncoated bubble with a radius of 1.5 μm for a bubble in the unbounded fluid (blue, $d_{\text{wall}} = 100R_0$) and at the wall (red, $d_{\text{wall}} = R_0$). The resonance frequency and the amplitude of oscillation are normalized with the response of the bubble in the unbounded fluid. A) bubble near a rigid wall; B) bubble near a viscoelastic OptiCell wall. The material properties of the OptiCell wall are given in Sec. 7.2.

images" due to the inclusion of the boundary layer in the model. The viscoelastic wall on the other hand decreases the maximum oscillation amplitude. In conclusion, the most noticeable difference between the interaction of the bubble with the rigid and the viscoelastic plate is expected for the maximum amplitude of oscillation at the wall, which increases in the case of a rigid surface and decreases for a viscoelastic plate. The relative change of the maximum amplitude of oscillation can be deduced from the resonance curve measured on one and the very same bubble measured first in the unbounded fluid, then at the wall.

7.2.2 Nonlinear behavior of the coating

UCA microbubbles exhibit a strong nonlinear behavior mainly as a result of the nonlinear behavior of the phospholipid-coating, see chapter 3. An increasing acoustic pressure decreases the frequency of maximum response by more than 50%. The decrease is the origin of the so-called "thresholding" behavior, where a small change in acoustic pressure causes a dramatic increase in the amplitude of oscillation. The dynamics is well-described by the shell-buckling model proposed by Marmottant *et al.* [12]. In chapter 3 the shell parameters were determined for BR-14 microbubbles, which are also used in this study, giving a shell elasticity $\chi = 2.5$ N/m and a shell viscosity $\kappa_s = 6 \cdot 10^{-9}$ kg/s. Even for apparently identical bubbles the dynamics strongly varies, which was attributed to a variation in the initial surface concentration of phospholipids. The relevant shell parameter here is the initial effective surface tension $\sigma(R_0)$, which may vary between 0 and 0.072 N/m. Throughout the chapter we use the shell elasticity and shell viscosity as given above. The initial surface tension will be obtained from the results far away from the wall.

We will now investigate in what parameter regime the bubble-wall interaction can be separated into changes in bubble dynamics due to the confining wall and those due to the lipid shell. Fig. 7.4A shows simulated resonance curves of a phospholipid-coated microbubble for varying initial surface tensions $\sigma(R_0)$ (see inset). The frequencies of maximum response of the "buckled" bubble ($\sigma(R_0) =$ 0 N/m) and the "elastic" bubble ($\sigma(R_0) = \sigma_w/2$) are very different. The amplitude of oscillation is very different below the frequency of maximum response f_{MR} of the "elastic" bubble, while above the frequency of maximum response the dynamics of the bubble is less dependent on $\sigma(R_0)$. The explanation is simple when we consider the analogy of the linear response of the mass-spring system: below resonance the stiffness mainly determines the amplitude of oscillation while above resonance the system is inertia-driven [32]. The shell of the bubble increases the stiffness of the system and is dominant below the frequency of maximum response, while the shell has minimal influence above the frequency of maximum response,

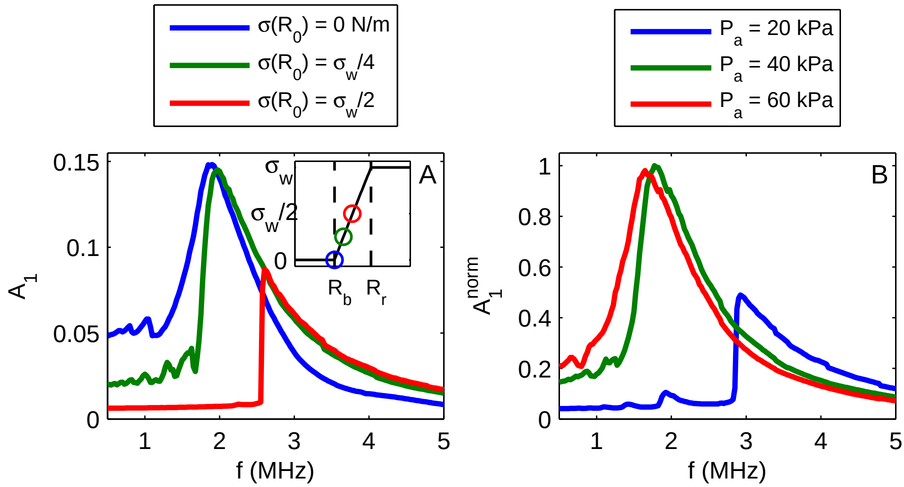

Figure 7.4: Simulated resonance curves of a phospholipid-coated bubble in the unbounded fluid. The parameters are $R_0 = 2.2$ μm, $\chi = 2.5$ N/m, $\kappa_s = 6 \cdot 10^{-9}$ kg/s, and $\sigma_w =$ 0.072 N/m. A) Varying initial surface tensions $\sigma(R_0)$, $P_a = 30$ kPa. B) Varying applied acoustic pressures P_a, $\sigma(R_0) = 0.02$ N/m.

see also [83]. Therefore the dynamics of the bubble resembles a more linear response above the frequency of maximum response, which makes its response much more predictable. Furthermore, in chapter 3 it was found that a strong decrease in the frequency of maximum response was observed as a result of the nonlinear influence of the coating especially at low driving pressure amplitudes. This effect can be appreciated in Fig. 7.4B where the simulated resonance curves are plotted for three different pressures. The amplitude of oscillation A_1 is divided by the acoustic pressure P_a and then normalized by the maximum of the three curves for easy comparison $A_1^{\mathrm{norm}} = (A_1/P_a)_{\mathrm{norm}}$. From both results we therefore conclude that the influence of the phospholipid-coating can be minimized by insonifying the bubble above its frequency of maximum response or at relatively high acoustic pressures. We should, on the other hand, avoid destruction and shrinkage of the bubbles and limit the amplitude of oscillations, which are known to also change the bubble dynamics.

7.3 Experimental methods

7.3.1 Setup

Fig. 7.5 shows the coupled optical tweezers and ultra-high speed Brandaris 128 camera [39] setup allowing for simultaneous micromanipulation of single microbubbles in 3D space and temporally resolving the bubble dynamics. The optical tweezers consist of a 1064 nm CW laser (YLM-5, IPG Photonics) converted into a Laguerre-Gaussian mode by a phase diffractive optical element implemented on a spatial light modulator (X8267-15, Hamamatsu). Before the laser beam enters the objective (LUMPLFL 100x, water immersed, NA = 1.00, Olympus) the laser light is reflected by a dichroic mirror (CVI-laser), mounted in a customized upright BXFM Olympus microscope. The Brandaris 128 camera [39] has a maximum framerate of 25 million frames per second (Mfps). Up to 6 movies of 128 frames can be stored with a minimum time interval of 80 milliseconds before the data is transferred to a PC. The Brandaris camera is designed to run in a segmented mode where 12 movies of 64 frames are recorded in a single run.

The 100x objective is used both for trapping and for imaging of the bubble. With a telescope (focal distances 125 and 150 mm) the divergence of the laser beam is adjusted to match the trapping and the imaging plane. The sample is back-illuminated with an intense flashlight (MVS-7010, Perkin-Elmer). The image is transmitted by the dichroic mirror, then magnified with a 2x magnifier (U-CA, Olympus). A beam splitter reflects 80% of the light into the Brandaris camera, the remaining 20% is used for monitoring with a CCD camera (LCL-902HS, Watec).

A custom designed Perspex module, filled with demineralized water, holds the

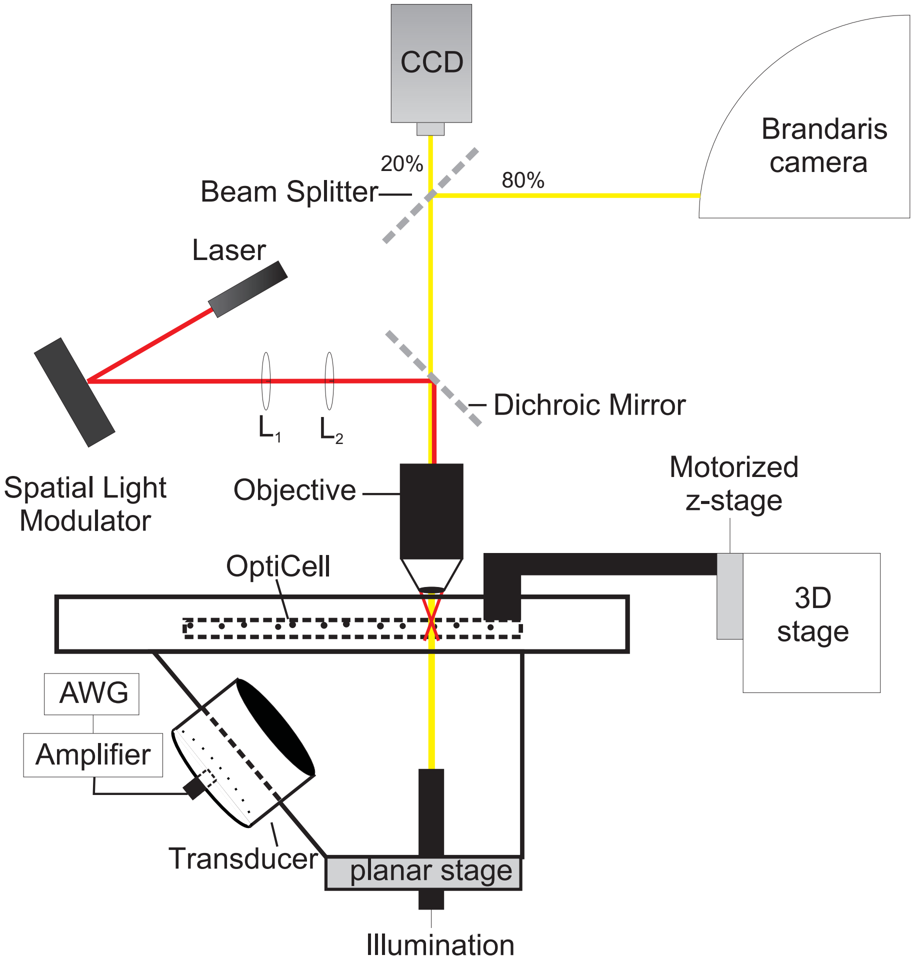

Figure 7.5: Schematic drawing of the setup (not to scale). The setup can be divided in three parts the ultra-high speed Brandaris 128 camera, the optical tweezers setup, and the Perspex module. The Brandaris camera can record up to 25 Mfps and is described in detail in [39]. The optical tweezers setup consists of a infrared laser, a spatial light modulator and a telescope. The Brandaris camera and the tweezers setup are coupled through the same 100x objective. The Perspex module is designed to align the ultrasound, the light and the sample with the objective.

light fiber and the transducer. The ultrasound contrast agent BR-14 (Bracco S.A., Geneva, Switzerland) is injected in an OptiCell^{TM} (Biocrystal, Inc.), which can be moved separately from the Perspex module, and is mounted on top of the water tank. The microbubbles were trapped near the upper wall of the OptiCell. Two translation stages (Thorlabs PT3/M) allowed to manually move the chamber in xyz-direction. A motorized micro-translation stage (M-110.2DG, PI) was used for precise translation of the OptiCell along the z-direction, with a unidirectional repeatability of 0.2 μm and a backlash smaller than 1 μm. The distance between the bubble and the wall was changed by moving the OptiCell upwards, while the position of the trap remained unchanged. The OptiCell was decoupled from the Perspex module and therefore the bubble always stayed in the exact same position with respect to the focus of the transducer.

The computer-generated driving pulse programmed in a Matlab® script was fed to an arbitrary waveform generator AWG (8026, Tabor Electronics) and a power amplifier (350L, ENI). A single element transducer (PA081, Precision Acoustics) was calibrated with a 0.2 mm needle hydrophone (SN1143, Precision Acoustics) between 0.7 and 6 MHz and the amplitude of driving pulse was compensated for the frequency-dependent response of the transducer. The length of the driving pulse was 8 cycles with a Gaussian envelop tapering the first and last two cycles. The applied pressure was chosen to be between 10 and 60 kPa depending on the bubble radius, the applied frequency, and the distance from the wall. The acoustical and optical focus were aligned with a 500μm diameter glass bead and a pulse-receiver system (5077PR, Panametrics).
The timing error of the Brandaris camera master controller is of the order of 1 frame, resulting in a maximum error of 70 ns at a framerate of 15 Mfps. In the case where two or more *R(t)*-curves were recorded under identical conditions the curves were correlated and a maximum time shift of 1 frame was allowed.

7.3.2 Analysis

Each movie captures the radial dynamics at a single acoustic pressure and frequency. The radius vs. time curve (*R(t)*-curve) of the bubble was determined by tracking the contour of the bubble in each frame with a code programmed in Matlab®. Fig. 7.6A shows a typical oscillation of a bubble with a resting radius of $R_0 = 2$ μm which was insonified at a frequency $f = 1.7$ MHz and at an acoustic pressure $P_a = 37.5$ kPa. The *R(t)*-curve (blue) is Fourier-transformed to a frequency domain representation, where we remove the low frequency component (red), which originates from the so-called "compression-only" behavior [10]. Then the time-domain is reconstructed by an inverse Fourier transform of the filtered result, see Fig. 7.6B. For a detailed explanation see chapter 4. We use as a

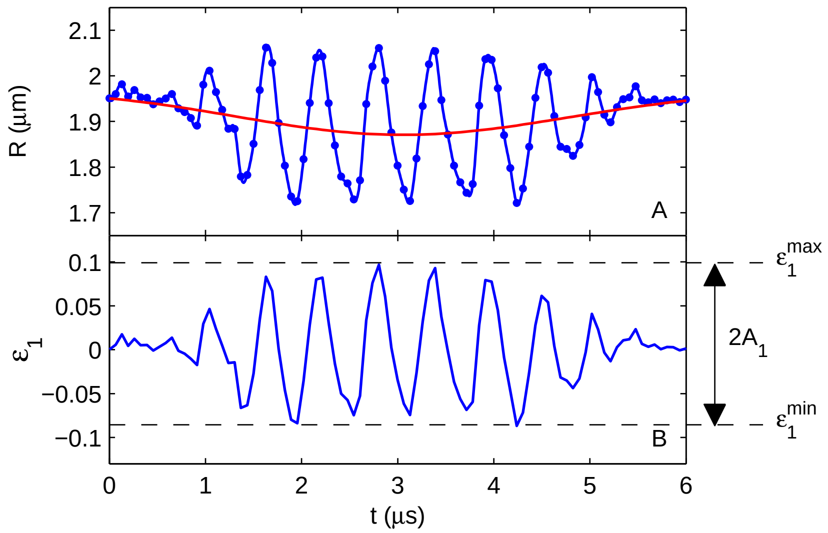

Figure 7.6: A) Experimental *R(t)*-curve (blue) of a BR-14 microbubble in the unbounded fluid with a radius $R_0 = 2\ \mu$m insonified with an acoustic pressure $P_a = 37.5$ kPa and a frequency $f = 1.7$ MHz and the low frequency component (red). B) The relative fundamental response ε_1

measure for the maximum radial excursion at the fundamental frequency A_1:

$$A_1 = \frac{\varepsilon_1^{max} - \varepsilon_1^{min}}{2} \tag{7.8}$$

where ε_1^{max} is the maximum relative expansion and ε_1^{min} the minimum relative expansion, see Fig. 7.6. The response of the bubble from the simulations is obtained with the same procedure. The absolute error in the radial oscillations is 40 nm, see chapter 8. For a typical bubble with a radius $R_0 = 2\ \mu$m this corresponds to a noise level of the oscillation amplitude A_1 of approximately 0.02.

7.3.3 Distance from the wall

The *R(t)*-curves of individual bubbles were recorded at various distances from the wall by micromanipulation of the bubble position with the optical tweezers. To exclude a potential disruption of the bubble behavior by the laser radiation the bubble dynamics was recorded with the bubble released from the trap. The laser beam was momentarily blocked (order s) and a photodiode signal triggered the recording mode in the master controller of the Brandaris 128 camera. When the laser beam passage was cleared the bubble was instantly trapped again. We define the distance from the wall d_{wall} as 0 μm when the bubble is in contact with the wall. In this case the center of the bubble is at a distance R_0 from the wall.

7.3.4 Resonance curves

To investigate the influence of the wall on the resonance frequency the Brandaris camera was running in the segmented mode recording 12 movies of 64 frames. This mode allowed us to perform a spectroscopic investigation of the microbubble response, as described by Van der Meer *et al.* [41]. The bubble response was recorded 12 times; one recording without ultrasound and 11 recordings at different frequencies. while recording the amplitude response. No ultrasound was send in the first movie. The total time of a single run of 12 recordings was of the order of 1 s. It therefore required the optical tweezers system to be operational during the spectroscopy experiment to prevent the bubble from rising out of focus.

The optical trapping force F_T counterbalances the buoyancy force F_B (neglecting the gravity force) and is given by:

$$F_T = F_B = \rho_l g V_B$$

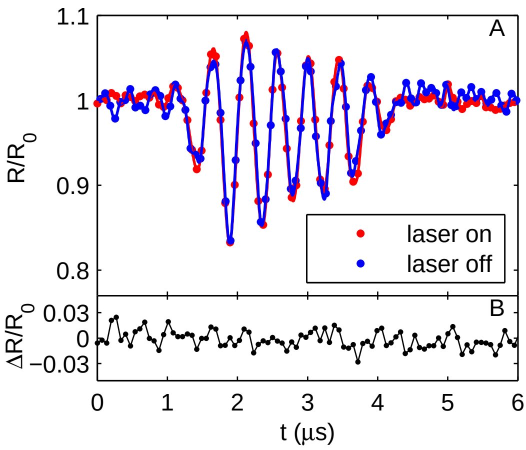

Figure 7.7: The laser trap has no influence on the bubble dynamics. The applied acoustic pulse has a pressure of 150 kPa and a frequency of 2.25 MHz. The bubble $R_0 = 2.6$ μm is positioned at a distance of 50 μm from the wall. A) Radius-time curves of a bubble with the laser on (red) and the laser off (blue) show no change in behavior. B) Residue $\Delta R = R_{\text{laser on}} - R_{\text{laser off}}$. The standard deviation is 0.01, the mean of the residue is 0, and the frequency domain shows that the residue contains only white noise.

with ρ_l the density of the liquid, g the gravity and V_B the volume of the bubble. The force is in the order of 0.1 pN for a 1.5 μm radius bubble and 5 pN for a 5 μm radius bubble. An estimate of the force associated with the bubble wall acceleration, is given by the added mass force:

$$F_M = C_M \rho_l V_B \ddot{R}$$

with $C_M = 1/2$ the added mass coefficient and $\ddot{R}$ the bubble wall acceleration. For an applied frequency of 2 MHz and an amplitude of oscillation $A_1 = 0.1$ the added mass force is of the order of 0.1 μN for a 1.5 μm radius bubble and 20 μN for a 5 μm radius bubble. The added mass force is therefore 6 orders of magnitude larger than that of the trapping force. To confirm experimentally that the laser trap indeed does not change the bubble dynamics, ten bubbles were insonified with the laser trap on and off. No substantial difference was observed in these experiments, as expected, see Fig. 7.7.

7.4 Results

Fig. 7.8 shows the results of an experimental interrogation of a single micro-bubble with a radius $R_0 = 2.9$ μm at a series of distances away from the wall. The bubble was insonified with a driving pressure pulse (8 cycles; frequency $f = 2.25$ MHz and a pressure $P_a = 30$ kPa), see Fig. 7.8A. The distances fange from 0 to 200 μm from the wall. *R(t)*-curves of the bubble at 4 distances from the wall ($d_{\text{wall}} = 200, 50, 10$ and 0 μm) are shown in Fig. 7.8B-E. The distance between the bubble and the wall was first decreased from 200 to 0 μm (blue) and then increased again from 0 to 200 μm (red). The reproducibility of the *R(t)*-curves verifies that the change in the dynamics of the bubbles is caused by the interaction with the wall, not by a change in the bubble properties. Two effects in the radial dynamics of the bubble are observed with changing distance from the wall. First, the amplitude of oscillation decreases with decreasing distance to the wall, which is in agreement with the observations shown in chapter 6. Second, the oscillations of the bubble far from the wall, $d_{\text{wall}} = 200$ μm, start at $t \sim 3$ μs, at ultrasound arrival, while the response of the bubble at the wall, $d_{\text{wall}} = 0$ μm, is delayed by another microsecond, which corresponds to 2 cycles of ultrasound or 15 samples of the high-speed camera. As the second effect is a transient effect which is enhanced by the phospholipid coating, not by the bubble-wall interaction, we will focus her only on the change in the maximum amplitude of oscillations.

The relative amplitude of oscillation A_1 is obtained from the *R(t)*-curves and is plotted as a function of the distance from the wall (circles) in Fig. 7.9. At a distance of 200 μm the amplitude of oscillation A_1 is 0.07. The bubble experiences

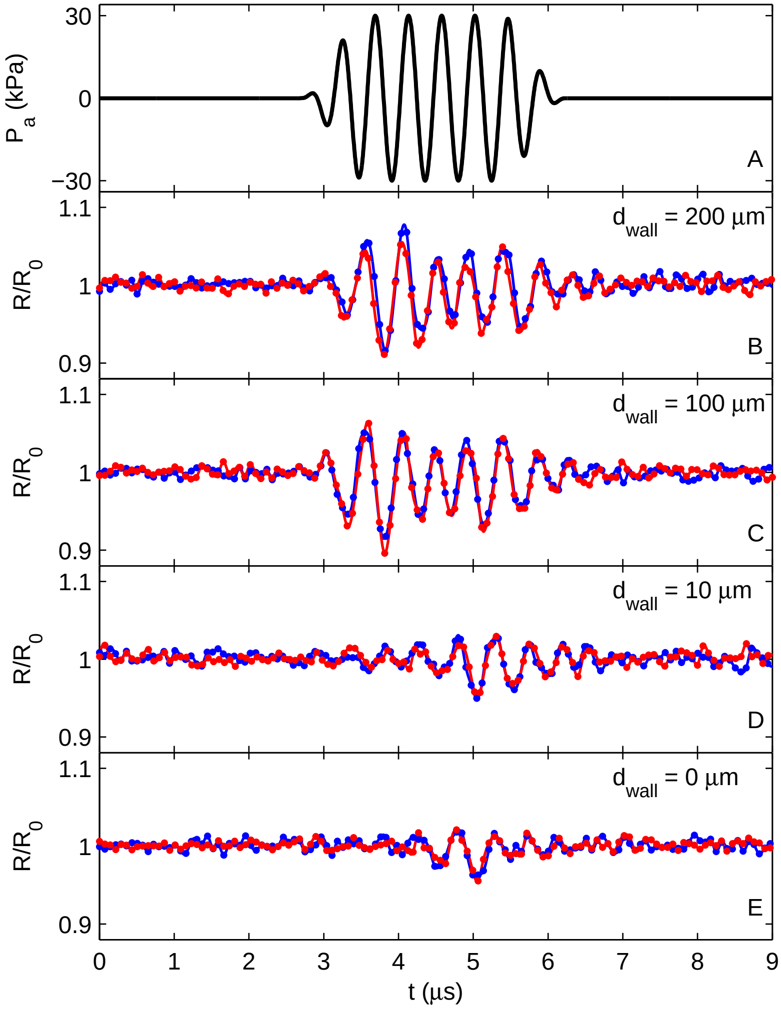

Figure 7.8: The bubble is insonified twice to assure the repeatability of the experiment (dashed line). A) shows the applied acoustic pulse with a frequency $f = 2.25$ MHz and a pressure $P_a = 30$ kPa. B-E) Experimental ($R(t)$) curves for a single bubble with $R_0 =$ 2.9 μm at distances between 200 and 0 μm from the wall.

no interaction with the wall as a decrease in the distance only slightly decreases the amplitude of oscillation. Even at a distance $d_{\text{wall}} = 30\ \mu$m the amplitude of oscillation is still relatively high, $A_1 = 0.06$. The amplitude of oscillation decreases rapidly for distances $d_{\text{wall}} < 30\ \mu$m and the response A_1 is 0.03 at the wall. The experimental results are compared to the models accounting for a compliant wall (blue) and for a rigid wall (red). The initial surface tension of the bubble is taken to be $\sigma(R_0) = 0.02$ N/m to match the amplitude of oscillation at $d_{\text{wall}} = 200\ \mu$m. The trend of a decreasing response with decreasing distance to the wall as well as the ratio of the amplitude in free space and that at the wall is in qualitative agreement with the models accounting for a compliant and a rigid wall. A deviation between the experiments and simulations is found only close to the wall at distances $d_{\text{wall}} \geq 30\ \mu$m as both models show a faster decrease in the response close to the wall than was observed in experiments. At a distance of 70 μm a small peak is observed in the simulation accounting for the compliant wall. Further research will be performed to find an explanation for this peak.

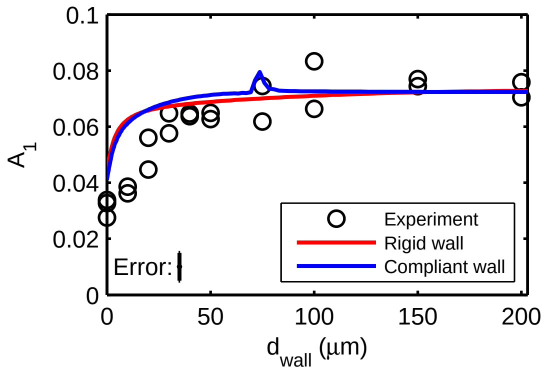

Figure 7.9: The relative amplitude of oscillation A_1, as defined in Eq. 7.8. The bubble oscillates above its frequency of maximum response. A_1 is derived from the experimental *R(t)*-curves at distances between 0 and 200 μm from the wall (circles), which are partly shown in Fig. 7.8. The radius of the bubble $R_0 = 2.9\ \mu$m and the ultrasound pulse has a frequency of 2.25 MHz and an acoustic pressure of 30 kPa. Simulations with the model accounting for a viscoelastic OptiCell wall (blue) and a rigid wall (red) are shown. The properties of the OptiCell wall and the phospholipid coating of the shell are given in Sec. 7.2. The initial surface tension is $\sigma(R_0) = 0.02$ N/m.

In the previous experiment we experienced a considerable influence of the wall on the bubble dynamics at distances below $d_{\text{wall}} < 30\ \mu$m, which is not reflected in the model. To investigate the bubble behavior near resonance, we scan the insonation frequency to measure the resonance curves for a bubble $R_0 = 2.2\ \mu$m at distances between 0 and 200 μm from the wall, see Fig. 7.10A. The bubble is insonated with a pressure $P_a = 30$ kPa and the amplitude of oscillations is kept relatively large $A_1^{\text{MR}} \geq 0.08$ to minimize nonlinear effects due to the phospholipid-coating, see chapter 3. The resonance curve was first measured at the wall, $d_{\text{wall}} = 0\ \mu$m (squares), and in the following frequency scan the distance from the wall was increased up to the maximum distance $d_{\text{wall}} = 200\ \mu$m (circles). Resonance curves were measured at intermediate distances from the wall of $d_{\text{wall}} = 5, 10, 20, 50, 100\ \mu$m (dots). A second resonance curve measured at the wall (triangles) concludes the set of resonance experiments. The results of the resonance exper-

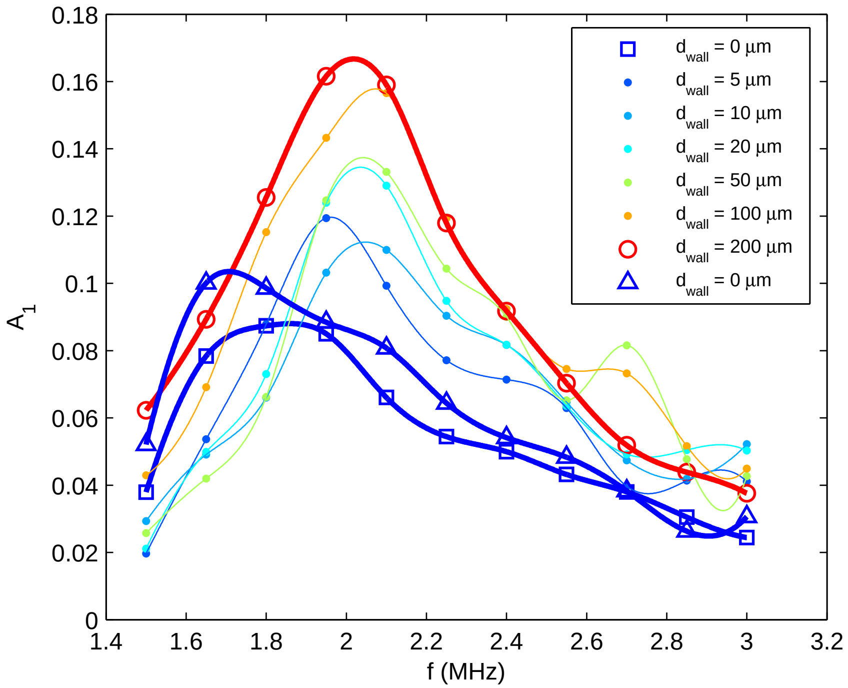

Figure 7.10: Experimental resonance curves for a bubble $R_0 = 2.2\ \mu$m at distances between 0 (squares and triangles) and 200 (circles) μm. The applied pressure is 30 kPa while the frequency is scanned between 1.5 and 3 MHz.

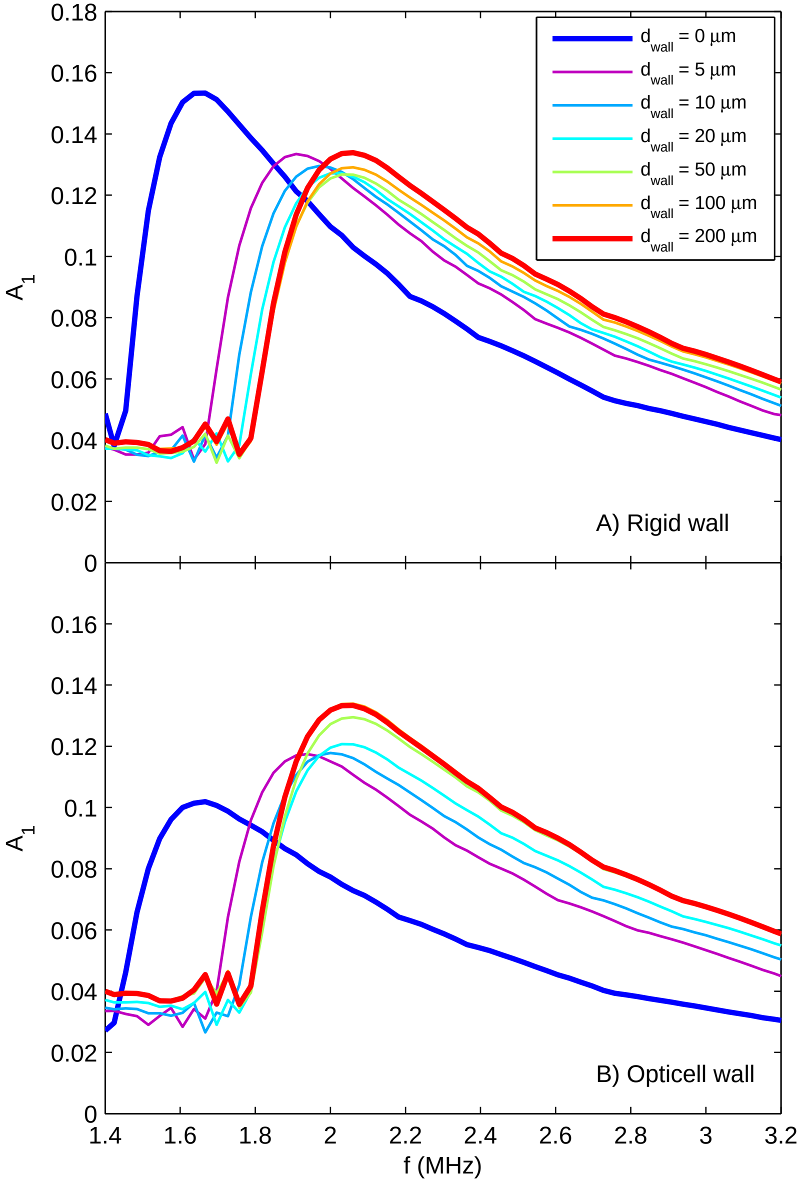

Figure 7.11: Simulation results for a bubble with a radius of 2.2 μm at distances between 0 μm (blue thick line) and 200 μm (red thick line). The applied pressure is 30 kPa. The simulations on the bubble dynamics account for a rigid wall (A) and an OptiCell wall (B). The initial surface tension $\sigma(R_0) = 0.02$ N/m. The other shell parameters as well as the material properties of the OptiCell wall are given in Sec. 7.2.

iments confirm that the wall decreases the frequency of maximum response and the maximum amplitude of oscillation A_1^{MR}. As soon as the bubble is positioned closer to the wall, we first observe a decrease of the response, then a change of the frequency of maximum response is observed, but only very close to the wall, at $d_{\mathrm{wall}} < 10\ \mu$m.

The experiments are compared to simulations accounting for the rigid wall and the compliant wall, see Fig.7.11. The initial surface tension $\sigma(R_0) = 0.02$ N/m is optimized to the shape of the resonance curve, the amount of "compression-only" behavior observed in the *R(t)*-curves (data not shown), and the frequency of maximum response at $d_{\mathrm{wall}} = 200\ \mu$m. Both models predict a decrease of the frequency of maximum response f_{MR} of approximately 20%, from 2.0 to 1.6 MHz, when approaching the wall, which is similar to the experimentally obtained change of the frequency of maximum response. In the case of the rigid wall the proximity of the wall increases the response, while the presence of a compliant wall decreases the response. The experiments resemble the modeled behavior of a compliant wall. In agreement with the experiments, the model also predicts that the change of the frequency of maximum response occurs mainly in the first 10 μm from the wall, while the change in amplitude is still appreciated at larger distances from the wall.

The experimental results are compared to the simulations for the compliant wall in more detail in Fig. 7.12, where we find overall good agreement. The frequency of maximum response as a function of the distance from the wall is in excellent agreement (Fig. 7.12A). The maximum amplitude of oscillation A_1^{MR} decreases with decreasing distance to the wall both in the experiments and the simulations,

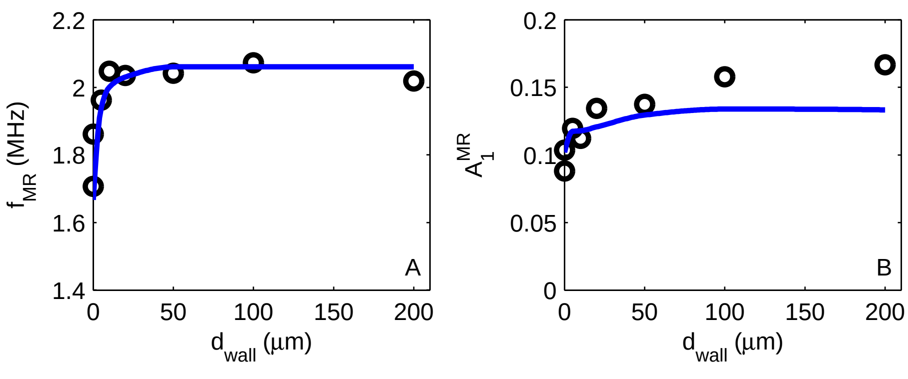

Figure 7.12: Comparison between the experimental results and the simulations accounting for a viscoelastic OptiCell wall as shown in Fig. 7.10 and 7.11. Frequency of maximum response (A) and maximum amplitude of oscillation A_1^{MR} (B). Parameters as in Fig. 7.11B.

see Fig. 7.10B. Nonetheless, there is still a small discrepancy of about 20%.

We now investigate the dynamics of coated bubbles interacting with a compliant wall while the bubbles are driven below their frequency of maximum response. Below the frequency of maximum response the nonlinear behavior of the coating is expected to contribute significantly to the bubble dynamics. A bubble $R_0 = 2.9\ \mu$m is insonified at a pressure of $P_a = 40$ kPa and a frequency $f = 1$ MHz, which is just below the resonance frequency of an uncoated bubble. At a distance $d_{\text{wall}} = 200\ \mu$m the relative amplitude of oscillation is $A_1 = 0.14$. The response A_1 decreases with decreasing distance to the wall until $A_1 = 0.03$ at the wall, $d_{\text{wall}} = 0\ \mu$m, see Fig. 7.13. Simulations performed with the model accounting for the compliant wall (blue) predict a very much constant response upon approach to the wall and a rapid increase in the amplitude of oscillation very close to the wall, contrary to the experimental observation. The initial surface tension $\sigma(R_0) = 0.01$ N/m was obtained from the amplitude of oscillation at $d_{\text{wall}} = 200\ \mu$m. Simulations performed for different $\sigma(R_0)$ do not change the observed trend. It is quite remarkable that the amplitude of oscillation of the bubble oscillating above the frequency of maximum response is predominantly disturbed at close distances from the wall (below 30 μm), while the bubble oscillating below the frequency of maximum response shows an influence up to a distance of at least 150 μm away from the wall.

To investigate the influence of the phospholipid-coating on the observed deviations between the experiments and simulations below the frequency of maximum response in more detail we measured the resonance curves for small amplitude oscillations. Fig. 7.14A shows the resonance curve of a bubble $R_0 = 2.5\ \mu$m at three different distances from the wall, $d_{\text{wall}} = 0,\ 50$, and 150 μm, and an acoustic pressure $P_a = 20$ kPa. The response far from the wall is twice as large as the response at the wall, very similar to the changes found in Fig. 7.10. On the other hand, the frequency of maximum response of the bubble at the wall is higher than the frequency of maximum response away from the wall, at $d_{\text{wall}} = 150\ \mu$m, while the wall was expected to decrease the frequency of maximum response with 20%. The resonance curves were also obtained at a series of distances between 0 and 150 μm and Fig. 7.14 show the influence of the wall as a function of the distance below (B) and above (C) the frequency of maximum response. The response below the frequency of maximum response is similar tot that of Fig. 7.13 ($f = 1.9$ MHz) the wall influences the response A_1 even at a distance $d_{\text{wall}} = 150\ \mu$m. Above the frequency of maximum response ($f = 2.3$ MHz) the response A_1 is unchanged for distances $d_{\text{wall}} > 50\ \mu$m, as was observed before in Fig. 7.9.

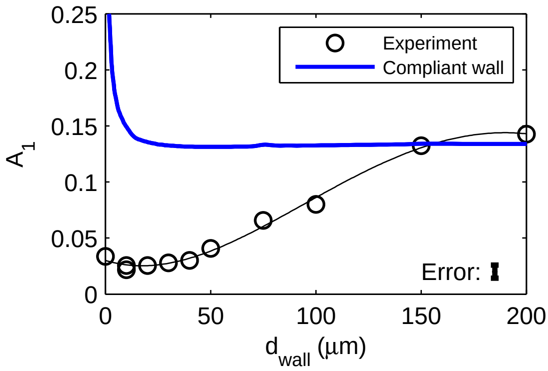

Figure 7.13: The relative amplitude of oscillation A_1 for a bubble insonified just below its frequency of maximum response. The bubble $R_0 = 2.9\ \mu$m is insonified with a frequency $f = 1$ MHz and a pressure $P_a = 40$ kPa. Simulations performed with $\sigma(R_0) = 0.01$ N/m accounting for a viscoelastic OptiCell wall. Other parameters as described in Sec. 7.2.

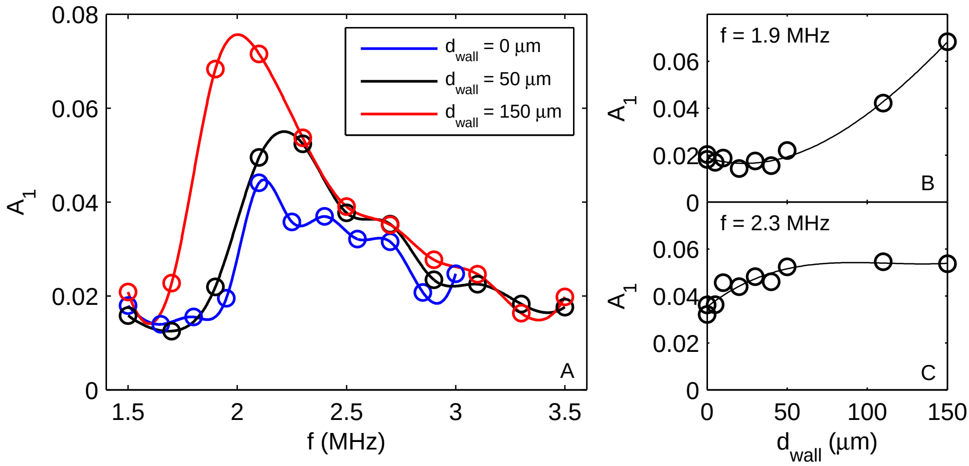

Figure 7.14: The relative amplitude of oscillation A_1 for varying frequencies and distances. The bubble $R_0 = 2.5\ \mu$m is insonified with an acoustic pressure $P_a = 20$ kPa. The resonance curves of the bubble at three distances from the wall (A). A_1 as a function of the distance from the wall insonified with a frequency $f = 1.9$ MHz just below the frequency of maximum response (B) and insonified with a frequency $f = 2.3$ MHz just above the frequency of maximum response (C).

7.5 Discussion

The experimental results and the numerical solutions, such as the ones depicted in Fig. 7.9-7.14, provide us with a couple of important observations. The first observation is that if the shell has a minor influence, i.e. when the bubble is driven above its frequency of maximum response or at an elevated pressure, such that the maximum bubble response $A_1^{\mathrm{MR}} > 0.1$, the experimental trend is well-predicted by the model accounting for a compliant wall. The proximity of the wall decreases the frequency of maximum response with 20% and it only affects the frequency of maximum response at distances $d_{\mathrm{wall}} < 5R_0$. The amplitude of oscillation at the frequency of maximum response on the other hand is changed at distances up to $50R_0$. The amplitude of oscillation of a bubble oscillating above its frequency of maximum response decreases with decreasing distance to the wall and deviations between the experiments and simulations are only observed at distances smaller than $10R_0$ from the wall. On the contrary, when the bubble is driven in its stiffness-dominated regime, i.e. when the phospholipid-coating has a substantial influence on the dynamics of the UCA microbubbles, a remarkable difference was found between the experiment and simulations. Insonation below the frequency of maximum response causes a decrease of the bubble response A_1 with decreasing distance to the wall, while the opposite is expected from the simulations. Furthermore the simulations predict a decrease in the frequency of maximum response of 20%, while in experiments a slightly higher frequency of maximum response is observed at low amplitude oscillations, with a maximum response $A_1^{\mathrm{MR}} < 0.1$, at the wall as compared to far from the wall. We will therefore now first discuss the possible mechanisms and potential flaws in the model or experiment, which may lead to the observed mismatch close to the wall, see Fig. 7.9. Second, we will discus the inconsistent behavior observed far from the wall when the bubble is driven below resonance, as depicted in Figs. 7.13 and 7.14B.

One of the assumptions in the model is that the bubble remains spherical during oscillation. The dynamics of the bubbles is recorded in top view, perpendicular to the wall, and the oscillations of the microbubble appear to oscillate purely spherical. Experiments with a setup allowing simultaneous observations in top and side view of microbubbles oscillating near a wall by Vos *et al.* [38, 117] showed that oscillations can appear perfectly spherical in top view and highly non-spherical in side view. The authors also showed that the non-spherical oscillations become more pronounced with increasing pressure. At an applied acoustic pressure near 30 kPa, which are those used in the experiments described here, no significant oscillations of a non-spherical nature were observed. Furthermore, Strassberg [102] showed numerically that non-spherical oscillations do not significantly contribute to a change of the resonance frequency and the amplitude of oscillations at resonance.

It was shown by Vos *et al.* [38, 117] that bubbles translate close to a wall. Translatory oscillations were not included in the numerical model and could not be observed in the experiment as a result of the optical configuration, viewing the bubble in top view. An estimate of the secondary radiation force, which drives the translatory oscillations (see chapter 8), shows that the force rapidly decreases with increasing distance from the wall, following a $1/d_{\mathrm{wall}}^2$ wall dependence. In conclusion, deviations due to non-spherical oscillations and translatory oscillations are expected to be mainly important in very close proximity to the wall.

We now discuss the influence of the coating as the main discrepancy was found for a bubble driven below resonance, where the coating has a strong influence on the bubble dynamics. An important consideration is that even up to a distance of 150 μm ($d_{\mathrm{wall}} = 50R_0$) changes in the bubble response A_1 were observed. As pointed out before, translatory oscillations and non-spherical oscillations are negligible at these distances and cannot explain deviations at these large distances. The non-linear contribution of the phospholipid-coating on the bubble dynamics is fully included in the numerical model. It was shown in chapter 3 that the shell-buckling model can predict the dynamics of the phospholipid-coated BR-14 microbubble very accurately for the full parameter space of frequency and pressure. Here we also use BR-14 microbubbles, and the shell parameters are well-known: $\chi = 2.5$ N/m and $\kappa_s = 6 \cdot 10^{-9}$ kg/s (chapter 3). The third shell parameter depends on the initial concentration of phospholipids on the surface of the bubble and is expressed in the initial surface tension $\sigma(R_0)$. The response of the bubble depends strongly on the value of $\sigma(R_0)$, see chapter 3. We obtain $\sigma(R_0)$ from the amplitude of oscillation of the bubble at a distance $d_{\mathrm{wall}} = 200$ μm and we verified that the observed decrease of the bubble response A_1 with decreasing d_{wall} does not depend on $\sigma(R_0)$. We therefore have full knowledge over the bubble shell properties. In addition, as discussed in the experimental methods section no deflation of the bubble was observed and therefore no change of the bubble properties is expected. The experiments also confirm that indeed identical behavior was measured, both for a series of measurements where the bubble was moved away from the wall, thereby increasing the amplitude of oscillations, as well as an experiment where the bubble was moved closer to the wall.

In chapter 3 we found that the frequency of maximum response depends strongly on the driving pressure P_a as a result of the nonlinear shell behavior. A decrease of 50% can be observed while increasing the driving pressure, the behavior is reproduced in Fig. 7.15. In section 7.2 the compliance of the wall is modeled by a pressure term P_{ref} which depends on the sound radiated by the bubble and the complex reflection coefficient of the wall. The direct coupling of P_{ref} with the radial oscillations of the bubble changes a priori the system properties. The real part of the reflected sound is similar in a qualitative sense for the compliant wall and for the rigid wall and changes the eigenfrequency of the system. The imaginary part of the reflected sound wave is very different for the two types of walls and can be seen as a change in the damping of the system. In the case of the compliant wall the decrease of the bubble response can be attributed to an increased damping of the system.

To investigate the effect of damping on the frequency of maximum response we performed simulations, included in Fig. 7.15. The simulations were performed with the shell-buckling model for a phospholipid-coated microbubble in the unbounded fluid [12]. The maximum amplitude of oscillation was varied by changing the damping (red) and the acoustic pressure (blue). The damping of the system was increased, by changing the shell viscosity between $\kappa_s = 4 \cdot 10^{-9}$ to $6 \cdot 10^{-8}$ kg/s, to cover a change of the maximum bubble response A_1^{MR} from 0.04 to 0.07, similar values as those obtained in Fig. 7.14. The acoustic pressure was varied between $P_a = 7$ to 22 kPa. Fig. 7.15 shows that in this regime a decrease of the frequency of maximum response of approximately 20% is observed when the driving pressure is changed, while almost no change in the frequency of maximum response is observed when the damping is changed. This exercise shows that the higher frequency of maximum response observed at the wall (Fig. 7.14A) might be a sig-

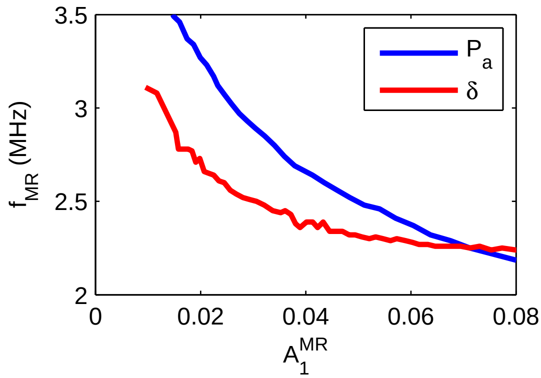

Figure 7.15: Simulated frequency of maximum response f_{MR} as a function of the maximum amplitude of oscillation A_1^{MR}. The simulations were performed with the shell-buckling model [12] for a bubble with a radius $R_0 = 2.5$ μm in the unbounded fluid. A_1^{MR} is changed by changing the applied acoustic pressure P_a (blue) and the damping (red). The shell elasticity $\sigma_R(0) = 0.02$ N/m and the shell elasticity $\chi = 2.5$ N/m. In case of a change in the acoustic pressure (blue), the shell viscosity $\kappa_s = 6 \cdot^{-9}$ kg/s and the acoustic pressure is varied between $P_a = 7$ to 22 kPa. In case of a change in the damping (red), the acoustic pressure $P_a = 20$ kPa and the shell viscosity is varied between $\kappa_s = 4 \cdot 10^{-9}$ to $6 \cdot 10^{-8}$ kg/s.

nature of a change in the primary pressure field, which we will now explore in more detail in the following.

The numerical model describing the bubble-wall interaction includes the reflection of the sound radiated by the oscillating bubble with an image bubble approach. It is assumed that the bubble emits the sound as a point source. What is not included in the model is the reflection of the wall of the primary insonifying ultrasound wave. Due to the reflection of the primary wave the bubble would experience a slightly different driving pressure field, both in amplitude as well as in phase. The primary ultrasound wave and its reflection can be described by a plane wave, therefore the reflected wave must be considered even for bubbles positioned far away from the wall. As shown in chapter 3 the so-called “thresholding” behavior can cause a dramatic change in the bubble response below the frequency of maximum response for a change of the driving pressure of only a few percent. And therefore, even though the reflection itself is expected to contribute up to only 10% of the total insonation pressure, we feel very much inclined to explain the striking difference between experiment and numerical simulations below the frequency of maximum response by a combined effect of the reflection of the primary ultrasound beam and the nonlinear response caused by the phospholipid-coated bubble.

While the pressure amplitude of the reflected primary wave was estimated to contribute up to a maximum of 10% of the total pressure, its complex behavior in phase space as a result of the compliance of the wall is much more difficult to incorporate into our current model. Measurements of the beam profile of the transmitted wave as a function of the angle of incidence and as a function of the acoustic properties of the compliant wall material have not lead to a quantitative and conclusive answer on the complex wave reflection properties. It should also be noted that the measurement presented in Fig. 7.13 was a result of tedious experiments on tens of bubbles. Most of the bubbles would show either no change of their response with changing distance or no response at all. This is now the more understandable: bubbles above resonance indeed show no change, bubbles below resonance show no response and only a very small selection of bubbles would be excited right near their “threshold”. Through our very delicate control over bubble position with the optical tweezers, and hence the contribution of the reflected wave in amplitude and phase, we were able to map out and quantify the extremely responsive details of the thresholding step with great accuracy.

7.6 Conclusions

We investigated the interaction of an UCA microbubble with a thin compliant wall. The non-linear influence of the coating on the bubble dynamics was minimized by insonation of the bubble above resonance or at amplitudes of oscillation

$A_1^{MR} > 0.1$. In the case where the shell has minor influence both the experiments and simulations showed that the frequency of maximum response is decreased with 20% at the wall with respect to a bubble far from the wall. The frequency of maximum response is decreased only at distances smaller than $5R_0$ from the wall. At the wall the amplitude of oscillation at the frequency of maximum response is about half the amplitude of the bubble far from the wall. In the case the coating dominates the bubble dynamics, large deviations are present between the experimental results and the simulated results. In experiments the proximity of the OptiCell wall decreases the response of the bubble even up to 50 bubble radii away, while the simulations show an increase in the dynamics near the wall and only for distances less than $10R_0$ from the wall. As shown in chapter 3 below the frequency of maximum response the dynamics of the bubble is strongly nonlinear and a small increase in the acoustic pressure can cause a dramatic increase in the amplitude of oscillation (so-called "thresholding" behavior), which allows for an extremely sensitive evaluation of the bubble-wall interactions.

8 Bubble-bubble interactions: oscillatory translations[1]

In this chapter the unsteady translation of coated microbubbles propelled by acoustic radiation force is studied experimentally. A system of two pulsating microbubbles of the type used as contrast agent in ultrasound medical imaging is considered, which attract each other as a result of secondary Bjerknes force. Optical tweezers are used to isolate the bubble pair from neighboring boundaries, so that it can be regarded as if in an unbounded fluid, and the hydrodynamic forces acting on the system can be identified unambiguously. The radial and translational dynamics, excited by a 2.25 MHz ultrasound wave, is recorded with an ultra-high speed camera at 15 million frames per second. The time-resolved measurements reveal a quasi-steady component of the translational velocity, at an average translational Reynolds number $\langle Re_t \rangle \approx 0.5$*, and an oscillatory component at the same frequency as the radial pulsations, as predicted by existing models. Since the coating enforces a no-slip boundary condition, an increased viscous dissipation is expected due to the oscillatory component, similar to the case of an oscillating rigid sphere that was first described by Stokes [Trans. Camb. Phil. Soc* ***9****, 8 (1851)]. A history force term is therefore included in the force balance, in the form originally proposed by Basset and extended to the case of time-dependent radius by Takemura and Magnaudet [Phys. Fluids* ***347****, 3247 (2004)]. The instantaneous values of the hydrodynamic forces extracted from the experimental data confirm that the history force accounts for the largest part of the viscous force. The trajectories of the bubbles predicted by numerically solving the equations of motion are in very good agreement with experiment.*

[1]Published as: V. Garbin, B. Dollet, M. Overvelde, D. Cojoc, E. Di Fabrizio, L. van Wijgaarden, A. Prosperetti, N. de Jong, D. Lohse, M. Versluis, *History force on coated microbubbles propelled by ultrasound*, Physics of Fluids **21** (2009)

8.1 Introduction

Bubbles in a sound wave translate unsteadily under the action of an effective force $F_G(t) = -V(t)\nabla p(t)$, where $V(t)$ is the volume and $\nabla p(t)$ is the local instantaneous pressure gradient. In a sound wave $\nabla p(t)$ is oscillatory, and the bubble volume $V(t)$ pulsates, resulting in a force, known as acoustic radiation force, which periodically changes both direction and magnitude [50]. The corresponding motion of the bubble is an oscillatory translation, at the frequency of the radial pulsations, around a position that slowly drifts. The time average of the acoustic radiation force $F_{Bj} = -\langle V(t)\nabla p(t)\rangle$, the so-called Bjerknes force, is non-zero and results in the net translation of a bubble. If the sound wave driving such motion is the secondary wave emitted by a neighboring pulsating bubble, a mutual interaction comes into effect and two bubbles pulsating in phase attract each other. The average force is then called secondary Bjerknes force.

The translation of uncoated bubbles due to acoustic radiation forces has been the subject of numerous studies over the past decades, only a few of which are mentioned here. Crum and Eller [118] and Crum [119] validated expressions for the primary and secondary Bjerknes forces against experimental data by measuring the mean terminal velocity of mm-sized bubbles. Good agreement of a time-averaged equation of motion with experiment was found by balancing the Bjerknes force with a quasi-steady drag force. Indeed, flow oscillations have no effect on the mean terminal velocity if the governing equations can be linearized. According to the analysis of Landau and Lifshitz [120], for a sphere of radius R oscillating with frequency ω and amplitude a, the convective term $(v \cdot \nabla)v$ is of order $\omega^2 a^2/R$, and therefore it can be neglected compared to $\partial v/\partial t \sim \omega^2 a$ for oscillations of small amplitude, $a \ll R$, which appears to be the case in the experiments of Crum [118, 119]. Oğuz and Prosperetti [121] developed an approximate formulation for the instantaneous dynamics of two interacting bubbles to investigate the influence of nonlinear effects. From numerical calculations, a richer behavior was found than what is predicted by the linear theory of Bjerknes forces, although viscous effects were neglected. Reddy and Szeri [122], in a numerical study on the propulsion of microbubbles by traveling ultrasound waves, included viscous effects through the expression obtained by Magnaudet and Legendre [123] for shear-free bubbles with time-dependent radius. The history force was found to be unimportant, consistent with the criterion given in Ref. [123] that it plays a role only if at least one of the two Reynolds numbers, Re_t and Re_r, is smaller than 1. Here $Re_t = R|U|/\nu$ is the Reynolds number for the translation and $Re_r = R|\dot{R}|/\nu$ the one for the radial dynamics.

History force effects have been shown to be important for shear-free bubbles, for instance in single bubble sonoluminescence [124]. It is well known that the history force on a rigid sphere is much larger than on a shear-free sphere [125], and surfactant molecules adsorbed on the surface of a bubble change the shear-free boundary condition to a no-slip one [126]. For the oscillatory motion of a rigid sphere, an increased viscous dissipation is to be expected since the vorticity remains confined in an oscillatory boundary layer of thickness $\delta \sim \sqrt{\omega/\nu}$, where ω is the frequency of the oscillations and ν the kinematic viscosity of the liquid. The Basset history integral [127] generalizes to an arbitrary velocity the expression for the drag on an oscillating sphere that was first obtained by Stokes [128]. Stokes' solution for an oscillating sphere was also found by Mei [129] to reproduce the numerical solution of the full Navier-Stokes equation in the limit of high frequency of oscillations. An expression for the history force on a no-slip bubble with time dependent radius was derived and validated experimentally by Takemura and Magnaudet [130] at finite Re_t.

Bubbles whose surface is immobilized by surfactants are encountered in a number of contexts, and they have proven particularly beneficial in ultrasound medical imaging. In this application, contrast enhancement is obtained by injecting in the blood vessels microscopic gas bubbles [88], ranging in size from 1 to 5 μm, coated by design with a surfactant monolayer to stabilize them against dissolution. Several models have been proposed to describe the effect of a coating on the radial dynamics of a pulsating microbubble [12, 33, 34, 36]. In contrast, its influence on the markedly unsteady translation in an ultrasound field has hardly been treated. Emerging applications of contrast agent microbubbles in drug delivery and targeted molecular imaging [8, 9, 131] demand a deeper understanding of the behavior on the time scale of competing phenomena, for instance the binding to target molecules or the interaction with the blood vessel walls. These applications ultimately require a detailed description of the *instantaneous* translation of *coated* microbubbles. The first experimental study on the instantaneous translation of contrast agent microbubbles in a traveling ultrasound wave, by Dayton *et al.* [132], compared time-resolved optical observations with a dynamical model which included a finite-Reynolds-number empirical extension of the quasi-steady drag on a no-slip bubble. The authors observed that such a model systematically overpredicted the total displacement, and ascribed the discrepancy to the fact that in the experiment the bubbles were in contact with the top wall of the sample chamber due to buoyancy, with the attendant difficulty of quantifying the friction coefficient between a bubble and the wall.

The purpose of the present chapter is to provide a time-resolved description of the unsteady translation of coated microbubbles propelled by ultrasound. We consider a system of two bubbles translating due to their mutual radiation force, which offers the advantage that the pressure gradient on one bubble is known with great accuracy from the time-resolved observations of the radial and translational dynamics of the neighboring bubble. We predict the trajectories of the two bubbles with the aid of the measured radial dynamics, and investigate the influence of the history force in a range of parameters (bubble size R_0, viscosity of the fluid ν, frequency ω, relative radial excursion $\Delta R/R_0$) of interest for medical ultrasound imaging.

8.2 Effect of confining geometry: micromanipulation of bubbles

Isolating bubbles from the walls of the container greatly simplifies the problem of determining the forces acting on them. Here we use optical tweezers to position bubbles at a prescribed distance from the sample chamber wall. The experimental technique is described in Sec. 8.3. As sketched in Fig. 8.1a, a bubble pair is pushed downward and away from the wall, with the line of centers parallel to the wall. The bubbles can be held in the prescribed position for the duration of the experiment. We therefore avoid the problem, encountered by Dayton *et al.* [132], of sliding friction at the wall.

The influence of a rigid wall on the flow field can be modeled in the inviscid case through the method of images where the wall is replaced by a virtual particle which mirrors the dynamics of the real particle and generates a flow that, by canceling out the primary flow, satisfies the zero normal velocity condition at the wall. In

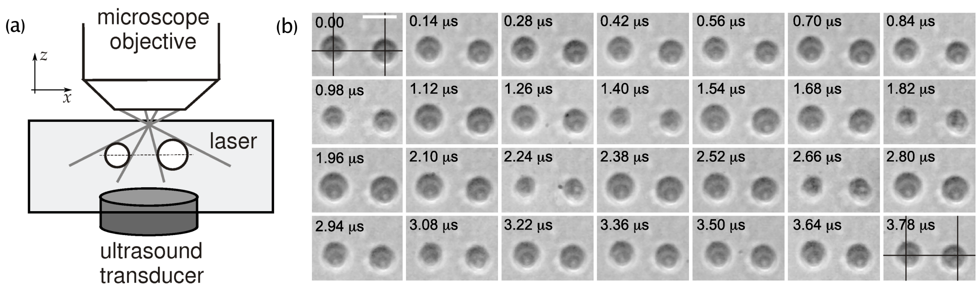

Figure 8.1: Observations of the dynamics of two coated bubbles in ultrasound. a) Layout of the experiment (side view). A microscope objective is used to focus the laser traps (optical tweezers) and for transmission imaging. The direction of incidence of the ultrasound beam is orthogonal to the line of centers x. b) Frames from an ultra-high speed time series of bubble dynamics (top view). The recording is taken at 13.4 million frames per second, corresponding to an interframe time of 70 ns. Here only every second frame is shown. The black crosses in the first and last frame indicate the initial positions of the bubble centers. The distance between the bubbles decreases due to the secondary Bjerknes force. White scale bar: 5 μm.

our experiments the sample chamber wall is not perfectly rigid; for a partially transparent wall the following considerations do not strictly hold, but the effect of a rigid wall can be considered as a limiting case.

The quasi-steady drag F_{QS} for a sphere translating near a rigid boundary can be written as $F_{QS} = -6\pi\eta\gamma RU$, where γ is Faxén's correction factor. Up to third order in the parameter R/r, where R is the sphere radius and r the distance from the boundary, one has $\gamma = \left(1 - 9/16\,(R/r) + 1/8\,(R/r)^3\right)^{-1}$, see [133]. For $R/r \sim 1/20$, the typical value in our experiments, the drag is increased by less than 5%.

The image of a pulsating bubble also generates a spherical wave, with the result that an acoustic radiation force arises between the bubble and the wall through the coupling of the bubble and its image. The acoustic radiation force between pulsating bubbles is derived in Sec. 8.4. The leading term depends on $(R/r)^2$, and therefore for $R/r \sim 1/20$ the net attraction force to the wall becomes negligible. Incidentally, this force acts in a direction orthogonal to the line of centers (see Fig. 8.1a) and would not affect the force balance in the direction of interest.

By positioning the bubbles at least 20 radii away from the wall we therefore minimize the effect of reflections on the translational dynamics, so that the bubbles can be regarded as if in an unbounded liquid. In eliminating these disturbances we can focus on the forces acting on the bubbles purely due to the interaction with the liquid.

8.3 Experimental procedure

The facilities and protocols used in this study to simultaneously control the experimental conditions with optical tweezers and optically record the dynamics of microbubbles in ultrasound have been presented in chapter 6 and 7. The optical tweezers setup was based on an upright microscope (Olympus) modified to couple a laser beam into a water-immersed 100× objective lens (Olympus, N.A. 1.00). A strongly focused Gaussian beam is known to produce a three-dimensional optical trap for dielectric microparticles with a refractive index greater than the surrounding medium. Since a bubble has a lower refractive index than the surrounding liquid, a suitable optical trap consists in this case of a laser beam exhibiting a minimum of intensity on the optical axis, such as a Laguerre-Gaussian beam [134]. We produced the intensity distribution required to generate two traps by converting a 1064 nm continuous-wave linearly polarized laser beam (CVI) through a computer-generated phase diffractive optical element. The implementation of diffractive optical elements on a spatial light modulator device enabled us to adjust in real-time the separation distance between the traps [58].

A suspension of microbubbles of an experimental phospholipid-coated ultrasound contrast agent (Bracco S.A., Geneva, Switzerland) was injected in a chamber enclosed by two optically clear polystyrene matrix membranes (Opticell^{TM}, Thermo Fisher Scientific) which ensure high acoustic transmission. We selected pairs of bubbles with a size close to the resonant size for the frequency of the driving ultrasound, set the initial distance between the centers, and positioned them away from the wall using a micropositioning stage. The chamber was coupled to a single-frequency unfocused ultrasound transducer (Panametrics) by immersion in a water bath. An 8-cycle 2.25 MHz ultrasound pulse with a 2-cycle Gaussian taper was produced by a waveform generator (Tabor Electronics) and amplified by a RF power amplifier (ENI) before being transmitted by the transducer. The ultrasound beam overlapped with the focal volume of the microscope objective and its angle of incidence with the optical axis (z in Fig. 8.1a) was 45°, so that the acoustic reflection from the objective did not reach the bubbles. Furthermore, the direction of incidence of the beam was orthogonal to the line of centers (x in Fig. 8.1a) to decouple the effects of the primary acoustic radiation force from the mutual interaction through the secondary acoustic radiation force. The sample was illuminated from below and the same microscope objective that was used to focus the optical traps was used to produce a top view transmission image, in conjunction with a 2× magnifier. The ultra-high speed digital camera Brandaris 128 [39] recorded the dynamics at near 15 million frames per second, corresponding to a temporal resolution under 70 ns.

Fig. 8.1b shows 28 frames extracted from the movie of two microbubbles undergoing radial pulsations and experiencing mutual attraction. The marks in the first and last frame indicate the initial positions of the bubble centers. The bubbles remain spherical during the radial pulsations; we discard the experiments where the bubbles significantly deviate from spherical symmetry. To prevent optical forces from interfering with the dynamics, the laser was briefly blocked during the recording, even though the magnitude of the optical force in the horizontal plane ($\sim 10^{-11}$ N) is four orders of magnitude smaller than the secondary acoustic radiation force we typically measure.

The radius and position as a function of time are extracted from the 128 frames of each recording, using the minimum cost tracking algorithm described in [41]. The optical resolution is 100 nm per pixel; image analysis results in sub-pixel resolution on the extracted quantities, with a typical accuracy of $30-40$ nm for the radius and $70-80$ nm for the distance. The pattern of rings generated in the image plane by the Mie scattering of light transmitted by a bubble [135] introduces an experimental uncertainty in setting the in-focus position of a bubble. This ultimately leads to a systematic uncertainty in the determination of the initial bubble radius for each experimental run, and the edge detected through the minimum cost algorithm may not correspond to the correct radius. By conducting a series of control experiments where the focus of the image was varied we estimated a maximum systematic uncertainty of 10%.

The radius-time and distance-time curves obtained from image tracking were resampled using a cubic interpolation and filtered using a low-pass filter to remove high-frequency noise. The frequency components of the noise close to the frequency of oscillations cannot be removed by filtering. Therefore, we impose the radius before and after oscillations to be equal to the resting radius, or else the residual noise would give rise to an apparent acoustic radiation force. The maximum difference between the processed data and the measured data points is less than 3%. This is taken as the maximum error on the radius and distance data, and is used to estimate the error on the derived quantities. From the resampled and filtered data we compute the radial and translational velocities and accelerations.

8.4 Hydrodynamic model

The system of coordinates is shown in Fig. 8.2. We take x along the line of centers of the two bubbles with radius R_1 and R_2; the distance between the bubbles is $d = x_2 - x_1$. Buoyancy and the primary radiation force act along a direction orthogonal to x and do not affect the translation in the $x-$direction. From conservation of momentum one has the force balance in the x direction for a bubble of radius R:

$$\begin{aligned} 0 &= \rho\frac{4}{3}\pi R^3\frac{Du}{Dt} - \frac{1}{2}\rho\frac{d}{dt}\left(\frac{4}{3}\pi R^3 U\right) - 6\pi\eta RU - 6\pi\rho\sqrt{\frac{\nu}{\pi}}\int_0^t \frac{d\tau}{\sqrt{\int_\tau^t R(s)^{-2}ds}}\frac{d(RU)}{d\tau} \\ &= F_G + F_A + F_{QS} + F_H \end{aligned} \tag{8.1}$$

$U = \dot{x} - u$ is the velocity of the bubble relative to the fluid, $\dot{x}$ the velocity of the bubble relative to the laboratory frame, with the dot representing differentiation with respect to time. d/dt is the time derivative on the particle trajectory, u the velocity of the fluid, initially quiescent, generated by the dynamics of the neighboring bubble, and Du/dt is evaluated on the fluid trajectory.

The first term in the r.h.s. is the force due to the acceleration imparted to the fluid by the neighboring bubble, i.e. the radiation pressure F_G due to the secondary ultrasound wave emitted by a pulsating bubble, the pressure gradient being $\partial p/\partial x = -\rho\ Du/Dt$; if convective effects are negligible, as is the case here, it reduces to $\partial p/\partial x = -\rho\ \partial u/\partial t$. The second term is the added mass force F_A on a sphere, which is independent of the boundary condition and of the Reynolds number [125]. Note that, since R is time-dependent, the added mass force is $F_A = -1/2\ \rho\ d/dt\left(4/3\ \pi R^3 U\right) = -\pi\rho\left(2/3\ R^3\dot{U} + 2R^2\dot{R}U\right)$. The third term, F_{QS}, accounts for the quasi-steady component of the viscous force and the last term for

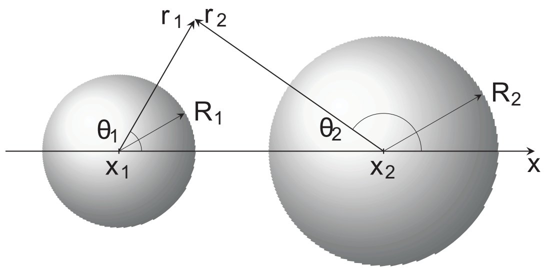

Figure 8.2: System of coordinates. R_i ($i = 1,2$) is the radius of bubble i and x_i its position on the line of centers x. $\mathbf{r}_i$ denotes the position of a fluid element relative to bubble i.

the unsteady component through the history force, F_H. A boundary condition of no-slip is assumed at the bubble interface, which is fully immobilized by the layer of surfactant molecules. The quasi-steady drag only depends on the instantaneous values of $R(t)$ and $U(t)$. The modification of the kernel of the history integral that accounts for time-dependent radius effects was first introduced by Magnaudet and Legendre for bubbles with shear-free boundary condition [123] and subsequently extended by Takemura and Magnaudet to the case of bubbles that obey a no-slip condition [130]. The integral is evaluated from the time $t = 0$ when the bubbles start oscillating. For $t < 0$ the velocity of the bubbles is zero, and so is the integral for $-\infty < t < 0$. The velocity of the fluid generated by bubble j is evaluated at the center of bubble i ($i, j = 1,2,\ i \neq j$), assuming that the other bubble is absent and that the flow is spatially uniform. The frequency of insonation $f = 2.25$ MHz corresponds to a boundary layer of thickness $\delta \sim 300$ nm, and in this study we only consider bubbles of radius $R \sim 2\ \mu$m. When the viscous boundary layer on the bubble is small with respect to the radius ($\delta \ll R$, or $\omega R^2 > \nu$), as is the case here, we may use inviscid theory for determining the flow velocity outside the boundary layer. A pulsating and translating bubble generates a fluid velocity at distance r whose potential has a contribution from a source of strength q, $\Phi_s = -q/4\pi r$, due to the radial pulsations, with the kinematic boundary condition that the velocity at $r = R$ equals $\dot{R}$, and a contribution from a dipole of strength p, $\Phi_p = -p\cos\theta/4\pi r^2$, due to the translation, with p given by the boundary condition that the velocity at $r = R$ is equal to $\dot{x}$. The fluid velocity u is the sum of the two velocities $u = u_r + u_t = \dot{R}\cos\theta\ R^2/r^2 + \dot{x}\ R^3/r^3$ ($\theta = 0,\ \pi$). If the distance between the bubbles becomes small, the assumption of uniform flow breaks down. In addition, if the wall-to-wall distance between the bubbles becomes comparable with the thickness of the boundary layer, $d - (R_1 + R_2) \sim 2\delta$, a description of the viscous dissipation in the boundary layer becomes necessary. We limit ourselves to the case $d - (R_1 + R_2) \gg 2\delta$.

By substituting in Equation 8.1 for bubble i the fluid velocity generated by bubble

j and retaining terms up to order 3 in R/d, we obtain two coupled equations of motion, identical to this order of accuracy to those obtained by other authors using a Lagrangian formalism [107, 108, 136]. The difference with previous models is in the terms that account for viscous effects, since only shear-free bubbles were considered before.

The resulting equation of motion describes the translation of a no-slip bubble for a given radial dynamics. The radial dynamics can be modeled through two coupled Rayleigh-Plesset-type equations [107, 108, 136] coupled to the translation equations. For coated bubbles this would introduce at least two fitting parameters [12, 33, 34, 36] to describe the viscoelastic properties of the coating. For most coating materials the parameters are not known with satisfactory accuracy, and may depend on the dilatational rate [41]. Therefore, we use experimental values of R_1, R_2 and their derivatives as time-dependent coefficients.

The numerical integration of the history force was treated in an approximate fashion to handle the singularity at $\tau = t$ in the kernel of the history integral:

$$\int_0^t d\tau \left(\int_\tau^t R(s)^{-2} ds \right)^{-1/2} d(RU)/d\tau.$$

The integral in the interval $[0, t-dt]$ can be evaluated using standard numerical schemes. By defining the nonlinear mapping $\theta = \int_0^\tau R(s)^{-2} ds$ we write the integral near the singularity as:

$$\int_{\theta(t-dt)}^{\theta(t)} d\theta \, (\theta(t) - \theta(t-dt))^{-1/2} \, d(RU)/d\theta.$$

Since in our experiments $d(RU)/d\theta$ varies slowly near the singularity, it can be taken as constant over the interval $[\theta(t-dt), \theta(t)]$ and the resulting integral can be evaluated analytically. We tested our approximation against the numerical scheme proposed by Chung [137], which is commonly used to compute the history integral [130, 138], and found the results to agree to within 0.5%.

8.5 Results and discussion

Fig. 8.3A and 8.3B show the time evolution of the radius of the two bubbles and the distance d between their centers. The radial pulsations are in phase with a relative radial excursion $\Delta R/R_0 < 0.3$. The positions of the centers display small translational oscillations, (typical amplitude $200 - 300$ nm) with the same frequency as the radial pulsations, around a position that slowly drifts, resulting in the net attraction expected for bubbles pulsating in phase. When the external forcing is turned off, and the radial pulsations have damped out ($t \approx 3.6\ \mu$s), the bubbles decelerate subject only to viscous drag. Fig. 8.3C and 8.3D shows the time evolution of the Reynolds numbers, $Re_r = R|\dot{R}|/\nu$ for the radial dynamics and $Re_t = R|U|/\nu$ for the translation. The values of the Reynolds numbers during the motion are below 5 for the translation and below 25 for the radial dynamics. The time averages are $\langle Re_t \rangle \approx 0.5$ and $\langle Re_r \rangle \approx 3$, respectively. Therefore, we hypothesize that high-*Re* effects can be neglected in the translational dynamics, an assumption that is confirmed *a posteriori*. We also expect that time-dependent radius effects do

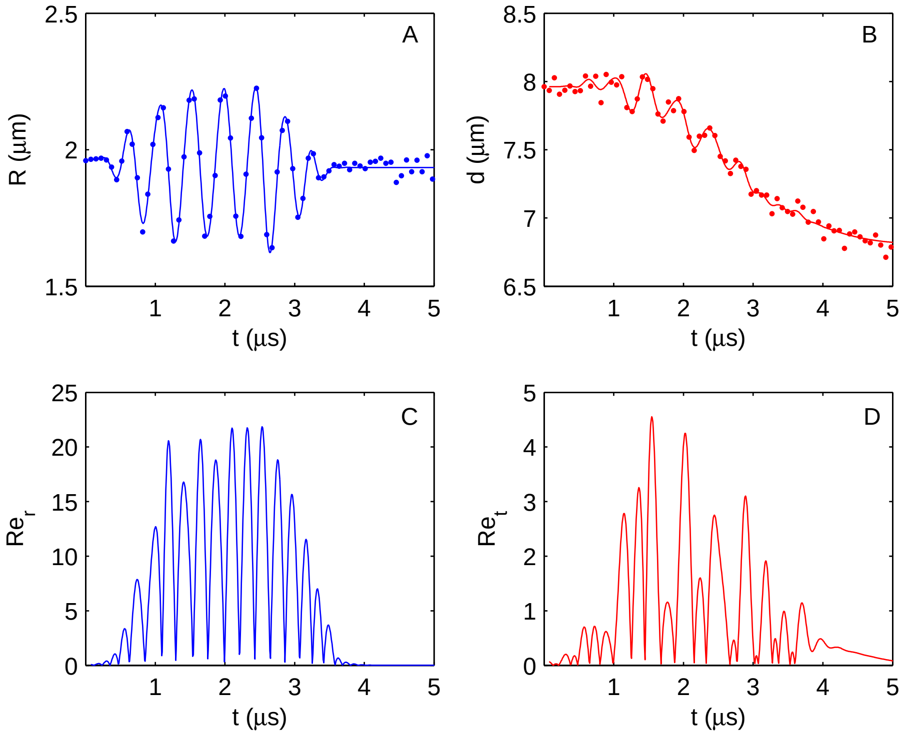

Figure 8.3: (A) Time evolution of the radii obtained by image tracking. The solid symbols represent experimental data points, and the lines the resampled and filtered radius-time curves. The bubbles oscillate in phase and have relative radial excursions $\Delta R/R_0 \sim 0.3$. (B) Time evolution of the distance between the centers, $d = x_2 - x_1$. The solid symbols represent experimental data points, and the line the resampled and filtered distance-time curve. (C-D) Time evolution of the Reynolds numbers computed from the experimental radial and translational dynamics. Only the values for bubble 1 are plotted for clarity. The radial Reynolds number $Re_r = R|\dot{R}|/\nu$ is below 25 with a time average $\langle Re_r \rangle \approx 3$. The translational Reynolds number $Re_t = R|U|/\nu$ is below 5 with a time average $\langle Re_t \rangle \approx 0.5$.

not significantly influence the transport of vorticity, but we use the version of the history force for a bubble with time-dependent radius for consistency.

Following Takemura and Magnaudet [130], we begin our analysis by determining the values of $F_A(t)$, $F_G(t)$, $F_{QS}(t)$ and $F_H(t)$ from the experimental values of $R_1(t)$, $R_2(t)$, $d(t)$ and their derivatives. We can then test the expression for the viscous force $F_{QS} + F_H$ against the value deduced from the force balance, $F_{QS} + F_H = -(F_A + F_G)$. The comparison is shown in Fig. 8.4. The value of the viscous force determined from experiment is indicated by the red line. The black line shows that the zero-*Re* expression for $F_{QS} + F_H$ shown in Equation 8.1 gives a good prediction of the viscous force. The value of F_{QS} is also plotted (blue line) to emphasize how neglecting the history force would result in a large underestimation of the total viscous force.

Since the governing equations can be linearized if convective effects are negligible, the velocity can be decomposed into its quasi-steady and oscillatory components. The oscillatory component experiences an increased viscous dissipation, since the vorticity generated at the bubble surface does not diffuse away during one period of oscillation and remains confined to the viscous boundary layer of thickness $\delta \sim \sqrt{\nu/\omega}$. The drag force experienced by an oscillating sphere can be

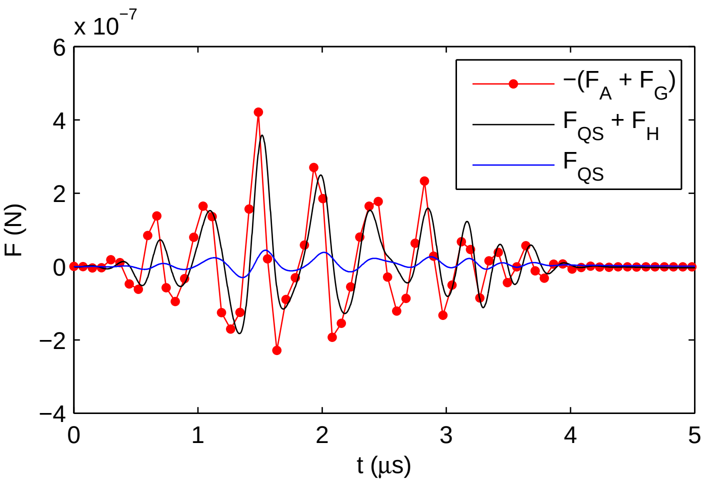

Figure 8.4: Comparison of models for the viscous force. The values are computed for one bubble from the experimental values of the radius and position and their derivatives. Red line: experimental value from the force balance $-(F_A + F_G)$. The red symbols show the values corresponding to the experimental data points. Black line: model including quasi-steady drag and history force $F_{QS} + F_H$. Blue line: a model including only quasi-steady drag F_{QS}, neglecting history force, largely underestimates viscous dissipation.

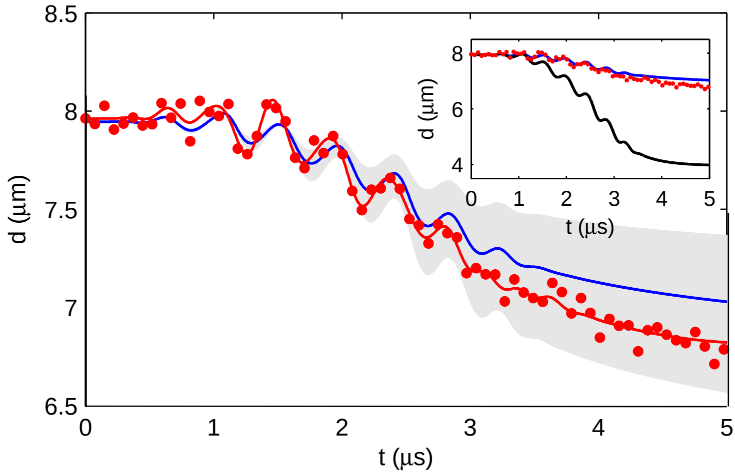

Figure 8.5: Time evolution of the distance between the centers of the bubbles. Red line: experimental value (after resampling and filtering). The red symbols are the measured data points. Blue line: prediction using the model including history force and quasi-steady drag, $F_{QS}+F_H$. The shaded area represents the tolerance ($\pm 5\%$) on the prediction due to the systematic experimental uncertainty on the resting radius of a bubble. Inset: comparison of the model including only the quasi-steady drag F_{QS} (black) with the model including history force, $F_{QS}+F_H$ (blue).

estimated, in the high-frequency limit, as $6\pi\eta(1+R/\delta)RU$ [120]. In the range of parameters of our experiments, the drag on the oscillatory component of the velocity is increased by a factor $(1+R/\delta)\sim 5$ compared to the quasi-steady value $6\pi\eta RU$. The Basset expression for the history force is only strictly valid at zero Reynolds number, or for an oscillatory motion. The main limitation in the applicability of this expression to the present case is probably the $\tau^{-1/2}$ time decay, which was observed to be too slow for a particle accelerating from rest [139] and is not strictly valid for the quasi-steady component of the velocity.

We now proceed to test the performance of the model by integrating the equations of motion and predicting the displacement of the bubbles. The experimental values of $R_1(t)$, $R_2(t)$ and their derivatives are substituted in the equations of motion as time-dependent coefficients, and the equations are integrated numerically to obtain the time evolution of $x_1(t)$ and $x_2(t)$. The agreement between the predicted displacement and the experiment is fully satisfactory, as shown in Fig. 8.5. The comparison with the result obtained by neglecting the history force (inset) emphasizes again how crucial the influence of this force is for coated bubbles as opposed to shear-free bubbles. As described in Section 8.3, for each experimental run the extracted bubble radii can differ from the true radii due to the systematic uncertainty in the imaging. To test the robustness of our findings in this respect, we compute the numerical solution for two limiting cases, $R \pm 5\%$. The solution corresponding to the true radii R_1, R_2 then lies in the shaded area in Fig. 8.5. The prediction remains highly satisfactory and the model can be used to predict the low-*Re* translation of coated bubbles of known radius due to acoustic radiation pressure.

8.6 Summary and Conclusions

We performed a time-resolved study of the translation of coated microbubbles propelled by ultrasound radiation pressure in a range of parameters that is relevant for medical ultrasound imaging. By positioning the bubbles with optical tweezers we were able to exclude the influence of confining geometries and to unambiguously identify the contributions of the several hydrodynamic forces acting on the bubbles. The use of an ultra-high speed camera operated near 15 million frames per second ensured the required temporal resolution to characterize the unsteady translation of the bubbles. We developed a point-particle model to describe the translation of bubbles subject to secondary radiation pressure due to a neighboring pulsating bubble, and found that the inclusion of the history force is crucial for a correct description of the unsteady motion of coated microbubbles. Neglecting this force results in a large underestimation of the viscous dissipation. This can be understood from the fact that the translational velocity has an oscillatory component, which experiences an increased dissipation due to the oscillatory boundary layer that develops around the bubble.

One of the limits of applicability of this model is that the bubbles should be far enough from each other so that the approximation of uniform flow holds, and dissipative effects in the boundary layer are unimportant ($d-(R_1+R_2) \gg 2\delta$). Furthermore we restricted ourselves to the case of spherical bubbles, an approximation that breaks down when the bubbles get too close. For longer insonation pulses the bubbles are often observed to lose their spherical symmetry, with non-spherical oscillations arising as a parametric instability [85]. Viscous effects are then more difficult to account for [140].

9 Dynamics of coated bubbles adherent to a wall[1]

Molecular imaging with ultrasound is a promising non-invasive technique for disease-specific imaging, enabling for instance the diagnosis of thrombus and inflammation. Selective imaging is performed by using ultrasound contrast agents containing ligands on their shell, which bind specifically to the target molecules. Here, we investigate the influence of adherence on the dynamics of the microbubbles, in particular on the frequency of maximum response, by recording the radial response of individual microbubbles as a function of the applied acoustic pressure and frequency. The frequency of maximum response of adherent microbubbles was found to be over 50% lower than for bubbles in the unbounded fluid and over 30% lower than that of a bubble in contact with the wall. The change is caused by adhesion of the bubbles to the wall as no influence was found solely by the presence of the targeting ligands on the bubble dynamics. The shift in the frequency of maximum response may prove to be important for molecular imaging applications with ultrasound as these applications would benefit from an acoustic imaging method to distinguish adherent from freely circulating microbubbles.

[1]M. Overvelde, V. Garbin, B. Dollet, N. de Jong, D. Lohse, and M. Versluis

9.1 Introduction

The use of ultrasound contrast agents in medical imaging with ultrasound is well established. The contrast agent is injected intravenously and is designed to enhance the contrast of the blood pool. The most common ultrasound contrast agent (UCA) is composed of a suspension of microbubbles (radius 1-5 μm), which are coated with a phospholipid, albumin or polymer shell. The coating reduces the surface tension σ and therefore the capillary pressure $2\sigma/R$. Moreover the coating increases the diffusive timescales and the combined effect prevents the bubble from quickly dissolving in the blood.

A promising application is non-invasive molecular imaging for selective diagnosis with ultrasound using ultrasound contrast agents. The ultrasound contrast agent microbubbles contain targeting ligands that bind to selective biomarkers on the membrane of endothelial cells, which constitute the blood vessel wall. A series of challenges are encountered in the development of targeted microbubbles for molecular imaging applications. The first question, as was stated by Lindner [8], is whether bubbles adhering to a target cell produce strong enough acoustic signals. It was found that the response of adherent microbubbles is comparable to that of phospholipid-coated microbubbles [96, 97]. However, it remains to be seen if the concentration of adherent microbubbles *in vivo* will be high enough to produce signals in the order of normal contrast-enhanced ultrasound in perfusion imaging. In the extreme limit even the signal of a single bubble must be detected. Another challenge that has received significant attention is the adhesion of the bubbles to the vessel wall under shear flow. Primary radiation force has been used to effectively push the bubbles towards the vessel [132, 141–144]. New biochemical engineering of the ligands has lead to a method to increase the number of adherent microbubbles. The use of two distinct antibody-receptor pairs has been proposed [145], as well as the use of a polymeric version of the ligand to increase the ligand surface density [146, 147], and the use of increasing the length of the spacer arm [148]. Finally, one would be able to distinguish adherent microbubbles from freely circulating ones [8]. The simplest approach is to wash-out all the freely circulating microbubbles and image the remaining bubbles. The disadvantage is that it takes 5 to 10 minutes before all freely circulating bubbles are cleared by the liver and that there is no new supply of bubbles. Therefore it would be beneficial to distinguish acoustically between adherent and freely circulating microbubbles. Considerable changes between adherent and non-adherent microbubbles were found, such as a decrease in the acoustic response of adherent microbubbles with respect to non-adherent microbubbles [96] and a change in the spectral response [97]. In chapters 6 and 7 of this thesis it was shown that the close proximity of a wall changes the bubble dynamics. As the bubbles circulate freely in the blood vessel, their position with respect to the wall is unknown. Therefore it is important to understand the influence of adherence to a wall on the bubble dynamics. Furthermore, we would like to investigate under what conditions the response of adherent and freely circulating can be differentiated, as to optimize them for pulse-echo techniques.

Here, we investigate the change in the dynamics of adherent microbubbles with respect to bubbles in the unbounded fluid. In Sec. 9.2 we describe the setup, experimental methods and the preparation of the bubbles. The influence of targeting ligands, the proximity of the wall, and the adhesion to the wall at the frequency of maximum response and the amplitude of oscillation will be shown and discussed in the Sec. 9.3. The conclusions and an outlook on future experiments are given in Sec. 9.4.

9.2 Experimental methods

9.2.1 Setup

Fig. 9.1 shows a schematic drawing of the experimental setup. An OptiCell chamber was mounted in a water tank and connected to a 3D micropositioning stage. The water tank was mounted on a planar-stage and was designed to hold an illumination fiber and the ultrasound transducer (PA168, Precision Acoustics). The driving pulse for the transducer was generated by an arbitrary waveform generator (8026, Tabor Electronics) and amplified by a RF-amplifier (350L, ENI). The sample was imaged through an upright microscope equipped with a water-immersed 100× objective (Olympus). The dynamics of individual microbubbles was captured with the ultra high-speed camera Brandaris 128 [39] at a framerate of 14 million frames per second (Mfps). An optical tweezers setup allowed for the positioning of a single microbubble in 3D [58]. The infrared laser beam of the optical tweezers was coupled into the microscope using a dichroic mirror. The optical trap was formed through the imaging objective. The setup combining the Brandaris 128 camera with optical tweezers is described in detail chapter 6 and 7.

The bubbles were insonified with an ultrasound burst of 10 cycles whose first and last 3 cycles were tapered with a Gaussian envelope. To scan the frequency with a constant acoustic pressure , the transducer was calibrated prior to the experiments with a needle hydrophone (HPM02/1, Precision Acoustics). To align the acoustic focus of the transducer and the optical focus of the objective the OptiCell was removed, the tip of the hydrophone was positioned in the focus of the objective, and the transducer was aligned with the planar-stage. The 3D-stage connected to the OptiCell chamber allowed for the movement of the sample independently of the transducer to keep the acoustical and optical focus aligned.

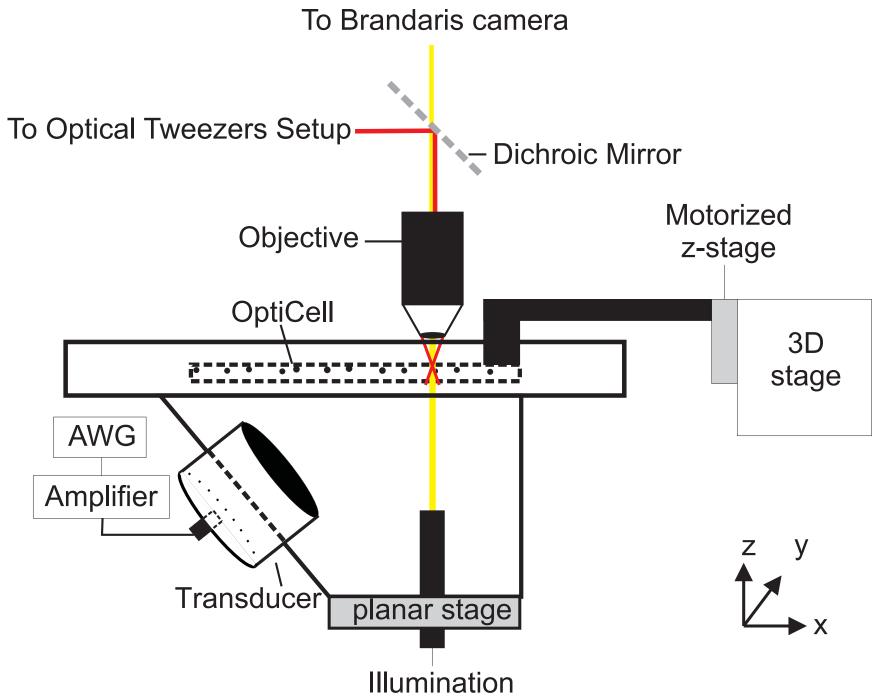

Figure 9.1: Schematic drawing of the experimental setup. The solution containing contrast agent microbubbles is injected in an OptiCell chamber. The chamber is located in a water tank which holds the transducer and illumination fiber. The driving ultrasound pulse is produced by an arbitrary waveform generator (AWG), amplified, and sent to the transducer. The bubbles are imaged and manipulated with optical tweezers through the same 100× objective.

The experimental protocol is based on the microbubble spectroscopy method by Van der Meer *et al.* [41]. Each resonance curve is a result 12 movies with the Brandaris 128 camera with increasing frequencies at constant acoustic pressure. The experiment was repeated several times for increasing acoustic pressure on the very same bubble, until the full parameter space of acoustic pressure and frequency ranges was covered. Control experiments to confirm that the bubble properties were not altered by this protocol of repeated insonations can be found in Chapter 3.

Far from the wall

Individual microbubbles were trapped with the optical tweezers and positioned away from the OptiCell wall to study their dynamics in the approximation of unbounded fluid. A motorized stage (M110-2.DGm, PI) was used to accurately control the distance between the bubble in the trap and the OptiCell wall. In all experiments the minimum distance between the bubble and the wall was 100 μm. The laser trap was turned on during the experiments to prevent the bubbles from rising out of the optical focus due to buoyancy. In chapter 7 it was demonstrated that the laser trap does not influence the radial dynamics of the bubbles. Twelve movies of 128 frames were recorded in 2 runs with the Brandaris camera. The second run started after the data of the first run was transferred to the computer. The time between the two runs is of the order of 20 s and the time between two movies is 80 ms. The bubble was insonified with a ultrasound pulse at 12 different frequencies and at constant acoustic pressure.

At the wall

The optical tweezers were not used for the experiments on the bubbles in contact with the wall and those adherent to the wall. During these experiments the Brandaris camera was running in a segmented mode, which allowed us to record 12 movies of 64 frames in a single run. The time between the movies was 80 ms. No ultrasound was applied during the first movie. In the consecutive 11 movies the insonation frequency was changed while the pressure was kept constant.

9.2.2 Analysis

Each movie captures the radial dynamics at a single acoustic pressure and frequency. The radius-time curve (*R(t)*-curve) of the bubble was determined by tracking the contour of the bubble in each frame with a code programmed in Matlab®.
Fig. 9.2A shows a typical oscillation of a bubble (blue) with a radius $R_0 = 2\ \mu$m insonified with an ultrasound pulse at a frequency $f = 1.7$ MHz and at an acoustic pressure $P_a = 37.5$ kPa. The compression phase of the oscillations is larger than the expansion phase, which refers to the so-called “compression-only” behavior of an oscillating bubble [10], which results in a low frequency component (red) during insonation. For the analysis we use the relative excursion near the fundamental frequency ε_1, see Fig. 9.2B. As there are minor amplitudes of higher harmonics observed in the spectral responses, only the lower frequency components are removed, for more information see chapter 4. The maximum radial excursion A_1 is defined as:

$$A_1 = \frac{\varepsilon_1^{\max} - \varepsilon_1^{\min}}{2}, \qquad (9.1)$$

where $\varepsilon_1^{\max}$ is the maximum relative expansion and $\varepsilon_1^{\min}$ the minimum relative expansion, see Fig. 9.2B.
The absolute error in the radial oscillations is 40 nm, see chapter 8. For a typical bubble with a radius $R_0 = 2\mu$m, $A_1^{\text{noise}} \approx 0.02$. We use the non-dimensional

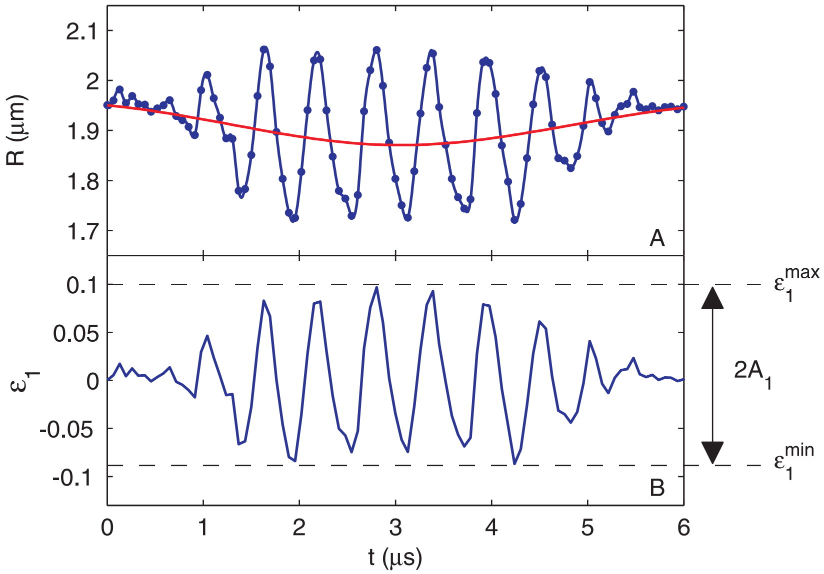

Figure 9.2: A) Experimental radius-time (*R(t)*) curve (blue) of a BR-14 microbubble $R_0 = 2\ \mu$m insonified with an acoustic pressure $P_a = 37.5$ kPa and a frequency $f = 1.7$ MHz and the low frequency response ε_0 (red). B) The relative fundamental response ε_1.

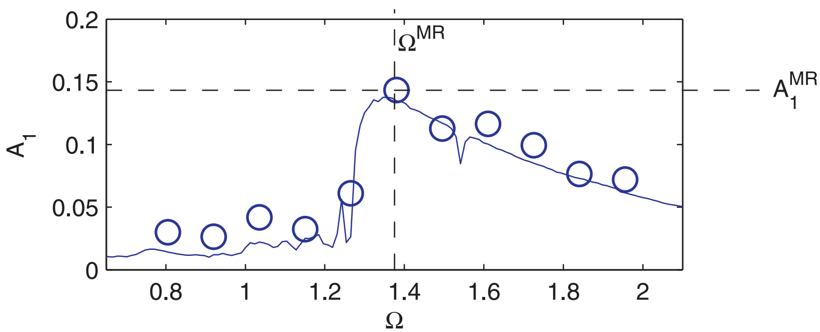

Figure 9.3: Experimental resonance curve (circles), A_1 as a function of Ω. The bubble has a radius $R_0 = 2\ \mu$m and is insonified with an acoustic pressure $P_a = 32.5$ kPa. We obtain the frequency of maximum response Ω_{MR} and the maximum relative response A_1^{MR} from the resonance curve. The simulations are performed with the shell buckling model [12] (line). The shell parameters are $\chi = 2.5$ N/m, $\kappa_s = 5 \cdot 10^{-9}$ kg/s, and $\sigma(R_0) = 0.025$ N/m.

frequency Ω to compare the results with the well-known response of an uncoated bubble:

$$\Omega = \frac{f}{f_0^{\mathrm{unc}}} \tag{9.2}$$

with the eigenfrequency of the uncoated bubble [29, 30]:

$$f_0^{\mathrm{unc}} = \frac{1}{2\pi}\sqrt{\frac{1}{\rho R_0^2}\left(3\kappa P_0 + (3\kappa - 1)\,\frac{2\sigma_w}{R_0}\right)} \tag{9.3}$$

The frequency of maximum response Ω_{MR} and the maximum relative amplitude of oscillation A_1^{MR} is obtained from the resonance curves, A_1 as a function of Ω, see Fig. 9.3.

9.2.3 Preparation

The experimental contrast agents BG-6437 and BG-6438 (Bracco S.A., Geneva, Switzerland) were prepared following the protocol described below. The BG-6437 bubbles were prepared by injecting 1 ml of sterile saline (BBraun, 0.9% Sodium Chloride) through the rubber cover of the vial, while a second needle was used for venting the excess pressure. The vial was shaken for 5-10 s and the suspension was left to rest for 5 minutes. BG-6438 is similar to BG-6437 while the shell contains streptavidin. The BG-6438 microbubbles were reconstituted following the same protocol (0.7 ml of sterile saline). A solution of biotinylated anti-fluorescein antibody (anti-FITC, 10 μg in 300 μl of saline solution) was injected through the rubber cover of the reconstituted vial, while venting the excess pressure. The vial was shaken and incubation took place for 10 minutes at room temperature. All prepared microbubbles were used within the same day.

The OptiCell was coated in the following manner. Fluorescein-labeled bovine serum albumin (FITC-BSA) was diluted in phosphate-buffered saline (PBS, pH 7.4, GIBCO, 10010023) to a concentration of 0.1 mg/l. The OptiCell was filled with this solution and incubation took place overnight at room temperature. Before usage, the OptiCell was rinsed 3 times with PBS and finally it was filled with 10 ml of sterile saline solution.

9.2.4 Method

We investigated the radial dynamics of 2 different types of UCA microbubbles for a total of 4 different situations. The dynamics of a phospholipid-coated BG-6437 microbubble was measured far away from the wall to obtain the viscoelastic parameters of the shell [12], see Fig. 9.4A. To investigate the influence of antibodies on the dynamics of phospholipid-coated microbubbles the results were compared to the functionalized BG-6438 microbubbles, see Fig. 9.4B. In the experiment these microbubbles were positioned far away from the wall to exclude the influence of the boundary. In the third experiment the BG-6437 microbubble was in contact with the wall, see Fig. 9.4C. The results of a BG-6437 bubble at the wall and in free space were compared to confirm the influence of the boundary as discussed in chapter 7. In the previous three experiments the bubbles were injected in an uncoated OptiCell. In the fourth experiment the functionalized BG-6438 microbubbles adhere to the inside of an OptiCell coated with BSA-FITC solution. The schematic of this situation is shown in Fig. 9.4D and in the following these bubbles are referred to as adherent bubbles.

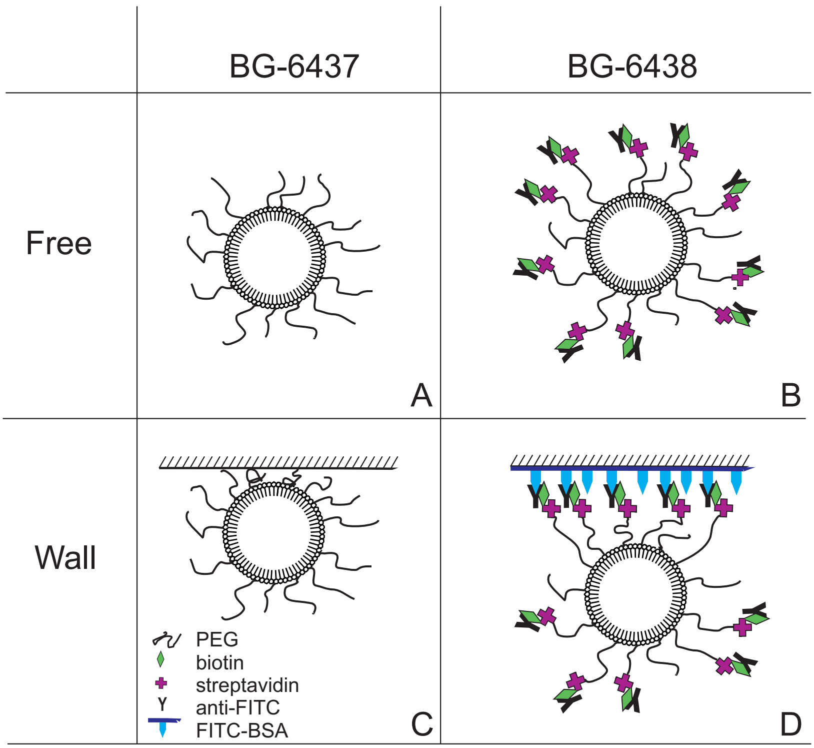

Figure 9.4: Schematic drawing of the 4 experimental situations. A) Phospholipid coated microbubble away from the wall. B) Functionalized microbubble away from the wall. C) Phospholipid bubble floating at the OptiCell wall. D) Functionalized microbubble adherent to the FITC-BSA coated wall.

9.3 Results and discussion

Fig. 9.5A shows the frequency of maximum response Ω_{MR} as a function of the maximum amplitude of oscillation A_1^{MR}. The results for a phospholipid-coated microbubble (circles) are compared to a functionalized microbubble (squares). The radius of both microbubbles is 2.0 μm and the applied pressure and frequency are scanned to recover the full parameter space from $P_a = 15$ to 45 kPa and from $f = 1.2$ to 4 MHz. The bubbles are located in the unbounded fluid at a distance of 150 μm from the OptiCell wall.

We observe a decrease in Ω_{MR} with increasing P_a. At small amplitude oscillations $A_1^{MR} \approx 0.05$ the frequency of maximum response is $\Omega_{MR} \approx 2$. For larger amplitude of oscillation $A_1^{MR} > 0.15$ the frequency of maximum response tends to converges to $\Omega_{MR} = 1.3$. The obtained frequency of maximum response is very similar to the frequency Ω_{MR} of phospholipid-coated BR-14 microbubbles, see chapter 3. Simulations with the shell-buckling model (see details in chapter 3) are depicted in Fig. 9.5A and are in good agreement with the experimental results, except maybe at an amplitude $A_1^{MR} > 0.15$ where a small deviation is encountered.

The relative amplitude of oscillation at Ω_{MR} as a function of the driving pressure P_a is shown in Fig. 9.5B. The smallest oscillations are observed at an acoustic pressure $P_a = 20$ kPa. The increase of the maximum amplitude of oscillation with the acoustic pressure is very similar for phospholipid-coated microbubbles and func-

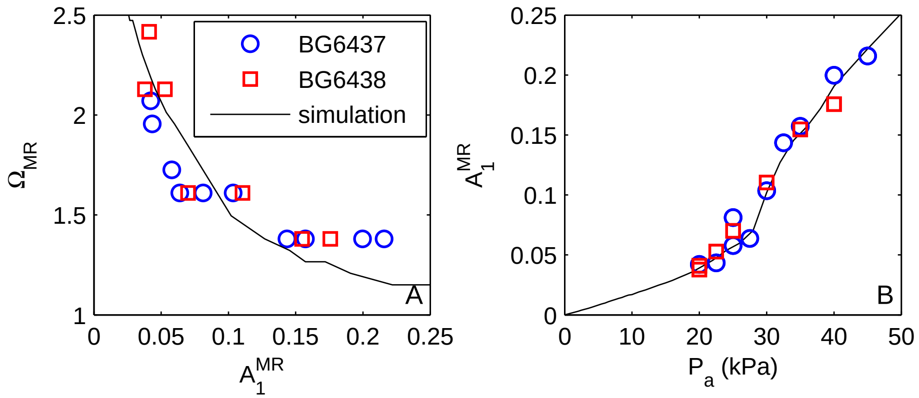

Figure 9.5: Response of a phospholipid-coated microbubble (BG-6437) and a functionalized microbubble (BG-6438) in the unbounded fluid, both with an radius $R_0 = 2$ μm. The simulations are performed with the shell buckling model [12]. The shell parameters are $\chi = 2.5$ N/m, $\kappa_s = 5 \cdot 10^{-9}$ kg/s, and $\sigma(R_0) = 0.025$ N/m. A) The frequency of maximum response Ω_{MR} as a function of the amplitude of oscillation A_1^{MR}. B) A_1^{MR} as a function of the applied acoustic pressure P_a.

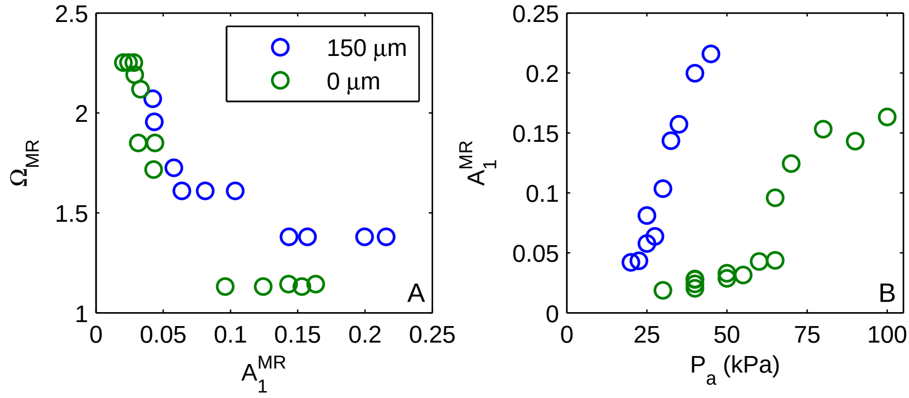

Figure 9.6: Response of a phospholipid-coated microbubble (BG-6437) with a radius $R_0 = 2$ μm far away from the wall ($d_{\text{wall}} = 0$ μm, blue) and the response of a BG-6437 bubble with a radius $R_0 = 2.1$ μm at the wall ($d_{\text{wall}=0}$ μm, green). A) The frequency of maximum response Ω_{MR} as a function of the amplitude of oscillation A_1^{MR}. B) A_1^{MR} as a function of the applied acoustic pressure P_a.

tionalized microbubbles. The nonlinear increase of the amplitude A_1^{MR} with pressure is in excellent agreement with the prediction of the shell-buckling model [12]. The shell parameters are $\chi = 2.5$ N/m, $\kappa_s = 5 \cdot 10^{-9}$ kg/s, and $\sigma(R_0) = 0.025$ N/m, which is comparable to the values used for BR-14 microbubbles. We therefore conclude that the ligands do not influence in any way the frequency of maximum response and the maximum amplitude of oscillation of phospholipid-coated microbubbles.

Fig. 9.6A shows the frequency of maximum response as a function of the amplitude A_1^{MR} for a phospholipid-coated bubble at a distance of 150 μm away from the wall (blue circles) and for a phospholipid-coated microbubble in contact with the wall (green circles). The influence of the wall on the frequency of maximum response is most noticeable at an amplitude $A_1^{\text{MR}} > 0.15$, where Ω_{MR} reaches an almost constant value. This “plateau” is reached for the bubble in free space at $\Omega_{\text{MR}} = 1.3$ and for the bubble at the wall the frequency of maximum response is 20% lower $\Omega_{\text{MR}} = 1.1$. Fig 9.6B shows the amplitude of oscillation A_1^{MR} at Ω_{MR} as a function of P_a for both cases: at the wall and away from the wall. The maximum amplitude of oscillation A_1^{MR} of the bubble in free space increases rapidly with increasing pressure, reaching an amplitude $A_1^{\text{MR}} = 0.15$ at a pressure $P_a = 37.5$ kPa, while the bubble at the wall reaches the same amplitude of oscillation only for a much higher pressure $P_a = 80$ kPa. The results are in good agreement with the results found in chapter 7, where we found a decrease of about 20% in Ω_{MR} and a decrease of 50% in the response A_1^{MR}, respectively.

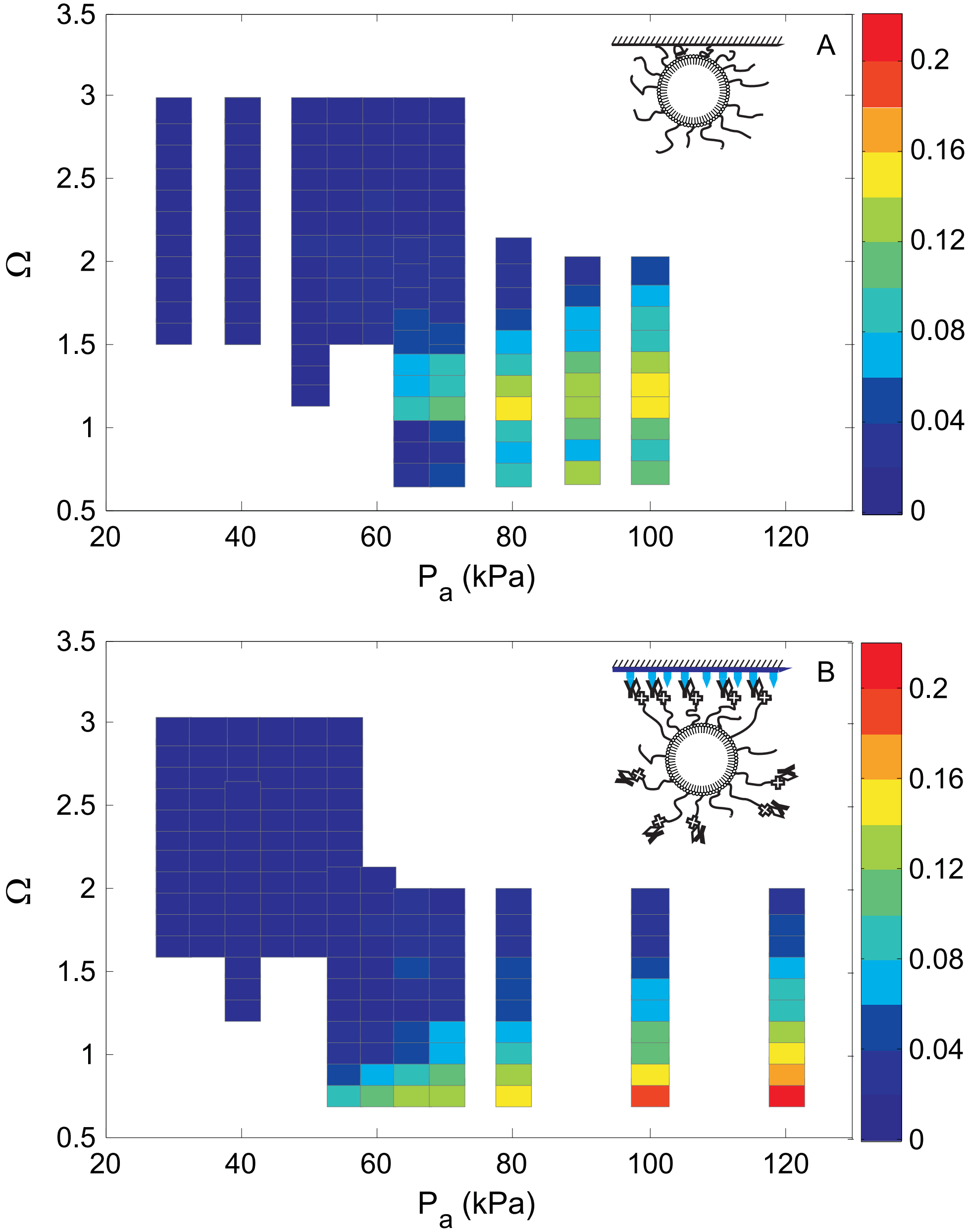

Figure 9.7: The relative amplitude of oscillation A_1 as a function of the acoustic pressure P_a and frequency Ω. A) The response of a bubble $R_0 = 2.1$ μm in contact with the wall. B) The response of a bubble $R_0 = 2.2$ μm adherent to the wall.

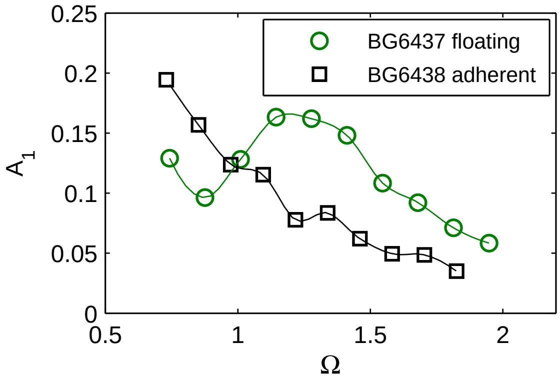

Figure 9.8: Resonance curve of a phospholipid-coated bubble (BG-6437) in contact with the wall (green) and a functionalized bubble (BG-6438) adherent to the wall (black) insonified with a pressure $P_a = 100$ kPa. The resonance curves are obtained from Fig. 9.7.

Each frequency of maximum response is obtained from the radial response of a bubble insonified with at least 11 subsequent frequencies. The experiment is then repeated for different acoustic pressures. The response of the bubble A_1 is shown in the iso-contour plot in Fig. 9.7 for the full set of applied pressures and frequencies. The response of a phospholipid-coated microbubble with a radius $R_0 = 2.1\mu$m at the wall (A) is compared to the response of a microbubble with similar radius $R_0 = 2.2$ μm adherent to the wall (B). As observed in Fig. 9.6A, the frequency of maximum response Ω_{MR} of the bubble in contact with the wall decreases with increasing pressure as shown in Fig. 9.7, reaching a frequency $\Omega_{\text{MR}} = 1.1$ at a pressure $P_a \geq 65$ kPa. For the bubble adherent to the wall the highest response is observed at the lowest applied frequency $\Omega = 0.7$ at acoustic pressures $P_a \geq$ 55 kPa. Due to the limited bandwidth of the transducer the bubbles could not be insonified at even lower frequencies and the exact frequency of maximum response could therefore not be obtained for the bubble adherent to the wall.

The resonance curves of the bubble in contact with the wall and those of the adherent bubble shown in Fig. 9.7 are compared in Fig. 9.8. The acoustic pressure is 100 kPa. We observe that the amplitude of oscillation of the adherent bubble at $\Omega = 0.7$ (which we already indicated above, is not its frequency of maximum response) is already 25% higher than the amplitude A_1^{MR} of the bubble at the wall. Comparing the frequency of maximum response of the adherent bubble $\Omega_{\text{MR}} \leq 0.7$ with the bubble in the unbounded fluid $\Omega_{\text{MR}} = 1.4$ a decrease is observed of at least 50%. A second adherent bubble was present in the field of view (distance $d =$ 15 μm $\approx$ $7R_0$). Therefore we performed simulations to verify if this remarkable difference was due to the interaction with the second bubble. The simulations show that the neighboring bubble decreases the frequency of maximum response with 6% and consequently it cannot account for the 50% change in response.

We now try to interpret the observed change in response by drawing the analogy with the harmonic oscillator model (see e.g. [29]). An oscillating bubble can be thought of as a harmonic oscillator, where the inertia ("mass" m of the oscillator) is due to the surrounding fluid that is displaced, and the restoring force (with "spring" constant k) comes from the gas inside the bubble that is compressed. For a coated bubble, the dilatation and compression of the viscoelastic coating contributes to the stiffness of the system. The bubble-wall interaction can be modeled through the method of images [32]. The wall is replaced by an "image" bubble, which mirrors the dynamics of the real bubble and generates a flow that, by canceling out the primary flow, satisfies the zero normal velocity condition at the wall. The oscillations of the image bubble effectively result in an increased "mass" of the system, and therefore in a decrease of the eigenfrequency $\omega_0 = \sqrt{(}k/m)$ of about 20% for a perfectly rigid wall. The much larger decrease of the frequency of maximum response for a bubble adherent to a wall can be interpreted as a larger decrease in k/m. Following the linear approach, we can see the bubble adherent to the wall as two coupled harmonic oscillators. The coupling can cause a change in the total k/m as well as a change in the total damping. However, the microscopic mechanisms that cause the decrease in the frequency of maximum response remain unclear at this stage.

Future research on adherent bubbles at lower insonation frequencies must be performed to reveal frequency of maximum response of the adherent bubble. Furthermore, increased statistics and additional control experiments are required (negative control) where the functionalized bubbles are positioned at an uncoated OptiCell wall and vice versa phospholipid-coated bubbles at a target-ready OptiCell wall. Finally, in this research the focus was on bubbles with a radius $R_0 \approx 2\mu$m, which is relatively large with respect to the mean radius of the bubble solution. The dynamics of smaller ultrasound contrast agent microbubbles should be investigated to see whether they respond similarly to the applied ultrasound.

9.4 Conclusions and outlook

We investigated the influence of adhesion of a functionalized bubble to a target membrane on its frequency of maximum response and amplitude of oscillation. The bubble dynamics in the unbounded fluid was unchanged for bubbles containing with targeting ligands as compared to phospholipid-coated microbubbles alone. Comparing the response of functionalized bubbles in the unbounded fluid with the response of an adherent bubbles a decrease of over 50% of the frequency of maximum response was observed for the adherent microbubbles. The frequency of maximum response of a phospholipid-coated bubble floating at the OptiCell wall was observed to decrease with 20%, which is in excellent agreement with the results found in chapter 7. This finding might prove useful for developing image protocols to discriminate between adherent and freely circulating bubbles.

10 Conclusion and outlook

Bubbles are ideal ultrasound contrast agents because of their high scattering cross-section, which is 9 orders of magnitude higher than of a solid particle of the same size. Moreover bubbles scatter ultrasound nonlinearly, which boosts the contrast-to-tissue ratio through the use of elegant pulsing schemes such as those used in pulse inversion and power modulation imaging. It was always believed that damping as a result of the viscoelastic bubble coating, which was added to prevent the bubbles from quickly dissolving in the blood, would reduce the bubble response and suppress the nonlinear bubble echoes.

There has been extensive experimental evidence that the behavior of coated bubbles is much more nonlinear than expected from theoretical considerations. These include the observations of "compression-only" behavior [10], strong subharmonic response at low acoustic driving [7, 47, 59], and the "thresholding" behavior [11]. In this thesis it was shown that the nonlinear behavior of the phospholipid monolayer is responsible for many of the observed nonlinear bubble dynamics phenomena. We show that the shell-buckling model of Marmottant *et al.* [12], which includes an elastic regime as well as buckling and rupture of the shell, captures in detail the nonlinear echo responses. The key factor turned out to be the initial surface concentration of phospholipids at the bubble surface, which in the model is expressed in the effective surface tension $\sigma(R_0)$ at rest. A bubble with a relatively low surfactant concentration behaves elastically, at least initially, and shows a strong decrease of the frequency of maximum response for increasing acoustic pressures. This leads to a pronounced skewness of the resonance curve, which we show to be the origin of the "thresholding" behavior (Ch. 3). On the other hand, a bubble with a high packing of surfactants, such that the interface will buckle upon compression, shows a strong "compression-only" behavior (Ch. 4), as well as subharmonics (Ch. 5). The other two shell parameters, the shell elasticity χ and the dilatational viscosity κ_s, have a minor influence and change only qualitatively the observed nonlinear phenomena.

We have shown that the elastic regime of the coating of the bubble is only of the order of 1% of the resting radius of the bubble R_0. For a bubble with $R_0 = 3\ \mu$m, this corresponds to a change of only 30 nm, which falls within the noise level of our optical high-speed camera Brandaris 128 and acoustic detection likewise. We can therefore conclude that if bubble oscillations were to be observed, in principle the shell behavior is then no longer purely elastic. The coating was also observed to influence the dynamics primarily below the frequency of maximum response and at low amplitude oscillations.

We also show that the proximity of a wall changes the bubble dynamics. The bubble-wall interaction decreases the frequency of maximum response and the amplitude of oscillation at the frequency of maximum response (Ch. 6 and 7). Nonetheless, all observed nonlinear phenomena are a result of the nonlinear behavior of the bubble coating. The previously mentioned nonlinear bubble dynamics, subharmonics, “compression-only” and “thresholding” behavior can be identified in experiments performed while the bubbles are in contact with the wall. This means that in the description of bubble-wall interactions the frequency or pressure may change at which the phenomena occur as a result of the presence of the wall, or an acoustic image bubble, the nonlinearities are still governed by the behavior of the phospholipid shell. We also show that once the bubble is driven below its frequency of maximum response, where the coating strongly increases the nonlinear behavior, a small change of the driving pressure as a result of the position of the bubble with respect to the wall allows for an extremely sensitive evaluation of the bubble-wall interaction. Moreover we quantify the sound radiated by an oscillating bubble which causes a secondary radiation force on neighboring bubbles and we show that the history force plays a major role in the translational dynamics of coated bubbles (Ch. 8).

In a pilot study we show that the frequency of maximum response of bubbles bound to a target substrate was decreased by 30% as compared to a bubble floating up freely, but in contact with the substrate. At this stage the microscopic details of the targeting mechanism remain unexplored and future research may reveal the intrinsic properties of the targeting strategies for adherent microbubbles designed for molecular imaging with ultrasound.

In medical ultrasound imaging there is an ongoing effort related to the clinical requirement to resolve in more and smaller details the acquired images. By increasing the ultrasound driving frequency the image resolution can be increased at the expense of loss of penetration depth. Moreover an increase of the frequency requires the use of smaller bubbles in contrast-enhanced ultrasound imaging, while in this thesis the focus was on the larger contrast microbubbles within the size distribution of the sample, for smaller bubbles the dilatational viscosity becomes more important and it is quite likely that the smallest bubbles are critically damped or even overdamped. The dynamics can therefore change drastically and it is important to explore the parameter space for these smaller bubbles.

In this thesis the general phenomena were well predicted with a constant dilation viscosity. On the other hand, we have shown (Ch. 3) that for the typical values for the shell viscosity used here, a constant dilatational viscosity κ_s would predict oscillations that decay gradually with time after the ultrasound has been switched off, while these oscillations are not observed experimentally. Van der Meer *et al.* [41] found a decrease in the dilatational viscosity of the coating with increasing dilation rate, which could support also the above observations. Furthermore, it is expected that not only the shell elasticity, but also the shell viscosity of the coating depends on the state of the shell, i.e. whether it is elastic, buckled, or ruptured. And as said, for the larger bubbles studied in this thesis the relative contribution of the shell viscosity can be small, for smaller bubbles the viscous contribution can be important, if not dominant.

All single bubble dynamics experiments presented in this thesis were performed in an *in-vitro* setup in a chamber filled with a saline solution at room temperature. Here, we briefly discuss the potential changes when the microbubbles would be injected intravenously in an *in-vivo* application. As blood has a higher liquid viscosity the bubble oscillations will be more damped. On the other hand, the shell viscosity contributes to 75% of the total damping, hence we expect very little change as a result of viscous damping of the liquid. The influence of the temperature on the bubble dynamics has been investigated and described by Vos (PhD thesis 2010). The nonlinear shell behavior such as "compression only" behavior and "thresholding" behavior were still observed at body temperature, which indicates that the shell still behaves as described by the shell-buckling model by Marmottant *et al.* [12]. UCA microbubbles injected in blood will be surrounded by red blood cells which will cause an interaction between the bubbles and the cells. Moreover, in narrow vessels there will be a strong interaction with the endothelial wall, including its associated boundary layer flow. And while the pressure in the vasculature periodically changes during the cardiac cycle, its effect on the ambient radius of the bubble, consequently on the local surfactant concentration at the bubble interface will modulate the effective surface tension of the bubble and its dynamics. In fact, this highly sensitive feature of the bubble coating can be applied for an *in-vivo* non-invasive local pressure measurement [59, 149].

Our detailed knowledge of the nonlinear shell behavior has introduced us to the explanation of new nonlinear bubble dynamics such as the "thresholding" behavior and subharmonics, which can be exploited by pulse-echo techniques to increase the contrast-to-tissue ratio. Power modulation would benefit from "thresholding" behavior. Power modulation imaging for instance would benefit tremendously from the "thresholding" behavior. As power modulation was already proven to be beneficial for perfusion imaging at low mechanical index, e.g. [150], the question arises whether we were not using the “thresholding” behavior of contrast bubbles already. Subharmonic imaging will benefit from the strong subharmonics produced by a “buckled” bubble. The frequencies and pressures used for medical ultrasound imaging can be optimized numerically with the use of the shell-buckling model and thereby improve the current pulsing schemes for power modulation, pulse inversion and subharmonic imaging. Altogether, we now have the excellent opportunity to develop new pulsing schemes with improved sensitivity and specificity.

Bibliography

[1] L. T. Szabo. *Diagnostic ultrasound imaging*. Elsevier Academic Press, London, 2004. ISBN 0126801452.

[2] D. Kish. Echo vision: The man who sees with sound. *New scientist*, 2703, 2009.

[3] R. Gramiak and P. Shah. Echocardiography of the aortic root. *Invest. Radiol.*, 3:356 366, 1968.

[4] A. Bouakaz, S. Frigstad, F. J. ten Cate, and N. de Jong. Super harmonic imaging: a new imaging technique for improved contrast detection. *Ultrasound Med. Biol.*, 28(1):59 – 68, 2002.

[5] D. Hope Simpson, C. T. Chin, and P. N. Burns. Pulse inversion doppler: a new method for detecting nonlinear echoes from microbubble contrast agents. *IEEE Trans. Ultrason. Ferroelec. Freq. Contr.*, 46(2):372–382, 1999.

[6] G. A. Brock-Fisher, M. D. Poland, and P. G. Rafter. Means for increasing sensitivity in non-linear ultrasound imaging systems. US patent no. 5577505, 1996.

[7] P. M. Shankar, P. D. Dala Krishna, and V. L. Newhouse. Advantages of subharmonic over second harmonic backscatter for contrast-to-tissue echo enhancement. *Ultrasound Med. Biol.*, 24(3):395–399, 1998.

[8] J. R. Lindner. Microbubbles in medical imaging: current applications and future directions. *Nat. Rev. Drug Discov.*, 3:527–533, 2004.

[9] A. L. Klibanov. Microbubble Contrast Agents: Targeted ultrasound imaging and ultrasound-assisted drug-delivery applications. *Invest. Radiol.*, 41(3): 354–362, 2006.

[10] N. de Jong, M. Emmer, C. T. Chin, A. Bouakaz, F. Mastik, D. Lohse, and M. Versluis. “Compression-Only” behavior of phospholipid-coated contrast bubbles. *Ultrasound Med. Biol.*, 33(4):653–656, 2007.

[11] M. Emmer, A. Van Wamel, D. E. Goertz, and N. de Jong. The onset of microbubble vibration. *Ultrasound Med. Biol.*, 33(6):941–949, 2007.

[12] P. Marmottant, S. M. van der Meer, M. Emmer, M. Versluis, N. de Jong, S. Hilgenfeldt, and D. Lohse. A model for large amplitude oscillations of coated bubbles accounting for buckling and rupture. *J. Acoust. Soc. Am.*, 118(6):3499–3505, 2005.

[13] L. Rayleigh. On the pressure developed in a liquid during the collapse of a spherical cavity. *Philos. Mag.*, 34:94–98, 1917.

[14] M. S. Plesset. The dynamics of cavitation bubbles. *J. Appl. Phys.*, 16: 277282, 1949.

[15] B. E. Noltingk and E. A. Neppiras. Cavitation produced by ultrasonics. *Proceedings of the Physical Society. Section B*, 63(9):674–685, 1950.

[16] E. A. Neppiras and B. E. Noltingk. Cavitation produced by ultrasonics: Theoretical conditions for the onset of cavitation. *Proceedings of the Physical Society. Section B*, 64(12):1032–1038, 1951.

[17] H. Poritsky. The collapse or growth of a spherical bubble or cavity in a viscous fluid. *Proceedings of the first US National Congress on Applied Mechanics*, pages 813–821, 1952.

[18] C. Herring. Theory of the pulsations of the gas bubble produced by an underwater explosion. Technical report, OSRD report 236, 1941.

[19] F. R. Gilmore. The growth or collapse of a spherical bubble in a viscous compressible liquid. Technical report, Hydrodynamics Laboratory, California Institute Technology, Pasadena, report 26-4, 1952.

[20] L. Trilling. The collapse and rebound of a gas bubble. *J. Appl. Phys.*, 23(1): 14–17, 1952.

[21] J. B. Keller and I. I. Kolodner. Damping of underwater explosion bubble oscillations. *J. Appl. Phys.*, 27(10):1152–1161, 1956.

[22] H. G. Flynn. Cavitation dynamics. i. a mathematical formulation. *J. Acoust. Soc. Am.*, 57(6):1379–1396, 1975.

[23] H. G. Flynn. Cavitation dynamics: Ii. free pulsations and models for cavitation bubbles. *J. Acoust. Soc. Am.*, 58(6):1160–1170, 1975.

[24] J. B. Keller and M. Miksis. Bubble oscillations of large amplitude. *J. Acoust. Soc. Am.*, 68(2):628–633, 1980.

[25] A. Prosperetti, L. A. Crum, and K. W. Commander. Nonlinear bubble dynamics. *J. Acoust. Soc. Am.*, 83(2):502–514, 1988.

[26] C. Devin Jr. Survey of thermal, radiation, and viscous damping of pulsating air bubbles in water. *J. Acoust. Soc. Am.*, 31(12):1654–1667, 1959.

[27] A. I. Eller. Damping constants of pulsating bubbles. *J. Acoust. Soc. Am.*, 47 (5B):1469–1470, 1970.

[28] A. Prosperetti. Thermal effects and damping mechanisms in the forced radial oscillations of gas bubbles in. *J. Acoust. Soc. Am.*, 61(1):17–27, 1977.

[29] M. S. Plesset and A. Prosperetti. Cavitation and bubble dynamics. *Ann. Rev. Fluid Mech.*, 9(1):145–185, 1977.

[30] S. Hilgenfeldt, D. Lohse, and M. Zomack. Response of bubbles to diagnostic ultrasound: a unifying theoretical approach. *Eur. Phys. J. B*, 4(2): 247–255, 1998.

[31] M. Minnaert. On musical air-bubbles and sounds of running water. *Philosophical Magazine*, 16:235–248, 1933.

[32] T. G. Leighton. *The Acoustic Bubble*. Academic Press, 1994. ISBN 0124419208.

[33] C. C. Church. The effects of an elastic solid surface layer on the radial pulsations of gas bubbles. *J. Acoust. Soc. Am.*, 97(3):1510–1521, 1995.

[34] N. de Jong, R. Cornet, and C. T. Lancée. Higher harmonics of vibrating gas-filled microspheres. Part one: simulations. *Ultrasonics*, 32(6):447–453, 1994.

[35] L. Hoff, P. C. Sontum, and J. M. Hovem. Oscillations of polymeric microbubbles: Effect of the encapsulating shell. *J. Acoust. Soc. Am.*, 107(4): 2272–2280, 2000.

[36] K. Sarkar, W. T. Shi, D. Chatterjee, and F. Forsberg. Characterization of ultrasound contrast microbubbles using in vitro experiments and viscous and viscoelastic interface models for encapsulation. *J. Acoust. Soc. Am.*, 118(1):539–550, 2005.

[37] J. M. Gorce, M. Arditi, and M. Schneider. Influence of bubble size distribution on the echogenicity of ultrasound contrast agents. *Invest. Radiol.*, 35 (11):661–671, 2000.

[38] H. J. Vos, B. Dollet, J. G. Bosch, M. Versluis, and N. de Jong. Nonspherical vibrations of microbubbles in contact with a wall–a pilot study at low mechanical index. *Ultrasound Med. Biol.*, 34(4):685–688, 2008.

[39] C. T. Chin, C. Lancée, J. Borsboom, F. Mastik, M. E. Frijlink, N. de Jong, M. Versluis, and D. Lohse. Brandaris 128: A digital 25 million frames per second camera with 128 highly sensitive frames. *Rev. Sci. Instr.*, 74(12): 5026–5034, 2003.

[40] K. Chetty, E. Stride, C. A. Sennoga, J. V. Hajnal, and R. J. Eckersley. High-speed optical observations and simulation results of sonovue microbubbles at low-pressure insonation. *IEEE Trans. Ultrason. Ferroelec. Freq. Contr.*, 55(6):1333–1342, 2008.

[41] S. M. van der Meer, B. Dollet, C. T. Chin, A. Bouakaz, M. Voormolen, N. de Jong, M. Versluis, and D. Lohse. Microbubble spectroscopy of ultrasound contrast agents. *J. Acoust. Soc. Am.*, 121(1):648–656, 2007.

[42] A. Prosperetti. Nonlinear oscillations of gas bubbles in liquids: steady-state solutions. *J. Acoust. Soc. Am.*, 56(3):878–885, 1974.

[43] O. Lotsberg, J. M. Hovem, and B. Aksum. Experimental observation of subharmonic oscillations in infoson bubbles. *J. Acoust. Soc. Am.*, 99(3): 1366–1369, 1996.

[44] P. M. Shankar, P. D. Krishna, and V. L. Newhouse. Subharmonic backscattering from ultrasound contrast agents. *J. Acoust. Soc. Am.*, 106(4):2104–2110, 1999.

[45] P. D. Krishna, P. M. Shankar, and V. L. Newhouse. Subharmonic generation from ultrasonic contrast agents. *Phys. Med. Biol.*, 44(3):681–694, 1999.

[46] P. H. Chang, K. K. Shung, S. Wu, and H. B. Levene. Second harmonic imaging and harmonic Doppler measurements with Albunex. *IEEE Trans. Ultrason. Ferroelec. Freq. Contr.*, 42(6):1020–1027, 1995.

[47] E. Biagi, L. Breschi, E. Vannacci, and L. A. Masotti. Stable and transient subharmonic emissions from isolated contrast agent microbubbles. *IEEE Trans. Ultrason. Ferroelec. Freq. Contr.*, 54(3):480–497, 2007.

[48] P. J. A. Frinking and N. de Jong. Subharmonic imaging. In *Fourth Annual Ultrasound Contrast Research Symposium in Radiology*, San Diego, USA, 1999.

[49] P. J. A. Frinking, E. Gaud, J. Brochot, and M. Arditi. Subharmonic scattering of phospholipid-shell microbubbles at low acoustic pressure amplitudes. *submitted to IEEE Trans. Ultrason. Ferroelec. Freq. Contr.*, 2009.

[50] M. P. Brenner, S. Hilgenfeldt, and D. Lohse. Single-bubble sonoluminescence. *Rev. Mod. Phys.*, 74(2):425–484, 2002.

[51] E. Stride. The influence of surface adsorption on microbubble dynamics. *Phil. Trans. R. Soc. A*, 366:2103–2115, 2008.

[52] A. A. Doinikov and P. A. Dayton. Maxwell rheological model for lipid-shelled ultrasound microbubble contrast agents. *J. Acoust. Soc. Am.*, 121 (6):3331–3340, 2007.

[53] J. M. Crane and S. B. Hall. Rapid compression transforms interfacial monolayers of pulmonary surfactant. *Biophys. J.*, 80(4):1863–1872, 2001.

[54] M. A. Borden and M. L. Longo. Dissolution behavior of lipid monolayer-coated, air-filled microbubbles: Effect of lipid hydrophobic chain length. *Langmuir*, 18(24):9225–9233, 2002.

[55] L. Pocivavsek, R. Dellsy, A. Kern, S. Johnson, B. Lin, K. Y. C. Lee, and E. Cerda. Stress and fold localization in thin elastic membranes. *Science*, 320(5878):912–916, 2008.

[56] A. Prosperetti. Nonlinear oscillations of gas bubbles in liquids: transient solutions and the connection between subharmonic signal and cavitation. *J. Acoust. Soc. Am.*, 57(4):810–821, 1975.

[57] W. Lauterborn. Numerical investigation of nonlinear oscillations of gas bubbles in liquids. *J. Acoust. Soc. Am.*, 59(2):283–293, 1976.

[58] V. Garbin, D. Cojoc, E. Ferrari, R. Z. Proietti, S. Cabrini, and E. Di Fabrizio. Optical micro-manipulation using Laguerre-Gaussian beams. *Jpn. J. Appl. Phys.*, 44(7B):5773–5776, 2005.

[59] P. J. A. Frinking, E. Gaud, and M. Arditi. "compression-only" behavior and subharmonic scattering of phospholipid shell microbubbles. *Abstract of* 14^{th} *European symposium on ultrasound contrast imaging*, pages 80–87, 2009.

[60] E. Stride, K. Pancholi, M. J. Edirisinghe, and S. Samarasinghe. Increasing the nonlinear character of microbubble oscillations at low acoustic pressures. *J. R. Soc. Interface*, 5(24):807–811, 2008.

[61] P. N. Burns, J. E. Powers, D. H. Simpson, A. Brezina, A. Kolin, C. T. Chin, and T. Fritzsch. Harmonic imaging: New imaging and doppler method for contrast enahanced us. *Radiology*, 185:142, 1992.

[62] V. Mor-Avi, E. G. Caiani, K. A. Collins, C. E. Korcarz, J. E. Bednarz, and R. M. Lang. Combined assessment of myocardial perfusion and regional left ventricular function by analysis of contrast-enhanced power modulation images. *Circulation*, 104(3):352–357, 2001.

[63] N. de Jong and L. Hoff. Ultrasound scattering properties of albunex microspheres. *Ultrasonics*, 31(3), 1993.

[64] M. I. Sández, A. Suárez, and A. Gil. Surface pressure-area isotherms and fluorescent behavior of phospholipids containing labeled pyrene. *J. Coll. Interf. Sci*, 250(1):128–133, 2002.

[65] F. Pétriat, E. Roux, J. C. Leroux, and S. Giasson. Study of molecular interactions between a phospholipidic layer and a ph-sensitive polymer using the langmuir balance technique. *Langmuir*, 20(4):1393–1400, 2004.

[66] X. Wen and E. I. Franses. Adsorption of bovine serum albumin at the air/water interface and its effect on the formation of dppc surface film. *Colloid. Surface. A*, 190(3):319–332, 2001.

[67] C. C. Cheng and C. H. Chang. Retardation effect of tyloxapol on inactivation of dipalmitoyl phosphatidylcholine surface activity by albumin. *Langmuir*, 16(2):437–441, 2000.

[68] K. Y. C. Lee. Collapse mechanisms of langmuir monolayers. *Ann. Rev. Phys. Chem.*, 59(1):771–791, 2008.

[69] D. L. Miller. Ultrasonic detection of resonant cavitation bubbles in a flow tube by their second-harmonic emissions. *Ultrasonics*, 19(5):217, 1981.

[70] F. B. Feinstein. The powerful microbubble: From bench to bedside, from intravascular indicator to therapeutic delivery system, and beyond. *Am. J. Physiol. Heart Circul. Physiol.*, 287:H450–H457, 2004.

[71] P. J. A. Frinking, A. Bouakaz, J. Kirkhorn, F. J. ten Cate, and N. de Jong. Ultrasound contrast imaging: current and new potential methods. *Ultrasound Med. Biol.*, 26(6):965–975, 2000.

[72] P. Rafter, P. Phillips, and M. A. Vannan. Imaging technologies and techniques. *Cardiol. Clin.*, 22(2):181–197, 2004.

[73] D. E. Goertz, M. E. Frijlink, N. de Jong, and A. F. W. van der Steen. High frequency nonlinear scattering from a micrometer to submicrometer sized lipid encapsulated contrast agent. *Ultrasound Med. Biol.*, 32(4):569–577, 2006.

[74] D. E. Goertz, M. E. Frijlink, D. Tempel, V. Bhagwandas, A. Gisolf, R. Krams, N. de Jong, and A. F. W. van der Steen. Subharmonic contrast intravascular ultrasound for vasa vasorum imaging. *Ultrasound Med. Biol.*, 33(12):1859–1872, 2007.

[75] R. Esche. Untersuchung der schwingungskavitation in flussigkeiten. *Acustica*, 2:208–218, 1952.

[76] E. A. Neppiras. Subharmonic and other low-frequency emission from bubbles in sound-irradiated liquids. *J. Acoust. Soc. Am.*, 46(3B):587–601, 1969.

[77] P. De Santis, D. Sette, and F. Wanderlingh. Cavitation detection: The use of the subharmonics. *J. Acoust. Soc. Am.*, 42(2):514–516, 1967.

[78] A. I. Eller and H. G. Flynn. Generation of subharmonics of order one-half by bubbles in a sound field. *J. Acoust. Soc. Am.*, 46(3B):722–727, 1969.

[79] A. I. Eller. Subharmonic response of bubbles to underwater sound. *J. Acoust. Soc. Am.*, 55(4):871–873, 1974.

[80] A. Prosperetti. Application of the subharmonic threshold to the measurement of the damping of oscillating gas bubbles. *J. Acoust. Soc. Am.*, 61(1): 11–16, 1977.

[81] G. Bhagavatheeshwaran, W. T. Shi, F. Forsberg, and P. M. Shankar. Subharmonic signal generation from contrast agents in simulated neovessels. *Ultrasound Med. Biol.*, 30(2):199–203, 2004.

[82] E. Kimmel, B. Krasovitski, A. Hoogi, D. Razansky, and D. Adam. Subharmonic response of encapsulated microbubbles: Conditions for existence and amplification. *Ultrasound Med. Biol.*, 33(11):1767–1776, 2007.

[83] J. Sijl, E. Gaud, P. Frinking, M. Arditi, N. de Jong, D. Lohse, and M. Versluis. Acoustic characterization of single ultrasound contrast agent microbubbles. *J. Acoust. Soc. Am.*, 124(6):4091–4097, 2008.

[84] V. Garbin, D. Cojoc, E. Ferrari, E. Di Fabrizio, M. L. J. Overvelde, S. M. van der Meer, N. de Jong, D. Lohse, and M. Versluis. Changes in microbubble dynamics near a boundary revealed by combined optical micromanipulation and high-speed imaging. *Appl. Phys. Lett.*, 90:114103, 2007.

[85] B. Dollet, S. M. van der Meer, V. Garbin, N. de Jong, D. Lohse, and M. Versluis. Nonspherical oscillations of ultrasound contrast agent microbubbles. *Ultrasound Med. Biol.*, 34(9):1465–1473, 2008.

[86] R. Veldhuizen, K. Nag, S. Orgeig, and F. Possmayer. The role of lipids in pulmonary surfactant. *Biochim. Biophys. Acta Mol. Basis Dis.*, 1408(2-3): 90–108, 1998.

[87] G. Enhorning. Pulsating bubble technique for evaluating pulmonary surfactant. *J. Appl. Physiol.*, 43:198–203, 1977.

[88] B. B. Goldberg, J. Raichlen, and F. Forsberg. *Ultrasound Contrast Agents: Basic Principles and Clinical Applications*. Dunitz, London, 2nd edition, 2001.

[89] J. E. Chomas, P. A. Dayton, D. May, J. S. Allen, A. L. Klibanov, and K. W. Ferrara. Optical observation of contrast agent destruction. *Appl. Phys. Lett.*, 77(7):1056, 2000.

[90] N. de Jong, P. J. A. Frinking, A. Bouakaz, M. Goorden, T. Schourmans, X. Jingping, and F. Mastik. Optical imaging of contrast agent microbubbles in an ultrasound field with a 100-MHz camera. *Ultrasound Med. Biol.*, 26 (3):487492, 2000.

[91] N. Kudo, T. Miyaoka, K. Kuribayashi, K. Yamamoto, and M. Natori. Study of the mechanism of fragmentation of a microbubble exposed to ultrasound using a high-speed observation system . *J. Acoust. Soc. Am.*, 108(5):2547, 2000.

[92] A. Bouakaz, M. Versluis, and N. de Jong. High-speed optical observations of contrast agent destruction. *Ultrasound Med. Biol.*, 31(3):391–399, 2005.

[93] P. Marmottant and S. Hilgenfeldt. Controlled vesicle deformation and lysis by single oscillating bubbles. *Nature*, pages 153–156, 2003.

[94] C.-D. Ohl, M. Arora, R. Ikink, N. de Jong, M. Versluis, M. Delius, and D. Lohse. Sonoporation from jetting cavitation bubbles. *Biophys. J.*, 91 (11):4285–4295, 2006.

[95] S. Zhao, K. W. Ferrara, and P. A. Dayton. Asymmetric oscillation of adherent targeted ultrasound contrast agents. *Appl. Phys. Lett.*, 87(13):134103–3, 2005.

[96] M. Lankford, C. Z. Behm, J. Yeh, A. L. Klibanov, P. Robinson, and J. R. Linder. Effect of microbubble ligation to cells on ultrasound signal enhancement. implications for targeted imaging. *Invest. Radiol.*, 41(10), 2006.

[97] S. Zhao, D. E. Kruse, K. W. Ferrara, and P. A. Dayton. Acoustic response from adherent targeted contrast agents. *J. Acoust. Soc. Am.*, 120(6):EL63–EL69, 2006.

[98] P. A. Prentice, M. P. Macdonald, T. G. Frank, A. Cuschier, G. C. Spalding, W. Sibbett, P. A. Campbell, and K. Dholakia. Manipulation and filtration of low index particles with holographic Laguerre-Gaussian optical trap arrays. *Opt. Express*, 12(4):593–600, 2004.

[99] P. H. Jones, E. Stride, and N. Saffari. Trapping and manipulation of microscopic bubbles with a scanning optical tweezer. *Appl. Phys. Lett.*, 89(8): 081113, 2006.

[100] P. A. Prentice, A. Cuschieri, K. Dholakia, M. Prausnitz, and P. Campbell. Membrane disruption by optically controlled microbubble cavitation. *Nat. Phys.*, 1(2):107–110, 2005.

[101] M. J. Padgett and L. Allen. The Poynting vector in Laguerre-Gaussian laser modes. *Opt. Commun.*, 1995.

[102] M. Strasberg. The pulsation frequency of nonspherical gas bubbles in liquids. *J. Acoust. Soc. Am.*, 25(3):536–537, 1953.

[103] C. E. Brennen. *Cavitation and bubble dynamics*. Oxford University Press, New York, 1995. ISBN 0195094093.

[104] A. L. Klibanov. *Ultrasound Contrast Agents: Development of the Field and Current Status*, volume 222 of *Top. Curr. Chem.* 2002.

[105] H. N. O guz and A. Prosperetti. The natural frequency of oscillation of gas bubbles in tubes. *J. Acoust. Soc. Am.*, 103(6):3301–3308, 1998.

[106] J. Cui, M. F. Hamilton, P. S. Wilson, and E. A. Zabolotskaya. Bubble pulsations between parallel plates. *J. Acoust. Soc. Am.*, 119(4):2067–2072, 2006.

[107] A. Harkin, T. J. Kaper, and A. Nadim. Coupled pulsation and translation of two gas bubbles in a liquid. *J. Fluid Mech.*, 445:377–411, 2001.

[108] A. A. Doinikov. Translational motion of two interacting bubbles in a strong acoustic field. *Phys. Rev. E*, 64(2):026301, 2001.

[109] P. Marmottant, M. Versluis, N. de Jong, S. Hilgenfeldt, and D. Lohse. High-speed imaging of an ultrasound-driven bubble in contact with a wall: ”narcissus” effect and resolved acoustic streaming. *Exp. Fluids*, 41(2):147–153, 2006.

[110] J. R. Blake and D. C. Gibson. Cavitation bubbles near boundaries. *Ann. Rev. Fluid Mech.*, 19(1):99–123, 1987.

[111] E. A. Brujan, K. Nahen, P. Schmidt, and A. Vogel. Dynamics of laser-induced cavitation bubbles near an elastic boundary. *J. Fluid Mech.*, 433: 251–281, 2001.

[112] S. D. Howkins. Measurements of the resonant frequency of a bubble near a rigid boundary. *J. Acoust. Soc. Am.*, 37(3):504–508, 1965.

[113] W. Lauterborn and H. Bolle. Experimental investigations of cavitation-bubble collapse in the neighbourhood of a solid boundary. *J. Fluid Mech.*, 72(02):391–399, 1975.

[114] S. W. Ohl, E. Klaseboer, and B. C. Khoo. The dynamics of a non-equilibrium bubble near bio-materials. *Phys. Med. Biol.*, 54(20):6313–6336, 2009.

[115] S. Martynov, E. Stride, and N. Saffari. The natural frequencies of micro-bubble oscillation in elastic vessels. *J. Acoust. Soc. Am.*, 126(6):2963–2972, 2009.

[116] T. A. Hay, Y. A. Ilinkskii, E. A. Zabolotskaya, and M. F. Hamilton. Model for bubble oscillation between viscoelastic parallel plates. *in preparation*.

[117] H. J. Vos, M. Versluis, and N. de Jong. Orthogonal observations of vibrating microbubbles. *Proceedings of IEEE Ultrasonics Symposium, IEEE*, pages 765–768, 2007.

[118] L. A. Crum and A. I. Eller. Motion of bubbles in a stationary sound field. *J. Acoust. Soc. Am.*, 48:181–189, 1970.

[119] L. A. Crum. Bjerknes forces on bubbles in a stationary sound field. *J. Acoust. Soc. Am.*, 57(6):1363–1370, 1975.

[120] L. D. Landau and E. M. Lifshitz. *Fluid Mechanics*. Pergamon, New York, 2nd edition, 1987. ISBN 0750627670.

[121] H. N. Oğuz and A. Prosperetti. A generalization of the impulse and virial theorems with an application to bubble oscillations. *J. Fluid Mech.*, 218: 143162, 1990.

[122] A. J. Reddy and A. J. Szeri. Coupled dynamics of translation and collapse of acoustically driven microbubbles. *J. Acoust. Soc. Am.*, 112(4):1346–1352, 2002.

[123] J. Magnaudet and D. Legendre. The viscous drag force on a spherical bubble with a time-dependent radius. *Phys. Fluids*, 10(3):550–554, 1998.

[124] R. Toegel and D. Luther, S.and Lohse. Viscosity Destabilizes Sonoluminescing Bubbles. *Phys. Rev. Lett.*, 96(11), 2006.

[125] J. Magnaudet and I. Eames. The motion of high-Reynolds-number bubbles in inhomogeneous flows. *Ann. Rev. Fluid Mech.*, 32(1):659708, 2000.

[126] V. G. Levich. *Physicochemical Hydrodynamics*. Prentice-Hall, Englewood Cliffs, 1962. ISBN 0136744400.

[127] A. B. Basset. *A Treatise on Hydrodynamics*. Deighton Bell, London, Vol. 2 edition, 1888. ISBN 0559314574.

[128] G. G. Stokes. On the effect of the internal friction of fluids on the motion of pendulums. *Trans. Cmabridge Philos. Soc.*, 9(8):1–86, 1851.

[129] R. Mei. Flow due to an oscillating sphere and an expression for unsteady drag on the sphere at finite Reynolds number. *J. Fluid Mech.*, 270:133174, 1994.

[130] F. Takemura and J. Magnaudet. The history force on a rapidly shrinking bubble rising at finite Reynolds number. *Phys. Fluids*, 16(9):3247–3255, 2004.

[131] S. Qin, C. F. Caskey, and K. W. Ferrara. Ultrasound contrast microbubbles in imaging and therapy: physical principles and engineering. *Phys. Med. Biol.*, 54:R27–R57, 2009.

[132] P. A. Dayton, J. S. Allen, and K. W. Ferrara. The magnitude of radiation force on ultrasound contrast agents. *J. Acoust. Soc. Am.*, 112(5):2183–2192, 2002.

[133] J. Happel and H. Brenner. *Low Reynolds Number Hydrodynamics*. Kluwer Academic, Dordrecht, 1983. ISBN 9024728770.

[134] B. T. Unger and P. L. Marston. Optical levitation of bubbles in water by the radiation pressure of a laser beam: an acoustically quiet levitator. *J. Acoust. Soc. Am.*, 83(3):970–975, 1988.

[135] C. F. Bohren and D. R. Huffman. *Absorption and Scattering of Light by Small Particles*. Wiley, New York, 1983. ISBN 0471293407.

[136] Y. A. Ilinskii, M. F. Hamilton, and E. A. Zabolotskaya. Bubble interaction dynamics in Lagrangian and Hamiltonian mechanics. *J. Acoust. Soc. Am.*, 121(2):786–795, 2007.

[137] J. N. Chung. The motion of praticles inside a droplet. *Trans. ASME, Ser. C: J. Heat Transfer*, 104:438–445, 1982.

[138] I. Kim, S. Elghobashi, and W. A. Sirignano. On the equation for spherical-particle motion: effect of Reynolds and acceleration numbers. *J. Fluid Mech.*, 367:221–253, 1998.

[139] P. M. Lovalenti and J. F. Brady. The hydrodynamic force on a rigid particle undergoing arbitrary time-dependent motion at small Reynolds number. *J. Fluid Mech.*, 256:561–605, 1993.

[140] A. Prosperetti. Viscous effects on perturbated spherical flows. *Quart. Appl. Math.*, 34(4):339–352, 1977.

[141] P. A. Dayton, A. L. Klibanov, G. Brandenburger, and K. W. Ferrara. Acoustic radiation force in vivo: a mechanism to assist targeting of microbubbles. *Ultrasound Med. Biol.*, 25(8):1195–1201, 1999.

[142] A. M. Takalkar, A. L. Klibanov, J. J. Rychak, J. R. Lindner, and K. Ley. Binding and detachment dynamics of microbubbles targeted to P-selectin under controlled shear flow. *J. Contr. Rel.*, 96(3):473–482, 2004.

[143] J. J. Rychak, A. L. Klibanov, K. F. Ley, and J. A. Hossack. Enhanced targeting of ultrasound contrast agents using acoustic radiation force. *Ultrasound Med. Biol.*, 33(7):1132–1139, 2007.

[144] D. Zhang, Y. Gong, X. Gong, Z. Liu, K. Tan, and H. Zheng. Enhancement of subharmonic emission from encapsulated microbubbles by using a chirp excitation technique. *Phys. Med. Biol.*, 52(18):5531–5544, 2007.

[145] A. O. Eniola, P. J. Willcox, and D. A. Hammer. Interplay between rolling and firm adhesion elucidated with a cell-free system engineered with two distinct receptor-ligand pairs. *Biophys. J.*, 85(4):2720–2731, 2003.

[146] A. L. Klibanov, J. J. Rychak, W. C. Yang, B. Alikhani, S. Acton, J. R. Lindner, K. Ley, and S. Kaul. Targeted ultrasound contrast agent for molecular imaging of inflammation in high-shear flow. *Molecular Imaging*, 266:259–266, 2006.

[147] A. L. Klibanov. Preparation of targeted microbubbles: ultrasound contrast agents for molecular imaging. 47(8):875–882, 2009.

[148] A. S. Ham, A. L. Klibanov, and M. B. Lawrence. Action at a distance: lengthening adhesion bonds with poly(ethylene glycol) spacers enhances mechanically stressed affinity for improved vascular targeting of microparticles. *Langmuir*, 25(17):10038–10044, 2009.

[149] A. Bouakaz, P. J. A. Frinking, N. de Jong, and N. Bom. Noninvasive measurement of the hydrostatic pressure in a fluid-filled cavity based on the disappearance time of micrometer-sized free gas bubbles. *Ultrasound Med. Biol.*, 25(9):1407–1415, 1999.

[150] A. Bhan, S. Kapetanakis, B. S. Rana, E. Ho, K. Wilson, P. Pearson, S. Mushemi, J. Deguzman, J. Reiken, M. D. Harden, N. Walker, P. G. Rafter, and M. J. Monaghan. Real-time three-dimensional myocardial contrast echocardiography: is it clinically feasible? *Eur. J. Echocardiogr.*, 9(6): 761–765, 2008.

Summary

To enhance the visibility of the blood pool, ultrasound contrast agents (UCA) have been developed, enabling the visualization of the perfusion of organs. The typical UCA is composed of a suspension of microbubbles (radius 1-5 μm) which are coated with a phospholipid, albumin or polymer shell to prevent the bubble from quickly dissolving in the blood. The key feature of ultrasound contrast agent microbubbles is their nonlinear response. Special pulse-echo techniques such as power modulation and pulse-inversion have been developed to distinguish the nonlinear echoes of the microbubbles in the blood pool echo from the tissue echo to optimize the contrast-to-tissue ratio. A new promising non-invasive technique for disease-specific imaging is molecular imaging with ultrasound, enabling the diagnosis of for instance thrombus and inflammation. Selective imaging is performed by using ultrasound contrast agents containing ligands on their shell that bind specifically to selective biomarkers on the membrane of endothelial cells, which constitute the blood vessel wall. For these molecular imaging applications it would be highly beneficial to distinguish acoustically between adherent and freely circulating microbubbles.

To increase the contrast-to-tissue ratio of the blood pool it is important to develop pulse-echo techniques based on the nonlinear acoustic response of the bubbles. The optimization of pulse-echo techniques for molecular imaging applications demands an even deeper understanding of the nonlinear dynamics of the microbubbles, in particular the interaction of (targeted) bubbles with a neighboring wall. For all these reasons we must investigate the dynamics of single phospholipid-coated microbubbles in great detail. Before we discuss the new results, we start with an overview of the experimentally observed phenomena of phospholipid-coated bubbles and the existing in chapter 2. The subsequent chapters can be divided basically in three subjects: the phospholipid-coating, the proximity of a boundary, and the adherence of bubbles to a boundary.

In the first part of this thesis we investigate experimentally the influence of the phospholipid-coating on the dynamics of ultrasound contrast agent microbubbles. We record the radial dynamics of individual microbubbles with an ultra-high speed

camera as a function of the driving pressure and frequency. We observe a strong nonlinear contribution of the coating on the dynamics in agreement with previous experimental observations. These include the "thresholding" behavior (chapter 3), 'compression-only' behavior (chapter 4) and subharmonics (chapter 5). The phospholipid-coating is found to enhance the nonlinear bubble response at acoustic pressures as low as 5 kPa. For increasing acoustic pressures a decrease of the frequency of maximum response is observed for a distinct class of bubbles, leading to a pronounced skewness of the resonance curve, which we show to be the origin of the "thresholding" behavior. For other bubbles the frequency of maximum response is found to lie just above the resonance frequency of an uncoated microbubble, and to be independent of the applied acoustic pressure. The shell-buckling bubble model by Marmottant *et al.*, which accounts for buckling and rupture of the shell, captures both cases for a single value of the shell elasticity and shell viscosity. The difference in the observed nonlinear dynamics between the two sets of bubbles can be explained by a difference in the initial surface tension, which is directly related to the phospholipid concentration at the bubble interface. A bubble oscillating in the elastic regime shows "thresholding" behavior and is specifically beneficial for power modulation imaging. A bubble with an initial radius that equals the buckling radius shows "compression-only" behavior and subharmonic behavior as these phenomena depend strongly on the second derivative of the effective surface tension. The subharmonic behavior is very interesting for imaging purposes, as the tissue signal lacks a subharmonic component. We found that the elastic regime is in the order of 1% of the bubble radius, and a small change in the initial bubble radius is sufficient to change the initial surface tension, leading to a dramatic change of the observed behavior. As the shell-buckling model describes the dynamics of phospholipid coated bubbles in great detail the model allows for an optimization of current pulse-echo techniques and for the development of new pulse-echo techniques.

The second part of the thesis focuses on the interaction of single phospholipid-coated bubbles with a boundary. A combined optical tweezers and Brandaris 128 ultra-high speed camera setup allowed us to investigate the dynamics of a single bubble at controlled distances from an OptiCell wall, and is described in detail in chapter 6. In chapter 7 the proximity of the OptiCell wall is investigated below, at, and above the bubble's frequency of maximum response. We first investigate the influence of the wall in case the coating of the bubble has little influence, i.e. above its frequency of maximum response and at high amplitude of oscillations. We observe that the radial response of the bubbles decreases with decreasing distance from the wall. The frequency of maximum response was found to decrease with about 20% at the wall as compared to the bubble oscillating far from the wall. The experimental results are compared to simulations performed with a numeri-

cal model, which accounts for the interaction of a coated bubble with a compliant boundary. The trend in the experiments and simulations are in good agreement when the bubble is driven above resonance where the shell contributions are small. Below resonance, where the bubble response is dominated by the nonlinear shell behavior, simulations predict an increase in the amplitude of oscillation with decreasing distance from the wall, while we measure quite the opposite namely a decreasing response with decreasing distance. We anticipate that the nonlinear dynamics caused by the phospholipid-coating of the bubble allows for an extremely sensitive assessment of the boundary conditions of the bubble-wall interaction, and reveals the presence of a primary reflection of the ultrasound beam.

A bubble near a boundary oscillates radially, but also translatory. In chapter 8 we investigate the translatory oscillations caused by radiation force of a two bubble system. Optical tweezers are used to isolate a bubble pair from neighboring boundaries, so that it can be regarded as if in an unbounded fluid, and the hydrodynamic forces acting on the system can be identified unambiguously. Since the coating enforces a no-slip boundary condition, an increased viscous dissipation is expected due to the oscillatory component, which is accounted for by the inclusion of a history force term in the force balance equations. The instantaneous values of the hydrodynamic forces extracted from the experimental data confirm that the history force accounts for the largest part of the viscous force.

In the third part of the thesis we investigate the influence of adherence on the dynamics of the microbubbles, in particular on the frequency of maximum response, by recording the radial response of individual microbubbles as a function of the applied acoustic pressure and frequency. We show that the frequency of maximum response of adherent microbubbles is lower than for bubbles in the unbounded fluid by as much as 50%, while it is more than 30% lower for a bubble in contact with the wall. The strong change of the frequency of maximum response is caused by adhesion of the bubbles to the wall as no influence was found solely by the presence of the targeting ligands on the bubble dynamics. The shift in the frequency of maximum response may prove to be important for molecular imaging applications with ultrasound as these applications would benefit from an acoustic imaging method to distinguish adherent from freely circulating microbubbles.

Samenvatting

Van alle medische beeldvormingtechnieken is ultrageluid de meest gebruikte techniek. Ultrageluid is relatief goedkoop, bovendien kunnen beelden *real-time* en aan het bed van de patiënt worden gemaakt. Echobeelden van de doorbloeding van organen vertonen een relatief laag contrast wat een direct gevolg is van de lage verstrooiingseigenschappen van de rode bloedcellen. Het contrast van bloed kan worden verhoogd door gebruik te maken van een contrastmiddel. Het contrastmiddel bestaat uit microscopisch kleine belletjes met een straal van 1-5 micrometer. De compressibiliteit van de bellen zorgen voor een weerkaatsing van het ultrageluid die circa 9 ordes hoger ligt dan van een vast deeltje van dezelfde grootte. De bellen hebben een schil, een coating, die de bel stabiliseert en voorkomt dat de bellen oplossen in het bloed. De echo van de bellen is sterk niet-lineair ten opzichte van de echo van het weefsel. Het niet-lineaire gedrag van de bellen wordt gebruikt in de verschillende puls-echo technieken, zoals ‘power modulation’ en ‘pulse-inversion’ die zijn ontwikkeld om het contrast tussen contrastbellen en het weefsel zo optimaal mogelijk te versterken. Een nieuwe veelbelovende toepassing van contrastbellen is beeldvorming op moleculair niveau (molecular imaging), waarbij bellen worden beplakt met antilichamen welke zich hechten aan biomarkers op celmateriaal. Op deze manier kan bijvoorbeeld trombose en ontstekingen in het lichaam zichtbaar worden gemaakt. Voor deze toepassingen is het van belang om akoestisch onderscheid te maken tussen bellen die vastgehecht zitten aan de celwand en bellen die vrij door de bloedbaan circuleren. Voor deze nieuwe toepassingen moeten de puls-echo technieken verder worden geoptimaliseerd, want naast het begrip van het akoestische gedrag van de bellen in de vrije vloeistof is hier ook de interactie van de bellen met de wand belangrijk. Daarom is het essentieel dat we allereerst het niet-lineaire gedrag van fosfolipide gecoate bellen onder instraling van ultrageluid volledig in kaart brengen en daarna de interactie met de wand. We beginnen daarom met een korte beschrijving van het ons bekende gedrag van fosfolipide bellen. De daaropvolgende hoofdstukken kunnen worden onderverdeeld in drie onderwerpen: de invloed van de fosfolipide coating, de interactie van de bel met de wand en het gedrag van een bel die vastgehecht zit aan de wand.

In het eerste deel van dit proefschrift onderzoeken we experimenteel de dynamica van fosfolipide gecoate microbellen. De radiële oscillaties van enkele bellen worden vastgelegd met een hogesnelheidscamera, de Brandaris 128, terwijl de aangelegde druk en frequentie van de ultrageluidspuls wordt gevarieerd. We vinden, in overeenstemming met eerder gerapporteerd werk, een sterk niet-lineair gedrag zoals het zogenoemde "thresholding" gedrag (hoofdstuk 3), "compression-only" gedrag (hoofdstuk 4) en opwekking van subharmonische frequenties (hoofdstuk 5). De fosfolipide coating veroorzaakt niet-lineair gedrag bij zeer lage drukken van 5 kPa. Voor een specifieke groep bellen vinden we bij toenemende druk een sterke asymmetrie van de resonantiecurves. We laten zien dat deze asymmetrie tezamen met een afname van de maximale responsfrequentie ten grondslag ligt aan het "thresholding" gedrag. De frequentie waarbij een maximale respons optreedt ligt voor de overige gemeten bellen net boven de eigenfrequentie van een ongecoate bel. Het gedrag van gecoate bellen kan worden gemodelleerd met een aangepaste Rayleigh-Plesset vergelijking, de standaard bewegingsvergelijking van de bel. Het model van Marmottant *et al.* is gebaseerd op het quasi-statisch gedrag van fosfolipide monolagen en neemt naast elastisch gedrag van de schil ook het kreukelen van de schil bij hoge fosfolipiden concentraties en het opbreken van de monolaag bij een relatief lage concentratie van de fosfolipiden. Dit model beschrijft het niet-lineaire gedrag van de gecoate bellen voor een unieke waarde van de elasticiteit en viscositeit van de schil. Het verschil in gedrag kan worden verklaard door de initiële concentratie van fosfolipiden die weer wordt uitgedrukt in de initiële oppervlaktespanning. De coating van een bel die "thresholding" gedrag vertoont is aanvankelijk elastisch. "Thresholding" gedrag is zeer interessant voor beeldvor- ming met behulp van de power modulation pulse-echo techniek. Aan de andere kant, bellen die dichtbij de overgang van het elastische en gekreukelde gebied zitten vertonen "compression-only" gedrag en laten subharmonische frequenties zien. Aangezien de lineaire echo van weefsel geen subharmonische frequentie kan bevatten is het zeer interessant om deze subharmonische belrespons te gebruiken voor contrastbeeldvorming. Het gebied waarin de coating zich elastisch gedraagt is totaal maar ongeveer 1% van de belstraal. Een kleine verandering in de belstraal is dus genoeg om een drastische verandering van het belgedrag te bewerkstelligen. Met een juiste keuze van de schilparameters maakt het model van Marmottant *et al.* het mogelijk om grotendeels numeriek de bestaande puls-echo technieken te optimaliseren en nieuwe technieken te ontwikkelen.

In deel twee van dit proefschrift ligt het focus op de interactie van fosfolipide gecoate bellen met een wand. Een optisch laser pincet (optical tweezers) gekoppeld aan de hogesnelheidscamera Brandaris 128 maakt het mogelijk om de positie van de bel ten opzichte van de wand nauwkeurig te controleren. De gecombineerde opstelling wordt in detail besproken in hoofdstuk 6. In hoofdstuk 7 onderzoeken we de nabijheid van een polystyreen membraan onder, op en boven de maximale responsfrequentie. Boven de maximale responsfrequentie, waar de coating weinig invloed heeft op de beldynamica, neemt de oscillatieamplitude af dichter bij de wand. De maximale responsfrequentie van een bel aan de wand is 20% lager dan die van een bel in de vrije vloeistof. De resultaten zijn vergeleken met een model dat speciaal ontwikkeld is voor gecoate bellen dicht bij een dunne flexibele wand. De gemeten trend in het gedrag wordt inderdaad goed voorspeld door het model wanneer de invloed van de fosfolipide coating minimaal is. Onder de maximale responsfrequentie, waar de invloed van de coating het belgedrag domineert, neemt de oscillatieamplitude af dichterbij de wand. Dit in tegenstelling tot het model dat een toename van de oscillatieamplitude voorspelt. We merken op dat het sterk niet-lineaire gedrag van de fosfolipide gecoate bellen gebruikt kan worden om heel kleine veranderingen in de omgevingsdruk te meten. De niet-lineaire invloed van de fosfolipide coating op de beldynamica onthulde hierbij dat een reflectie van de primaire ultrageluidspuls aan het membraan niet werd meegenomen in het model.

Een bel dichtbij een wand oscilleert radieel en vertoont bovendien een translatie. In hoofdstuk 8 onderzoeken we met behulp van de *optical tweezers* opstelling de translaties van een geïsoleerd bellenpaar. De twee bellen worden gepositioneerd in de vrije vloeistof om *sec* de hydrodynamische krachten te onderzoeken. De fosfolipide coating van de bellen zorgt voor een *no-slip* randvoorwaarde op de belwand en door de beloscillaties neemt de viskeuze dissipatie toe. Een krachtenbalans laat zien dat de zogenaamde “history force”, die veroorzaakt wordt door een interactie met de door de bel zelf veroorzaakte wervels het grootste deel van het energieverlies veroorzaakt.

In het derde deel wordt gekeken naar het gedrag van fosfolipide gecoate bellen die vastgehecht zitten aan een wand. De frequentie waarbij de amplitude maximaal is wordt gemeten voor enkele bellen door het meten van de radiele oscillaties bij verschillende drukken en frequenties van het ultrageluid, zie hoofdstuk 9. De resonantiecurves van vastgehechte bellen worden vergeleken met die van enkele bellen in de vrije vloeistof. De frequenties van maximale respons blijken 50% lager te zijn dan die van een bel in de vrije vloeistof en 30% lager dan die van een bel los tegen de wand. Er werd geen noemenswaardige verandering gevonden in het gedrag van gefunctionaliseerde bellen, d.w.z. bellen beplakt met antilichamen, ten opzichte van normale contrastbellen. Hieruit leiden wij af dat de sterke verandering in de frequentie van maximale respons wordt veroorzaakt door het fysische mecha- nisme van hechting van de bellen aan de wand. De verschillende respons kan het mogelijk maken om akoestisch onderscheid te maken tussen bellen die vastgehecht zittend aan de wand en bellen die vrij circuleren door de bloedbaan. Deze verandering van het resonantiegedrag is dus in hoge mate interessant voor toepassingen in *molecular imaging* met ultrageluid.

Dankwoord

Het is de vooravond voor het drukken van mijn proefschrift, beter bekend als “het boekje”, waarmee er dan na vijf jaar een einde komt aan mijn *bellen geblaas*. De keuze om te gaan promoveren was snel gemaakt na mijn plezierig afstuderen. Niet alleen het onderwerp beviel goed, maar ook de wetenschappelijke omgeving en natuurlijk de collega’s. De vier jaar van mijn promotie zijn ook voorbij gevlogen. Ik wil een ieder die dit leest bedanken voor zijn interesse in mij en mijn onderzoek.

Allereerst wil ik graag mijn promotoren Detlef Lohse, Nico de Jong en Michel Versluis bedanken. Detlef, bedankt voor de mogelijkheid om mijn promotie in jouw excellente groep te doen. Bedankt voor je oprechte en duidelijke mening tijdens de efficïente en verhelderende discussies. Wat ik altijd nog wilde zeggen: “ik heb echt geen hekel aan fietsen”. Nico, ondanks dat je normaal in Rotterdam werkt, hadden we regelmatig contact. Je bent altijd geïnteresseerd in, en betrokken geweest bij mijn onderzoek. Ik waardeer het zeer dat alles bespreekbaar is en dat je altijd open staat voor mijn mening. Natuurlijk wil ik ook mijn dagelijks begeleider, Michel, bedanken voor het vertrouwen in mijn werk en de vrijheid die ik van je kreeg om alles op mijn manier aan te pakken, zowel in het onderzoek, als in organisatorische taken. Het heeft me erg geholpen om uit te vinden wat mijn kwaliteiten zijn en wat ik leuk vind. Jouw kennis van presenteren en schrijven zorgde er regelmatig voor dat alles weer aangepast moest worden, maar het resultaat was er dan ook altijd naar. Daarnaast waren de conferenties en Tamirut meetings waar we heen gingen altijd erg gezellig; jij zorgde voor een plezierige combinatie van werk en ontspanning.

Daarnaast wil ik alle ondersteunende medewerkers bedanken. Jullie zijn een essentieel onderdeel geweest van mijn onderzoek. Gert-Wim Bruggert en Martin Bos, bedankt dat jullie meedachten en altijd snel en nauwkeurig de essentïele onderdelen voor de Brandaris-tweezers opstelling maakten. Bas Benschop, mijn laptop was jouw eerste Vista uitdaging, maar dankzij jou heeft hij het de afgelopen vier jaar goed doorstaan. Joanita Leferink, met iedere vraag weet jij raad. Als je al eens iets niet wist dan wist je wel in no-time de juiste persoon te pakken te krijgen. Mieke Pruijsten, Marianne Immerzeel, Cees Pakvis, Leo Bekkering, Frits Mas-

tik en Jan Honkoop, bedankt voor alle ondersteuning tijdens de verhuizingen van de Brandaris. Ook op momenten dat wij er hier in Twente niet meer uitkwamen stonden jullie altijd klaar. Jan, ik heb met veel plezier het practicum van Medical Acoustics met jou samen begeleid.

I would like to thank all my co-authors for their work, support, and discussions. All together we made great progress in understanding the influence of the phospholipid-coating, the proximity of a boundary, and the effect of targeting on the dynamics of microbubbles. Furthermore, I would like to thank all the people who worked on medical bubbles in Twente: Sander van der Meer, Valeria Garbin, Benjamin Dollet, Jeroen Sijl, Todd Hay, Erik Gelderblom, Michel Versluis. It was a great pleasure to work with you all. During my promotion I had the pleasure to work with several bachelor and master students. Pieter van der Deijl, Peter Eerkes, Anne Maas, Timo Rozendal, Erik Gelderblom en Nynke Zandstra, I would like to thank you all for hard work and the great results. I would also like to thank the people working on bubbles and ultrasound at the Erasmus MC: Rik Vos, Marcia Emmer, Klazina Kooiman, Paul van Neer, David Maresca, Telli Faez. Although you were on the other side of the country, it always felt like working in the same group. You kept us closely focused on the applications of medical ultrasound. It was a great pleasure working together with all of you. In addition I would like to thank Klazina for everything you learned Anne about targeting. Bracco Research S.A. thank you for supplying the microbubbles. Special thanks to Peter Frinking, Thierry Bettinger, and Marcel Arditi for the inspiring discussions about microbubbles.

Erg belangrijk voor mijn supertijd binnen de vakgroep waren mijn (ex-)kantoorgenoten. Henk Jan, Sander, Ramon en Hanneke, niet alleen hadden we wetenschappelijke discussies, maar we losten ook elkaars matlab en latex problemen op. Toch wil ik jullie vooral bedanken voor het altijd luisteren en het delen van lief en leed. Valeria and Paolo as signs say more than words, VFC is all I need to say. My current office mates Alvaro, Koen, and Laura thank you for being so patient with me during these last stressed months.

An essential part of what made my time at PoF wonderful was the atmosphere and the great colleagues. With you I spent lots of evenings were spent in bars in Enschede and all over the world. Thanks go to all current and past PoF members and hopefully the atmosphere will continue to stay this great! Behalve goede collega's heb ik er ook een aantal goede vrienden aan over gehouden. Bedankt voor de support, koffiepauzes, lunchwandelingen, borrels, feestjes, conferenties en vakanties samen. De zeiltrip van afgelopen jaar is zeker voor herhaling vatbaar! Rory en Anja, Arjan, Erik en Lonneke, Aaldert, Wim, Jeroen, Henk Jan en Ingrid, Peter en Janneke, Jos en Miranda, Hanneke, Sander en Hester, Ramon, Valeria en Lorenzo, Benjamin, Alvaro en Angela, Sylvain, Amy, Chao, James en Catherine, hopelijk

houden we contact.

James and Arjan thank you for helping me with the chapter and the cover layout. I appreciate it very much that you didn't kick me out of your office, during the repeating question: "can we change this just a little bit more".

Carin and Valeria thank you for being my paranymphs. Carin, ook al zagen we elkaar vier jaar geleden veel vaker dan tegenwoordig. Ik vind het nog steeds erg leuk om af te spreken. Bedankt dat je altijd bereid bent om te luisteren en sparren als ik even niet wist wat ik moest doen. Valeria, thanks for being my colleague, neighbour, and especially my friend. Working with you was a pleasure and I enjoyed the times in the lab, our conferences, and dinners together.

Mama, Jan, Rik, Bas en Sanne bedankt dat jullie er altijd voor mij zijn. Opa, omdat je stiekem toch heel trots bent op je kleindochter. Papa bedankt dat je altijd zo trots op me was. "Het leven is mooi, meestal dan."

Arjan, dankjewel voor al je liefde, knuffels, lol, en gezelligheid. Je houdt me met beide benen op de grond en laat me zien dat stress nergens voor nodig is. Ik geniet van onze tijd samen!

About the author

Maria Levina Joanna (Marlies) Overvelde was born on July 9th, 1980, in Hardenberg, the Netherlands. She received her high school education (HAVO) at ’t Noordik in Almelo and graduated in 1997. In the same year she started studying Applied Physics at the Saxion hogeschool Enschede in Enschede. Her studies included two internships of five months, an experimental study at Energy Research Centre of the Netherlands (ECN) in Petten and a numerical study at the Nederlands Centrum voor Laser Research (NCLR) in Enschede. She obtained her Bsc. degree in 2001 on her final project at X-Flow in Wierden.

After her graduation she went to Kurunegala, Sri Lanka, to volunteer at the women’s development foundation (WDF). She taught English, computer lessons to the local government, and worked on the awareness of the position of women. In 2002 she started her master study in Applied Physics at the University of Twente. In March 2006 she obtained her MSc. degree and continued her research on the dynamics of ultrasound contrast agents as a PhD student. The resarch was performed in the Physics of Fluids Group at the University of Twente under guidance of dr. Michel Versluis, prof. dr. ir. Nico de Jong, and prof. dr. Detlef Lohse.

Marlies will continue her career at the Reinier de Graaf Groep in Delft as a Medical Physicist Trainee.